

# High- $Q$ Microresonators as Lasing Elements for Silicon Photonics

Thesis by

Matthew Borselli

In Partial Fulfillment of the Requirements

for the Degree of

Doctor of Philosophy



California Institute of Technology

Pasadena, California

2006

(Defended May 17, 2006)

© 2006

Matthew Borselli

All Rights Reserved

To my wife,  
Amy.

# Acknowledgements

I would first like to thank my advisor, Oskar Painter. Oskar's contagious passion for science gave my research a steady momentum during my entire graduate career. He was nothing short of exuberant over our research successes while giving me optimism and fortitude during extended times of disappointment. He also supported my desire to balance our difficult workload with a life outside of Caltech. He was always respectful of my personal time and showed great concern whenever I would push myself too hard. Although difficult at times, Oskar's hands-on leadership style gave me one of the most educational experiences of my life. I can say with some assurance that virtually every single day of my graduate career was well spent in Oskar's group. I feel privileged to have been one of his first students because of the close friendship that we have formed over the years. Starting our group from empty rooms, each day I tried to pick up as many skills from him as I could, for one very good reason: Whether it is theory or experiment, Oskar always "gets it to work." I cannot explain how humbling and yet inspiring this quality is. I will not soon forget the many things that I have learned while working with Oskar, and I hope always to have the opportunity to learn from him.

I would also like to thank Mark Gyure for helping me get into graduate school and for his steadfast guidance over the years. With his help, I was able to secure two graduate fellowships from NPSC and the Moore Foundation. I thank both institutions for giving me the freedom to pursue my academic dreams without financial worry. At Caltech, there were several classes that shaped the rest of my graduate research. Inside and outside of my research, I have used the intuition that Rob Phillips imparts on his students countless times. Kerry Vahala and Amnon Yariv also formed the basis for my understanding of quantum electronics, and I greatly appreciate the

precision and depth of their teachings on the subject. As part of the EPIC program, Axel Scherer provided us with essential materials and processing capabilities, and Eli Yablonovitch gave us unwavering encouragement and insightful advice on the complex nature of silicon surfaces. I also thank Joe Shmlovich and Inplane Photonics for providing us with remarkable erbium-doped glass for our microlaser devices.

I am forever indebted to Kartik Srinivasan for his tremendous help over the years. Kartik is undoubtedly one of the smartest people I have every met, and his genius is only outdone by his modesty. A person doesn't have to know Kartik for very long before they realize that Kartik's "I'm not sure" is worth more than most everyone else's "it's definitely...". I will forever try to emulate Kartik's unique combination of intelligence, modesty, and happy demeanor. My happiest memories in graduate school were hysterically laughing with Kartik over anything...good or bad. I also had the pleasure of working closely in class and research with colleague Paul Barclay. I have great respect for Paul's capacity to understand any subject inside and out. Paul brings an intense clarity of thinking and courage to any research project. Tom Johnson has been my officemate, colleague, and friend throughout our graduate careers. I cannot say how much I have valued sitting next to this brilliant man. The sum total of knowledge in his head is astonishing. Whether it be swagelok fittings or the religious symbology on the backs of automobiles, I doubt there is a conversational topic that Tom wouldn't be able to contribute meaningfully to. I greatly enjoyed the many inspiring conversations that Kartik, Paul, Tom, and I had while we worked as a team to help build Oskar's group. I constantly strive to be a better person after being humbled by all of their great minds. I would not be earning a PhD without them.

This thesis work could not have been completed without the help from many other Caltech graduate students and staff. I would like to thank: Sean Spillane for his significant help in getting started with finite-element simulations; David Henry for his help on surface passivation techniques; Chris Michael for working out the engineering for the dimpled fiber taper probe; Hermes Huang for his help in the cleanroom; Colin Chrystal for figuring out how to reliably make a fiber taper; David Gleason and Patrick Hurley for useful discussions on silicon surface chemistry; Deniz Armani, Ali Ghaffari, Will Green, and Michael Hochberg for sharing materials and

processing advice; and Joe Haggerty at the aero shop for help in designing the many necessary machined parts. I would also like to thank the many people who gave me so much indirect help during my graduate career, even if it was just someone to talk to: Raviv Perahia, Orion Crisafulli, Jessie Rosenberg, Matt Eichenfield, Stefan Maier, Andrea Martin, Tobias Kippenberg, Brett Maune, Jeff Fingler, Martin Smith-Martinez, Robb Walters, and everyone else I'm sure I've forgotten. Thank you all.

As a child, I spent nearly every other weekend helping my father work around the house. Together, my Dad and I built block walls, garages, culverts, bicycles, and so much more. My dad taught me how to solve problems, use tools, work as part of a team, and have fun the entire time. Although I didn't know it at the time, my Dad made many sacrifices in his life so that he could have time for his kids. I never imagined how valuable those experiences could be until I began helping to build Oskar's research lab. Rarely a day would go by in the lab when I wouldn't mention some pearl of wisdom from my dad. I cherish every minute that my dad and I spent working together, and I cannot wait to start helping him around the house again. Just as my father gave me the skills necessary to succeed in life, my mother gave me the capacity to believe in myself. My mom's infinite love for her kids inspires me to be a better person to this day. There was nothing that my mom would not do to help me, and there is no possible way I could ever repay her. My mother has always been, and will continue to be, my biggest fan. I hope she knows that I am hers as well.

I also have to thank my wonderful family. I thank them for putting up with the know-it-all child that I was, and I thank them for putting up with my idealist rants of today. I dearly miss seeing my family as often as I used to because being with them fills me with such joy. I am rarely as happy as when I am able to attend one of our many family gatherings. To my friends back home and my friends with me now, thank you for keeping me sane. I apologize for the many nights that I spent too much time consumed by numbers and equations, when I should have been more fully enjoying my time with you. I appreciate all that you have done for me, from planning our vacations to protecting my sense of humor from atrophy. A special thanks goes out to all those family and friends that are planning to attend my graduation commencement. You have no idea how much it means to me. You will recognize me on the graduation

stage by the one whose smile is ear to ear and eyes are glassy.

To Amy, my wonderful wife. It would take me another thesis to express how I feel about you. You have done more for me and this thesis than any other. For the past six weeks, you have given me the food by which I have survived, the strength to persevere, and the love that held me together. Thank you for proofreading through 200+ pages of boring physics just to make me feel better. Thank you for putting up with my stress, and thank you for doing your best to reduce it. I respect and revere your intelligence, patience, and devotion more than ever. It was your beautiful smile and contagious laugh that continuously reminded me that happiness is the true goal of life. I dedicate this thesis, and the rest of my life, to you.

# List of Publications

- [1] P. E. Barclay, K. Srinivasan, M. Borselli, and O. Painter, “Experimental demonstration of evanescent coupling from optical fiber tapers to photonic crystal waveguides,” *IEE Elec. Lett.* **39**(11), 842–844 (2003).
- [2] P. E. Barclay, K. Srinivasan, M. Borselli, and O. Painter, “Efficient input and output optical fiber coupling to a photonic crystal waveguide,” *Opt. Lett.* **29**(7), 697–699 (2004).
- [3] P. E. Barclay, K. Srinivasan, M. Borselli, and O. Painter, “Probing the dispersive and spatial properties of planar photonic crystal waveguide modes via highly efficient coupling from optical fiber tapers,” *Appl. Phys. Lett.* **85**(1) (2004).
- [4] K. Srinivasan, P. E. Barclay, M. Borselli, and O. Painter, “Optical-fiber-based measurement of an ultrasmall volume, high- $Q$  photonic crystal microcavity,” *Phys. Rev. B* **70**, 081306(R) (2004).
- [5] M. Borselli, K. Srinivasan, P. E. Barclay, and O. Painter, “Rayleigh scattering, mode coupling, and optical loss in silicon microdisks,” *Appl. Phys. Lett.* **85**(17), 3693–3695 (2004).
- [6] M. Borselli, T. J. Johnson, and O. Painter, “Beyond the Rayleigh scattering limit in high- $Q$  silicon microdisks: theory and experiment,” *Opt. Express* **13**(5), 1515–1530 (2005).
- [7] K. Srinivasan, M. Borselli, T. J. Johnson, P. E. Barclay, O. Painter, A. Stintz, and S. Krishna, “Optical loss and lasing characteristics of high-quality-factor AlGaAs microdisk resonators with embedded quantum dots,” *Appl. Phys. Lett.* **86**, 151106 (2005).

- [8] K. Srinivasan, P. E. Barclay, M. Borselli, and O. Painter, “An optical fiber-based probe for photonic crystal microcavities,” *IEEE Journal on Selected Areas in Communications* **23**(7), 132–139 (2005).
- [9] K. Srinivasan, M. Borselli, O. Painter, A. Stintz, and S. Krishna, “Cavity  $Q$ , mode volume, and lasing threshold in small diameter AlGaAs microdisks with embedded quantum dots,” *Opt. Express* **14**(3), 1094–1105 (2006).
- [10] T. J. Johnson, M. Borselli, and O. Painter, “Self-induced optical modulation of the transmission through a high- $Q$  silicon microdisk resonator,” *Opt. Express* **14**(2), 817–831 (2006).
- [11] M. Borselli, T. J. Johnson, and O. Painter, “Measuring the role of surface chemistry in silicon microphotonics,” *Appl. Phys. Lett.* **88**, 131114 (2006).
- [12] M. Borselli, T. J. Johnson, and O. Painter, “Accurately measuring absorption in semiconductor microphotonics,” (2006). In preparation.

# Abstract

Although the concept of constructing active optical waveguides in crystalline silicon has existed for over twenty years, it is only in the past few years that silicon photonics has been given serious attention as a displacing technology. Fueled by the predicted saturation of “Moore’s Law” within the next decade, universities and industries from all over the world are exploring the possibilities of creating truly integrated silicon opto-electronic devices in a cost effective manner. Some of the most promising silicon photonics technologies are chip-to-chip and intra-chip optical interconnects. Now that compact high-speed modulators in silicon have been achieved, the limiting factor in the widespread adoption of optical interconnects is the lack of practical on-chip optical sources. These sources are critical for the generation of the many wavelengths of light necessary for high-speed communication between the logical elements between and within microprocessors. Unfortunately, crystalline silicon is widely known as a poor emitter because of its indirect bandgap.

This thesis focuses on the many challenges in generating silicon-based laser sources. As most CMOS compatible gain materials possess at most 1 dB/cm of gain, much of our work has been devoted to minimizing the optical losses in silicon optical microresonators. Silicon microdisk resonators fabricated from silicon-on-insulator wafers were employed to study and minimize the different sources of scattering and absorption present in high-index contrast Si microcavities. These microdisks supported whispering-gallery modes with quality factors as high as  $5 \times 10^6$ , close to the bulk limit of lightly doped silicon wafers. An external silica fiber taper probe was developed to test the microcavities in a rapid wafer-scale manner. Analytic theory and numerical simulation aided in the optimization of the cavity design and interpretation of experimental results. After successfully developing surface chemistry treatments

and passivation layers, erbium-doped glasses were deposited over undercut microdisks and planar microrings. Single-mode laser oscillation was observed and carefully characterized for heavily oxidized silicon microdisks. Dropped power thresholds of 690 nW, corresponding to 170 nW of absorbed power, were measured from gain-spectra and Light in–Light out curves. In addition, quantum efficiencies for these lasers were as high as 24%, indicating that this technology may be ready for further development into real-world devices.

# Contents

<b>Acknowledgements</b>	<b>iv</b>
<b>List of Publications</b>	<b>viii</b>
<b>Abstract</b>	<b>x</b>
<b>Glossary of Acronyms</b>	<b>xxviii</b>
<b>Preface</b>	<b>1</b>
<b>1 Introduction</b>	<b>2</b>
1.1 Thesis Organization . . . . .	6
<b>2 Microdisk Optical Resonances</b>	<b>7</b>
2.1 Introduction . . . . .	7
2.1.1 Quality Factor, Photon Lifetime, and Loss . . . . .	8
2.1.2 FSR and Group Velocity . . . . .	9
2.1.3 Finesse . . . . .	10
2.1.4 Mode Volume . . . . .	11
2.1.5 Overlap Factors . . . . .	11
2.2 Master Equation for Systems with Azimuthal Symmetry . . . . .	12
2.3 Analytic Approximation for the Modes of a Microdisk . . . . .	14
2.4 Finite-Element Simulations . . . . .	20
<b>3 Fabrication of Silicon Microdisks</b>	<b>29</b>
3.1 Introduction . . . . .	29
3.2 Material Selection . . . . .	30

3.3	Sample Preparation . . . . .	31
3.4	Lithography . . . . .	33
3.5	Etching and Cleaning . . . . .	37
3.6	Conclusion . . . . .	42
<b>4</b>	<b>Optical Coupling via Fiber Taper Probes</b>	<b>45</b>
4.1	Introduction . . . . .	45
4.2	Optical Properties of Silica Fiber Tapers . . . . .	46
4.3	Fabrication of Fiber Taper Probes . . . . .	49
4.4	Test Setup . . . . .	52
4.5	Modal Coupling . . . . .	58
4.5.1	Optical Coupling to Doublet Modes . . . . .	58
4.5.2	Efficient Taper-Disk Coupling . . . . .	62
<b>5</b>	<b>Optical Loss in Silicon Microdisks</b>	<b>69</b>
5.1	Introduction . . . . .	69
5.2	Surface Scattering . . . . .	71
5.2.1	Derivation of $Q_{ss}$ from the Volume Current Method . . . . .	71
5.2.2	Derivation of $Q_{\beta}$ . . . . .	74
5.2.3	Experiments . . . . .	75
5.3	Beyond the Rayleigh Scattering Limit . . . . .	82
5.3.1	Derivation of $Q_{sa}$ . . . . .	82
5.3.2	Experimental Results and Analysis . . . . .	83
5.3.3	Conclusion . . . . .	92
5.4	Measuring the Role of Surface Chemistry in Silicon Microphotonics . . . . .	94
5.4.1	Design of Surface-Sensitive Optical Modes . . . . .	95
5.4.2	Fabrication and Measurement Technique . . . . .	98
5.4.3	Results and Discussion of Chemical Surface Treatments . . . . .	102
5.4.4	Conclusion . . . . .	110
5.5	Accurately Measuring Absorption in Semiconductor Microresonators . . . . .	111
5.6	Surface Encapsulation Layers . . . . .	117
5.6.1	Silicon Nitride Cap . . . . .	118

5.6.2	Thermal Oxide Cap . . . . .	120
5.6.3	Conclusion . . . . .	123
<b>6</b>	<b>Silicon-Based Lasers</b>	<b>124</b>
6.1	Introduction . . . . .	124
6.2	Raman Effect . . . . .	125
6.3	Erbium-Doped Cladding Lasers . . . . .	130
6.3.1	Introduction . . . . .	130
6.3.2	Achieving Inversion in a “Two-State” System . . . . .	131
6.3.3	Rate Equations . . . . .	132
6.3.4	Cavity Design . . . . .	138
6.3.5	Fabrication and Test Setup . . . . .	144
6.3.6	Saturable Pump Absorption Measurements . . . . .	153
6.3.7	Identification of Optimum Pump Mode . . . . .	158
6.3.8	Swept Piezo Scans . . . . .	163
6.3.9	Stepped Piezo OSA Scans . . . . .	176
6.4	Outlook . . . . .	181
<b>A</b>	<b>Time-Dependent Perturbation Theory</b>	<b>183</b>
<b>B</b>	<b>Approximate <math>\bar{u}_s</math> for the TM case</b>	<b>185</b>
	<b>Bibliography</b>	<b>188</b>

# List of Figures

2.1	The south face of St. Paul’s Cathedral in London . . . . .	7
2.2	Effective slab index, $\bar{n}$ , for a 215 nm thick Si microdisk. The TE slab index (blue curve) extends farther to long wavelengths versus the TM slab index (red curve) because the TE mode is the fundamental mode and possesses no cut-off frequency. . . . .	15
2.3	Analytic dispersion diagram for a 5 $\mu\text{m}$ radius, 215 nm thick Si microdisk against <i>angular</i> momentum. Shown in black are light lines at the disk edge for air and bulk silicon. Thick blue and red lines are light lines at the disk edge using the effective slab indices of refraction. Frequencies outside the testable range (1400 – 1600 nm) have been made slightly transparent. . . . .	17
2.4	Analytic mode spectra for a 5 $\mu\text{m}$ radius, 215 nm thick Si microdisk for the 1500 nm wavelength band. Bars have been drawn from an arbitrary maximum $m$ number and drop <i>down</i> to mimic the mode’s predicted coupling characteristics in a transmission spectrum . . . . .	19
2.5	Geometry plot from Femlab 3.1 for a 5 $\mu\text{m}$ radius, 250 nm thick Si microdisk. . . . .	21
2.6	FEM mesh for a highly resolved 5 $\mu\text{m}$ radius, 250 nm thick Si microdisk. Mesh elements are at most 1/25 a wavelength in the material and have been refined by a factor of 2 around the disk edge periphery. Maximum element size is 0.3 $\mu\text{m}$ in PML, but nearest neighbor mesh points are specified to differ in size by < 5% . . . . .	23
2.7	Zoomed-in view of the FEM mesh in Fig. 2.6 for a highly resolved 5 $\mu\text{m}$ radius, 250 nm thick Si microdisk. . . . .	23

2.8	Plot of $10 * \log_{10}( \mathbf{E} ^2)$ for the $\text{TM}_{1,35}$ mode at $\lambda_0 = 1548.1$ nm using the mesh shown in Fig. 2.6 for a $5 \mu\text{m}$ radius, 250 nm thick Si microdisk. . . . .	24
2.9	Plot of $E_\rho, E_\phi, E_z$ for the $\text{TM}_{1,35}$ mode at $\lambda_0 = 1548.1$ nm using the mesh shown in Fig. 2.6 for a $5 \mu\text{m}$ radius, 250 nm thick Si microdisk. . . . .	25
2.10	Comparison of the approximate versus the FEM dispersion diagram for a $5 \mu\text{m}$ radius, 215 nm thick Si microdisk. The blue dots and circles represent the resonance locations for the $\text{TE}_{1,m}$ family, solved via the approximate and finite-element methods, respectively. Similarly, the red dots and circles represent the resonance locations for the $\text{TM}_{1,m}$ family, solved via the approximate and finite element methods, respectively. . . . .	27
3.1	SEM micrograph of an undercut $9 \mu\text{m}$ diameter microdisk made from an SOI wafer. . . . .	30
3.2	Schematic illustration showing an SOI microdisk after device layer dry-etching. . . . .	32
3.3	(a) $100\times$ magnification optical microscope image of electron-beam resist after develop. Shown is a region where electron beam rests for a short period and then tracked to the left of the image resulting in a very narrow gap in the ZEP resist. (b) Optical microscope image of the same region taken at same magnification after reflowing the resist at $160^\circ\text{C}$ for 5 minutes. . . . .	35
3.4	(a) $100\times$ magnification optical microscope image of electron-beam resist after develop and reflow at $160^\circ\text{C}$ for 5 minutes. Shown is a $10 \mu\text{m}$ radius microdisk etch pattern. . . . .	36
3.5	SEM micrograph of a $5 \mu\text{m}$ radii microdisk after mask reflow and low bias voltage ICP/RIE etching. (a) The optimized etch using 12.0 sccm each of $\text{C}_4\text{F}_8$ and $\text{SF}_6$ . (b) An unoptimized etch using 14.5 sccm $\text{C}_4\text{F}_8$ and 12.0 sccm $\text{SF}_6$ , resulting in heavy polymerization on the sidewalls. . . . .	37
3.6	(a) SEM micrograph of a $5 \mu\text{m}$ radii microdisk after mask reflow and low bias voltage ICP/RIE etching with ZEP mask still in place. (b) Close-up view of the same device showing the smooth sidewalls. . . . .	39

3.7	SEM micrograph of a $4.5 \mu\text{m}$ radii microdisk after mesa isolation etching and HF undercut. . . . .	41
3.8	SEM micrograph of an undercut $5 \mu\text{m}$ radius microdisk. (a) Top view highlighting highly circular definition. (b) Side view of the same disk on the same scale to show the detail of the silica pedestal. . . . .	43
4.1	Electric field components for the $HE_{11}$ mode of a silica fiber taper with $a = 0.5 \mu\text{m}$ at $\lambda_0 = 1550 \text{ nm}$ . The direction of propagation is assumed to be in the $y$ -direction, and the parity is such that the largest field component is in the vertical direction labeled as $z$ . . . . .	47
4.2	Plot of the propagation constant $\beta_f$ of the $HE_{11}$ mode versus the fiber radius, $a$ . The wavelength was held fixed at $\lambda_0 = 1550 \text{ nm}$ . The index of refraction inside the core and cladding was assumed to be 1.45 and 1.0, respectively. . . . .	48
4.3	Digital photographs of the custom taper pulling apparatus. Part (a) shows the torch and fiber mounts on motorized stages. Also shown is the acrylic enclosure used to stabilize the air currents inside the rig. (b) Close-up view of the fiber mounts and hydrogen “hush” tip used to draw the fiber preform gently. . . . .	50
4.4	Schematic drawing of the optimal placement of the fiber taper within the hydrogen torch flame. The reaction zone of hydrogen fuel and ambient oxygen is labeled at the “hot zone” in blue. . . . .	51
4.5	An approximately $1.5 \mu\text{m}$ diameter fiber taper after dimpling and subsequent re-tensioning. . . . .	52
4.6	Acrylic enclosure used for testing optical devices with its front lid raised. On the left is the micropositioning system holding the fiber taper probe, and on the right are the x-y motorized stages that move the samples laterally. The ultra-long working distance objective lens and zoom barrel used to monitor the probing can be seen at the top of the image. . . . .	53

4.7	Optical image taken while testing a non-undercut $5\ \mu\text{m}$ radius microdisk with a $\sim 1.5\ \mu\text{m}$ diameter dimpled fiber taper. Dimple extends down into focus from this view. . . . .	54
4.8	(a) Acquired “wave out” voltage from the Velocity laser versus time since initiating the sweep through GPIB. (b) A close-up view of the software triggering region. . . . .	55
4.9	(a) Acquired waveform generator voltage output used to control the Velocity laser’s fine frequency piezo-stack. (b) Hysteresis curve generated from fiber-based Mach-Zehnder interferometer. . . . .	56
4.10	Spectral dependence of the input power loss channels for the doublet model with unequal standing wave linewidths assuming equal coupling rates. Blue and green lines are the fraction of power that was transmitted and reflected, while red and cyan dashed lines are the dissipated power from the symmetric and anti-symmetric standing waves, $P_c = \gamma_{c,i} a_c ^2$ and $P_s = \gamma_{s,i} a_s ^2$ . Purple dashed line shows the sum of the four loss channels, indicating power conservation. . . . .	61
4.11	Oscillatory dependence on the $\phi$ component of the integrand in Eq. (4.11) for a traveling wave with $m = 25$ coupled to a fiber with propagation constant $4.8\ \mu\text{m}^{-1}$ . Shown in white is a hypothetical $5\ \mu\text{m}$ radius microdisk. . . . .	63
4.12	Analytic dispersion diagram for a $5\ \mu\text{m}$ radius, $215\ \text{nm}$ thick Si microdisk against <i>angular</i> momentum. Shown in black are light lines at the disk edge for air and bulk silicon. Thick blue and red lines are light lines at the disk edge using the effective slab indices of refraction. Frequencies outside the testable range ( $1400 - 1600\ \text{nm}$ ) have been made slightly transparent. Thick magenta line is the dispersion diagram for a $1.2\ \mu\text{m}$ diameter fiber taper positioned at the disk edge. . . . .	65

4.13	Fiber taper coupling measurements of a $\text{TM}_{1,30}$ WGM centered at 1437.5 nm. (a) Normalized transmission minimum as a function of taper-disk gap with undercoupled and overcoupled regions are highlighted. (Inset) High-magnification optical image taken with fiber taper $2\ \mu\text{m}$ from edge of microdisk. (b,c) Selected high-resolution transmission scans taken from the undercoupled and overcoupled regime, as indicated by colored astericks in (a). . . . .	67
5.1	SEM micrographs of a $R = 2.5\ \mu\text{m}$ Si microdisk: (a) side-view illustrating $\text{SiO}_2$ undercut and remaining pedestal, (b) high-contrast top-view of disk, and (c) zoomed-in view of top edge showing disk-edge roughness and extracted contour (solid white line). . . . .	76
5.2	Fiber taper measurements of a $\text{TM}_{1,44}$ WGM of a microdisk with $R = 4.5\ \mu\text{m}$ . (a) Lorentzian full-width half-maximum (FWHM) linewidth versus taper-microdisk gap. (inset) Taper transmission showing high- $Q$ doublet. (b) Resonant transmission depth versus taper-microdisk gap. (inset) loading versus taper-microdisk gap. . . . .	78
5.3	Plot of extracted contour versus arc length. . . . .	80
5.4	Autocorrelation function of the microdisk contour and its Gaussian fit. . . . .	80
5.5	Schematic representation of a fabricated silicon microdisk. (a) Top view showing ideal disk (red) against disk with roughness. (b) Top view close-up illustrating the surface roughness, $\Delta r(s)$ , and surface reconstruction, $\zeta$ . Also shown are statistical roughness parameters, $\sigma_r$ and $L_c$ , of a typical scatterer. (c) Side view of a fabricated SOI microdisk highlighting idealized $\text{SiO}_2$ pedestal. . . . .	83
5.6	Taper transmission versus wavelength showing a high- $Q$ doublet mode for the $R = 30\ \mu\text{m}$ disk. $Q_c \equiv \lambda_0/\delta\lambda_c$ and $Q_s \equiv \lambda_0/\delta\lambda_s$ are the unloaded quality factors for the long and short wavelength modes, respectively, where $\delta\lambda_c$ and $\delta\lambda_s$ are resonance linewidths. Also shown is the doublet splitting, $\Delta\lambda$ , and normalized splitting quality factor, $Q_\beta \equiv \lambda_0/\Delta\lambda$ . . .	85

5.7	Normalized doublet splitting ( $Q_\beta$ ) versus disk radius. (inset) Taper transmission data and fit of deeply coupled doublet demonstrating 14 dB coupling depth. . . . .	86
5.8	Measured intrinsic quality factor, $Q_i$ , versus disk radius and resulting breakdown of optical losses due to surface scattering ( $Q_{ss}$ ), bulk doping and impurities ( $Q_b$ ), and surface absorption ( $Q_{sa}$ ). . . . .	88
5.9	Plot showing absorbed power versus intra-cavity energy for a $R = 5 \mu\text{m}$ disk to deduce linear, quadratic, and cubic loss rates. (inset) normalized data selected to illustrate bistability effect on resonance. . . . .	90
5.10	Composite of surface-sensitive thin-disk optical resonance. (a) SEM micrograph of a $5 \mu\text{m}$ radius SOI microdisk. (b) Zoomed-in view of disk edge showing a TM polarized whispering gallery mode (WGM) solved via the finite-element method, emphasizing large electric field in air cladding. (c) Plot of energy density of the same WGM, emphasizing that 78% of the energy remains in the silicon for future opto-electronic integration . . . . .	96
5.11	Normalized spectral transmission response of a $5 \mu\text{m}$ radius microdisk resonator with the fiber taper placed $0.6 \pm 0.1 \mu\text{m}$ away from the disk edge and optimized for TM coupling. The spectrum was normalized to the response of the fiber taper moved $3 \mu\text{m}$ laterally away from the disk edge. Classification of the modes is done via the notation $\{p, m\}$ where $p$ and $m$ are the number of antinodes radially and azimuthally, respectively.	99
5.12	(a) Normalized high-resolution scan of the $\text{TM}_{1,31}$ mode at $\lambda = 1459 \text{ nm}$ in Fig. 5.11. $\Delta\lambda$ and $\delta\lambda$ indicate the CW/CCW mode splitting and individual mode linewidth, respectively. (b) Electric energy density plot and high-resolution scan of a $40 \mu\text{m}$ radius microdisk, showing the reduced loss of a bulk TE WGM. . . . .	101

5.13	Taper transmission versus wavelength showing $\text{TM}_{1,31}$ doublet mode after each chemical treatment and accompanying schematic of chemical treatment. (a) Initial fabrication, illustrating surface roughness and absorption loss mechanisms. (b) Triple Piranha/HF cycle described in Table 5.3 removes damaged material and partially passivates surfaces states. (c) Single Piranha/HF cycle followed by an additional Piranha allowing controlled measurement of Piranha oxide. (d) HF dip to remove chemical oxide from previous treatment and restore passivation. . . . .	104
5.14	(a) Schematic representation of testing apparatus. (b) Examples of power-dependent transmission versus wavelength data used to separate the absorption from the total loss using the thermal bistability effect. .	112
5.15	Plot of normalized nonlinear absorption versus relative electric-field cavity energy along with a linear fit. . . . .	113
5.16	(a) Plot of thermally-induced wavelength shift ( $\Delta\lambda_{th}$ ) versus relative dropped power ( $P_d$ ) along with nonlinear and linear absorption model fits. (inset) Global slope, $\Delta\lambda_{th}/P_d$ , versus $P_d$ for the same dataset. (b) Wavelength dependent intrinsic linewidth for a family of high- $Q$ WGMs, along with the measured delineation between scattering loss and linear absorption. Note that the fit shown in (a) was used to generate the data point at 1447.5 nm in (b). . . . .	116
5.17	Summary of best linewidths after selected processing steps for 5 – 10 $\mu\text{m}$ radii disks fabricated with a stoichiometric $\text{SiN}_x$ encapsulation layer and forming gas anneal. . . . .	119
5.18	Summary of best linewidths after selected processing steps for 5 – 10 $\mu\text{m}$ radii disks fabricated with a thermal oxide encapsulation layer along with various annealing trials. . . . .	121
5.19	(a) Summary of best linewidths after selected processing steps for 5 – 10 $\mu\text{m}$ radii disks fabricated without an initial protective cap. This sample also had a thermal oxide encapsulation layer but no FGA. (b) High-resolution transmission spectrum of 1444.2 nm resonance on a 7.5 $\mu\text{m}$ radius disk after the final high-temperature anneal. . . . .	122

6.1	Schematic depiction of two-photon absorption (TPA) and the resulting free-carrier absorption (FCA). . . . .	126
6.2	Broad OSA scan of reflected power from a $R = 15 \mu\text{m}$ silicon microdisk showing reflected pump and stimulated Raman line. . . . .	128
6.3	(a) Narrow OSA scan with resolution bandwidth of 0.08 nm of Raman emission showing resonantly enhanced behavior, (b) similar narrow scan of a $R = 5 \mu\text{m}$ disk illustrating decrease in density of modes as compared to (a), (inset to (b)) Raman power, $P_R$ versus input power, $P_i$ , for the $R = 5 \mu\text{m}$ disk. . . . .	128
6.4	Multiplet energy levels for erbium-doped oxides for the telecommunications relevant $\sim 1550$ nm signal band with a $\sim 1480$ nm pump. The green dots represent $\text{Er}^{3+}$ ions in a highly inverted distribution. . . . .	131
6.5	Assumed $\text{Er}^{3+}$ spectrally varying absorption and emission cross sections, $\sigma^a(\lambda)$ and $\sigma^e(\lambda)$ used throughout this work (adapted from [1,2]). . . . .	133
6.6	FEM simulations of <b>TE polarized</b> Er-doped cladding laser modes at 1550 nm for various buffer layer thermal oxidation times. Starting disk parameters were: $R = 20 \mu\text{m}$ radius, $h_{\text{Si}} = 195$ nm, $h_{\text{Er}} = 300$ nm, $t_{\text{BOX}} = 3 \mu\text{m}$ . (a) Spatial dependence of $ \mathbf{E}(\rho, z) ^2$ for $\Gamma_{\text{Si}} = 0.28$ (highlighted by gray bar in (b)). (b) Fraction of electric energy in each dielectric component versus buffer layer thickness (and equivalent remaining silicon core). . . . .	139
6.7	FEM simulations of <b>TM polarized</b> Er-doped cladding laser modes at 1550 nm for various buffer layer thermal oxidation times. Starting disk parameters were: $R = 20 \mu\text{m}$ radius, $h_{\text{Si}} = 195$ nm, $h_{\text{Er}} = 300$ nm, $t_{\text{BOX}} = 3 \mu\text{m}$ . (a) Spatial dependence of $ \mathbf{E}(\rho, z) ^2$ for $\Gamma_{\text{Si}} = 0.30$ (highlighted by gray bar in (b)). (b) Fraction of electric energy in each dielectric component versus buffer layer thickness (and equivalent remaining silicon core). . . . .	140

6.8	FEM simulation of radiation $Q$ versus the thermal oxide buffer layer thickness (and equivalent remaining silicon core) for $\lambda_0$ fixed at 1550 nm. Starting disk parameters were: $R = 20 \mu\text{m}$ radius, $h_{\text{Si}} = 195 \text{ nm}$ , $h_{\text{Er}} = 300 \text{ nm}$ , $t_{\text{BOX}} = 3 \mu\text{m}$ . . . . .	141
6.9	SEM micrograph of an early erbium-doped cladding silicon microdisk after FIB cross-sectioning. Top image was taken with a 30 kV accelerating voltage for best resolution, while the bottom image was taken with a 5 kV accelerating voltage for best material contrast (note: 2 nm buffer layer is present but not discernable). . . . .	142
6.10	SEM images of rings after the final chemical treatments and 30 nm thermal oxidation. (a) Top-view of a $20 \mu\text{m}$ diameter, $2 \mu\text{m}$ width ring. (b) Side view showing smooth ring sidewalls and a slight BOX undercut due to the final chemical treatment. . . . .	145
6.11	Transmission spectrum of a high- $Q$ mode at $\lambda_0 = 1428.7 \text{ nm}$ on a $80 \mu\text{m}$ diameter, $2 \mu\text{m}$ width ring after final chemical treatments and 30 nm thermal oxidation. . . . .	147
6.12	SEM micrographs of silicon rings after chemical treatments, 30 nm thermal oxidation, and 300 nm erbium-cladding deposition. (a) $20 \mu\text{m}$ radius, $1 \mu\text{m}$ width ring. (b) $2 \mu\text{m}$ width ring after FIB cross-sectioning. (c) Higher magnification view of cross section where silicon core, thermal oxide and erbium oxide are clearly visible. . . . .	148
6.13	Test setup used to resonantly pump the silicon microresonators and collect the emitted light. “SP” (“LP”) refers to a short (long) pass edge filter. The top optical image was taken with a long working distance lens and CCD camera during testing. The dimpled fiber taper and $20 \mu\text{m}$ radius fully-oxidized microdisk with Er-doped cladding are shown. The bottom plot is an OSA power scan at the output of the two-stage filter at maximum input power showing that only erbium emission is being collected at lower detector. . . . .	150

- 6.14 Normalized transmission spectra of a 10  $\mu\text{m}$  radius silicon microdisk after a 60 nm thermal oxidation and 300 nm erbium-doped glass deposition. The blue scan was taken at 0.14  $\mu\text{W}$  of input power, while the green scan was taken at 45  $\mu\text{W}$ . The black dots indicate transmission minima for 50 intermediate powers. The red curve is a doublet fit to the lowest power scan, and fit parameters are listed in red. . . . . 152
- 6.15 (a) Total linewidth for the resonance described in Fig. 6.14 as a function of stored pump photons. The data was taken from a 10  $\mu\text{m}$  radius silicon microdisk after a 60 nm thermal oxidation and 300 nm erbium-doped glass deposition. (b) OSA scan of saturated emission. (Resolution bandwidth was 0.1 nm and sensitivity was 12 pW.) . . . . . 155
- 6.16 Loss characterization for a single family of modes in a 20  $\mu\text{m}$  radius fully oxidized microdisk after 300 nm of Er-doped cladding was deposited. Blue dots represent total “cold” decay rate and red dots represent measured  $\gamma_p^a$  at each wavelength for below-threshold data. (Inset) Threshold dropped powers needed to obtain lasing versus wavelength. Lasing was always single mode at 1560.2 nm, regardless of pump wavelength. Red curve in inset is a model for expected dropped power threshold using cross sections plotted in Fig. 6.5 and assuming  $\gamma_s = 1.3$  Grad/s. . . . . 156
- 6.17 Broad external pump laser scan of an undercoupled fully oxidized 20  $\mu\text{m}$  radius microdisk. Scan speed was 10 nm/s, and input power was 670  $\mu\text{W}$ . (a) Undercoupled broad-scan transmission spectrum (b) Corresponding photoluminescence excitation spectrum. Starred mode shows highest external efficiency. . . . . 159
- 6.18 (a) Composite spectrum of a fully oxidized 20  $\mu\text{m}$  radius microdisk. 1400 nm spectrum is normalized external pump laser scan, with taper position optimized for critical coupling to 1477.1 nm resonance. Red curve is normalized collected photoluminescence while pumping on 1477.1 nm resonance. Green dashed lines indicate the laser’s family. 1560 nm spectrum is normalized external laser scan with 1.4  $\mu\text{W}$  input power. (b) Zoomed-in view between 1560 – 1625 nm. . . . . 160

- 6.19 (a) Zoomed-in view of Fig. 6.18(a) between 1420 – 1500 nm. (b) Corresponding photoluminescence excitation spectrum, plotted on an arbitrary logarithmic scale (max peak to min peak is approximately two orders of magnitude). Green dashed lines indicate laser’s family (seen only in PLE). . . . . 162
- 6.20 Unidirectional photoluminescence spectrum, pumped at 1477.1 nm with 600  $\mu\text{W}$  of input power. (Resolution bandwidth was 0.1 nm and video bandwidth was 60 Hz). . . . . 162
- 6.21 Swept piezo spectra of a fully oxidized 20  $\mu\text{m}$  radius microdisk after 300 nm erbium-doped glass deposition. (a) Selected normalized transmission spectra for 0.1 to 38  $\mu\text{W}$  of input power. The black asterisks indicate transmission minima. The red curve is a doublet fit to the lowest power scan, and fit parameters are listed in red. (b) Selected corresponding photoluminescence excitation spectra, along with black asterisks marking the “on-resonance” condition. . . . . 164
- 6.22 Total linewidth for the resonance described in Fig. 6.21 as a function of stored pump photons. The data was taken on a fully oxidized 20  $\mu\text{m}$  radius microdisk after 300 nm erbium-doped glass deposition. Red curve is a saturable absorption fit using Eq. (6.17) for the below threshold data ( $M_p < 3000$ ). . . . . 166
- 6.23 Pump gain ( $g_p \equiv \gamma_p - \gamma_{\text{tot},p}$ ) for the resonance described in Fig. 6.21 as a function of stored pump photons. The data was taken on a fully oxidized 20  $\mu\text{m}$  radius microdisk after 300 nm erbium-doped glass deposition. Black curve is a full rate equation fit using Eqs. (6.19a - 6.19c). . . . . 168
- 6.24 Collected signal power for the resonance described in Fig. 6.21 as a function of stored pump photons. The data was taken on a fully oxidized 20  $\mu\text{m}$  radius microdisk after 300 nm erbium-doped glass deposition. Red curve is collected lasing mode emission  $P_L = (\gamma_{\text{ext}}/2)(M_L \hbar \omega_L)$ , and green curve is collected spontaneous emission  $P_x = (\gamma_{\text{ext}}/2)(M_x \hbar \omega_x)$  from all other modes. Black curve is total collected power  $P_s = P_L + P_x$ . 169

- 6.25 (a) Collected signal power for the resonance described in Fig. 6.21 as a function of absorbed power,  $P_{\text{abs}} = \ell_p(M_p \hbar \omega_p)$ . The data was taken on a fully oxidized 20  $\mu\text{m}$  radius microdisk after 300 nm erbium-doped glass deposition. Red curve is collected lasing mode emission  $P_L = (\gamma_{\text{ext}}/2)(M_L \hbar \omega_L)$ , and green curve is collected spontaneous emission  $P_x = (\gamma_{\text{ext}}/2)(M_x \hbar \omega_x)$  from all other modes. Black curve is total collected power  $P_s = P_L + P_x$ . (b) logarithmic version of (a) to emphasize low-power region. . . . . 172
- 6.26 (a) High-power data showing collected signal power for the resonance described in Fig. 6.21 as a function of dropped power. The data was taken on a fully oxidized 20  $\mu\text{m}$  radius microdisk after 300 nm erbium-doped glass deposition. (Inset) Normalized transmission versus wavelength for several input powers. (b) Zoomed-in view of the low power end of the dataset. Red dashed curve is a linear fit to all above threshold data, and green curve is a linear fit to above threshold data for  $P_d < 20 \mu\text{W}$ . 175
- 6.27 Transmission and OSA spectra used for a stepped piezo L-L curve. (a) Blue curve is a swept piezo scan taken immediately prior to stepping the piezo voltage (red dots) down the resonance for a fixed input power. An  $\sim 1$  pm drift caused by small temperature shifts between sample and external laser over the course of the stepped scan. (b) A representative OSA spectrum for each stepped piezo voltage. The specific scan was chosen to be near laser threshold and is marked with a star in (a). . . . 178
- 6.28 L-L curve for data extracted from stepped piezo scans. Blue dots represent laser mode's photon population while green circles represent a typical strongly coupled but nonlasing mode at 1556.3 nm. Red curve is the same fit as used in Fig. 6.24 except for a slightly modified  $\gamma_{\text{ext}}$  to account for slightly different taper positions. (b) Linear scale of (a) with inset of threshold region. . . . . 180
- B.1 Comparison of approximate form of  $\bar{u}_s(\hat{\mathbf{z}})$  and total  $\bar{u}_s$  calculated using the FEM. . . . . 187

# List of Tables

5.1	Summary of theoretical and measured mode parameters for $R = 2.5$ and $4.5 \mu\text{m}$ Si microdisks. Theoretical surface-scattering values for $Q_{ss}$ and $\Delta\lambda_{\pm m}$ are shown in parentheses. . . . .	77
5.2	Summary of $\text{TM}_{1,31}$ characteristics after various chemical treatments .	105
5.3	Summary of successive steps for a Piranha oxidation surface treatment	105

# Glossary of Acronyms

**DEMUX** Demultiplexed

**BOX** Buried oxide layer for SOI wafers

**FCA** Free-carrier absorption

**FEM** Finite-element method

**ICP/RIE** Inductively-coupled plasma / reactive ion etching

**MUX** Multi-plexed

**OSA** Optical spectrum analyzer

**Q** Quality factor

**PECVD** Plasma-enhanced chemical vapor deposition

**PL** Photoluminescence

**PLE** Photoluminescence excitation

**PVD** Physical vapor deposition

**SEM** Scanning electron microscope

**SOI** Silicon-on-insulator

**TPA** Two-photon absorption

**WGM** Whispering-gallery mode

# Preface

Being a part of Oskar Painter's group, I had many opportunities to work on one of his passions, photonic crystals, as did both of my contemporaries, Kartik Srinivasan and Paul Barclay. Photonic crystals represent the ultimate in control over light because of their unique ability to lithographically control the group velocity photons experience as a function of space. While this absolute control is necessary in some photonic applications, the proper design and fabrication of these structures is a formidable undertaking. Numerical simulations of photonic crystals require slow three-dimensional finite difference solvers, and high quality fabrication requires extensive lithography calibrations and etch optimizations. My brilliant friends Kartik and Paul, bravely chose to begin their research in photonic crystals and made significant contributions in that field, of which I played a small part. Over the years, my research gravitated towards high-index contrast whispering-gallery modes, partly because I did not feel optimistic in competing with Kartik and Paul and partly because my heart searched for a path of less resistance. I believe that it is the most elegant of solutions that produce the most utility for many reasons. An elegant solution is easily taught during a technology's maturity from initial idea to mass-produced widget, giving it an advantage in applied physics. As a corollary, fabrication and experiment will inevitably become derailed many times (as mine has done time and time again!) when attempting to prototype a technology. However, by definition the elegant solution lives in a smaller parameter space, always making it possible to rediscover the proper path quickly. Learning to have fortitude is one of the great lessons that my advisor and colleagues have taught me during graduate school. I would like to believe that I may have also impressed upon them that the desire for simplicity is not always a weakness but can be a guiding light during the course of invention.

# Chapter 1

## Introduction

In 1985, Richard Soref and others proposed that single-crystal silicon could be used as an optical waveguide material [3,4]. Inspired by silicon's transparency at the telecommunication wavelengths, 1300 and 1550 nm, they believed that silicon could be used to add optical functionality to microelectronics applications. Their seminal papers calculated that crystalline silicon could guide light on a chip with losses less than 0.01 dB/cm for lightly doped wafers. In addition, the guided light could also be switched at high speeds by electronically changing the local free-carrier density. During the next twenty years, the economies of scale present in lithographic fabrication allowed the microelectronics industry to grow to a \$160 billion dollar industry. As a consequence, the vast amounts of money spent on engineering silicon as an electronic material overshadowed Soref's early contributions. Today the gate oxide thickness of modern transistors is roughly five atomic layers, with eight metal wire layers required to transport all the signals within a microprocessor. The reduced-dimension of these metal wires amid increasing clock-speeds is beginning to cause significant cross-chip signal latencies. To make matters worse, "Moore's Law" scaling of transistor cost and density is predicted to saturate in the next decade [5]. Thus, silicon-based microphotonics is once again being explored for the routing and generation of high-bandwidth signals. Optical microprocessor interconnects offer the promise of decreased latencies, reduced power consumption, and immunity to electromagnetic interference. The relatively large pitch of the top global interconnects makes the optical waveguide an interesting alternative to existing copper interconnects. In May of 2004, a large group of researchers at Intel compared the performance and cost of optical intercon-

nects to Cu interconnects for clock distribution and intrachip global signaling [6]. They concluded that in conjunction with wavelength division multiplexing, optical interconnects offer a low latency alternative to existing metallic wire technologies for global signaling.<sup>1</sup> These optical interconnects would need to be high-index contrast to achieve small footprints and tight waveguide turning radii. Optical losses of the waveguides and potential on-chip laser sources would need to be kept to a minimum for power-efficiency and heat management. Wavelength division multiplexing (WDM) would be essential to cost effectively use all of the available bandwidth in each optical waveguide. On-chip modulators and detectors would also be crucial for transducing the information between optical and electronic carriers. Most importantly, the fabrication processes would need to maintain CMOS compatibility in order to leverage the near half-century of processing development in the microelectronics industry [7, 8].

At the same time, research groups around the world were making revolutionary advances in Si optoelectronics. The first major achievement was the demonstration of an Si optical modulator working in excess of 1 Gbit/sec [9], a 50 fold improvement over prior art. Based on the concepts that Soref suggested 20 years prior, fast optical modulation was achieved with free-carrier dispersion in a MOS structure. Subsequent refinements to this technique realized modulation rates of 10 Gbit/sec [10]. Then an all-optical high-speed switch was created [11]. Using free-carriers generated from two-photon absorption (TPA), this work managed to switch light in less than 500 ps using light pulses with energies as low as 25 pJ. Within a year, the same group demonstrated compact all-optical gigabit modulation with control powers of 4.5 mW [12, 13]. Photonic crystal versions using thermal bistabilities and then free-carrier dispersion reported on similar performance with drastically reduced switching energies [14–16]. These high- $Q$  photonic crystal cavities were based on small perturbations to photonic crystal waveguides along with exquisite fabrication [17–22]. Around the same time, researchers at UCLA and Intel reported the first demonstrations of a pulsed [23, 24] and then CW silicon laser [25] based on the Raman effect.

Aiding in these and previous developments of integrated optical and electronic Si circuits is the availability of high-index contrast silicon-on-insulator (SOI) wafers.

---

<sup>1</sup>Signaling refers to the high-speed communication between different logical units within the chip.

SOI provides the tight optical confinement of light necessary for high-density optoelectronic integration and nonlinear optics. In addition, the high-quality underlying thermal oxide provides simultaneous exceptional photonic and electronic isolation. As Si microphotonic device functionality and integration advances, and light is more often routed into the Si, it will be important to develop low-loss Si microphotonic circuits in addition to the already low-loss glass-based planar lightwave circuits (PLCs) [26,27]. One key element in such circuits is the microresonator. Microresonators allow light to be distributed by wavelength or localized to enhance nonlinear interactions.

This thesis details several advances in optical design and silicon microfabrication that have allowed for the creation of SOI-based microdisk and microring optical resonators with extremely smooth high-index-contrast etched sidewalls [28]. These microdisks and microrings provide tight optical confinement down to radii of  $1.5 \mu\text{m}$ , while maintaining the low loss of the high-purity crystalline silicon. Resonant mode quality factors as high as  $Q \sim 5 \times 10^6$  are measured, corresponding to an effective propagation loss as small as  $\alpha \sim 0.1 \text{ dB/cm}$ . Inspired by the ultra-smooth glass microspheres [29,30] and microtoroids [31] formed under surface tension, this work uses an electron-beam resist reflow technique [32] and low DC-bias etch [33] to significantly reduce surface imperfections at a resonator's edge. A fiber-based, wafer-scale probing technique was also developed to rapidly and non-invasively test the optical properties of these fabricated devices. This fiber taper probe allowed for a comprehensive analysis and in some cases reduction of the different optical loss mechanisms in SOI microdisks, including the absorption of the surface-states at the edge of the disk (for smaller microdisks) and the bulk Si free-carrier absorption due to ionized dopants (for larger microdisks).

After carefully studying the properties of all-silicon microcavities, we sought to create silicon optical waveguides and resonators in a hybrid material environment capable of displacing a significant fraction of the energy from the silicon into an engineered cladding while maintaining the best qualities of silicon as an optoelectronic material. The cladding of the hybrid silicon-on-insulator (HySOI) waveguide could be functionalized in a variety of ways for applications that benefit from large field intensities in the cladding. A HySOI waveguide could be used to create functional-

ized biological and chemical sensors, lasers, and nonlinear optical components. While many research groups around the world are also developing similar technology, the methodology described in this thesis presents several technological advantages. The basic concept is the following: in order to effectively use the engineered cladding, the optical field of the mode must cross a silicon boundary. However, the optical engineer is free to choose which silicon surface will be exposed to large field intensities. Through chemo-mechanical polishing, the top surface of the SOI wafer can be made to be of epitaxial quality. In contrast, the etched sidewalls of Si waveguides and microcavities will always possess significantly worse surfaces by comparison. Thus, we optimized our mode profiles for maximum overlap with a top cladding as opposed to a lateral cladding.

Through a combination of theory and simulation, we designed and fabricated devices of predominantly TM polarization (dominant component of the electric field polarization perpendicular to the top surface of the SOI). We found that the use of TM modes enhanced the energy overlap with the active material around the top silicon layer while decreasing the sensitivity to fabrication-induced imperfections in the vertical sidewall. Upon testing, it became clear that the newly designed microresonators possessed extreme sensitivity to the top silicon surface. As a result, surface treatments and thin encapsulation layers had to be developed in order to preserve the quality factor upon deposition of the functionalized cladding [34,35]. As an initial example of the power of this technique, erbium-doped glass cladding was deposited over the optimized structures. Through resonant optical pumping with the fiber probe, efficient single-mode microlasers with thresholds below a microwatt were demonstrated. In addition, resonant pumping permitted a detailed laser performance characterization, and many key parameters were extracted from gain curves and Light in–Light out measurements. With further engineering, these microlaser designs will hopefully provide the first high-volume-manufacturing ready SOI optical sources that are electrically tunable while being capable of delivering technologically relevant power levels with broadband gain.

## 1.1 Thesis Organization

This thesis is separated into the five basic components needed to create a silicon microlaser: microcavity theory, fabrication, optical coupling, loss minimization, and laser realization. Chapter 2 lays the mathematical and optical physics framework upon which this thesis is based. Beginning from some basic microcavity terminology and the Maxwell equations, this chapter unfolds a set of results that will be useful in understanding the later experimental observations and interpretations. Chapter 3 provides a basic but detailed fabrication recipe that is common to all of the devices presented in this thesis. Chapter 4 not only describes the method and apparatus used to test the microcavities, but also includes a theoretical description of how to interpret the acquired transmission spectra. Doublet modes, evanescent coupling, and phase matching considerations are presented in the final section of this chapter. Chapter 5 provides a more or less chronological account of our journey that was required to make high- $Q$  devices that were suitable for engineered claddings. Much of the later work in this chapter was done in conjunction with my colleague Thomas Johnson. The final chapter, Chapter 6, provides a brief overview of previous work on silicon-based lasers before taking a detailed look at Raman and erbium-doped glass lasers. The majority of the chapter is devoted to the proper design, fabrication, and modeling of an erbium-doped cladding laser on silicon. The appendices provide supporting mathematical treatments that are used throughout various sections of the thesis.

## Chapter 2

# Microdisk Optical Resonances

### 2.1 Introduction



Figure 2.1: The south face of St. Paul's Cathedral in London

In the early 20th century, a quirk of the top gallery in St. Paul's Cathedral, shown in Fig. 2.1, allowed whispers to be audibly heard evenly around the perimeter of the gallery. Many top physicists including Lord Rayleigh and Raman posited explanations for this effect. Subsequent testing for the next several decades showed that Lord Rayleigh's observations were the most telling. In describing the problem of the whispering gallery, he wrote, "the whisper seems to creep round the gallery horizontally, not necessarily along the shorter arc, but rather along that arc towards which the whisperer faces" [36]. While these experiments were done with sound waves, the mental picture of a packet of sound repeatedly bouncing off the edges of the smooth,

hard walls of the gallery proves to be the same mental picture for their optical counterpart. When properly excited, optical waves can be coerced to circulate around the periphery of a circular material with high index of refraction. By optimizing the lithographic etching, these devices can support modes that hold onto packets of light for hundreds of thousands of round-trips before escaping to the environment. This chapter serves as an introduction to optical microcavities, with special attention paid to whispering-gallery modes (WGM) of silicon microdisks. After discussing the essential microcavity terminology, the master equation for these resonances will be outlined. Then approximate and numerically exact solutions of the master equation will be described in great detail.

### 2.1.1 Quality Factor, Photon Lifetime, and Loss

Much of this thesis is concerned with maximizing the quality factor,  $Q$ , of silicon microcavities. The definition of the quality factor extends well beyond that of microphotonics and is generally defined for all resonant elements as [37, 38]

$$Q \equiv \frac{\omega \cdot U_c}{P_{\text{loss}}}, \quad (2.1)$$

where  $\omega$  is the frequency of the oscillation,  $U_c$  is the stored energy in the resonator, and  $P_{\text{loss}}$  is the power dissipated by the resonator. In words,  $Q$  is defined as  $2\pi$  times the ratio of the time-averaged energy stored in the cavity to the energy loss per cycle. From conservation of power, this definition immediately implies that the time-dependence for the decay of energy inside the resonator is given by

$$U_c(t) = U_0 e^{-\omega t/Q}, \quad (2.2)$$

in the absence of further sourcing of the cavity. By a simple Fourier transform, the quality factor can also be measured spectrally rather than by the “ring down” of the previous equation according to

$$Q = \frac{\omega}{\delta\omega} \quad (2.3)$$

where  $\delta\omega$  is the full width at half maximum (FWHM) of the resonance. One can also measure the quality factor by wavelength according to  $Q = \lambda_0/\delta\lambda$ , provided the resonance is very low loss. Another common term in optical microcavity research is the photon lifetime,  $\tau$ . The photon lifetime is the time required for the energy to decay to  $e^{-1}$  its original value and is given by  $\tau \equiv Q/\omega$ . The quality factor can be related to standard absorption coefficients,  $\alpha$ , via the group velocity of the optical energy, such that  $\alpha = \omega/(Qv_g)$ .<sup>1</sup>

$Q$  is the single most important parameter to optimize for silicon microlasers because the loss in a microcavity must be overcome by the gain in the microcavity. To date, there are few high-gain materials that can be placed in the near field of a silicon microcavity. Therefore one must create a laser through extraordinary  $Q$ 's. High- $Q$  cavities are also important for narrowband filtering, as well as the observation of large nonlinear and cavity QED effects.

### 2.1.2 FSR and Group Velocity

The free-spectral range (FSR) is defined as the frequency spacing ( $\delta\omega_{\text{FSR}}$ ) or wavelength spacing ( $\delta\lambda_{\text{FSR}}$ ) between the modes of an optical cavity. Generally speaking, the FSR always increases as the physical size of the resonator is shrunk. The FSR is important for both technological and scientific reasons. From a technology standpoint, a large FSR permits the development of single-mode and high-efficiency lasers from materials with broadband gain. A large FSR also allows for narrowband filtering for dense wavelength division multiplexing (DWDM) applications without the risk of channel cross-talk (assuming a constant  $Q$ ). From a scientific perspective, the FSR provides an indirect measure of the speed of propagating packets of light inside the resonator, otherwise known as the group velocity,  $v_g \equiv \partial\omega/\partial\beta$  [37, 39]. For the case of azimuthally symmetric resonators, the wavevector,  $\beta$ , changes as a function of radius within an optical mode. However, the angular wavevector,  $m$ , is always a well-defined quantity and can be used to find the linear momentum<sup>2</sup> of the photons in the material at any radius,  $\rho$ , according to  $\beta = m/\rho$ . This relation can then be

---

<sup>1</sup>All of the above relations are somewhat arbitrary and circular, but one should be careful to maintain a set of self-consistent definitions.

<sup>2</sup>From this point on, I shall use the term ‘‘momentum’’ and ‘‘angular momentum’’ interchangeably with ‘‘wavevector’’ and ‘‘angular wavevector’’ in order to make a connection with the reader’s intuitions in classical mechanics.

used to relate group velocity to FSR for the case of whispering-gallery modes:

$$v_g \equiv \frac{\partial \omega}{\partial \beta} = \frac{\delta \omega_{\text{FSR}}}{\frac{m+1}{\rho} - \frac{m}{\rho}} = \rho \delta \omega_{\text{FSR}}. \quad (2.4)$$

For all but the smallest of microdisks,  $v_g$  is approximately constant across the optical mode and is given by

$$v_g \approx R \delta \omega_{\text{FSR}} = \frac{2\pi R}{\tau_{\text{rt}}}, \quad (2.5)$$

where  $\tau_{\text{rt}}$  is an optical packet's round-trip time. Defining the group index in terms of the speed of light in vacuum,  $n_g \equiv c/v_g$ , allows connection to standard Fabry-Perot resonators by rewriting the last equation as  $\delta \nu_{\text{FSR}} = c/(2n_g \pi R)$ .

### 2.1.3 Finesse

The two previous sections have laid the ground work to describing the oftentimes huge cavity build-up of photons inside the resonator proportional to a quantity called the finesse,  $\mathcal{F}$ . The finesse of a cavity is defined by [37]

$$\mathcal{F} \equiv \frac{\delta \omega_{\text{FSR}}}{\delta \omega}, \quad (2.6)$$

and for azimuthally symmetric modes can be quickly calculated by  $\mathcal{F} = Q/m$ . In this thesis,  $\mathcal{F}$  can be as high as  $7 \times 10^4$ , among the highest reported values of finesse to date in semiconductor resonators. A simple argument based on the previous two sections can put the finesse into a physically intuitive context. In steady-state, the average number of round-trips a photon makes before leaving the cavity is given by  $\tau/\tau_{\text{rt}} = \mathcal{F}/(2\pi)$ . Assuming a linear relationship between dropped power,  $P_d$ , and stored cavity energy implies that the circulating power is  $\mathcal{F}/(2\pi)P_d$ . Consequently, hundreds of watts can be made to circulate inside a microcavity by dropping only  $\sim 1\text{--}3$  mW from an external waveguide.

### 2.1.4 Mode Volume

The volume an optical mode occupies is an essential but nebulous quantity to define in microphotonics. A mode's volume is crucial in relating the number of photons that reside in a mode to any nonlinear effect that those photons could produce. Thus, a common use of mode volume is in a relation such as

$$I = \frac{\lambda_0}{2\pi n_g} \left( \frac{Q}{V} \right) P_d, \quad (2.7)$$

where  $I$  is the optical intensity of the field inside the resonator. One way to calculate the mode volume would be to calculate the mode's FWHM for each spatial direction and multiply them together. A more common definition of mode volume is

$$V = \frac{\int n^2(\mathbf{r}) |\mathbf{E}(\mathbf{r})|^2 dV}{\max [n^2(\mathbf{r}) |\mathbf{E}(\mathbf{r})|^2]}. \quad (2.8)$$

By comparing the above definition to Eq. (2.7), it becomes clear that this definition of mode volume relates dropped power to the *maximum* intensity inside the microcavity. This mode volume is thus a lower bound for the volume that a mode "occupies." In some instances, this definition makes sense as is the case in optimally placed quantum dots [40–42], or if one is trying to avoid nonlinearities in the cavity. However, usually one wishes to know the spatially averaged behavior of the resonator, so a more accurate mode volume would replace the denominator of Eq. (2.8) with an average energy density instead of a maximum energy density. Fortunately, all of these definitions give similar results for most cavity geometries.

### 2.1.5 Overlap Factors

Many physical process, including gain and loss rates, depend upon not the volume of the optical mode, but the energy distribution throughout the mode. Whether it be a volume or a surface, the impact that a specific region has on the loss or gain rate of energy for a mode depends upon the fraction of electric-energy in the region, as illustrated by the derivation in Appendix A. For volumetric regions of interest ( $\delta V$ ), this fraction is defined as

$$\Gamma = \frac{\int_{\delta V} n^2(\mathbf{r}) |E(\mathbf{r})|^2 dV}{\int n^2(\mathbf{r}) |E(\mathbf{r})|^2 dV}. \quad (2.9)$$

An important example of the utility of this definition is in determining the modal gain or loss rate of a homogeneous dielectric region based on its material characteristics.

Sometimes, these regions cannot be accurately described as a volume because they are just monolayers thick [43]. As described in Section 5.4, surface chemistries oftentimes simply terminate dangling bonds or allow for energetically favorable dimer formations. In addition, high-temperature anneals of Si/SiO<sub>2</sub> interfaces have imperceptible volumetric effects but demonstrably account for large changes in optical loss due to surface reconstructions. Thus for surface regions of interest ( $\delta A$ ), the best modal parameter to use is

$$\Gamma' = \frac{\int_{\delta A} n^2(\mathbf{r}) |E(\mathbf{r})|^2 dA}{\int n^2(\mathbf{r}) |E(\mathbf{r})|^2 dV}. \quad (2.10)$$

As most surface effects occur at regions of dielectric and field discontinuity, the arithmetic average of each side of the discontinuity is used in calculating the above surface integral.  $\Gamma'$  can always be related back to a volumetric energy fraction by assuming some physical depth to the surface,  $t_s$ , and writing  $\Gamma = \Gamma' t_s$ .

## 2.2 Master Equation for Systems with Azimuthal Symmetry

In 1865, J. C. Maxwell predicted that the light around us was an electromagnetic phenomenon and that “light” of all frequencies could be produced using a symmetrized form of the once *static* laws of electricity and magnetism [38]. In the absence of free charges or currents, these equations become

$$\begin{aligned} \nabla \cdot \mathbf{D}(\mathbf{r}, t) &= 0 & \nabla \times \mathbf{E}(\mathbf{r}, t) &= -\frac{\partial \mathbf{B}(\mathbf{r}, t)}{\partial t} \\ \nabla \cdot \mathbf{B}(\mathbf{r}, t) &= 0 & \nabla \times \mathbf{H}(\mathbf{r}, t) &= \frac{\partial \mathbf{D}(\mathbf{r}, t)}{\partial t}, \end{aligned} \quad (2.11)$$

where  $\mathbf{D}(\mathbf{r}, t) = \epsilon(\mathbf{r})\mathbf{E}(\mathbf{r}, t)$  and  $\mathbf{H}(\mathbf{r}, t) = \frac{1}{\mu_0}\mathbf{B}(\mathbf{r}, t)$  are the linear constitutive relations.<sup>3</sup> Without free charges or currents, the only solutions to Eqs. (2.11) are elec-

---

<sup>3</sup>The constitutive relations must always be specified for a complete set of electromagnetic equations because there

tromagnetic waves so that a sinusoidal time-dependence  $\exp(-i\omega t)$  can be assumed to give

$$\begin{aligned}\nabla \cdot \mathbf{D}(\mathbf{r}) &= 0 & \nabla \times \mathbf{E}(\mathbf{r}) &= i\omega \mathbf{B}(\mathbf{r}) \\ \nabla \cdot \mathbf{B}(\mathbf{r}) &= 0 & \nabla \times \mathbf{H}(\mathbf{r}) &= -i\omega \mathbf{D}(\mathbf{r}),\end{aligned}\tag{2.12}$$

where, the real physical fields are given by  $\Re[\mathbf{E}(\mathbf{r}, t)]$ ,  $\Re[\mathbf{B}(\mathbf{r}, t)]$ , etc. Taking the curl of the top right equation, representing Faraday's Law, gives the master equation for the electric field,

$$\nabla \times \nabla \times \mathbf{E}(\mathbf{r}) - k_0^2 n^2(\mathbf{r}) \mathbf{E}(\mathbf{r}) = 0,\tag{2.13}$$

where  $k_0 = \omega/c$ ,  $c^2 = 1/(\mu_0\epsilon_0)$ , and  $n^2(\mathbf{r}) = \epsilon(\mathbf{r})/\epsilon_0$ . Equation (2.13) (or the similar version for the magnetic field) can be viewed as the most general of eigenvalue equations for the optical modes of a microcavity. This work will focus on a particular simplification of the master equation where the index of refraction possesses an azimuthal symmetry so that  $n^2(\mathbf{r}) = n^2(\rho, z)$ , working in cylindrical coordinates. Another useful form of Eq. (2.13) can also be derived from the Maxwell equations according to

$$\nabla^2 \mathbf{E} + \nabla \left( \frac{1}{n^2(\rho, z)} \mathbf{E}(\mathbf{r}) \cdot \nabla n^2(\rho, z) \right) + k_0^2 n^2(\rho, z) \mathbf{E}(\mathbf{r}) = 0,\tag{2.14}$$

where the relation  $\nabla \cdot \mathbf{E} = -(1/\epsilon) \mathbf{E} \cdot \nabla \epsilon$  was used [38]. This form of the master equation provides additional insight into the nature of whispering-gallery modes, because the equation directly reduces to the vector wave equation for a piecewise homogeneous material. Whenever a curvilinear translational symmetry is assumed to the Maxwell equations, a reduction in the equation space takes place. This is because Eq. (2.14) can always be separated into solving for just the transverse electric fields, just the transverse magnetic fields, or just the two longitudinal fields [44].

---

are 12 variables in the Maxwell equations but only 8 relationships by themselves.

### 2.3 Analytic Approximation for the Modes of a Microdisk

At this point, it is useful to make a few rather large approximations which allow us to arrive at approximate but analytic solutions to the still general Eq. (2.14). Assuming a piecewise homogeneous medium, Eq. (2.14) can be reduced to the Helmholtz equation

$$\nabla^2 \mathbf{F} + k_0^2 n^2(\rho, z) \mathbf{F}(\mathbf{r}) = 0, \quad (2.15)$$

where  $\mathbf{F} = \{\mathbf{E}, \mathbf{H}\}$ . Explicitly writing out the Laplacian operator in cylindrical coordinates,

$$\left[ \frac{\partial^2}{\partial \rho^2} + \frac{1}{\rho} \frac{\partial}{\partial \rho} + \frac{1}{\rho^2} \frac{\partial^2}{\partial \phi^2} + \frac{\partial^2}{\partial z^2} + k_0^2 n^2(\rho, z) \right] \mathbf{F}(\mathbf{r}) = 0. \quad (2.16)$$

In a semiconductor microdisk, the vertical confinement restricts the movement of the photon to travel in a plane rather than in three dimensions, effectively reducing the problem to a two-dimensional one. As long as the vertical thickness is not smaller than half a wavelength in the material, the optical mode's field distribution becomes quite simple. In this case, there are two dominant polarizations labeled as TE ( $E$  field parallel to the disk plane) and TM ( $E$  field perpendicular to the disk plane), where Eq. (2.16) becomes scalar in the  $\hat{z}$  direction. As a consequence,  $F_z$  corresponds to  $H_z(E_z)$  for TE(TM) modes. For  $\rho < R$ , where  $R$  is the disk radius, separation of variables can be used to rewrite Eq. (2.16) as

$$\frac{1}{W} \left( \frac{\partial^2 W}{\partial \rho^2} + \frac{1}{\rho} \frac{\partial W}{\partial \rho} + \frac{1}{\rho^2} \frac{\partial^2 W}{\partial \phi^2} \right) + \frac{1}{Z} \frac{d^2 Z}{dz^2} + k_0^2 n^2(\rho, z) = 0, \quad (2.17)$$

where  $F_z = W(\rho, \phi) Z(z)$ . Thus we have two differential equations,

$$\left( \frac{\partial^2 W}{\partial \rho^2} + \frac{1}{\rho} \frac{\partial W}{\partial \rho} + \frac{1}{\rho^2} \frac{\partial^2 W}{\partial \phi^2} \right) + k_0^2 \bar{n}^2(\rho) W = 0 \quad (2.18)$$

$$\frac{d^2 Z}{dz^2} + k_0^2 (n^2(z) - \bar{n}^2) Z = 0, \quad (2.19)$$

to self-consistently solve for the free-space wave vector,  $k_0$  and the effective index,  $\bar{n}$ . The solution of Eq. (2.19) follows the standard slab mode calculations as in [44]

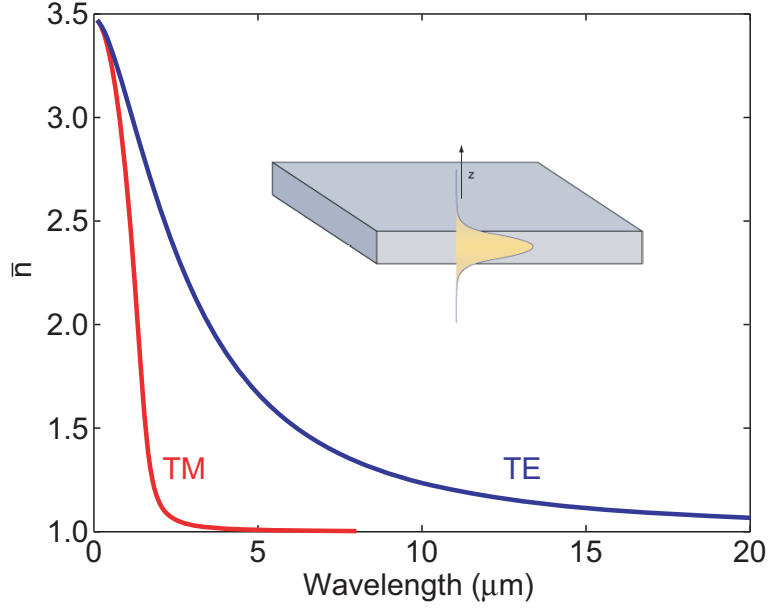


Figure 2.2: Effective slab index,  $\bar{n}$ , for a 215 nm thick Si microdisk. The TE slab index (blue curve) extends farther to long wavelengths versus the TM slab index (red curve) because the TE mode is the fundamental mode and possesses no cut-off frequency.

taking note that  $F_z$  is continuous(discontinuous) across the interfaces for the TE(TM) modes. Figure 2.2 plots  $\bar{n}$  for both the TE and TM slab modes for a 215 nm thick Si microdisk. As the TE mode (blue curve) is the fundamental mode and possesses no cut-off frequency, the TE effective index is always larger than the TM effective index (red curve).

Equation (2.18) can be solved by again using separation of variables,  $W(\rho, \phi) = \Psi(\rho)\Omega(\phi)$ , to rewrite it as

$$\frac{\partial^2 \Psi}{\partial \rho^2} + \frac{1}{\rho} \frac{\partial \Psi}{\partial \rho} + \left( k_0^2 \bar{n}^2(\rho) - \frac{m^2}{\rho^2} \right) \Psi = 0 \quad (2.20)$$

$$\frac{\partial^2 \Omega}{\partial \phi^2} + m^2 \Omega = 0. \quad (2.21)$$

While the solution to Eq. (2.21) is simply  $\Omega(\phi) \sim \exp(im\phi)$ , the solution to Eq. (2.20) is most tractably solved approximately [45]. Inside the disk, the radial solutions are Bessel functions,  $\Psi(\rho) \sim J_m(k_o \bar{n} \rho)$ . Outside the disk, the solutions

are Hankel functions, which can be approximated by a decaying exponential<sup>4</sup> with decay constant  $\alpha = k_0(\bar{n}^2 - n_0^2)^{1/2}$ . The free-space wavelength can then be found by matching the boundary conditions at  $\rho = R$  using Eq. (2.11). Matching  $H_z(E_z)$  and  $E_\phi$  for TE(TM) leads to the transcendental equation

$$k_0\bar{n}(k_0)J_{m+1}(k_0\bar{n}(k_0)R) = \left(\frac{m}{R} + \eta\alpha\right) J_m(k_0\bar{n}(k_0)R), \quad (2.22)$$

where  $\eta = \bar{n}^2/n_0^2$  for TE and unity for TM modes. Using the self-consistent solution of Eq. (2.19) and Eq. (2.22), the unnormalized radial mode dependence is given by

$$\Psi(\rho) \sim \begin{cases} J_m(k_0\bar{n}\rho) & \rho \leq R \\ J_m(k_0\bar{n}R) \exp(-\alpha(\rho - R)) & \rho > R \end{cases}. \quad (2.23)$$

Because the above analysis used only one of the three field components to solve for the modes of the cavity, Eq. (2.23) cannot be used to rigorously calculate the field distributions, especially for the case of very thin disks. However, the approximations made in the above analysis do not prevent extracting the resonance locations to within a few percent. By first parameterizing the solution to Eq. (2.19) (for example by interpolating the solution to Fig. 2.2), thousands of resonance locations can be calculated within tens of seconds. Figure 2.3 shows a calculated dispersion diagram for a 5  $\mu\text{m}$  radius, 215 nm thick Si microdisk against *angular* momentum. The reason behind plotting frequency versus angular momentum is because each mode's linear momentum is a function of distance from the center of the disk. The resonance locations and angular momentum for each mode are rigorously defined quantities. It is still very useful to make the connection to more standard dispersion diagrams as in References [39, 46] by plotting the light lines for air, silicon, and the slab's effective index. Shown in black are light lines at the disk edge for air and bulk silicon. Modes cannot exist above the light line for air because above this line, the solution to Eq. (2.19) is oscillatory versus evanescent, implying a radiation mode. Modes cannot exist beneath silicon's light line because this would similarly mean that the modes would be evanescent even inside the disk. Thus, the only region where propagating electromagnetic waves can exist inside the silicon but decay in the air cladding is in

---

<sup>4</sup>Note that by keeping the Hankel functions, the solution would be accurate over a wider range of parameters.

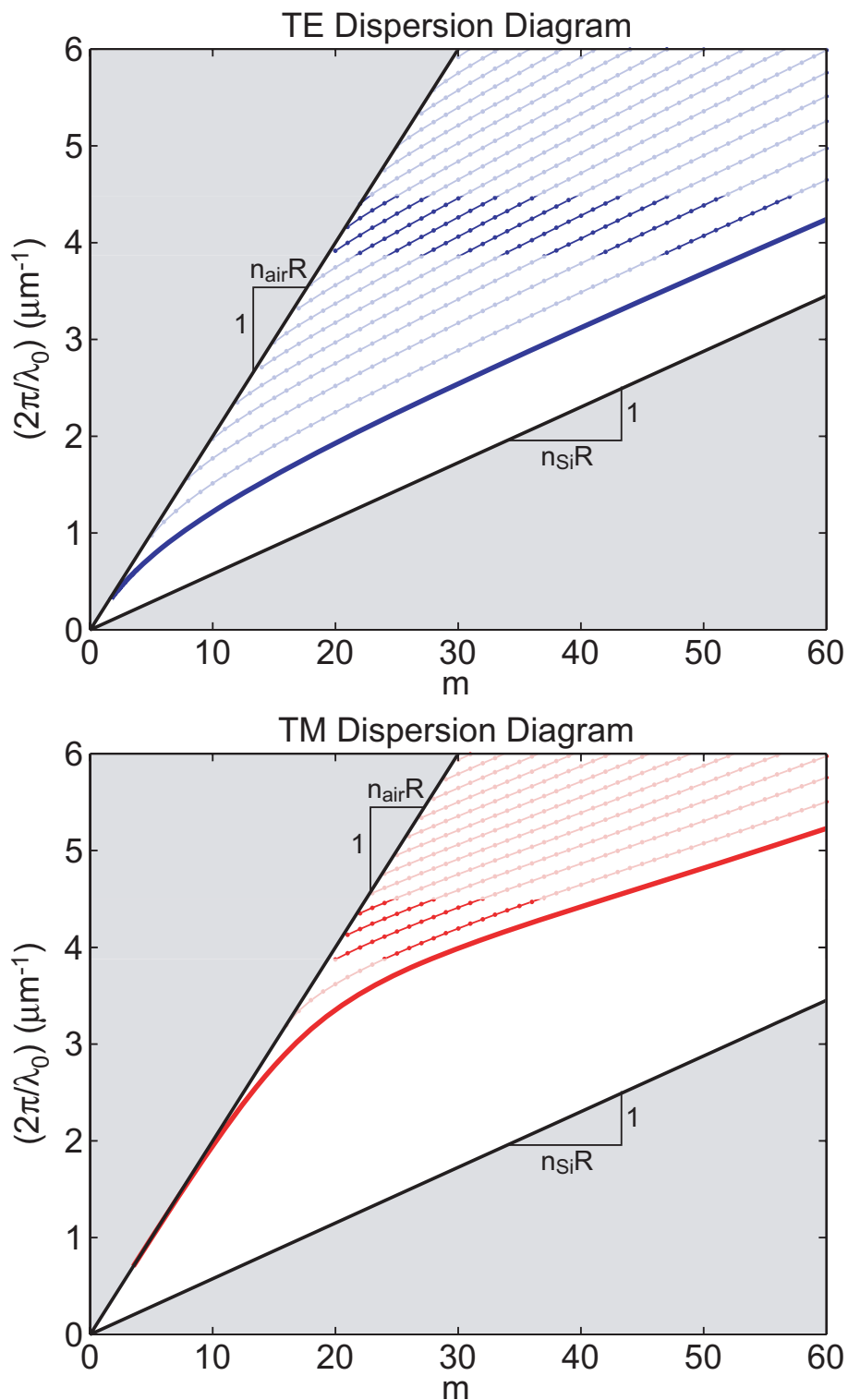


Figure 2.3: Analytic dispersion diagram for a  $5 \mu\text{m}$  radius,  $215 \text{ nm}$  thick Si microdisk against *angular* momentum. Shown in black are light lines at the disk edge for air and bulk silicon. Thick blue and red lines are light lines at the disk edge using the effective slab indices of refraction. Frequencies outside the testable range ( $1400 - 1600 \text{ nm}$ ) have been made slightly transparent.

the white region between the two lines. Furthermore, the solution to Eq. (2.20) can be viewed as the solution to an infinitely tall cylinder with index given by  $\bar{n}$ . This implies that in order for modes to whisper around the periphery, a more stringent requirement exists such that the phase velocity must also be greater than  $c/\bar{n}$ , which is a function of free-space wavelength. The thick blue and red curves are the TE and TM light lines at the disk edge using the effective slab indices of refraction. As expected, the bound modes, plotted as blue and red dots, exist only between air's light line and the slab's light line. Blue and red lines connect the modes of similar radial orders. The family with one radial antinode,  $p = 1$ , exists closest to the slab's light line. Higher radial order families are labeled in order of increasing frequency. Frequencies outside the testable range (1400 – 1600 nm) have been made slightly transparent in order to emphasize the relatively narrow frequency window for which these modes have been designed.

While dispersion diagrams offer a global perspective on the modes of a microdisk, they can be difficult to use to directly compare to transmission spectra. Figure 2.4 is a plot of the same analytic mode spectra, but focuses only on the 1500 nm wavelength band. Additionally several visual changes do much to aid in developing an intuition for experiment. Classification of the microdisk modes is done by determining the dominant polarization (TE or TM), the number of radial antinodes in the electric field ( $p$ ), and the number of azimuthal antinodes ( $m$ ). Note that only the fundamental slab modes are supported for our disk heights, so the vertical mode quantization will be omitted. For the purposes of this thesis, the notation used to specify all three parameters will be either  $\text{TE}_{p,m}$  or  $\text{TM}_{p,m}$ , depending upon the polarization. Mode “families” are defined as having a similar polarization and radial mode quantization and are indicated in the figure by color of bars representing the resonance locations. The bars become wider as the modes approach the light line, in anticipation of the fact that the  $Q$  of the resonances becomes exponentially worse with decreased confinement from the cladding. The bars have also been drawn from an arbitrary maximum  $m$  number and drop *down* to specify the  $m$  number for that particular mode. As will be discussed in further depth in Chapter 4, this was done to mimic the mode's predicted coupling characteristics in a transmission spectrum because of phase matching

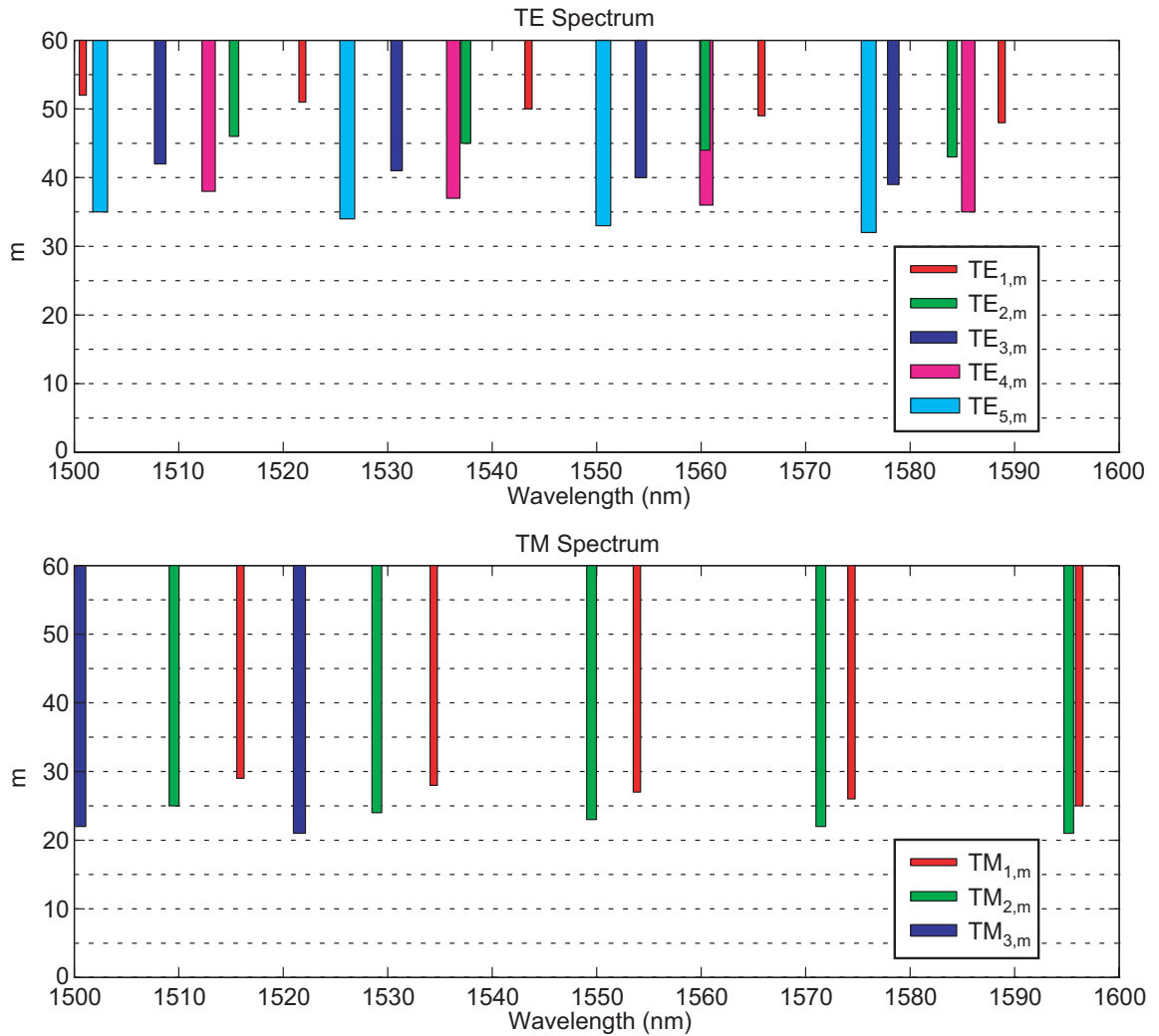


Figure 2.4: Analytic mode spectra for a  $5 \mu\text{m}$  radius,  $215 \text{ nm}$  thick Si microdisk for the  $1500 \text{ nm}$  wavelength band. Bars have been drawn from an arbitrary maximum  $m$  number and drop *down* to mimic the mode's predicted coupling characteristics in a transmission spectrum

considerations to silica fiber tapers positioned near the disk. Plotted in this visual way, many predictions can be made about experiment. The most obvious of which is that for a microdisk of this geometry, TM modes should couple much better than their TE counterparts of similar radial order (indicated by color of the bars). Furthermore, it will also be expected to always observe modes approaching cut-off (loosely defined as a  $Q \sim 1 - 10$ ), as is the case for the  $TM_{3,m}$  family in the figure. Lastly, FSR increases with radial order, and TM modes are expected to have smaller FSRs than their TE counterparts, both explained by the fact that the group velocity of the modes becomes equal to that in the cladding as they approach the light line for the cladding (See Fig. 2.3).

## 2.4 Finite-Element Simulations

In order to augment the information gleaned from the approximate analytic models, numerical simulations using the finite-element method (FEM) were implemented in Comsol's Femlab 3.1 software. FEM calculations [47] differ from those of finite-difference time-domain (FDTD) calculations in that instead of specifying the field on a grid of points, approximating *functions* are specified on a mesh. Each of the mesh elements is related to its nearest neighbor and is then formulated into a sparse matrix. This difference results in a greater flexibility in specifying the mesh because mesh elements can drastically vary in size globally without sacrificing the code's performance or accuracy, as long as the mesh elements do not vary much locally. Thus, the computational resources can be allocated based on the goal of the solution, whether it be calculating resonance locations, quality factors, mode volumes, etc. Although the elements can be optimally placed for the solution, one major disadvantage of the FEM is the kernel size required to find the solutions when compared to FDTD. FDTD's kernel is trivially small because it simply calculates the field's next iteration of time using the Maxwell equations. In contrast, FEM must hold a sparse matrix in memory, which at worst requires the square of the memory needed to hold the field. Obviously, much research has gone into minimizing the memory required to hold the kernel, but this limitation puts most three-dimensional microphotonic eigenvalue problems out

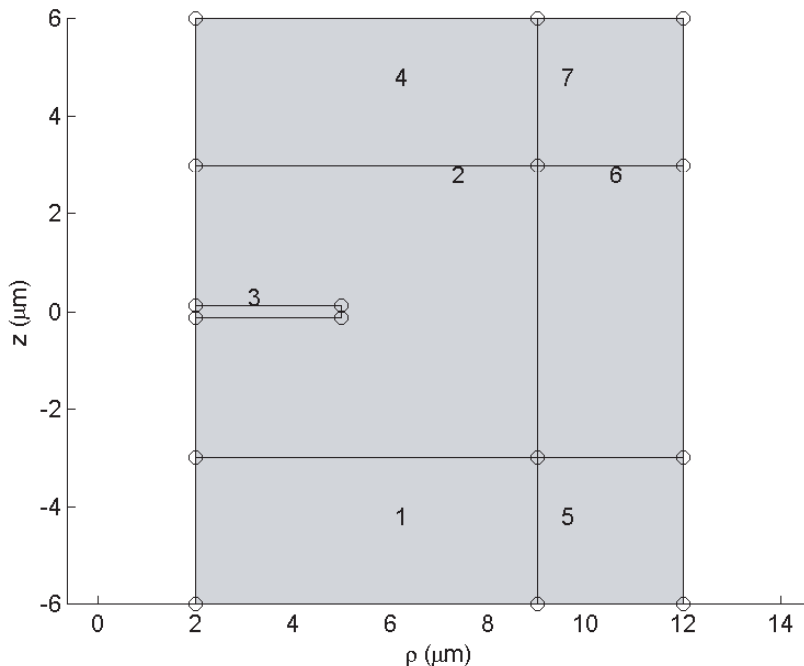


Figure 2.5: Geometry plot from Femlab 3.1 for a 5  $\mu\text{m}$  radius, 250 nm thick Si microdisk.

of reach for computers running FEM with modest computer resources.<sup>5</sup> Fortunately, azimuthally symmetric problems can be mapped onto an equivalent two-dimensional problem allowing numerically exact field distributions to be calculated along with radiation  $Q$ 's up to  $\sim 10^{13}$ .

Originally analyzed and coded by Sean Spillane [48,49], the azimuthally symmetric eigenvalue solver in Femlab has proven to be an invaluable tool for high- $Q$  microcavity research. Although it is possible to use just the in-plane components ( $E_\rho, E_z$ ) to solve problems of azimuthal symmetry, the FEM implementation of such an equation system cannot handle discontinuities in the index of refraction, a necessity for any microphotonic component. Thus, a fully vectorial Cartesian waveguide solver with a Cartesian translation invariance was used as the starting equation system. Then Eq. (2.13) was rewritten in the form of Cartesian differential operators plus the extra operators resulting from the change in coordinates along with the hardcoded  $e^{im\phi}$  dependence. Figure 2.5 shows a plot of the subdomains used to model rotationally symmetric systems using a 5  $\mu\text{m}$  radius, 250 nm thick Si microdisk as a prototypical

<sup>5</sup>The advent of 64-bit computing architectures promises to lift this limitation in coming years as memory prices continue to fall, allowing Femlab to solve problems with millions of degrees of freedom.

resonator. The same vectorial Helmholtz equation was specified for all subdomains, but special attention had to be paid to the boundary conditions. Because of the “centrifugal force” that the extra operators exerted on the field distributions, the computational box could be terminated by a perfect electrical conductor generally just a few microns in from the disk edge. Because the complex eigenvalue was sought, the outer boundaries had to allow for optical energy to escape from the computational box. This was accomplished with an additional domain that surrounded the disk and cladding called a perfectly matched layer (PML) [47]. The PML contains an anisotropic and highly attenuating permittivity and permeability that produces no reflections for incident plane waves from all directions. Once added, the PML need only be placed in the cavity’s far field to properly absorb the radiated energy. PML then allows for the quality factor of the resonance to be calculated according to the  $\Re(k_0)/(2 \cdot \Im(k_0))$ .

To vet the equation changes to Femlab’s master equation, silicon microspheres were modelled and compared to available analytic solutions. Silicon microspheres were chosen because the completely one-dimensional Helmholtz equation has analytic spherical Bessel function solutions for all values of index contrast [48, 50, 51]. The high-index contrast offered by silicon microspheres provides a good test of the vector element implementation in Femlab because of the large field discontinuities present across boundaries. Complex eigenvalue FEM solutions for microspheres of 1–1.5  $\mu\text{m}$  radii and  $n = 3.48$  for both TE and TM polarization were thoroughly tested against both analytic and approximate formulas, showing that agreement to better than 0.01% was possible for the real portion of the eigenvalue (the resonance wavelength) while agreement better than 2% was possible for the imaginary portion (corresponding to  $Q \sim 10^8$ – $10^{12}$ ).

Femlab’s integration with Matlab was utilized to create a high-level structure containing all the values of parameters necessary for each simulation. This allowed for parametric studies of the geometry, boundaries, and mesh in order to ensure convergence for the models. Figures 2.6 and 2.7 show a FEM mesh for a 5  $\mu\text{m}$  radius, 250 nm thick Si microdisk. While convergence tests showed that mesh elements could be as large as one-tenth of a wavelength in the silicon material, continued improvements

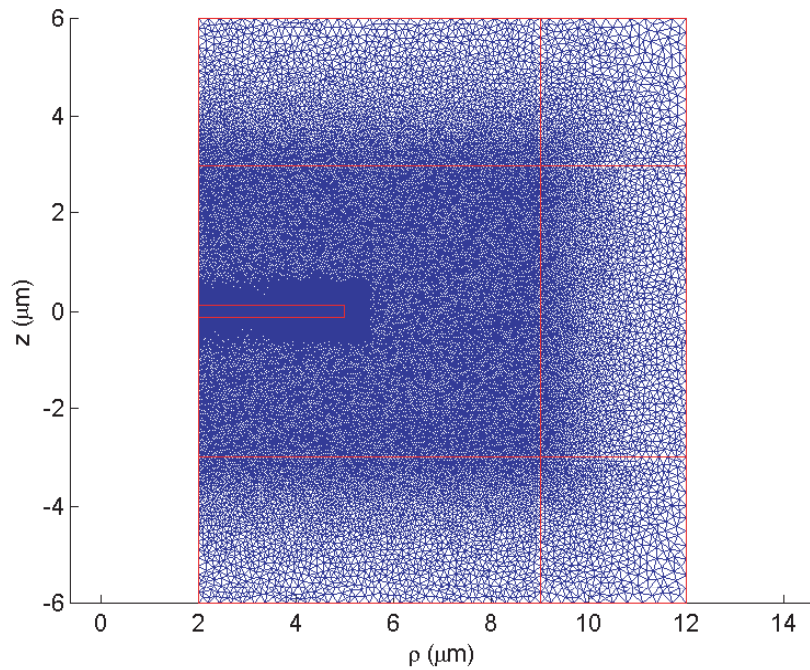


Figure 2.6: FEM mesh for a highly resolved  $5 \mu\text{m}$  radius,  $250 \text{ nm}$  thick Si microdisk. Mesh elements are at most  $1/25$  a wavelength in the material and have been refined by a factor of 2 around the disk edge periphery. Maximum element size is  $0.3 \mu\text{m}$  in PML, but nearest neighbor mesh points are specified to differ in size by  $< 5\%$

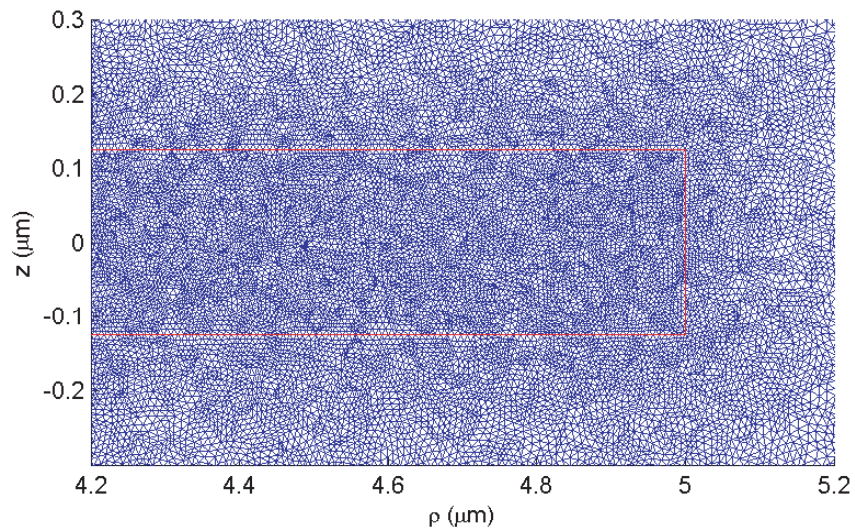


Figure 2.7: Zoomed-in view of the FEM mesh in Fig. 2.6 for a highly resolved  $5 \mu\text{m}$  radius,  $250 \text{ nm}$  thick Si microdisk.

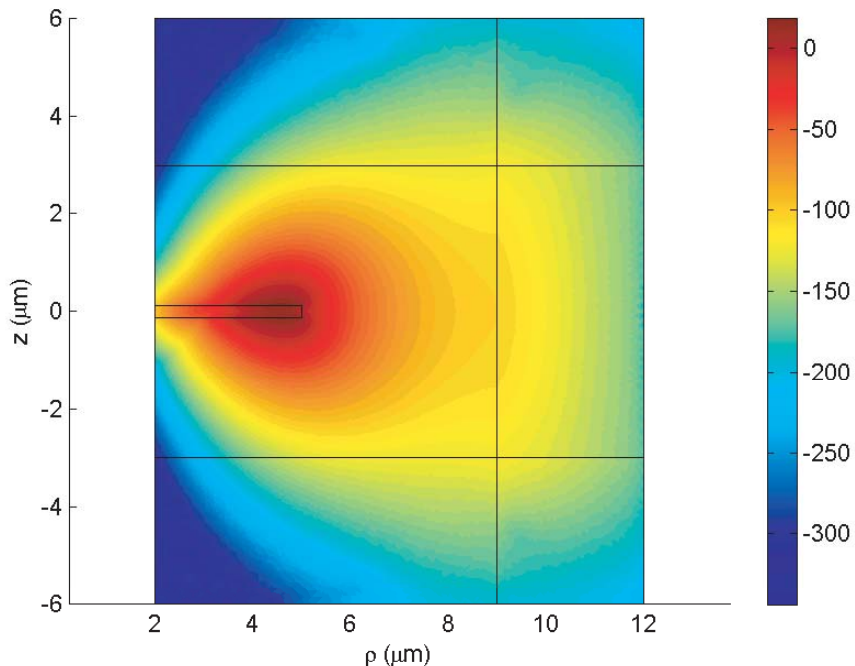


Figure 2.8: Plot of  $10 * \log_{10}(|\mathbf{E}|^2)$  for the  $\text{TM}_{1,35}$  mode at  $\lambda_0 = 1548.1$  nm using the mesh shown in Fig. 2.6 for a  $5 \mu\text{m}$  radius,  $250$  nm thick Si microdisk.

in accuracy were seen in resonance locations and quality factors as the mesh was refined. Femlab gives the ability to specify not only maximum mesh element size, but also the maximum mesh growth rate from element to element. With modest computing resources, the mentioned figures show a highly resolved mesh that contains hundreds of thousands of degrees of freedom. The mesh elements are at most  $1/25$  a wavelength in each of the materials and have been refined by a factor of 2 where the majority of the mode exists. The maximum element size is  $0.3 \mu\text{m}$  in the PML, but the nearest neighbor mesh points are specified to differ in size by  $< 5\%$ , resulting in a smoothly graded mesh into the absorbing layer.

Figure 2.8 shows a plot of  $10 * \log_{10}(|\mathbf{E}|^2)$  using the mesh shown in Figs. 2.6 and 2.7. The solution was for a  $\text{TM}_{1,35}$  mode at  $1548.1$  nm with radiation quality factor  $Q_r = 4.2 \times 10^{12}$ . Note that the field intensity is down more than 100 dB from its maximum at any of the boundaries ensuring an accurate simulation. An excellent example of the power of the FEM is most readily seen in the highly resolved field distributions in Fig. 2.9. Plotted top to bottom are  $E_\rho$ ,  $E_\phi$ , and  $E_z$  for the same

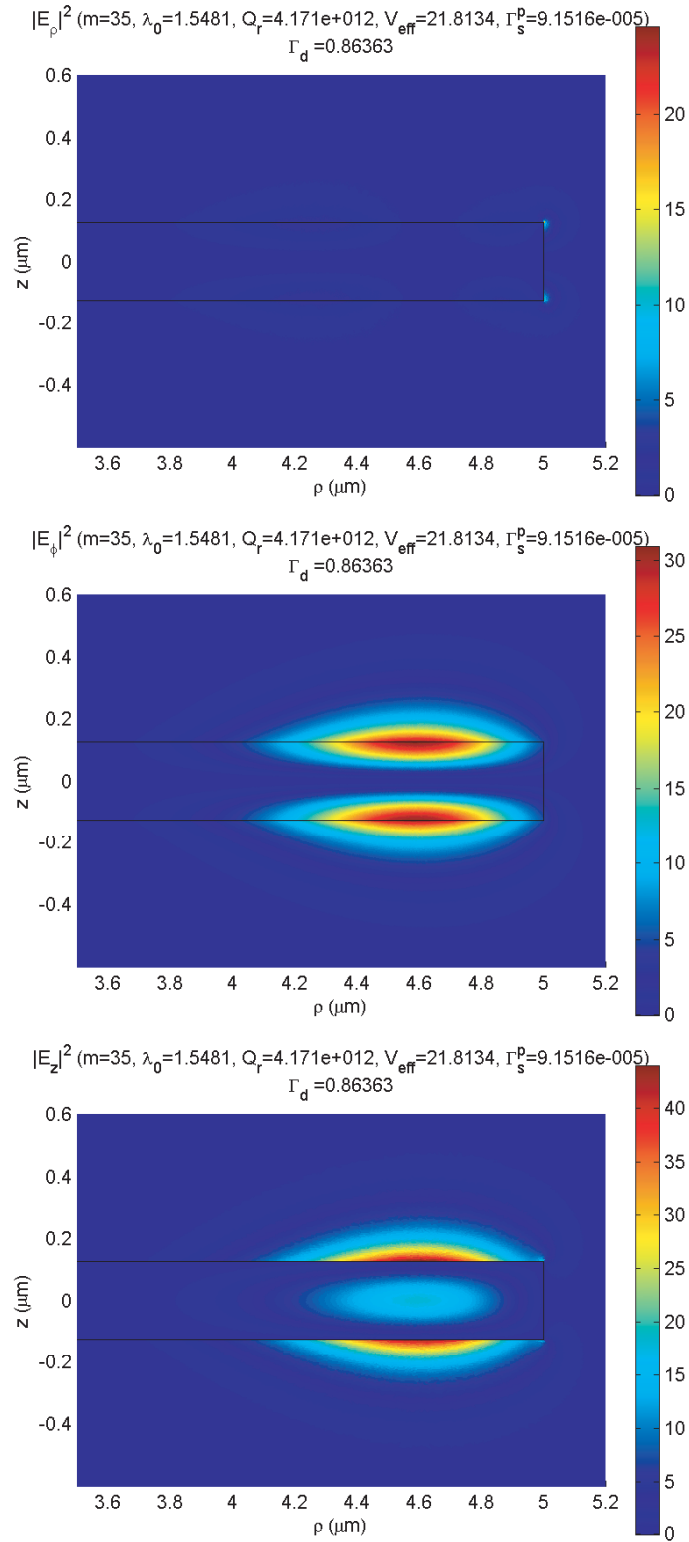


Figure 2.9: Plot of  $E_\rho, E_\phi, E_z$  for the  $\text{TM}_{1,35}$  mode at  $\lambda_0 = 1548.1$  nm using the mesh shown in Fig. 2.6 for a  $5 \mu\text{m}$  radius,  $250$  nm thick Si microdisk.

solution. While the in-plane components are adequately described by the analytic approximation in Section 2.3, a large longitudinal field also exists that could not be described with the TE/TM assumptions. Instead the terms TE and TM are used loosely to describe the two types of modes that are rigorously classified by the parity across the  $z = 0$  plane. In this classification scheme, TE modes are those with even parity, while TM modes possess odd parity. As a consequence, the sign of  $E_\rho$  and  $E_\phi$  changes from top to bottom in Fig. 2.9 because this mode has odd parity [38]. When this vertical mirror symmetry is broken by, for example, simulating slanted sidewalls, classification is done by tangential component with the maximum field strength. If  $E_\rho > E_z$ , the mode is called TE and vice versa.

Although the microdisks fabricated in this work routinely had slanted sidewalls, the disks were usually not simulated as such. It was found that, for the disk geometries under consideration, the non-vertical sidewall angle trivially reduced the radiation quality factor. Furthermore, the break in symmetry would cause up to 2 nm in resonance shifts due to occasional accidental degeneracies between high radial order “TE” modes and low radial order “TM” modes with identical  $m$  numbers. These accidental lifts in degeneracies became a nuisance from a design perspective when trying to calculate FSRs, etc. Interestingly, these resonance shifts could be observed experimentally when small amounts of silicon were removed in the repeated chemical treatments described in Section 5.4. The FSRs were also affected by whether or not a dispersive index of refraction was used in the simulation. Whenever simulation needed to be compared to experiment, the index of refraction for silicon was a Sellmeier-type dispersion fit to the tabulated values given in reference [52]. Unfortunately, the nature of the Femlab’s eigenvalue solver could not allow for eigenvalue-dependent parameters. When including dispersion, an iterative approach was used to self-consistently solve for the index of refraction and free-space wavelength. In practice, this could be accomplished in a maximum of two iterations because of the weak dispersion present in silicon at telecommunication wavelengths.

After calculation of the eigenmode solution, the many modal quantities of interest were evaluated using Femlab’s suite of built-in Matlab functions. First, the modes were approximately classified according to polarization and estimated radial number.

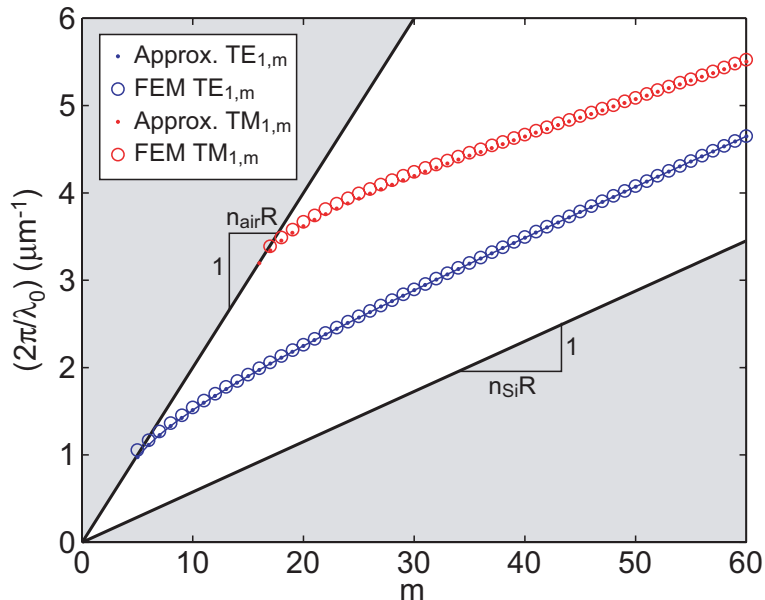


Figure 2.10: Comparison of the approximate versus the FEM dispersion diagram for a  $5 \mu\text{m}$  radius,  $215 \text{ nm}$  thick Si microdisk. The blue dots and circles represent the resonance locations for the  $\text{TE}_{1,m}$  family, solved via the approximate and finite-element methods, respectively. Similarly, the red dots and circles represent the resonance locations for the  $\text{TM}_{1,m}$  family, solved via the approximate and finite element methods, respectively.

Then calculations of  $\Gamma_{\text{Si}}$ ,  $\Gamma'_{\text{top}}$ ,  $\Gamma'_{\text{side}}$ ,  $\Gamma'_{\text{bot}}$ , and  $V$  were found through numerical integrations. One subtlety that arises when using Eq. (2.8) to calculate mode volume is that the  $E_\phi$  component is  $\pi/2$  out of phase with the tangential components. For traveling waves, the energy densities for each polarization are azimuthally uniform, but the energy densities for standing waves are oscillatory. Thus, there are two possible energy density maxima for a standing wave, one for the in-plane oscillation maxima and one for the longitudinal oscillation maxima.

The heavy use of scripting throughout the FEM simulation development permitted for a host of parametric studies. Convergence was assured by parametrically moving subdomain boundaries and mesh densities. Dispersion diagrams such as that shown in Fig. 2.10 were also calculated to compare against the approximate solutions. Plotted in the figure are the  $p = 1$  TE and TM families previously described in Fig. 2.3, along with the numerically exact solutions overlaid by circles of similar color. Not surprisingly, the approximate solution is most accurate for larger  $m$  numbers where the modes are more bulk-like. For modes far from the light line, the approximate

formulas predict the resonance locations to within a couple of nanometers. The errors become exponentially worse as the modes approach cut-off. Resonance location errors up to 10% were common in trying to evaluate highly radiating modes, with much larger errors for estimates of TM family FSRs.

Similar parametric studies were also conducted for the TE and TM modes as a function of radius and disk height while keeping the wavelength fixed. Resonance location correspondence between the approximate and FEM solutions better than fractions of a nanometer were observed for the largest  $R \sim 50 \mu\text{m}$ ,  $h \sim 1 \mu\text{m}$  microdisks. As will be described in more detail in the following chapters, these types of studies were also used to optimize the cavity designs to cater to the application at hand. The radius and polarization were varied to minimize the optical loss due to sidewall imperfections, creating ultra-low-loss resonators. The disk height was varied to optimize the coupling rate to bus waveguides while maximizing the sensitivity to surface chemistry on the top Si surface. Simulations of thermal and chemical oxidation were also employed to determine chemical reaction rates based on resonance shifts and changes in radiation  $Q$ . Finally, multiple cladding layers and high-index substrates were added to the simulations to calculate expected modal gain for erbium-doped cladding lasers.

## Chapter 3

# Fabrication of Silicon Microdisks

### 3.1 Introduction

Arguably, most advances in device physics have been a result of the increased availability of advanced materials. Even our earliest technological eras were named by their material advances: The Stone Age, Bronze Age, etc. This trend continues to be true even today. Much of the basic quantum mechanics needed in microelectronics had been known for decades before reliable semiconductors could be mass produced, enabling the birth of the industry. More recently, the telecommunications industry boom was a direct result of the mass production of the most transparent solid in the world, single-mode optical fiber. Fiber such as JDS Uniphase SMF-28 fiber ( $\alpha \sim 0.2$  dB/km) has been quite literally wrapped all over the world, spawning hundreds of breakthrough technologies like the distributed feedback laser, erbium-doped fiber amplifiers, and the arrayed waveguide grating.

This year was the first time in 35 years that computer chip technologies have failed to keep up with Moore's Law [5]. Predicting this eventuality, material scientists developed a new material called silicon-on-insulator (SOI), which is any thin crystalline layer of silicon atop an insulator that can be processed along with regular crystalline silicon wafers. With its increased electrical confinement, SOI promises a one-time factor of two improvement in computer chip performance extending the life of silicon microelectronics another 18 months. While this could not be considered a material revolution by any means, the sheer scale of the microelectronics industry has made SOI producers, like SOITEC, wafer giants, which annually produce millions of SOI

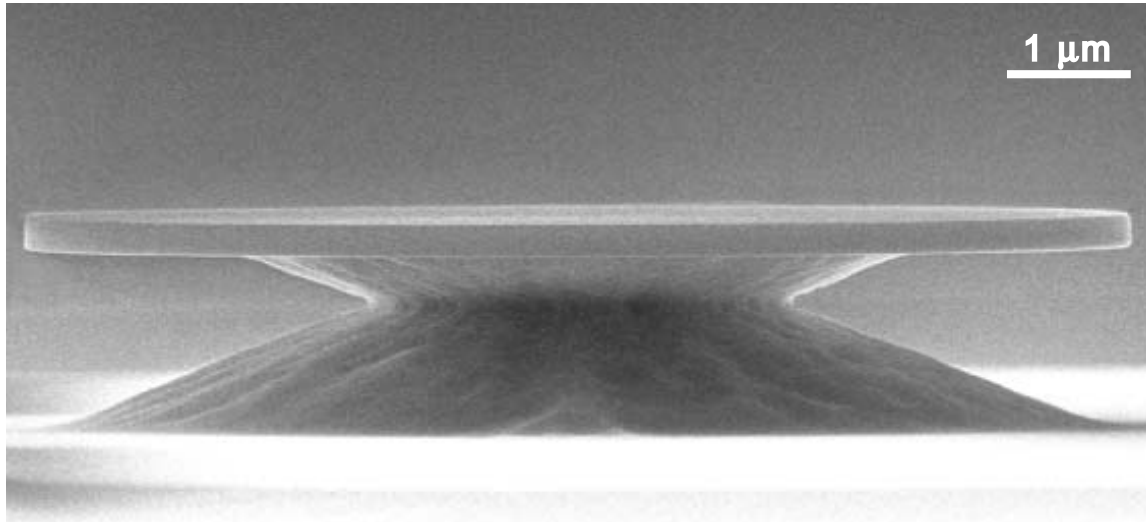


Figure 3.1: SEM micrograph of an undercut  $9\ \mu\text{m}$  diameter microdisk made from an SOI wafer.

wafers up to 300 millimeters in diameter. The immense economies of scale have made the marginal costs of SOI wafers so low that researchers and companies around the world are creating complete photonic integrated circuits from commercially available SOI at a fraction of the cost as compared to III-V wafers. The shared goal of all silicon photonics researchers is that by creating new photonics elements in a CMOS-compatible manner (see Fig. 3.1), optical functionality could be seamlessly added onto existing silicon microprocessors.

### 3.2 Material Selection

The silicon microdisks employed in this work were all fabricated from commercially available silicon-on-insulator (SOI) wafers from SOITEC®. The wafers consisted of a 217–344 nm thick silicon device layers (p-type, 1–20  $\Omega\cdot\text{cm}$  resistivity,  $\langle 100 \rangle$  orientation) on top of a 2–3  $\mu\text{m}$   $\text{SiO}_2$  buried oxide (BOX) layer. SOITEC wafers were chosen because of their patented Smartcut process, wherein a thermally oxidized silicon wafer has hydrogen implanted into it at a controllable depth. The wafer is then cleaned and bonded onto another thermally oxidized wafer. The top wafer is then broken on the amorphized silicon layer, annealed to remove defects, and chemo-mechanically

polished before being reoxidized for another bonding run. Figure 3.1 shows an SOI microdisk that has had much of the buried thermal oxide (BOX) removed with hydrofluoric acid. The characteristic hour-glass shape highlights the region of wafer bonding where the HF etch rate is highest. The silicon device layer thickness is chosen so as to provide good confinement for the WGM at the periphery while allowing optical waveguide access through evanescent coupling. The BOX thickness is chosen to minimize radiation into the substrate while still providing good thermal grounding of the device. Thermal contact becomes increasingly important for the smaller devices. The associated small pedestal radii greatly constrict the heat flow into the substrate causing power-dependent index of refraction variations. Furthermore, if isolation (see Section 3.5) is necessary, the BOX must be able to be etched through without putting too much stress on the processing equipment. The  $\langle 100 \rangle$  orientation is ideal for producing high-quality thermal oxides around the devices, encapsulating their sensitive silicon surfaces from the rest of the environment. The resistivity is chosen to be  $> 3 \Omega\cdot\text{cm}$  in order to minimize the effect of residual free-carrier absorption in the bulk device layer.

### 3.3 Sample Preparation

In order to aid in the turn-around-time for the fabrication of a working device, a large wafer is subdivided into small sections that are processed individually. Typically, a 150 mm wafer are sent directly to American Precision Dicing for dicing as opposed to individually cleaving shards for samples. Diced samples were preferable over cleaved samples because the resulting roughened but extremely vertical edges provided a higher yield when it came to the transporting of samples between various processing steps. In addition, the increased uniformity of the samples made it possible to eliminate many size-dependent variations in the processing. Among the various effects, the most problematic size-dependent variability was seen in edge effects during plasma material deposition or plasma dry etching, resist edge beading, and aqueous etchant consumption rates. American Precision Dicing would spin-coat and bake photoresist onto the wafer in a clean hood before dicing the wafer into 1

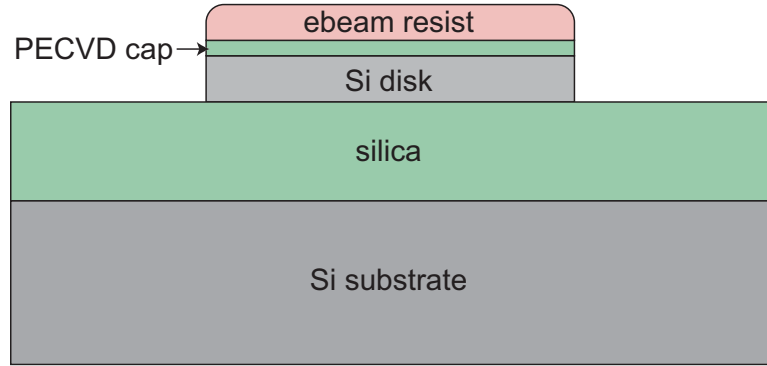


Figure 3.2: Schematic illustration showing an SOI microdisk after device layer dry-etching.

cm  $\times$  1 cm pieces. The diced wafer would be returned with photoresist intact on a “clam shell” holder, ready for pick and place processing of the individual samples.

After being diced into uniform pieces, the samples were degreased in acetone, isopropyl alcohol, methanol, and DI H<sub>2</sub>O in order to remove the photoresist and any other organic material on the samples. If the eventual devices needed to be isolated for taper testing, a 10–50 nm protective cap layer was deposited using plasma-enhanced chemical-vapor-deposition (PECVD). A protective cap was always used if the sample was to be isolated because of the many additional lithography, dry-etching, and wet-etching steps that could damage the thin Si device layer. The cap needed to be thick enough to adhere uniformly to the sample through the entire processing run while being thin enough to have a negligible impact on the etch-induced roughness that occurred during dry-etching. Although SiO<sub>x</sub> caps were originally used to protect the Si device layer, SiN<sub>x</sub> caps were found to be optimal because the initial dry-etching step could be optimized to etch through both cap and device layer in a single lit plasma step, greatly reducing the complexity of etch optimization. Figure 3.2 shows a schematic illustration of an SOI microdisk after device layer dry-etching through the cap and top silicon. The optimized SiN<sub>x</sub> cap was deposited using an Oxford Plasmalab 100 direct dual source RF plasma system. Several samples were affixed to a clean 100 mm Si carrier wafer with a minute amount of thermal paste and surrounded by “dummy” pieces to produce a uniformly thin film across the samples. A gas chemistry of 400 sccm of 5% SiH<sub>4</sub>/N<sub>2</sub>, 20 sccm of NH<sub>3</sub>, and 600 sccm of N<sub>2</sub> was applied to the chamber held at 650 mTorr and 350°C. Oxford’s SiN<sub>x</sub> recipe calls

for alternating the high frequency source (13.56 MHz) and low frequency source on a 20 second period with a 65% high frequency duty cycle. As each cycle deposited 4.4 nm of material, a  $\sim 50$  nm thick  $\text{SiN}_x$  cap was deposited with 11 cycles for a total of 220 seconds. An important note is that the plasma deposition of the cap was experimentally found to damage the top few monolayers of the device layer and was thus avoided whenever possible (see Section 5.6).

### 3.4 Lithography

Electron-beam lithography was used to create any critical feature in the device masks because of its superior resolution and easily modified masks as compared to photolithography. An electron-beam resist, Zeon ZEP520A, was used as the mask because of its increased dry-etch selectivity as compared with standard PMMA. After an approximately 7 second  $\text{N}_2$  blast, the ZEP was spin-coated at 5000 rpm for 120 sec, resulting in a  $\sim 350$  nm thick film. The ZEP was then oven-baked for 20 minutes at  $180^\circ\text{C}$ . A Hitachi S4300 cold-cathode field emission scanning electron microscope (SEM) was employed to raster expose the electron-beam resist, with the aid of Oliver Dial's Bewitch software. This was accomplished by intercepting the X-Y scanning coil voltage sources and replacing it with our own voltage sources provided by a 1 MHz Digital to Analog PCI card inside a standard desktop computer. An accelerating voltage of 15 kV and working distance of 6 mm was always used. The beam current was dynamically adjusted to maintain a constant dose during the beam write by monitoring the beam current ( $\sim 1\text{--}2$  nA) at the objective aperture. This relied on first measuring the beam current on the sample mount ( $\sim 5\text{--}35$  pA) utilizing a Faraday cup and then assuming a linear relationship between the current impinging on the objective aperture and the sample mount. Because the S4300 uses a cold-cathode electron source, the tip had to be flashed every 48 hours to prevent residual ion adsorption. It was empirically determined that cold-cathode's current stability was maximized by "flashing" the tip the night before the beam write. This allowed the tip to slowly accrue a uniform monolayer of material during the night without high voltages. A magnification of  $500\times$ , corresponding to a calibrated field of view

of 180  $\mu\text{m}$  on a side, was predominantly used to write microdisks of 2.5 – 40  $\mu\text{m}$  radii because it was empirically found that high scanning coil voltages ( $> 9\text{ V}$ ) and high voltage slew rates caused raster roughness on the silicon microresonators. The physical orientation of repeated device exposure was done along the axis parallel to the “tip” of the SEM in order to fix the working distance during the beam write. In addition, the electron beam’s direction of rastering had to be aligned to the direction of travel of the X-Y stages.<sup>1</sup>

The achievable resolution and the exposure times were determined by the constraints of the lithography tool and the resist beam used. The beam current on the sample was typically set to  $I_B \simeq 35\text{ pA}$  by opening the condenser lens to a value of 7 – 8. Because the scanning coils could not be reliably driven faster than  $\sim 250\text{ kHz}$ , the rastering speed was kept at  $S \simeq 100 - 150\text{ kHz}$ . 350 nm thick ZEP properly exposes between 37 to 39  $\mu\text{C}/\text{cm}^2$  for open areas and convex features such as microdisks. However, because of the subsequent reflow, the ZEP was always overexposed to 45  $\mu\text{C}/\text{cm}^2$  in order to remove nanoscopic traces of leftover resist that could have resulted in uneven resist wetting of the disk periphery. This additionally provided a better averaging of the beam current over the devices resulting in smoother features. Typical single field of view patterns were  $A_{\text{pat}} \simeq 4500\text{ }\mu\text{m}^2$ . With these values in hand, the physical grid resolution and pattern exposure time were found through simple dimensional analysis to be

$$\delta\ell = \sqrt{\frac{I_B}{\text{dose} \cdot S}} \approx 25\text{ nm} \quad (3.1a)$$

$$t_{\text{pat}} = \frac{\text{dose} \cdot A_{\text{pat}}}{I_B} \approx 60\text{ sec/pattern.} \quad (3.1b)$$

Although the Hitachi S4300 has a beam spot size of approximately 0.5 nm on a side, proximity effects limit the achievable resolution such that  $\delta\ell \approx 25\text{ nm}$  is sufficient to provide a smooth circular pattern. Typically, 10 – 20 patterns were written per beam write, making the total beam write time on the order of 20 minutes. This resulted in beam current variations of a couple percent from pattern to pattern. After exposure,

---

<sup>1</sup>for the sample orientation used, this corresponded to a stage rotation of 5.3 – 5.7 and a raster rotation of 17 on the SEM.

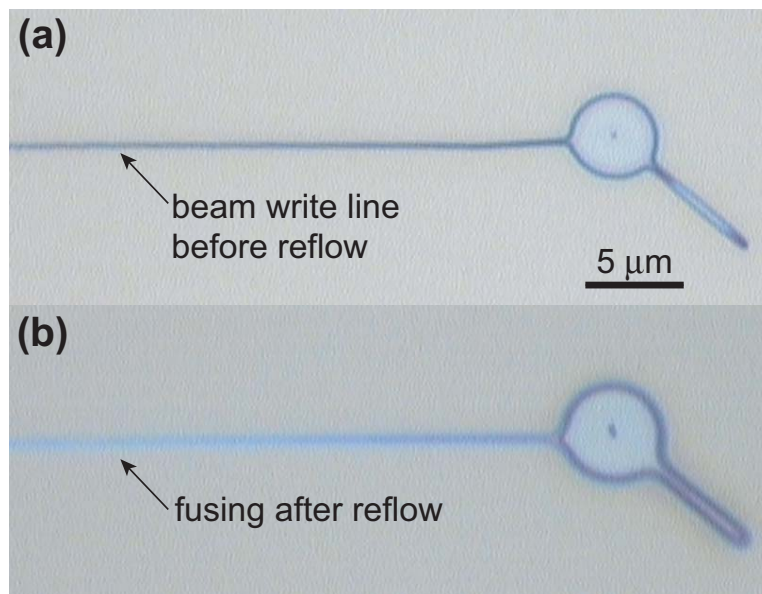


Figure 3.3: (a) 100 $\times$  magnification optical microscope image of electron-beam resist after develop. Shown is a region where electron beam rests for a short period and then tracked to the left of the image resulting in a very narrow gap in the ZEP resist. (b) Optical microscope image of the same region taken at same magnification after reflowing the resist at 160 $^{\circ}$ C for 5 minutes.

the sample was immediately transported to a fume hood for developing. The develop chemistry was 3 minutes in Zeon ZED-N50 developer, followed by a 10 second rinse in Zeon ZMD-D (or ZMD-B) solution and a final N<sub>2</sub> dry.

After close inspection of the mask under 100 $\times$  magnification in the Nikon optical microscope, the wafer was then subjected to a post-lithography bake. By suitable choice of temperature and duration, this bake can significantly reduce imperfections in the electron-beam resist pattern. Temperatures too low do not result in resist reflow, while temperatures too high can cause significant loss of resist to sublimation. A temperature high enough to allow the resist to reflow must be reached and maintained for the imperfections in the resist pattern to be reduced. The appropriate duration and temperature for the resist prepared as described above was empirically determined to be 5 minutes at 160 $^{\circ}$ C. The experimental standard that was used in order to measure resist reflow used a fortuitously narrow gap in electron-beam resist, as seen in Figure 3.3(a). The gap in the resist is caused by the slow stage translation in between patterns with the electron beam still being fired at the sample. The result is a sub-micron gap in the electron-beam resist that extends near but not affecting the

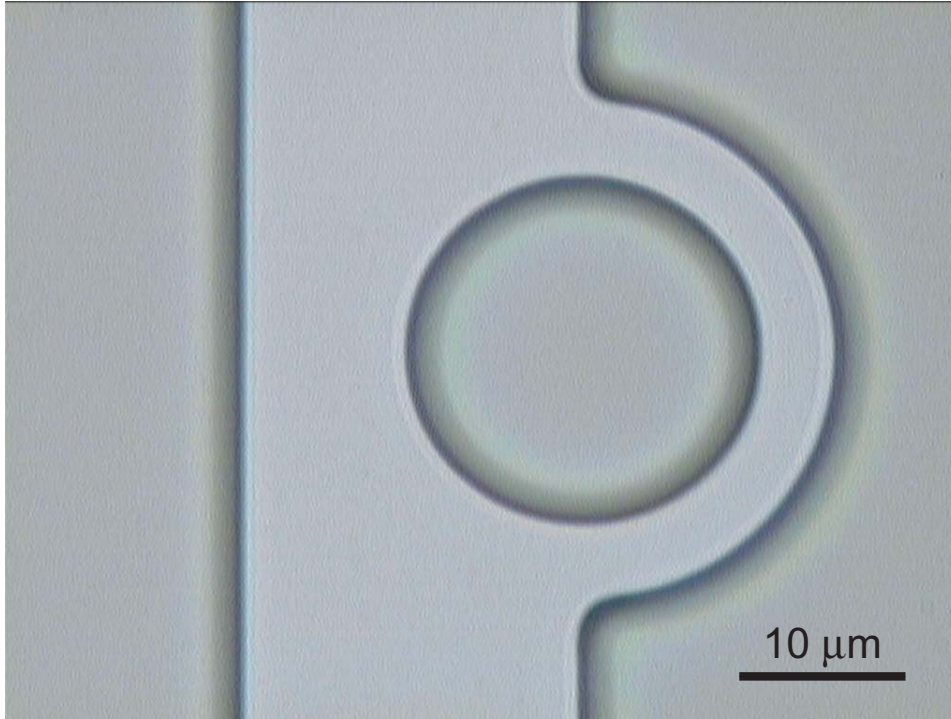


Figure 3.4: (a) 100 $\times$  magnification optical microscope image of electron-beam resist after develop and reflow at 160 $^{\circ}$ C for 5 minutes. Shown is a 10  $\mu$ m radius microdisk etch pattern.

device patterns. Five minutes at 160 $^{\circ}$ C was determined to be the minimum time and temperature that was necessary to allow this resist gap to fuse together (as shown in Fig. 3.3(b)) when the stage was translating at a linear rate (assuming  $I_B \sim 30\text{--}35$  pA). After the reflow process, the roughness in the patterns was greatly reduced, and the sidewall angle was reduced from 90 $^{\circ}$  to approximately 45 $^{\circ}$ .

Figure 3.4 shows an optical image of a typical electron-resist mask after reflow, where no discernible imperfections could be observed at visible wavelengths. While increasing the minimum radii of curvatures that were possible, the reflow process created nearly surface-tension limited patterns in a fashion similar to that used to create silica microspheres [29] or microtoroids [31]. The contact angle that the resist makes with the surface is a function of the materials used, the size of the microdisks, and the amount of remaining solvent in the resist. It was found empirically that the latter had the most drastic effect on the reflow. It was for this reason that the whole lithography process, from spin-coating through resist reflow, was treated as if the polymeric resists were continuously evaporating. Strict serial lithography

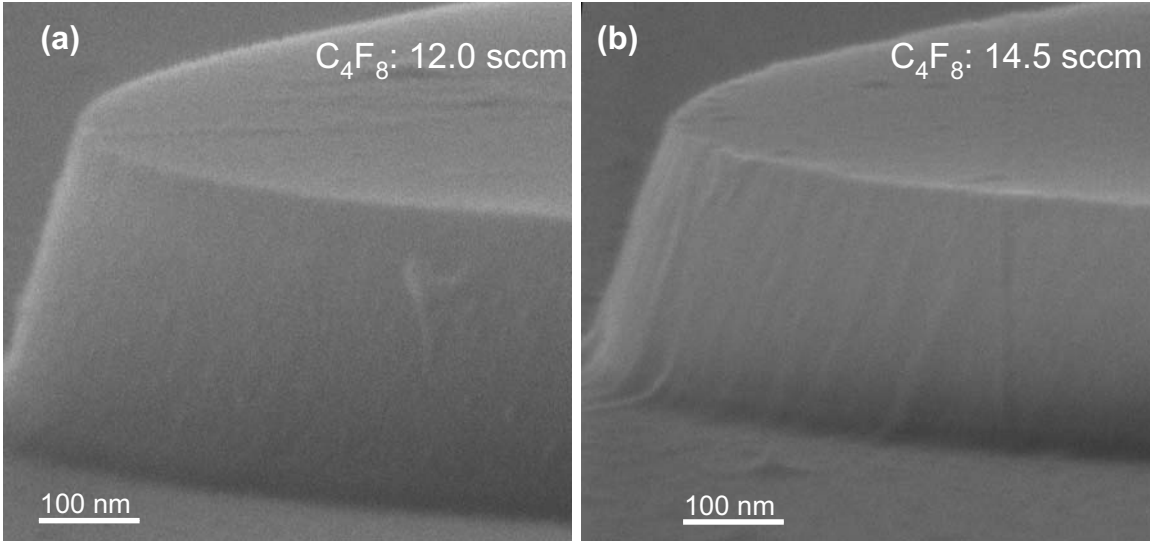


Figure 3.5: SEM micrograph of a  $5 \mu\text{m}$  radii microdisk after mask reflow and low bias voltage ICP/RIE etching. (a) The optimized etch using 12.0 sccm each of  $\text{C}_4\text{F}_8$  and  $\text{SF}_6$ . (b) An unoptimized etch using 14.5 sccm  $\text{C}_4\text{F}_8$  and 12.0 sccm  $\text{SF}_6$ , resulting in heavy polymerization on the sidewalls.

processing of samples and a careful choreography of transfer times was utilized to ensure reproducible reflow results.

### 3.5 Etching and Cleaning

The reflowed patterns were transferred with high fidelity into the Si device layer using a low DC-bias ( $\sim 30 \text{ V}$ ), inductively coupled plasma reactive-ion etch (ICP-RIE) on an Oxford Plasmalab 100 system with load-lock [33]. The angled mask was prone to erosion during the etch process, and so the ICP-RIE was optimized to minimize roughness caused by mask erosion. The ratio of the flow rates, 12.0 sccm  $\text{C}_4\text{F}_8$  to 12.0 sccm  $\text{SF}_6$ , and the 1000 watts ICP and 6 watts RF power were optimized to etch through the thin  $\text{SiN}_x$  cap and top Si layer in a single 2.5 minute etch, shown in Fig. 3.5(a). During the 2–3 minute etch, the chamber pressure was held at 15 mTorr with 15 Torr of helium backing on the  $20^\circ\text{C}$  stage. The  $\text{SF}_6$  etchant provides nearly isotropic etching of silicon. Conversely,  $\text{C}_4\text{F}_8$  results in heavy polymerization on the etched sidewalls leading to a very anisotropic etch [53, 54]. Etching with too little  $\text{C}_4\text{F}_8$ , resulted in very jagged but vertical sidewalls because the etch was too chemical in nature. Etching with too much  $\text{C}_4\text{F}_8$  (shown in Fig. 3.5(b)) resulted in highly

angled sidewalls with occasional larger chunks of silicon missing from the sidewall. This effect was hypothesized to be due to the slower etch rate using large flows of  $C_4F_8$ , which allowed uneven build-up of polymers on the silicon sidewalls. Note that optimized etches of just  $SiN_x$  did not possess this problem at high  $C_4F_8$  flow rates, allowing the etch to be continually smoothed by increasing  $C_4F_8$  at the expense of sidewall verticality.  $SiN_x$  cap was desirable over  $SiO_2$  because of the similarity in individually optimized Si and  $SiN_x$  etch recipes, allowing the plasma to be lit only once. The single well-calibrated dry-etch resulted in improved repeatability, simplified etch optimization, and shorter fabrication times. While this etch produced excellent device performance, the etched sidewalls were less than perfectly vertical at an angle of  $75^\circ$ . In addition, the optimized etch was found to give similarly excellent results with or without the  $SiN_x$  cap, allowing for increased design freedom of the process flow. The SEM micrographs in Figure 3.6 show a device after the optimized dry-etch but with the reflowed resist in place. The noticeable overetch of the silicon into the BOX layer was done to ensure a uniform sidewall.

After the device layer dry-etch, each sample was soaked in tetrachloroethylene (TCE) for 20 minutes to remove the electron-beam resist shown in Fig. 3.6.<sup>2</sup> The sample was removed and quickly rinsed in acetone, isopropyl alcohol (IPA), methanol, and DI  $H_2O$ . After a quick  $N_2$  dry, the remaining plasma-hardened organics on the surface were removed with a high-temperature Piranha clean as described below. If a straight taper probe was to be used to test the optical resonators, an etch-mask surrounding the disks was photolithographically defined and the wafer surrounding the disks etched down several microns, leaving the devices “isolated” on a mesa. The preferred method of isolation was a multi-step wet and dry etching process. First, AZ 5214 photoresist was spun on the sample at 2000 rpm for 60 seconds. Then the edge bead was removed from the sample with a clean wipe soaked in acetone. The sample was then oven-baked for 12 minutes at  $100^\circ C$ . An additional edge bead removal was accomplished with a UV exposure of 18 seconds while the central device region of the chip remained protected from UV. The outer, and now exposed, resist was developed away in AZ-300 MIF in approximately 60 seconds. At this point, a

---

<sup>2</sup>It was empirically determined that TCE is a superior etchant on electron-beam resist while acetone is superior at removing photoresist.

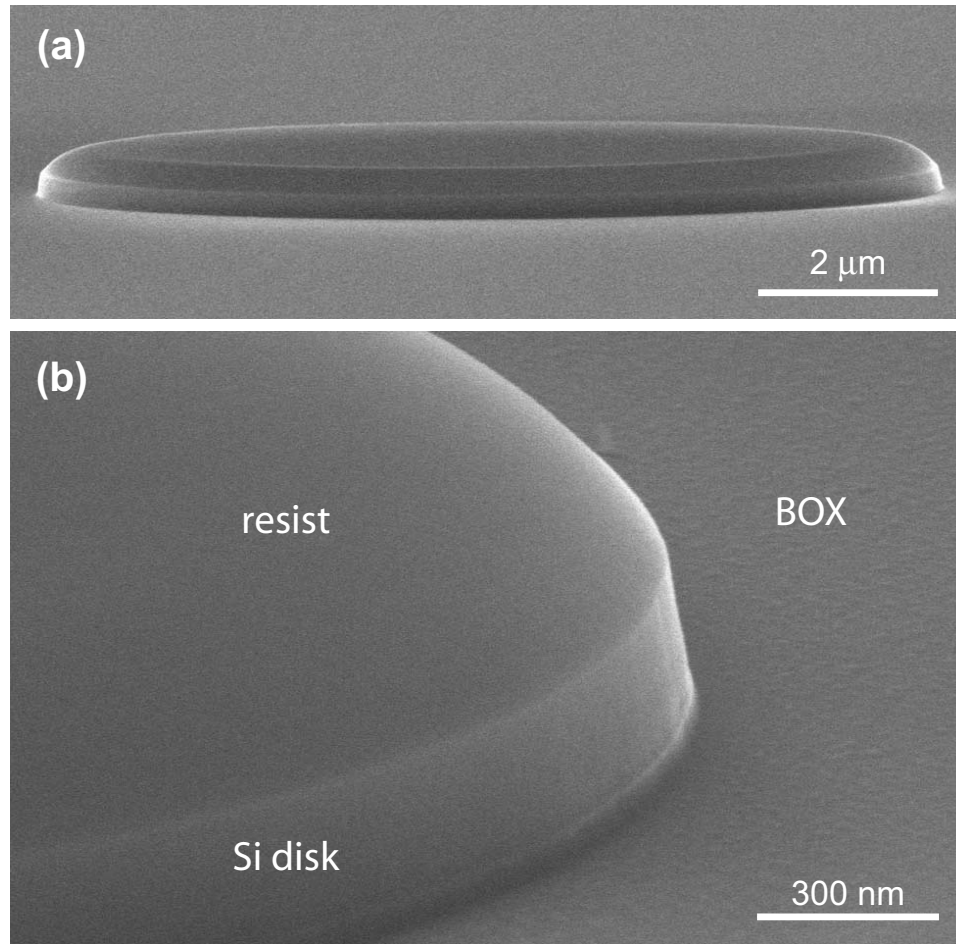


Figure 3.6: (a) SEM micrograph of a 5  $\mu\text{m}$  radii microdisk after mask reflow and low bias voltage ICP/RIE etching with ZEP mask still in place. (b) Close-up view of the same device showing the smooth sidewalls.

carefully aligned mesa stripe was aligned to the set of devices, ensuring that the edges of each device's fiber via would be left unprotected by the photoresist. After a second exposure and develop step, the sample was hard baked in an oven for 5 minutes at 180°C. The temperature of the second bake was enough to cause the resist to reflow, providing intimate contact with the sample, limiting undercutting during subsequent isotropic etching steps. The top  $\sim 10 \mu\text{m}$  of the sample was then etched away with dry and wet etches while the devices were protected by the photoresist. First, the aforementioned device layer etch was used to remove the top Si layer from the wafer. Then a 7 minute  $\text{SiO}_2$  etch removed approximately  $1 \mu\text{m}$  of the  $2 - 3 \mu\text{m}$  BOX layer. The etch parameters used were 15 sccm of  $\text{C}_4\text{F}_8$ , 4 sccm of  $\text{O}_2$ , 6 mTorr chamber pressure, 20 Torr helium backing, 10°C table temperature, 500 W of ICP power, 80 W of RF power, yielding a DC bias of 190 – 170 V. The remainder of the BOX was removed with a stirred 5:1  $\text{H}_2\text{O}:\text{HF}$  solution for approximately 20 minutes. Finally, the silicon substrate was etched down several microns with a pure  $\text{SF}_6$  dry-etch for 10 minutes. The “Si Mesa” etch parameters used were 20 sccm of  $\text{SF}_6$ , 15 mTorr chamber pressure, 10 Torr helium backing, 15°C table temperature, 1200 W of ICP power, 10 W of RF power, yielding a DC bias of 37 V. Finishing the BOX etch with a wet-etch prevented silicon pillar formation during the Si Mesa etch because the BOX silica was uniformly removed. Figure 3.7 shows an SEM micrograph of a  $4.5 \mu\text{m}$  radii microdisk after mesa isolation etching and HF undercut (described below). The figure is looking parallel to the direction of fiber placement. The mesa isolation lithography runs left and right in the figure.

After the completion of any lithography plus dry-etch step, a Piranha clean was needed in order to remove the hard baked resist [53]. Inside a 50 mL beaker, 30 mL of  $\text{H}_2\text{SO}_4$  was heated to 65°C on a 160°C hotplate with magnetic stirbar at 350 rpm. At this point, 7 mL of 30%  $\text{H}_2\text{O}_2$  was added to the solution. The exothermic reaction that resulted self-heated the solution up to the desired operating temperature of 100 – 110°C. Once the Piranha solution reached 100°C, the sample was suspended in the center of the swirling acid with solid fluorinate plastic (teflon-like) tweezers. Suspending the sample was essential because the evolved  $\text{CO}_2$  gas during the clean would otherwise collect on the sample surface raising its buoyancy. The sample was

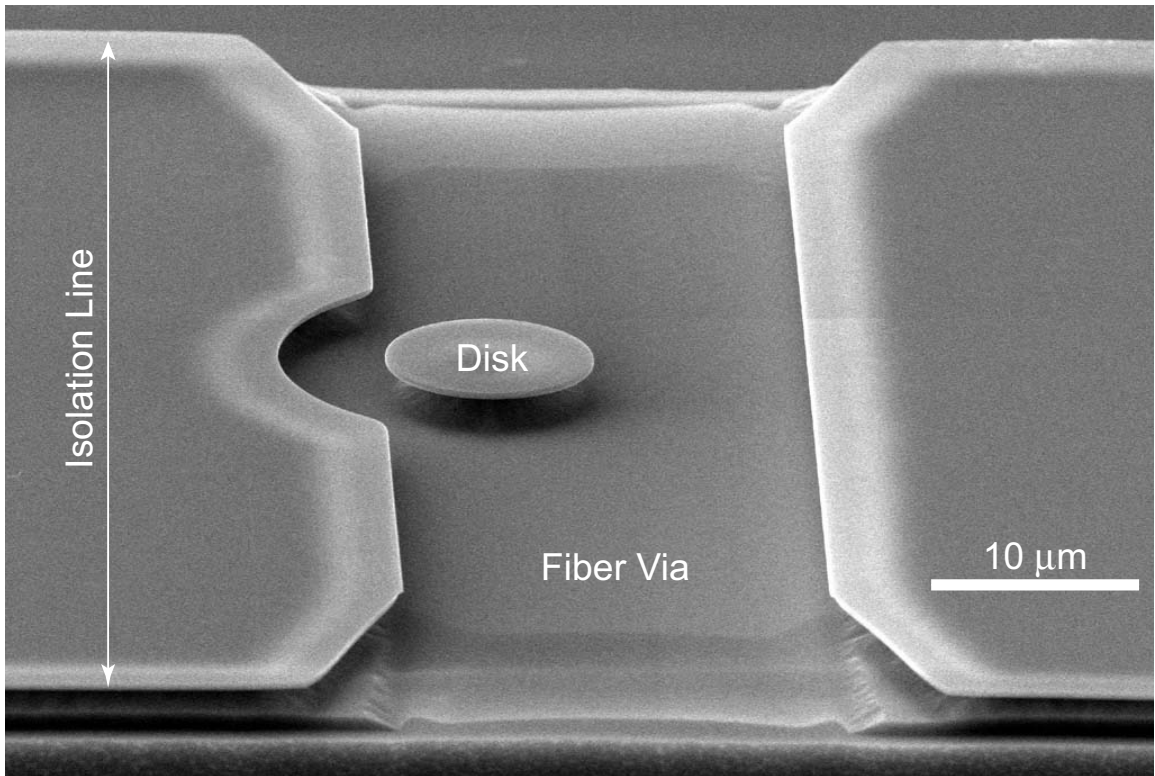


Figure 3.7: SEM micrograph of a  $4.5 \mu\text{m}$  radii microdisk after mesa isolation etching and HF undercut.

cleaned for 30 – 60 minutes in the Piranha during which additional  $\text{H}_2\text{O}_2$  was added to maintain the temperature. The sample was finally rinsed in three separate beakers of DI  $\text{H}_2\text{O}$  and subjected to  $\text{N}_2$ .

Following the Piranha etch to remove organic materials, a dilute hydrofluoric acid solution (typically 5:1  $\text{H}_2\text{O}:\text{HF}$ ) was used to remove the protective  $\text{SiO}_2$  or  $\text{SiN}_x$  layer and partially undercut the disk, as seen in Fig. 3.1. The process of undercutting is crucial in order to allow strong fiber coupling with high ideality [55]. The etch time was typically 45 – 65 minutes depending on the original BOX thickness and disk radius. The sample would be removed from the etchant several times during the etch to chart the undercut’s progress. The undercut pedestal takes on its angular hourglass shape due to a higher etch rate on the wafer Unibond® [8] versus the bulk silica. For disks of radii greater than 5  $\mu\text{m}$ , the BOX could be fully etched away beneath the disk while retaining a reasonably thick pedestal. After the HF etch, the wafer was rinsed in deionized water and again dried with clean, dry  $\text{N}_2$ . Upon completion of the processing, the wafers were immediately removed to an  $\text{N}_2$  purged enclosure for storage and/or characterization.

### 3.6 Conclusion

The true test of the above fabrication steps was in the microresonator’s ability to hold onto photons within a small volume for an extended period of time. Each of the above steps was optimized over a three-year period in a basically serial manner of processing samples, wherein each sample had a different processing parameter modified before it was tested for its quality factor. As can be seen in Fig. 3.8, the latest of the microdisks exhibit a virtually perfect circular topology, a result of well-calibrated electron-beam lithography, resist reflow, and low DC-bias device-layer etching. Also shown in the figure are the tiny silica pedestals situated microns from the disk periphery, optimized for their ability to allow fiber coupling to high-index contrast optical modes, negligible modal overlap, and mechanical stability. These clean and smooth samples produced the highest quality factors in silicon to date because of the intense effort that has

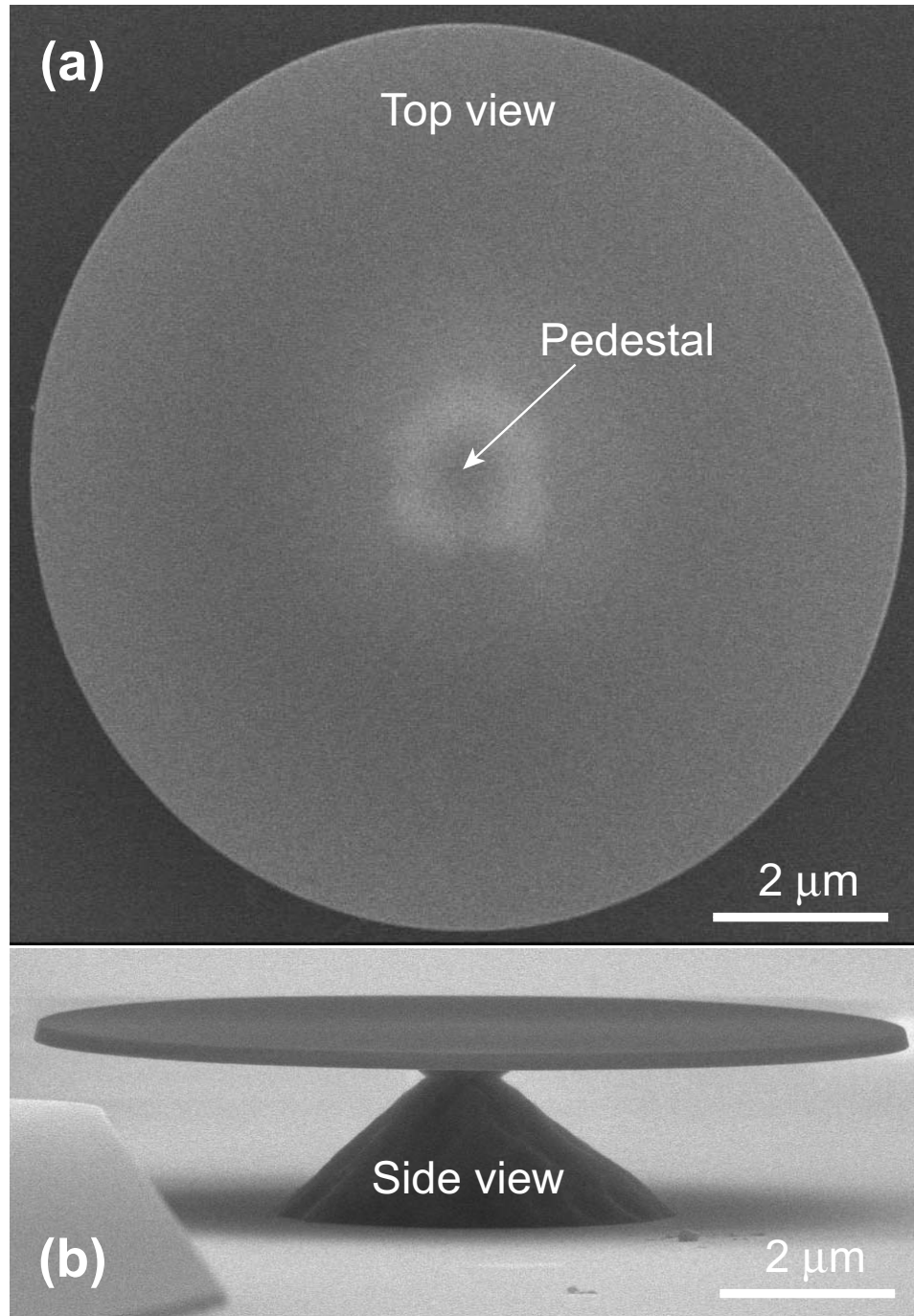


Figure 3.8: SEM micrograph of an undercut  $5\ \mu\text{m}$  radius microdisk. (a) Top view highlighting highly circular definition. (b) Side view of the same disk on the same scale to show the detail of the silica pedestal.

been put on mitigating the effect of Rayleigh scattering. Chapter 5 provides further details on the characterization of the microresonators as well as additional chemical treatments and surface passivation layers that were developed in order to further reduce interface state losses. Many of the lessons learned and the recipes outlined in this chapter can be directly ported to any silicon microphotronics application including microrings [56], photonic crystals [17, 18, 33], and waveguides [57]. As an example, Chapter 6 shows results of using the above recipe to create record-breaking  $Q$ 's in non-undercut silicon microrings.

## Chapter 4

# Optical Coupling via Fiber Taper Probes

### 4.1 Introduction

Advanced fabrication tools such as electron-beam lithography and focused ion beam etching have made it possible for researchers to create devices with new physical properties only observable at the nanoscale. However, creating devices at the nanoscale is really only half of the problem; providing access to and from these devices requires a similar degree of ingenuity. To pump and collect emission efficiently into and out of optical microcavities, a bus waveguide can be placed in the microcavity's near-field [30]. In this coupling scheme, the bus waveguide and resonator share small amounts of power without affecting the mode profiles to first order. Furthermore, this coupling junction can be made nearly ideal by reducing the number of modes in the bus that can couple to the resonances [55]. While most technologies require that the bus waveguide be integrated along with the microcavity, an external coupling waveguide has many research advantages. A movable external waveguide effectively orthogonalizes the research problem into microcavity optimization and efficient coupling, something that must be done statistically when using integrated waveguides. A movable waveguide can controllably change the loading in order to provide optimal power transfer to the microcavity. In addition, the spectrally dependent transmission through the waveguide can be normalized out, allowing for pure microcavity spectra to be obtained. To characterize the optical resonators described in this thesis, an evanescent fiber taper coupling technique is employed [28, 33, 58]. In this process, an

optical fiber is adiabatically drawn to a  $1 - 2 \mu\text{m}$  diameter using a hydrogen torch so that its evanescent field is made accessible to the environment [59]. Using DC motor stages with 50 nm encoded resolution, the fiber taper can be accurately positioned within the microdisk near-field so as to evanescently couple power into the microdisks.

## 4.2 Optical Properties of Silica Fiber Tapers

As step-index fibers are routinely used in long-haul telecommunications, many books have entire chapters devoted to their properties, such as Ref. [44]. The index of refraction for a step-index fiber taper is given by

$$n(\rho) = \begin{cases} n_c & 0 < \rho < a \\ n_0 & \rho > a \end{cases}, \quad (4.1)$$

where  $a$  is the radius of the fiber taper. As all of the testing in this thesis was conducted in nitrogen purged environments,  $n_c \simeq 1.45$  and  $n_0 = 1.0$ . For fiber tapers, it is not rigorously possible to separate the modes into TE and TM modes, but are rather an admixture of the two. Fortunately, the hybrid modes have analytic solutions in terms of Bessel functions of the first and second kind and can be calculated using the treatment in Ref. [44]. For step-index fibers, only one mode does not have a cut-off wavelength and is labeled as  $HE_{11}$ . For a given free-space wavelength, the criterion for the radius that will ensure single-mode behavior can be found according to

$$a = 2.405 \times \frac{\lambda_0}{2\pi\sqrt{n_c^2 - n_0^2}}. \quad (4.2)$$

Thus, at  $\lambda_0 \approx 1550 \text{ nm}$ , the fiber must have a radius less than  $0.56 \mu\text{m}$  in order to ensure that it is single mode.

Figure 4.1 shows the electric field components for the  $HE_{11}$  mode of a silica fiber taper with  $a = 0.5 \mu\text{m}$  at  $\lambda_0 = 1550 \text{ nm}$ . The direction of propagation is assumed to be in the  $y$ -direction, and the parity is such that the largest field component is in the vertical direction, labeled as  $z$ . The notation  $i * E_y$  is a short-hand notation to remind the reader that the longitudinal component is  $\pi/2$  out of phase from the tangential

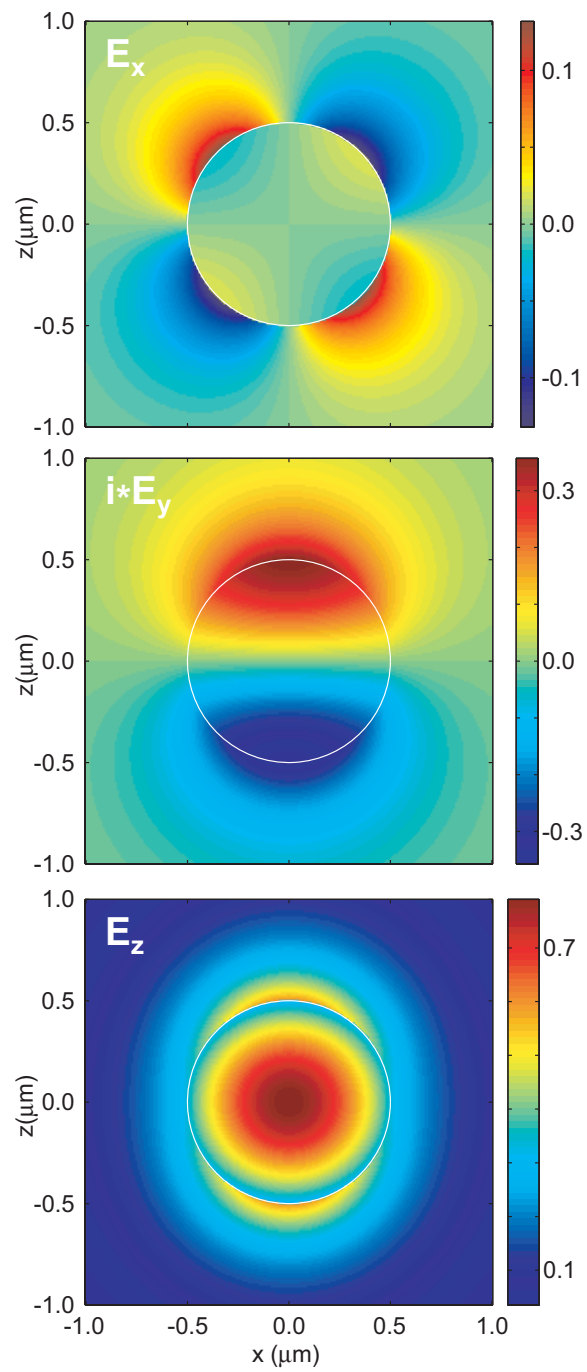


Figure 4.1: Electric field components for the  $HE_{11}$  mode of a silica fiber taper with  $a = 0.5 \mu\text{m}$  at  $\lambda_0 = 1550 \text{ nm}$ . The direction of propagation is assumed to be in the  $y$ -direction, and the parity is such that the largest field component is in the vertical direction labeled as  $z$ .

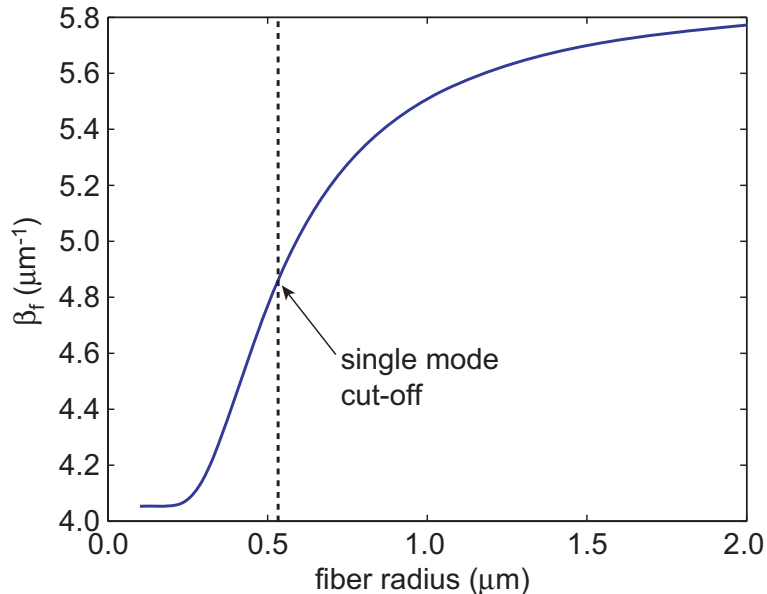


Figure 4.2: Plot of the propagation constant  $\beta_f$  of the  $HE_{11}$  mode versus the fiber radius,  $a$ . The wavelength was held fixed at  $\lambda_0 = 1550$  nm. The index of refraction inside the core and cladding was assumed to be 1.45 and 1.0, respectively.

( $E_x$ ,  $E_z$ ) components. Because of the large confinement, the mode has picked up a large longitudinal component. For this radius and wavelength, silica fiber tapers have longitudinal components that are 50% as large as the peak tangential component ( $E_z$  in this case).

As will be described in Section 4.5, the momentum of the light inside the fiber plays a crucial role in the amount of power that can be coupled to the microcavities. Figure 4.2 shows a plot of the propagation constant  $\beta_f$  of the  $HE_{11}$  mode versus the fiber radius,  $a$ . The wavelength was again held fixed at  $\lambda_0 = 1550$  nm, and the index of refraction inside the core and cladding was assumed to be 1.45 and 1.0, respectively. For very thick fiber tapers, the propagation constant approaches that in bulk silica,  $\beta_f \approx 2\pi n_c/\lambda_0$ . As the fiber radius become very small, much of the field leaks into the air cladding, giving an asymptotic value  $\beta_f \approx 2\pi/\lambda_0$ . An important note is that contrary to recent popular coverage on silica “nanowires,” the smallest beam waist occurs for  $a \sim \lambda_0/(2n_c)$ . For radii less than a half-wavelength in the material, the mode begins to expand dramatically as it loses confinement. This intuitively makes sense because in the limit of zero radius, the mode should return to a completely unguided plane wave.

Fiber tapers are created in much the same way that optical fibers are drawn, but scaled down by orders of magnitude in size. Starting with a commercial optical fiber as a preform, a local region of the preform is heated above the softening temperature of silica,  $\sim 1800^\circ\text{C}$ . Then the preform is drawn thinner by increasing the applied tension slowly. From simple conservation of volume arguments, the taper radius takes on an exponential dependence along the length of the tapered fiber [59]. The rate of radius change as a function of taper length is determined by the length of the hot zone. Larger hot zones result in longer tapers, resulting in a more adiabatic conversion of the photon populations amongst the optical modes with changing propagation constants. Shorter hot zones can begin to violate the need for adiabaticity, resulting in the fundamental mode coupling to higher order and lossy fiber modes. The ideal taper has a minimum length for an acceptable amount of insertion loss.

### 4.3 Fabrication of Fiber Taper Probes

In order to fabricate fiber tapers with micron diameters, a computer-controlled pulling apparatus was built, as shown in Figure 4.3. The first step was to strip approximately 1.5 cm of the acrylate cladding from the center of a 2 meter section of standard single mode fiber. For testing between 1280 and 1625 nm, Corning SMF-28e optical fiber (125  $\mu\text{m}$  cladding diameter with 8  $\mu\text{m}$  core diameter) was used at the taper preform. After stripping off the acrylate cladding, the fiber is thoroughly cleaned in IPA and placed in commercial fiber mounts (see Fig. 4.3(b)). The fiber mounts are attached to Suruga Seiki motorized stages with micron positioning accuracy. Great care must be taken to ensure that the fiber preform has been placed in the mounts with no torsional forces, as these lead to misshapen tapers. A third motorized stage holds a hydrogen torch affixed to the stage with a three-axis micrometer positioning system. The entire pulling rig is encased in an acrylic enclosure to provide for maximum flame stability. It was determined that mixing oxygen with the hydrogen behind the torch tip resulted in high-pressure jets of hot gases, which proved to be too violent for micron-diameter fiber tapers. Thus, with no oxygen in the fuel mixture, the torch consumed large quantities of ambient  $\text{O}_2$ , which need to be constantly replaced from

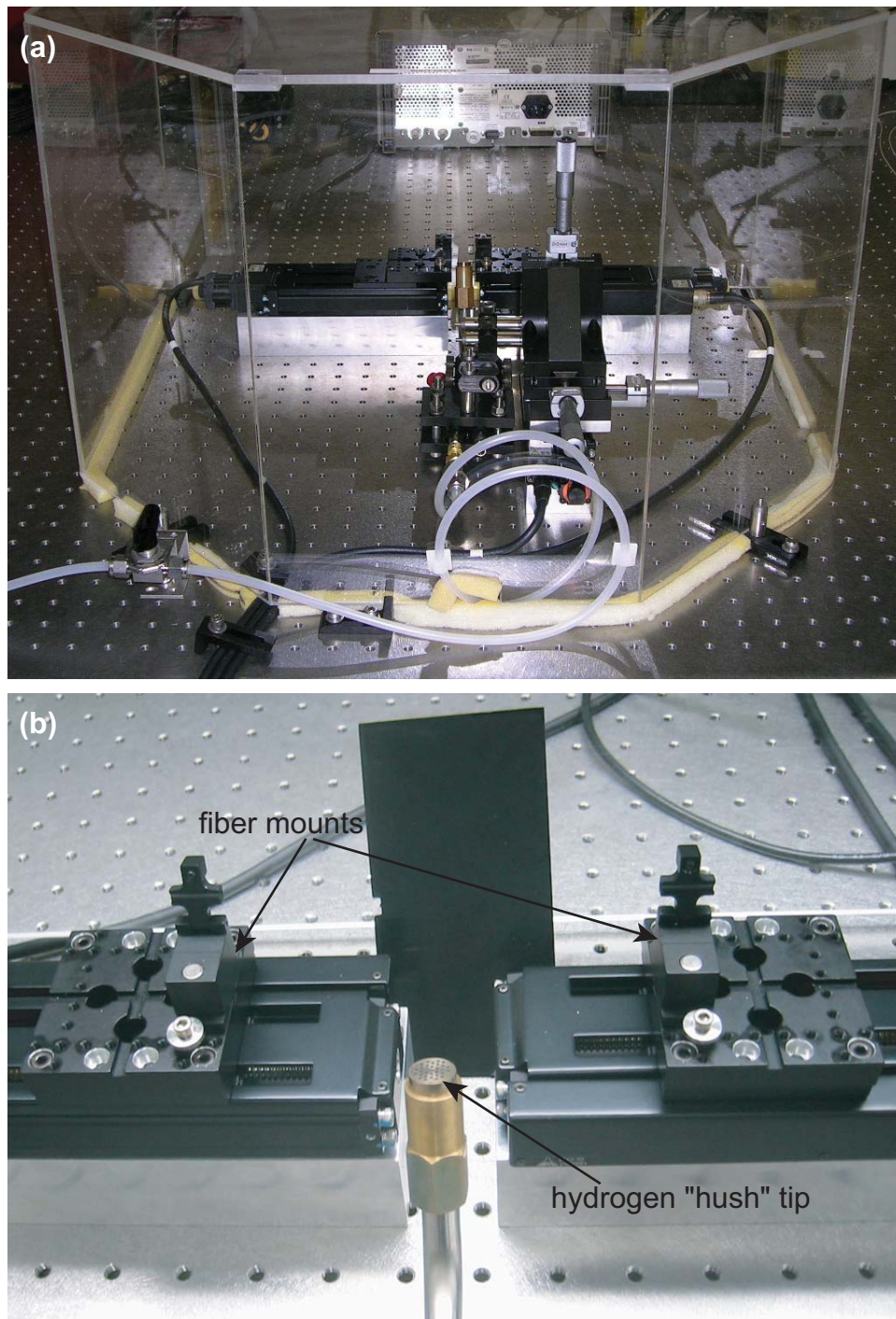


Figure 4.3: Digital photographs of the custom taper pulling apparatus. Part (a) shows the torch and fiber mounts on motorized stages. Also shown is the acrylic enclosure used to stabilize the air currents inside the rig. (b) Close-up view of the fiber mounts and hydrogen "hush" tip used to draw the fiber preform gently.

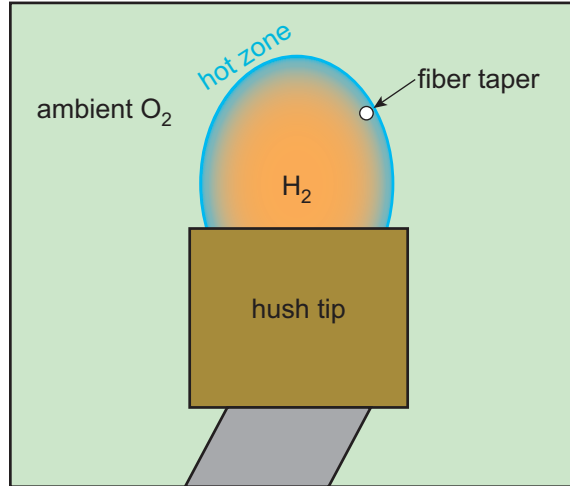


Figure 4.4: Schematic drawing of the optimal placement of the fiber taper within the hydrogen torch flame. The reaction zone of hydrogen fuel and ambient oxygen is labeled at the “hot zone” in blue.

outside the enclosure. The solution was to use the natural convection produced by the torch to wick new air through open-cell foam filters at the base of the enclosure. Then the hot water vapor was expelled through dozens of milled holes at the top of the enclosure in an attempt to make the air currents as laminar as possible.

The optimal type of torch tip was approximately 1 cm in diameter and consisted of 30 small apertures for the fuel to escape. Termed a “hush” tip, the diffuse addition of fuel into the region of the fiber taper resulted in a gentle and uniform heat source. Figure 4.4 shows a schematic drawing of the optimal placement of the fiber taper within the hydrogen torch flame. The reaction zone of hydrogen fuel and ambient oxygen is labeled at the “hot zone” in blue. The torch was carefully aligned such that when the motorized stages move the torch forward, the fiber preform just enters the reaction zone of flame. In order to improve repeatability, the torch’s hydrogen supply line was externally controlled and spring coiled in order to prevent torch misalignment. Once the torch had begun to heat the preform, the fiber mounts were set to retract at a linear speed of  $\sim 1\text{--}2 \mu\text{m}/\text{second}$ . The taper’s progress was monitored by launching a 1550 nm external cavity laser into the taper and using a photodetector to collect the emission on the other end. As the taper was stretched and thinned, the fundamental mode transiently coupled to many different higher order modes, the result of which looked like increased noise on the laser transmission as a

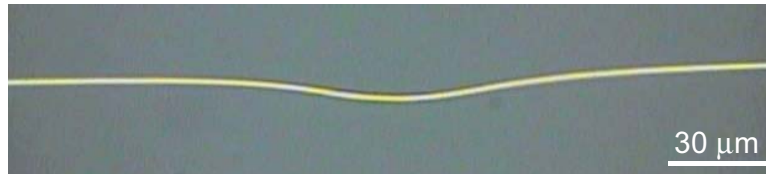


Figure 4.5: An approximately  $1.5 \mu\text{m}$  diameter fiber taper after dimpling and subsequent re-tensioning.

function of pull time. However, once the taper was thin and long enough such that the fundamental mode no longer coupled to other modes, the noise went completely away. This transition was used as a trigger to estimate the taper radius as a function of pull time and was verified by later SEM micrographs.<sup>1</sup>

After retracting the torch, the taper was removed from the fiber mounts by hand. Then the taper was bent into a U-shape and placed into an acrylic mount with the tapered region extending off the mount, shown in the center of Fig. 4.6. The U-shape mounting of fiber tapers has proved to be an essential technique in providing stable coupling to optical microresonators because of the self-tensioning that takes place at the bends of the taper. Once in the fiber taper probe mount, an optional process of “dimpling” the taper may be done at this time.<sup>2</sup> In the process of fiber dimpling, the mounted taper was brought into intimate contact with a second  $125 \mu\text{m}$  diameter clean fiber in the orthogonal direction. The point of contact was then slowly heated so that the taper relaxes with a  $\sim 125 \mu\text{m}$  diameter dimple in its smallest region, similar to the curved tapers in Ref. [60]. The tension on the fiber taper was then optimized with an integrated micrometer on the acrylic mount. Figure 4.5 shows an approximately  $1.5 \mu\text{m}$  diameter fiber taper after dimpling and subsequent further tensioning.

## 4.4 Test Setup

After the fiber taper probe fabrication was completed, it was immediately mounted inside the test setup shown in Fig. 4.6. The test setup consisted of an acrylic enclosure, probe micropositioning system, sample stage, and imaging setup. The acrylic

<sup>1</sup>Developing this repeatable pulling method was conducted during Colin Chrystal’s SURF 2005 project.

<sup>2</sup>The majority of fiber taper dimpling research was done by colleague Chris Michael.

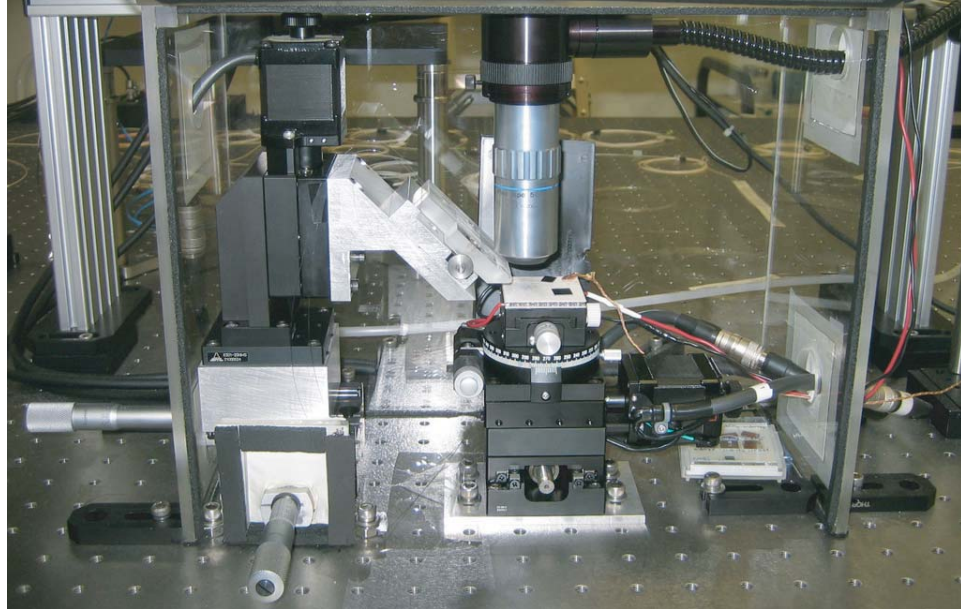


Figure 4.6: Acrylic enclosure used for testing optical devices with its front lid raised. On the left is the micropositioning system holding the fiber taper probe, and on the right are the x-y motorized stages that move the samples laterally. The ultra-long working distance objective lens and zoom barrel used to monitor the probing can be seen at the top of the image.

enclosure (seen in the figure with its front lid raised) was nitrogen purged in order to prevent ambient  $H_2O$  from developing microcracks in the fiber taper probe, thereby increasing the lifetime of the finished probes from days to months. Great care was also taken to seal the enclosure from leaks, as it was also found that laboratory air currents otherwise significantly reduced the spatial stability of the fiber taper. The fiber taper probe was secured on a Suruga Seiki optically encoded motorized stage with 50 nm stepping resolution. This assembly was then placed on top of an x-y micrometer stage for manual lateral movements of the taper probe. The sample stage consisted of two additional Suruga Seiki motorized stages with 50 nm accuracy, a goniometer, and a thermo-electric (TE) cooler. Thus, three-dimensional taper-device displacement was accomplished with the three motorized stages. Upon adding a new probe, an initial alignment was done such that the goniometer was iteratively adjusted until the taper was parallel with the sample's top surface. As the motorized stages provided an excess of heat, the average substrate temperature was an elevated temperature of  $30.5^\circ\text{C}$ , as measured by a thermocouple mounted to the top of the TE cooler. Achieving sample temperature stability required hours due to stage heating.

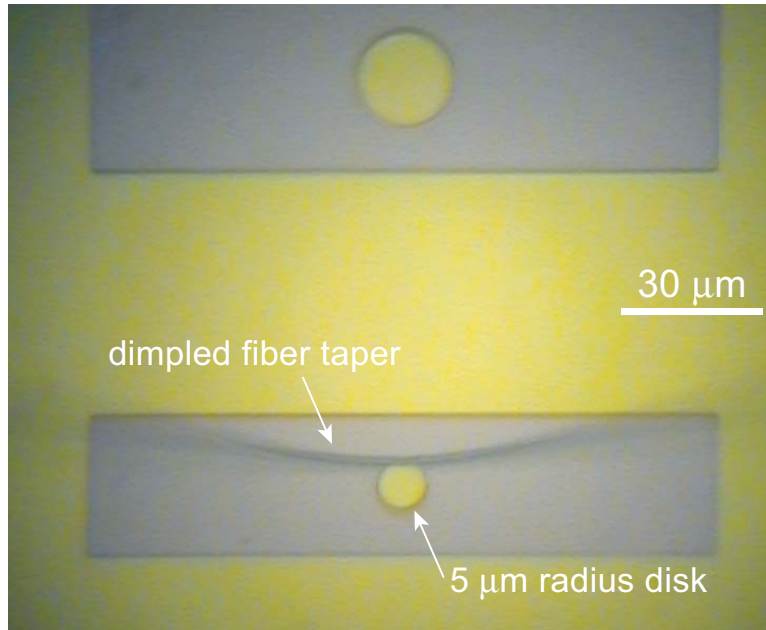


Figure 4.7: Optical image taken while testing a non-undercut  $5\ \mu\text{m}$  radius microdisk with a  $\sim 1.5\ \mu\text{m}$  diameter dimpled fiber taper. Dimple extends down into focus from this view.

Therefore, the power to the stages was kept on throughout the course of extended testing periods. The TE cooler and thermocouple were used to measure the thermo-optic coefficients,  $dn/dT$ , for later use in thermal modeling. In addition, the TE cooler could also be used for very fine resonance location adjustments, though this was less desirable when the taper was not in contact with the device due to thermal expansion induced taper-device gap variations.

The objective lens, zoom barrel, and CCD camera were used in conjunction to provide high-resolution images of the devices and taper while testing, seen in Fig. 4.7. In this figure, the same dimpled taper, as shown from the side in Fig. 4.5, extended down into focus at the top surface of the sample. The taper probe was used to couple power to the non-undercut  $5\ \mu\text{m}$  radius microdisk, which was one of a two-dimensional array on the sample. The truly localized nature of this probing is made very evident by the quick degree of defocusing that can be seen as the dimple rose vertically.

Optical power was provided by one of several external cavity lasers manufactured by New Focus, including the Vidia and Velocity series. The Vidia laser had exceptional swept scan performance and could measure quality factors on the order of

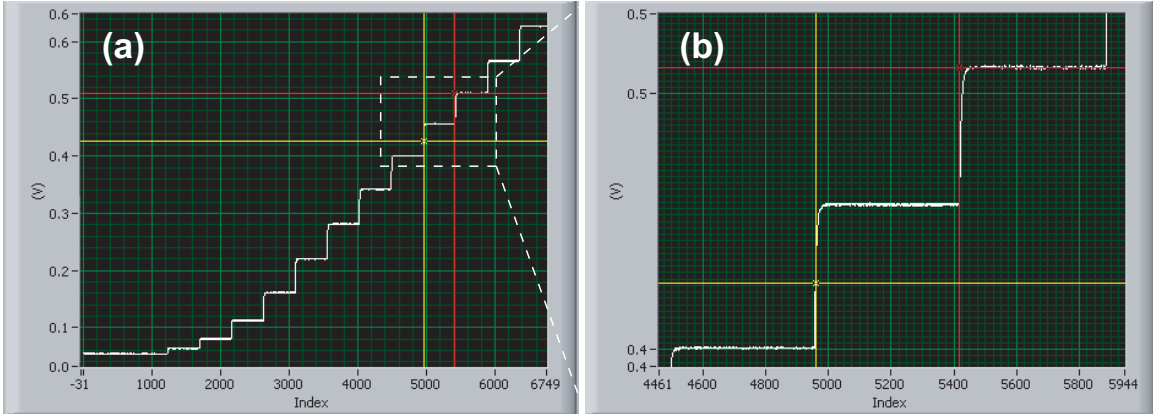


Figure 4.8: (a) Acquired “wave out” voltage from the Velocity laser versus time since initiating the sweep through GPIB. (b) A close-up view of the software triggering region.

$10^6 - 10^7$  in its wavelength range. The Velocity laser series performed poorly by comparison. However, the Velocity laser’s fine frequency control was critical in performing much of the advanced testing where extremely repeatable low-noise scans were needed. Thus, most of the testing development was done on the Velocity lasers to make up for their shortcomings.

One major drawback to the Velocity laser is the lack of an external or internal trigger that could be used to link the transmission spectrum collected in time with the wavelength of the laser versus time. In order to overcome this limitation, the Velocity has a 0 – 9 V BNC output, which specifies the position of the mirror arm and thus the wavelength. Figure 4.8(a) shows a plot of the “wave out” voltage versus time since initiating the sweep through GPIB. The staircase effect was a result of the  $\sim 30$  ms update frequency of the laser. In addition, the motor reached a linear speed only after  $\sim 300$  ms, as is apparent by the slow ramp of the wave-out voltage in the lower left portion of the figure. To compensate, 2–3 nm of extra data was taken in the beginning and end of every wavelength scan as a buffer region. Then post-processing in Labview was done to software trigger the beginning of the useful data. The yellow marker in Fig. 4.8(b) shows the voltage that would be expected for the desired start wavelength. However, this point could not be guaranteed to be an accurate start point in the data array because of the slow voltage update. Thus, the next stair-case was found through numerically triggering to determine the best point to start the real data array. Then a second-order polynomial fit to the rest of the wave-out array

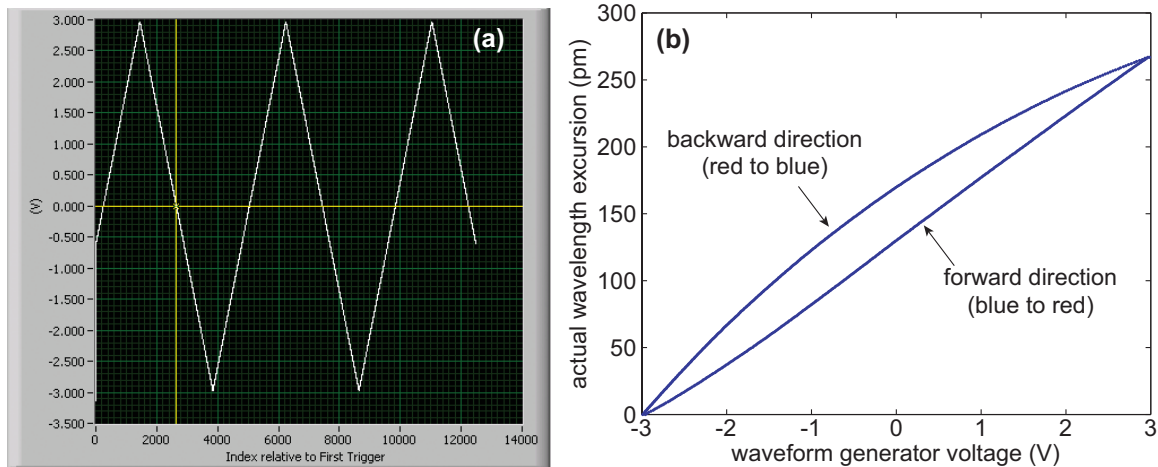


Figure 4.9: (a) Acquired waveform generator voltage output used to control the Velocity laser's fine frequency piezo-stack. (b) Hysteresis curve generated from fiber-based Mach-Zehnder interferometer.

was done to determine the proper wavelength axis for the transmission data. Finally, this data would be routinely divided by a background scan taken under identical conditions but with the taper moved laterally  $\sim 2 \mu\text{m}$  from the disk, as shown in Figure 5.11. It was only with these measures that resonance locations and FSR's could be accurately and precisely determined.

Once a broad scan was acquired, it was customary to further investigate each high- $Q$  resonance by repeatedly piezo-dithering the Velocity's wavelength while collecting transmission data. An Agilent 33120A arbitrary waveform generator was used to provide a saw-tooth voltage to the piezo-stack's  $\pm 3$  V input. The waveform was set to continuously scan at frequencies between 5 and 30 Hz, with a voltage amplitude that was dependent upon the desired wavelength span. Figure 4.9(a) shows the acquired waveform generator voltage output for 2.5 periods of data. This data was then used to software trigger the forward and backward laser scans across the resonances, as shown by the yellow marker in the figure. It was determined that the piezo's actual versus desired wavelength span varied as a function of both the waveform amplitude and time. Thus, a fiber-based Mach-Zehnder interferometer was used to calibrate the most critical scans to  $\pm 0.01$  pm linewidth accuracy. This was accomplished by acquiring transmission spectra before each testing session and for each waveform voltage amplitude. By accurately measuring the physical length difference between the arms,  $\Delta L$ , the actual wavelength span,  $\lambda_2 - \lambda_1$ , could be found using the equation

$$\lambda_2 - \lambda_1 = \frac{m\bar{\lambda}_0^2}{\bar{n}\Delta L} \quad (4.3)$$

where  $m$  is the number of interference oscillation periods,  $\bar{\lambda}_0$  is the center wavelength, and  $\bar{n}$  is the effective index of the fiber. For our Mach-Zehnder's arm difference of 1 meter, the transmission would oscillate every  $1.57 \pm 0.03$  pm. This number was then used to calibrate the most used voltage amplitudes. At the full  $\pm 3$  V waveform amplitude, the average wavespan was 275 pm and would vary by up to 20 pm day to day, depending on the laser's usage. Figure 4.9(b) plots the actual wavelength excursion for one complete waveform generator period. The actual wavelength excursion was found by assuming a constant wavelength spacing between each Mach-Zehnder interference fringe and plotting these from an arbitrary offset versus waveform voltage. As the piezo stack possessed significant hysteresis for large voltage sweeps, only the forward (blue to red) data was routinely used, exemplified in Fig. 4.13. Note that for smaller driving voltage excursions ( $< \pm 1.5$  V), the hysteresis "eye" closed as well as reduced in slope in Fig. 4.9(b). Thus, as the waveform voltage amplitude was reduced, the piezo would tune through marginally less wavelength.

With these modifications and calibrations in hand, the setup was used to bring the taper within the evanescent fields of hundreds of various different resonators, the majority of which were silicon microdisks. By sweeping both the DC motor and piezo-stack, wavelength-dependent spectra were acquired by monitoring the amount of transmission through the fiber taper probe. Paddle wheels were used to control the polarization of the launched laser in order to selectively couple to the differently polarized modes of the microcavities. Because the Velocity lasers operate best at maximum diode power, optical attenuators were used to vary both the input power and the collected power. Fiber-based edge pass filters, 50/50 splitters, and 90/10 splitters were routinely used to spatially and spectrally multiplex and demultiplex the signal in the taper. Conversion of optical power to electrical power was accomplished with several New Focus Nanosecond detectors operating in their 10 k $\Omega$  setting. Stanford voltage pre-amplifiers were used to both amplify the small voltages as well as impedance match the high speed circuit back to 50  $\Omega$ . Data acquisition was ac-

complished with National Instruments DAQ cards connected to a desktop computer that controlled the entire experiment through GPIB.

## 4.5 Modal Coupling

The eigenmodes of a microcavity are solved by enforcing the condition that each mode is orthogonal to each other and, therefore, form a basis for representing the electric field in and near the resonator. Similar reasoning holds for finding the modes of an optical fiber taper in its region of uniform radius. However, these solutions of the Maxwell equations say nothing about what happens when the waveguide and resonator are brought within each other's near-fields. In addition, fabrication of perfectly smooth and circular microcavities is not possible, so that the eigenmode orthogonality for the ideal structures are not always valid. Small nonverticalities in the sidewalls and the presence of pedestals or substrates break the vertical mirror symmetry typically assumed in these solutions. Etch-induced roughness and eccentricities destroy the azimuthal symmetry, collapsing the assumed  $\exp(im\phi)$  spatial dependence. Fortunately, for the case of high- $Q$  microcavities and low-loss bus waveguides, it becomes possible to treat the interactions of the ideal modes perturbatively. Appendix A shows the basic form for time-dependent perturbation theory of the mode of a microcavity, but all coupled mode theories follow a fairly similar framework [37, 61–65].

### 4.5.1 Optical Coupling to Doublet Modes

A whispering gallery mode for a truly azimuthally symmetric resonator possesses degenerate clockwise ( $cw$ ) and counterclockwise ( $ccw$ ) modes [66, 67]. However, with the use of high-quality materials, such as silica fibers and crystalline silicon wafers, whispering gallery resonators can be fabricated that show two distinct WGM resonance dips, called doublets. The observed doublet splitting is based on the small dielectric perturbations at the edge of the resonator, which lift the degeneracy of the  $cw$  and  $ccw$  modes. Based on the work of Gorodetsky, *et al.* [63], a time-dependent perturbation theory can be formulated to quantify this doublet splitting.

When all other modes are far off-resonance, the time rate of change of the energy

dependent amplitudes,  $a_{cw}$  and  $a_{ccw}$ , can be found from Eq. (A.6) to be

$$\frac{da_{cw}}{dt} = i\Delta\omega a_{cw} + i\frac{\gamma_\beta}{2}a_{ccw} \quad (4.4a)$$

$$\frac{da_{ccw}}{dt} = i\Delta\omega a_{ccw} + i\frac{\gamma_\beta}{2}a_{cw}, \quad (4.4b)$$

where  $\Delta\omega_{cw} = \Delta\omega_{ccw} \equiv \Delta\omega$ . In this description, the perturbations are assumed small enough that the backscattering rate for each mode is identical,  $\beta_{cw,ccw} = \beta_{ccw,cw} \equiv \gamma_\beta/2$ . The radius of the ideal disk in  $\epsilon^0(\mathbf{r})$  is chosen as the average radius of the perturbed disk so as to work in a basis where the strength of the perturbation does not create a self-term frequency shift (i.e.,  $\beta_{jj} = 0$ ).

To model power coupling into this resonant system, a phenomenological loss rate,  $\gamma_t \equiv \omega/Q_t$ , and a coupling coefficient to the  $cw$  mode,  $\kappa$ , can be added to obtain [61,67]

$$\frac{da_{cw}}{dt} = \left(i\Delta\omega - \frac{\gamma_t}{2}\right) a_{cw} + i\frac{\gamma_\beta}{2}a_{ccw} + \kappa s \quad (4.5a)$$

$$\frac{da_{ccw}}{dt} = \left(i\Delta\omega - \frac{\gamma_t}{2}\right) a_{ccw} + i\frac{\gamma_\beta}{2}a_{cw}, \quad (4.5b)$$

where  $a_j$  are normalized energy amplitudes,  $|s|^2$  is the normalized input power, and  $\gamma_t = \gamma_{\text{ext}} + \gamma'_i$ . The loss rate can be broken down into loss from the cavity back into the waveguide,  $\gamma_{\text{ext}}$ , and all other loss,  $\gamma'_i$ . Assuming the coupling itself is lossless and obeys time reciprocity, a scattering matrix formalism can further show that  $\kappa^2 = \gamma_{\text{ext}}$  [61]. Additionally, the transmitted and reflected powers are given by [67]  $|t|^2 = |-s + \kappa a_{cw}|^2$  and  $|r|^2 = |\kappa a_{ccw}|^2$ .

At this point, Eqs. (4.5a) and (4.5b) can also be orthogonalized by working in a new basis:

$$a_c = \frac{1}{\sqrt{2}}(a_{cw} + a_{ccw}) \quad (4.6a)$$

$$a_s = \frac{1}{\sqrt{2}}(a_{cw} - a_{ccw}). \quad (4.6b)$$

The new basis vectors are symmetric and anti-symmetric combinations of the two traveling waves, with azimuthal dependence given by  $\cos(m\phi)$  and  $\sin(m\phi)$ , respectively. By choosing standing waves rather than traveling waves as the basis, the differential equations become separable:

$$\frac{da_c}{dt} = \left( i\Delta\omega + i\frac{\gamma_\beta}{2} - \frac{\gamma_t}{2} \right) a_c + \frac{\kappa}{\sqrt{2}}s \quad (4.7a)$$

$$\frac{da_s}{dt} = \left( i\Delta\omega - i\frac{\gamma_\beta}{2} - \frac{\gamma_t}{2} \right) a_s + \frac{\kappa}{\sqrt{2}}s. \quad (4.7b)$$

Although either basis is valid from a mathematical perspective, the standing wave basis becomes more appropriate as the dielectric perturbations are increased. For very large dielectric perturbations, the concept of azimuthal symmetry breaks down completely. However, for intermediate dielectric perturbations, the standing waves will become locked in phase to the particular geometry of the perturbation. The lower frequency mode,  $a_c$ , will have more of its energy in the high dielectric regions, while the higher frequency mode,  $a_s$ , will see more of the low dielectric regions. The relative physical phase difference between the two standing waves can lead to real differences in their loss rates. Thus, the previous equations can be made slightly more general by allowing each standing wave to have its own loss rate according to

$$\frac{da_c}{dt} = \left( i\Delta\omega + i\frac{\gamma_\beta}{2} - \frac{\gamma_c}{2} \right) a_c + \frac{\kappa}{\sqrt{2}}s \quad (4.8a)$$

$$\frac{da_s}{dt} = \left( i\Delta\omega - i\frac{\gamma_\beta}{2} - \frac{\gamma_s}{2} \right) a_s + \frac{\kappa}{\sqrt{2}}s, \quad (4.8b)$$

where  $\gamma_c = \gamma_{c,i} + \gamma_{\text{ext}}$  and  $\gamma_s = \gamma_{s,i} + \gamma_{\text{ext}}$ . Furthermore, the coupling rates to each of the standing waves will actually depend on the phase of fields as compared to the point of taper coupling [68]. Thus, the coupling rates in Eqs. (4.8a) and (4.8b) will in general not be equal.

With unity input power,  $|s|^2 = 1$ , the steady-state energy amplitudes are given by

$$a_{c,s} = \frac{-\sqrt{\gamma_{\text{ext}}/2}}{-\gamma_{c,s}/2 + i(\Delta\omega \pm \gamma_\beta/2)}, \quad (4.9)$$

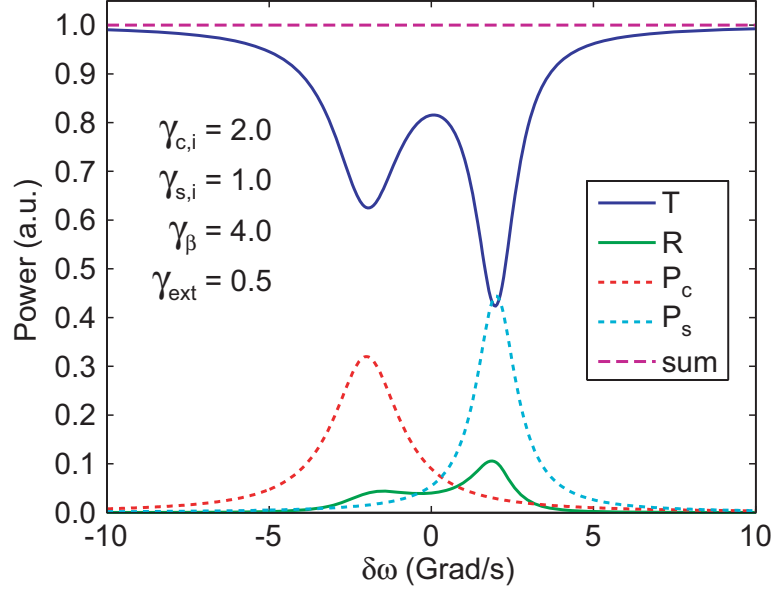


Figure 4.10: Spectral dependence of the input power loss channels for the doublet model with unequal standing wave linewidths assuming equal coupling rates. Blue and green lines are the fraction of power that was transmitted and reflected, while red and cyan dashed lines are the dissipated power from the symmetric and anti-symmetric standing waves,  $P_c = \gamma_{c,i}|a_c|^2$  and  $P_s = \gamma_{s,i}|a_s|^2$ . Purple dashed line shows the sum of the four loss channels, indicating power conservation.

and the fraction of optical power that passes the resonator ( $T$ ) and is reflected by the resonator ( $R$ ) can be found by taking the coherent sum of the Lorentzian responses according to

$$T = |-1 + \sqrt{\gamma_{\text{ext}}/2}(a_c + a_s)|^2 \quad (4.10a)$$

$$R = |\sqrt{\gamma_{\text{ext}}/2}(a_c - a_s)|^2. \quad (4.10b)$$

Figure 4.10 plots the spectral dependence of the input power loss channels for the doublet model with unequal standing wave linewidths assuming equal coupling rates. The standing wave losses (listed in the figure) were chosen to be severely different to best highlight the utility of such a model. The blue line is the fraction of input power that was transmitted, given by Eq. (4.10a), while the green line is the fractional reflected power given by Eq. (4.10b). Interestingly, the reflected power goes through a  $\pi$  phase shift when on-resonance with  $a_c$  versus  $a_s$ . The red and cyan dashed lines are the dissipated power from the symmetric and anti-symmetric standing waves,

$P_c = \gamma_{c,i}|a_c|^2$  and  $P_s = \gamma_{s,i}|a_s|^2$ , while the purple dashed line shows the sum of the four loss channels, indicating power conservation. The dissipated power from the standing waves is typically an undesired quantity, but for the cases of resonant pumping of a gain medium, it can also be used to determine the spectral absorption of the resonance in the absence of other intrinsic loss.

As Eq. (4.10a) shows transmission dips at  $\omega \approx \omega_0 \pm \gamma_\beta/2$ , a normalized measure of the backscattering rate is defined to be the natural frequency divided by the total resonance splitting,  $Q_\beta \equiv \omega_0/\gamma_\beta$ . To illustrate the utility of this definition, limiting cases are taken:  $Q_\beta \gg Q_i$  would indicate no doublet splitting and pure *cw* and *ccw* traveling WGMs; conversely,  $Q_\beta \ll Q_i$  would indicate large doublet splitting and consequently widely separated standing wave WGMs. In the latter case,  $Q_\beta$  gives a better measure of the required coupling strength and the useful bandwidth at *critical coupling*, where all power is transferred into the resonant cavity from a bus waveguide (see Fig. 4.13).

#### 4.5.2 Efficient Taper-Disk Coupling

The accurate calculation of the coupling rate from waveguide to cavity,  $\kappa$ , can in principle be calculated by the three-dimensional field overlap of the resonator field,  $\mathbf{E}_r(\mathbf{r})$ , with the waveguide field,  $\mathbf{E}_w(\mathbf{r})$ . Using a derivation similar to Ref. [68],  $\kappa$  can be found according to

$$\kappa = \frac{i\omega\epsilon_0}{4} \left\{ \int \delta n_r^2(\mathbf{r}) \mathbf{E}_r^*(\mathbf{r}) \cdot \mathbf{E}_f(\mathbf{r}) dV + \int \delta n_w^2(\mathbf{r}) \mathbf{E}_r^*(\mathbf{r}) \cdot \mathbf{E}_f(\mathbf{r}) dV \right\}. \quad (4.11)$$

The first integral is performed over the resonator's dielectric region,  $\delta n_r^2(\mathbf{r}) = n_r^2 - n_0^2$ , and the second integral<sup>3</sup> is performed over the waveguide's dielectric region,  $\delta n_w^2(\mathbf{r}) = n_w^2 - n_0^2$ . For silicon disks and silica tapers,  $n_r = 3.48$  and  $n_w = 1.45$ . The waveguide's propagation direction is assumed to be in the y-direction.

The brute force numerical evaluation of this three-dimensional integral for an arbitrary disk resonance and taper mode is computationally intensive due to the highly

---

<sup>3</sup>Note that the second integral in Eq. (4.11) has been posited by the analysis of Oskar Painter where he has taken into account a more rigorous power orthogonality condition. Measurements are being taken to verify its validity.

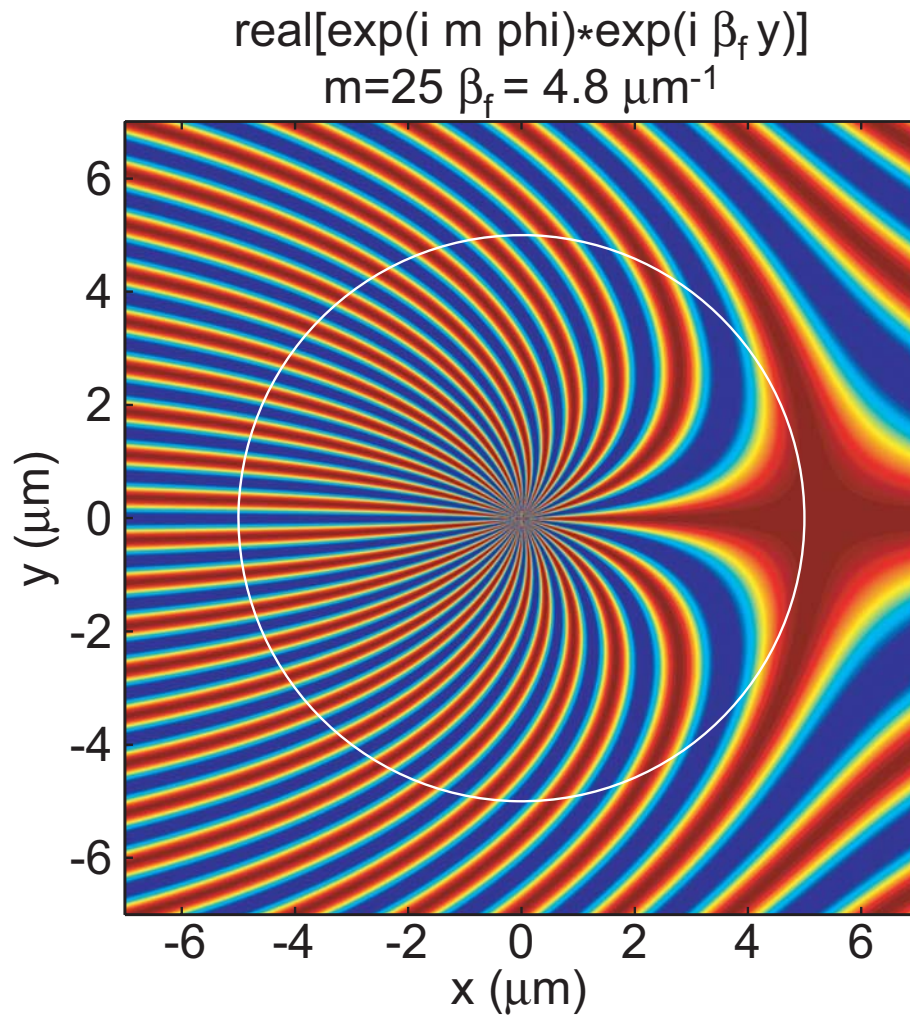


Figure 4.11: Oscillatory dependence on the  $\phi$  component of the integrand in Eq. (4.11) for a traveling wave with  $m = 25$  coupled to a fiber with propagation constant  $4.8 \mu\text{m}^{-1}$ . Shown in white is a hypothetical  $5 \mu\text{m}$  radius microdisk.

oscillatory nature of the integrand. The large momentum mismatch between high-index silicon microdisks and the low-index silica fiber taper results in rapidly varying exchanges of power along the taper. Using standard coupled mode theories [37, 69], the disparity between the indices of refraction would preclude any significant amount of power exchange. However, for very short interaction lengths (also known as point contacts), the momentum conservation requirements are relaxed significantly. Thus, if the point of contact can be made small enough to mitigate the power “sloshing” effect, it is possible to obtain coupling rates that are comparable to the loss rates for high- $Q$  and high-index contrast microcavities. Furthermore, by appropriate design of the optical modes, phase matched power coupling to high-index contrast modes also becomes possible.

While accurate evaluations of  $\kappa$  are needed to predict coupling rates for taper placement above and below the centerline of the microdisk or microring, simple phase matching considerations provide a great deal of intuition for the general behavior of  $\kappa$ . As the  $\phi$  dependence of the integrand is given by  $\exp(im\phi) \cdot \exp[-i\beta_f\rho \sin(\phi)]$ , it is clear that a relatively constant, and therefore non-zero, coupling rate could be attained for modes that have  $m \approx \beta_f R$ . As a graphical illustration, Figure 4.11 is a plot of the oscillatory nature of the  $\phi$  component of the integrand in Eq. (4.11) for a traveling wave with  $m = 25$  coupled to a fiber with propagation constant  $4.8 \mu\text{m}^{-1}$ . This fiber propagation constant was chosen based on Fig. 4.2 and the need for a single-mode taper to maintain high “ideality” [55]. Shown in white is the edge of a prototypical  $5 \mu\text{m}$  radius microdisk. Because of the finite region of mutual field overlap, the coupling rate for a taper placed at approximately  $x = 5 \mu\text{m}$  from the origin would be much higher than any other placement. For all other taper placement positions, the integral is approximately zero. However, the fact that it is not identically zero means that non-zero coupling would be seen for any resonance with extremely high intrinsic quality factors.

“Back of the envelope” estimates,  $m \sim 2\pi R n_{\text{Si}}/\lambda_0$ , for silicon microdisks shows that bulk-like WGM’s have almost twice the desired angular propagation constant for efficient fiber taper coupling. However, by pushing energy *up* into the low index air cladding, it is possible to dramatically reduce the in-plane momentum of the disk

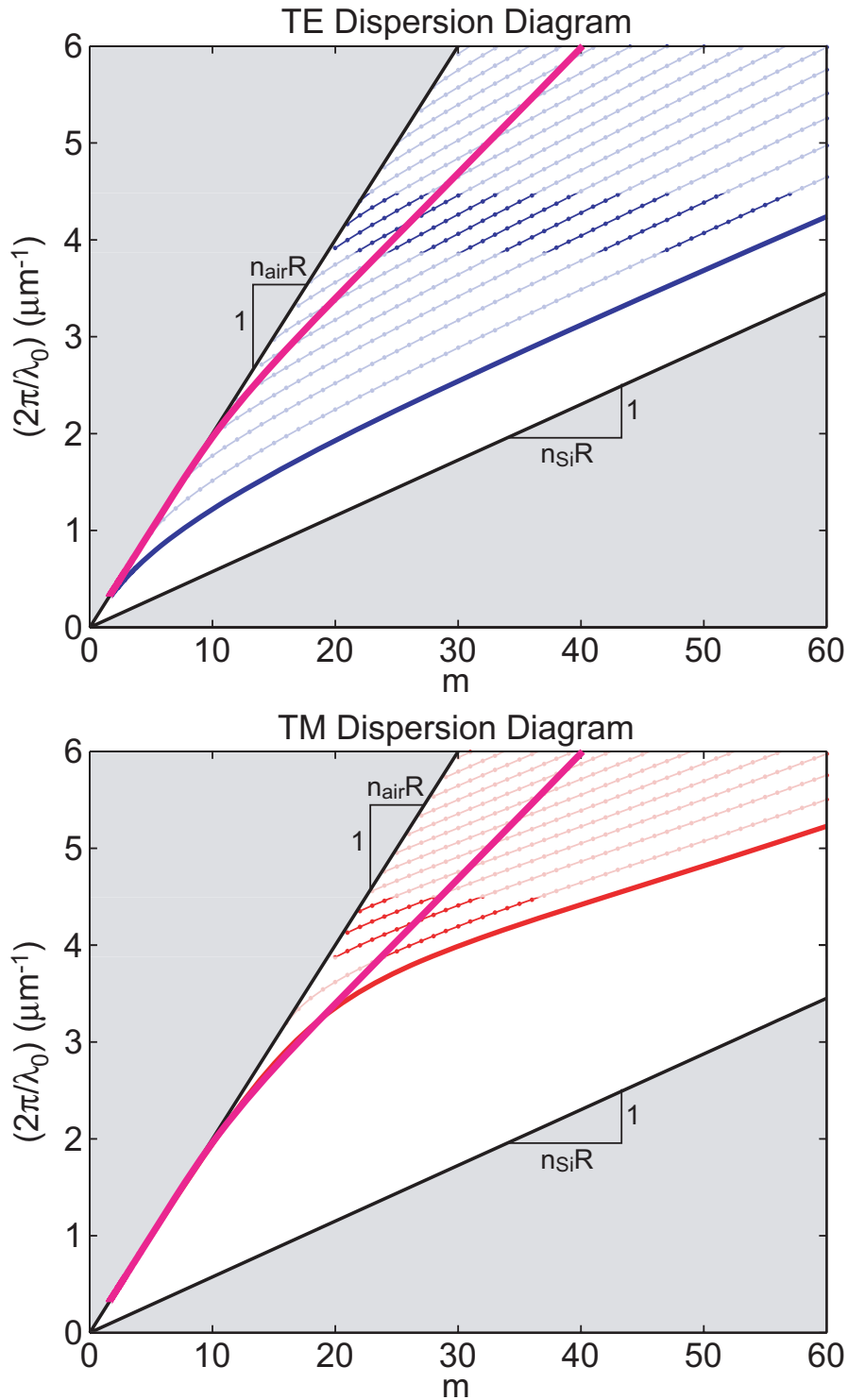


Figure 4.12: Analytic dispersion diagram for a  $5 \mu\text{m}$  radius,  $215 \text{ nm}$  thick Si microdisk against *angular* momentum. Shown in black are light lines at the disk edge for air and bulk silicon. Thick blue and red lines are light lines at the disk edge using the effective slab indices of refraction. Frequencies outside the testable range ( $1400 - 1600 \text{ nm}$ ) have been made slightly transparent. Thick magenta line is the dispersion diagram for a  $1.2 \mu\text{m}$  diameter fiber taper positioned at the disk edge.

modes, while maintaining extremely high radiation quality factors. This is most readily accomplished by using thinner device layers and working with the predominantly TM (vertically polarized) modes. The TM modes are preferable over the TE modes because of their reduced sensitivity to sidewall imperfections. In addition, the TM modes take on a naturally “hybrid” field distribution allowing for the incorporation of functionalized surfaces and cladding to be added to high- $Q$  structures.

Figure 4.12 shows the same analytic dispersion diagram for a 5  $\mu\text{m}$  radius, 215 nm thick Si microdisk against *angular* momentum as in Fig. 2.3. Overlaid on the top of this diagram is the dispersion diagram for a 1.2  $\mu\text{m}$  diameter fiber taper positioned at the disk edge, shown by a thick magenta line. This plot shows that for the wavelength regions of interest, the fiber taper mode should couple the best to  $\text{TE}_{8,m}$  and  $\text{TM}_{2,m}$  disk modes because of the previous phase matching arguments. As a  $p = 8$  family would possess horrible loss rates due to the high overlap with the rough silica pedestal, the  $\text{TM}_{p,m}$  families were seen as much better candidates for efficient coupling. However, because the fiber matched coupling occurs so close to the light-line, there must be a balance between phase matching the low radial order TM modes to the taper while maintaining enough high-index to prevent the modes from being radiation limited. By appropriately tailoring the disk thickness, proper momentum matching can be achieved over an extended coupling range.

Numerical simulations described in Chapter 2 were used to find that disk thicknesses of  $\sim 200 - 220$  nm provided a good compromise between small mode volume, fiber taper phase matching, and high radiation  $Q$ . Using the fabrication process detail in Chapter 3, disks of 5 and 10  $\mu\text{m}$  radii were fabricated from an SOI wafer with the optimized 215 nm thick device layer. After working through new fabrication challenges due to the increased overlap with the silicon surfaces, microdisks with sufficiently high  $Q$ 's were tested for their ability to efficiently exchange power with fiber tapers. Utilizing the repeated Piranha/HF etch recipe described in Section 5.4.3, the spectrum identified in Fig. 5.11 was shifted a controllably arbitrary amount to the blue by slowly thinning the microdisk. In this way the  $\text{TM}_{1,m}$  spectrum was shifted several  $m$  numbers to provide better momentum matching to the fiber taper. Figure 4.13 shows the results of fiber taper coupling to the  $\text{TM}_{1,30}$  centered at 1437.5 nm.

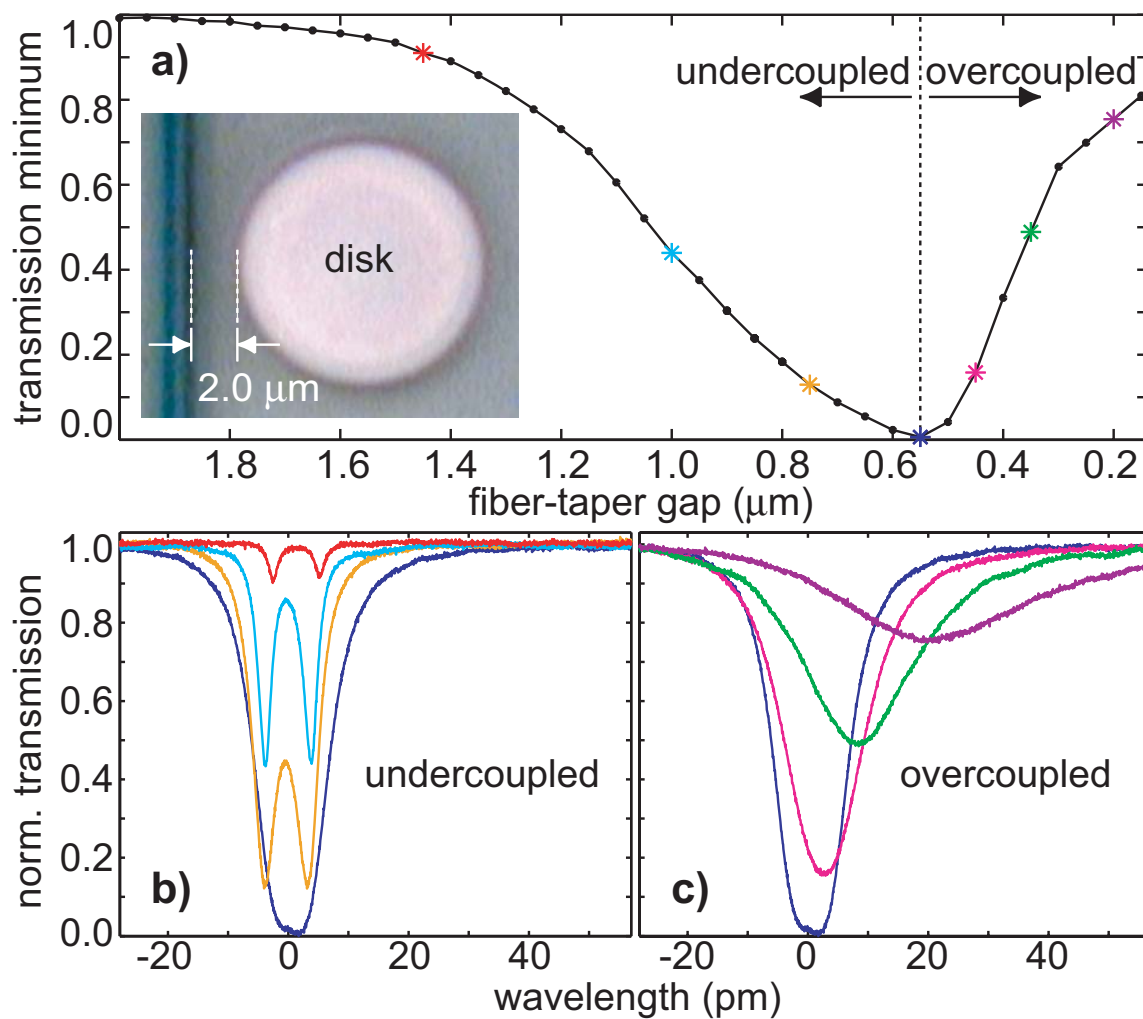


Figure 4.13: Fiber taper coupling measurements of a  $\text{TM}_{1,30}$  WGM centered at 1437.5 nm. (a) Normalized transmission minimum as a function of taper-disk gap with undercoupled and overcoupled regions are highlighted. (Inset) High-magnification optical image taken with fiber taper 2  $\mu\text{m}$  from edge of microdisk. (b,c) Selected high-resolution transmission scans taken from the undercoupled and overcoupled regime, as indicated by colored asterisks in (a).

As discussed in Section 5.4.2, an  $m = 30$  at the blue end of the spectrum provided nearly perfect momentum matching to the fiber taper waveguide mode. Momentum matching along with a  $Q = 1 \times 10^6$  enabled the resonance to become more than 90% overcoupled before the taper touched the edge of the disk. Large waveguide-resonator gaps increase the ease of fabrication of integrated structures, as high aspect ratio etches stress the limits of lithographic fabrication. This measurement illustrates critical coupling should be possible with waveguide-resonator gaps of  $> 0.5 \mu\text{m}$  for integrated structures as well.

## Chapter 5

# Optical Loss in Silicon Microdisks

### 5.1 Introduction

The *intrinsic* optical loss in these structures can be quantified by four different components of a modal quality factor,  $Q_i$ , according to

$$1/Q_i = 1/Q_r + 1/Q_{ss} + 1/Q_{sa} + 1/Q_b, \quad (5.1)$$

where  $Q_r$ ,  $Q_{ss}$ ,  $Q_{sa}$ ,  $Q_b$  are inversely proportional to the optical loss due to radiation, surface scattering, surface absorption, and any bulk impurities, respectively. This represents a complete accounting of all forms of loss because of the generality of each term.  $Q_r$ , sometimes referred to as whispering-gallery loss, takes into account that these resonances are quasi-modes and leak energy to the radiation modes even for ideal materials and fabrication.  $Q_{ss}$  and  $Q_{sa}$  represent the losses associated with real and imaginary index perturbations on the surfaces of the resonator. The physical process behind surface scattering, also called Rayleigh scattering, is elastic scattering of photons from the nonidealities on the surface. Surface absorption can be produced by contaminants adsorbed onto the resonator, improper termination of the Si-bonds, and impregnated etch products in the sidewalls. The remainder of the loss must then come from the bulk, and can in principle be due to scattering or absorption. In practice, the quality and purity of the crystal is assumed high enough that all bulk losses come from free-carrier absorption from the dopants [3, 4].

The optical losses associated with a silicon microresonator come from a variety of sources, and so it is fitting that a variety of techniques had to be developed to

overcome these losses. Our first silicon microdisks to be tested were made from a 344 nm thick device layer and had radii of 2.5 and 4.5  $\mu\text{m}$  [28]. As will be described in Section 5.2, the success of these microdisks was a result of high-resolution electron-beam lithography and a smooth dry-etch originally developed for silicon photonic crystals [33, 70–73]. The incredibly small size of these resonators coupled with an immature fabrication process resulted in these resonators being limited by etch-induced surface scattering ( $1/Q_{ss}$ ). Following up on this initial success, larger resonators of radii 5 – 30  $\mu\text{m}$  were fabricated to probe the bulk properties of the same SOI wafers. Section 5.3 describes the results of these larger disks along with an improved fabrication process, which further reduced surface scattering, and allowed for the first measurements of surface absorption ( $Q_{sa}$ ) and bulk losses ( $Q_b$ ) in silicon microcavities [32]. After creating highly circular and smooth microdisks, it was found that surface absorption had to be reduced in order to further improve the  $Q$ 's of the structures. Section 5.4 details the results of various microelectronic wet chemistries and their positive and negative effects on optical loss [34]. The microdisks used for this work were fabricated from a thinner 215 nm device layer wafer, and as a result required further improvements in lithography and dry-etching in order to maintain the sensitivity to the absorptive characteristics of the Si surfaces. During the course of these experiments, it was found that the accuracy of separating losses into scattering versus absorption was limited by the uncertainty in the thermal models for heat dissipation. Section 5.5 describes the experimental technique used to accurately measure absorption in these resonators and is of general applicability to any semiconductor microcavity [35]. It was found that the best surfaces were made by hydrogen passivation with hydrofluoric (HF) acid, the benefits of which were destroyed in tens of minutes if left in ambient environments. Thus, a surface encapsulation that put the properly terminated interface states into a permanent stasis was needed. Section 5.6 reports on the successful implementation using carefully annealed thermal oxides as a means of putting a thin but chemically inert surface on silicon microresonators. All of the fabrication processes were developed in an attempt to maintain CMOS compatibility, and our results indicate that it should be possible to add ultra-high- $Q$  resonant elements into existing and future silicon optoelectronics chips.

## 5.2 Surface Scattering

Recent studies of optical resonators in glass-based microspheres [29, 30, 66], microrings [74], and microtoroids [31] have highlighted the applications afforded by the extremely long photon lifetime of whispering-gallery modes (WGMs) supported by these structures. Furthermore, recent work by Ilchenko *et al.* illustrated the advantages of creating WGMs in crystalline materials [75]. Applications for such devices include quantum networking [76], low-threshold non-linear optical sources [77], and compact micro-optical circuits [74]. The ability to create similar high-quality-factor ( $Q$ ) WGM resonators in III-V or silicon (Si) semiconductors has thus far been hampered by the large refractive index of most semiconductors and the resulting sensitivity to surface roughness [78, 79]. In this Section, we describe measurements of micron-sized Si microdisk resonators supporting transverse-magnetic (TM) WGMs with significantly reduced sensitivity to disk-edge roughness. These modes have measured  $Q$  values as high as  $5.2 \times 10^5$  and effective modal volumes ( $V_{\text{eff}}$ ) as small as 5.3 cubic wavelengths in the material.<sup>1</sup> The largest  $Q/V_{\text{eff}}$  ratio is measured to be  $8.8 \times 10^4$ , of the same order as values measured in ultra-small-volume photonic crystals [33], ultra-high- $Q$  microspheres, and microtoroids [29, 31, 75].

### 5.2.1 Derivation of $Q_{ss}$ from the Volume Current Method

Optical losses in microresonators are oftentimes limited by index perturbations,  $\delta\epsilon$ , on the surfaces. These index perturbations are sourced approximately by the unperturbed field solutions,  $\mathbf{E}^0$ , to create polarization currents,

$$\mathbf{J} = -i\omega\delta\epsilon\mathbf{E}^0. \quad (5.2)$$

In analogy with microwave electronics, the polarization currents drive new electromagnetic fields that radiate into space. Optical losses due to the perturbations can be calculated from the far-field solutions setup by  $\mathbf{J}$  [80]. In most microdisk work, the dominant deviations from the ideal disk geometry occur on the sidewalls

---

<sup>1</sup>The mode volumes quoted here are approximate values based on the effective index model and are consistent with but smaller than more accurate FEM simulations.

during fabrication. Etch-induced sidewall roughness typically runs the height of the disk, providing a nearly one-dimensional way of representing this roughness along the arclength. In this way, the index perturbation (Fig. 5.5) can be approximated by

$$\delta\epsilon = \epsilon_0\delta n^2 h\Delta r(\phi)\delta(r - R)\delta(z), \quad (5.3)$$

where  $\epsilon_0$  is the free-space permittivity,  $\delta n^2 = n_d^2 - n_0^2$ ,  $n_d$  is the disk refractive index,  $n_0$  is the index of the surrounding medium,  $h$  is the disk height, and  $\Delta r(\phi)$  is the radial surface roughness relative to the unperturbed disk radius [81]. The parameters  $\rho$ ,  $\phi$ , and  $z$  correspond to the radius from the disk center, angle along the disk perimeter, and height along the disk edge, respectively. The far field vector potential sourced by  $\mathbf{J}$  is given by [80]

$$\mathbf{A}_{rad}(\mathbf{r}) = \frac{\mu_0}{4\pi} \left( \frac{e^{-ik_1 r}}{r} \right) \int \mathbf{J}(\mathbf{r}') e^{-ik_1 \hat{\mathbf{r}} \cdot \mathbf{r}'} d\mathbf{r}', \quad (5.4)$$

where  $k_1 \equiv n_0 k_0$  is the wave vector in the surrounding medium. Writing the unperturbed electric field at the disk edge as  $\mathbf{E}^0 = \mathbf{E}_m(\rho, z) \exp(im\phi)$ , Eq. (5.4) simplifies to

$$\mathbf{A}_{rad}(\mathbf{r}) = \frac{-i\mu_0\omega h\delta n^2\epsilon_0\mathbf{E}_m(R, 0)R}{4\pi} \left( \frac{e^{-ik_1 r}}{r} \right) \int_0^{2\pi} \Delta r(\phi') e^{im\phi'} \exp(ik_1 R \sin\theta \cos\phi') d\phi'. \quad (5.5)$$

For low-loss microdisks, the direct solution to Eq. (5.5) becomes increasingly sensitive to the limitations on the measurement of  $\Delta r(s)$ , where  $s \equiv \phi R$ , the arclength along the disk edge perimeter. However, a simple statistical solution becomes possible once surface roughness becomes much smaller than the wavelength in the material [81]. In effect, this simplification assumes that roughness separated by much more than a characteristic correlation length,  $L_c$ , is statistically independent. This allows each infinitesimal arclength along the perimeter to be treated as an ensemble member of all the possible processing outcomes under the same fabrication conditions. Ensemble averaging over Eq. (5.5) yields

$$\langle \mathbf{A}_{rad}(\mathbf{r}) \cdot \mathbf{A}_{rad}(\mathbf{r})^* \rangle = \left| \frac{\mu_0 \omega h \delta n^2 \epsilon_0 \mathbf{E}_m(R, 0)}{4\pi} \right|^2 \left( \frac{R}{r} \right)^2 \Theta \quad (5.6)$$

$$\Theta \equiv \int_0^{2\pi} \int_0^{2\pi} C(|\phi' - \phi''|) \exp(im(|\phi' - \phi''|)) \exp[ik_1 R \sin \theta (\cos \phi' - \cos \phi'')] d\phi' d\phi'', \quad (5.7)$$

where  $C(|\phi' - \phi''|) = \langle \Delta r(\phi') \Delta r(\phi'') \rangle$ , the correlation function for the etch roughness. With the substitutions,  $t = \phi' - \phi''$  and  $z = (\phi' + \phi'')/2$ , the integral is evaluated to be

$$\Theta = 2\pi \int_0^{2\pi} C(t) \exp(imt) J_0 \left[ 2k_1 R \sin \theta \sin \left( \frac{t}{2} \right) \right] dt. \quad (5.8)$$

With a Gaussian model for the correlation function given by  $C(s) = \sigma_R^2 \exp(-s^2/L_c^2)$ , this integral becomes

$$\Theta = \frac{2\pi}{R} \int_{-\pi R}^{\pi R} \sigma_R^2 \exp\left(-\frac{s^2}{L_c^2} + i\frac{m}{R}s\right) J_0 \left[ 2k_1 R \sin \theta \sin \left( \frac{sR}{2} \right) \right] ds \cong \frac{2\pi^{3/2} \sigma_R^2 L_c}{R}, \quad (5.9)$$

where  $\sigma_R$  is the standard deviation for the surface roughness. Combining Eqs. (5.9) and (5.6), the far-field Poynting vector is given by

$$\langle \mathbf{S}_{rad} \rangle = \hat{\mathbf{r}} \frac{\omega k_0}{2\mu_0} \langle |\hat{\mathbf{r}} \times \mathbf{A}_{rad}|^2 \rangle = \hat{\mathbf{r}} \frac{\omega k_1^3 n_0 (\delta n^2)^2 V_s^2 \epsilon_0 |\mathbf{E}_m(R, 0)|^2 |\hat{\mathbf{r}} \times \hat{\mathbf{e}}|^2}{16\sqrt{\pi} r^2}, \quad (5.10)$$

where  $\hat{\mathbf{e}}$  is the polarization of the electric field and  $V_s \equiv \sqrt{RL_c} h \sigma_r$  is the effective volume for a typical scatterer. The total power radiated,  $P_{rad}$ , far from the disk can be found by integrating the outward intensity over a large sphere and summing the polarization components to obtain

$$P_{rad} = \int (\mathbf{S} \cdot \hat{\mathbf{r}}) r^2 d\Omega = \sum_{\hat{\eta}} \frac{\pi^{7/2} \omega n_0 (\delta n^2)^2 V_s^2 \epsilon_0 |E_m(R, 0; \hat{\eta})|^2 G(\hat{\eta})}{\lambda_0^3}, \quad (5.11)$$

where  $\hat{\eta} = \{\hat{\rho}, \hat{\phi}, \hat{\mathbf{z}}\}$  and  $G(\hat{\eta}) = \{2/3, 2, 4/3\}$  is a geometrical radiation factor for the different electric field polarizations. Since the quality factor of a cavity mode is given by  $Q = \omega U_c / P_{rad}$ , where  $U_c = \frac{1}{2} \int \epsilon^0(\mathbf{r}) |\mathbf{E}^0|^2 d\mathbf{r}$  is the time-averaged stored energy in the cavity, we can rewrite Eq. (5.11) as a surface-scattering quality factor

$$Q_{ss} = \frac{\lambda_0^3}{\pi^{7/2} n_0 (\delta n^2)^2 V_s^2 \sum_{\hat{\eta}} \bar{u}_s(\hat{\eta}) G(\hat{\eta})}, \quad (5.12)$$

where  $\bar{u}_s(\hat{\eta})$  is the normalized, spatially averaged (see Appendix B)  $\hat{\eta}$ -polarized electric field energy density at the disk edge given by

$$\bar{u}_s(\hat{\eta}) = \frac{\epsilon_0 |\mathbf{E}^0(\hat{\eta})|_{s,avg}^2}{\frac{1}{2} \int \epsilon^0(\mathbf{r}) |\mathbf{E}^0|^2 d\mathbf{r}}. \quad (5.13)$$

Numerical calculations of  $\bar{u}_s(\hat{\eta})$  show that TE modes couple to far-field radiation modes roughly 50% more strongly than corresponding TM modes, mainly due to geometrical considerations through  $G(\hat{\eta})$ . Note that this and the following section has corrected minor errors present in Reference [28].

### 5.2.2 Derivation of $Q_\beta$

In addition to coupling to radiation modes, surface roughness on microdisks will also couple the degenerate clockwise (*cw*) and counterclockwise (*ccw*) modes [66]. Lifting this degeneracy creates a downshifted- and upshifted-frequency standing wave mode. A statistical approach similar to that of Little and Laine [81] can be used to relate the doublet frequency splitting,  $2\beta$ , to measured surface roughness.<sup>2</sup> Substituting the delta function approximation for the dielectric perturbation from Eq. (5.3) into Eq. (A.6) yields

$$\beta = \frac{\omega_0}{4U_c} \int \epsilon_0 \delta n^2 h \Delta r(s) \delta(r - R) \delta(z) (\mathbf{E}_{cw}(\mathbf{r}))^* \mathbf{E}_{ccw}(\mathbf{r}) d\mathbf{r}. \quad (5.14)$$

This integral is easily reduced to a Fourier-type integral by noting that at the disk edge  $\mathbf{E}_{cw} = \mathbf{E}_m(R, 0) \exp(-im\phi)$  and  $\mathbf{E}_{ccw} = \mathbf{E}_m(R, 0) \exp(im\phi)$ . Integrating over the  $\delta$ -functions yields

---

<sup>2</sup>A functional form for  $\beta$  can be analytically derived only for small amounts of etch roughness.

$$\beta = \frac{\omega_0 \delta n^2 h R \epsilon_0 |\mathbf{E}_m(R, 0)|^2}{4U_c} \Upsilon \quad (5.15)$$

$$\Upsilon = \int_0^{2\pi} \Delta r(\phi) e^{i2m\phi} d\phi. \quad (5.16)$$

As in Eq. (5.5), the integral,  $\Upsilon$ , becomes statistically solvable when surface roughness becomes much smaller than the wavelength in the material. Following the same method of solution and definitions as above,

$$\langle \Upsilon^2 \rangle = \frac{2\pi}{R} \int_{-\pi R}^{\pi R} \sigma_R^2 \exp\left(-\frac{s^2}{L_c^2} + i\frac{2m}{R}s\right) \cong \frac{2\pi^{3/2} \sigma_R^2 L_c}{R}. \quad (5.17)$$

Plugging Eq. (5.17) into Eq. (5.15) and solving gives  $\sqrt{\langle \beta^2 \rangle} = (\pi/4)^{3/4} \omega_0 \delta n^2 V_s \bar{u}_s$ , where  $\bar{u}_s \equiv \sum_{\hat{\eta}} \bar{u}_s(\hat{\eta})$ . Thus, the normalized measure of the backscattering rate is

$$Q_\beta \equiv \omega_0 / (2\beta) = \frac{\sqrt{2}}{\pi^{3/4} \delta n^2 V_s \bar{u}_s}. \quad (5.18)$$

### 5.2.3 Experiments

The silicon microdisks in this work were fabricated from a silicon-on-insulator (SOI) wafer consisting of a 344 nm thick p-doped Si layer of resistivity 1–3  $\Omega$ -cm atop a 2 micron  $\text{SiO}_2$  layer. Processing of the microdisks began with the deposition of a 20 nm  $\text{SiO}_2$  protective cap layer using plasma-enhanced chemical-vapor deposition. Electron-beam lithography was used to create a polymer resist etch mask, and a low-bias voltage inductively-coupled plasma reactive-ion etch with  $\text{SF}_6:\text{C}_4\text{F}_8$  gas chemistry [33] then transferred the circular microdisk pattern into the top Si layer. After dry-etching, the sample was immersed in buffered hydrofluoric acid to undercut the bottom  $\text{SiO}_2$  cladding, as shown in Figure 5.1. The thin 20 nm  $\text{SiO}_2$  top cap layer was also removed in this process, providing a clean, smooth top Si surface. A final rinse in deionized water was performed, followed by a high-purity nitrogen spray drying step.

Microdisks of two different sizes, radius  $R = 2.5$  and  $4.5 \mu\text{m}$ , were fabricated and tested. A broad wavelength scan covering the 1509–1625 nm wavelength range was

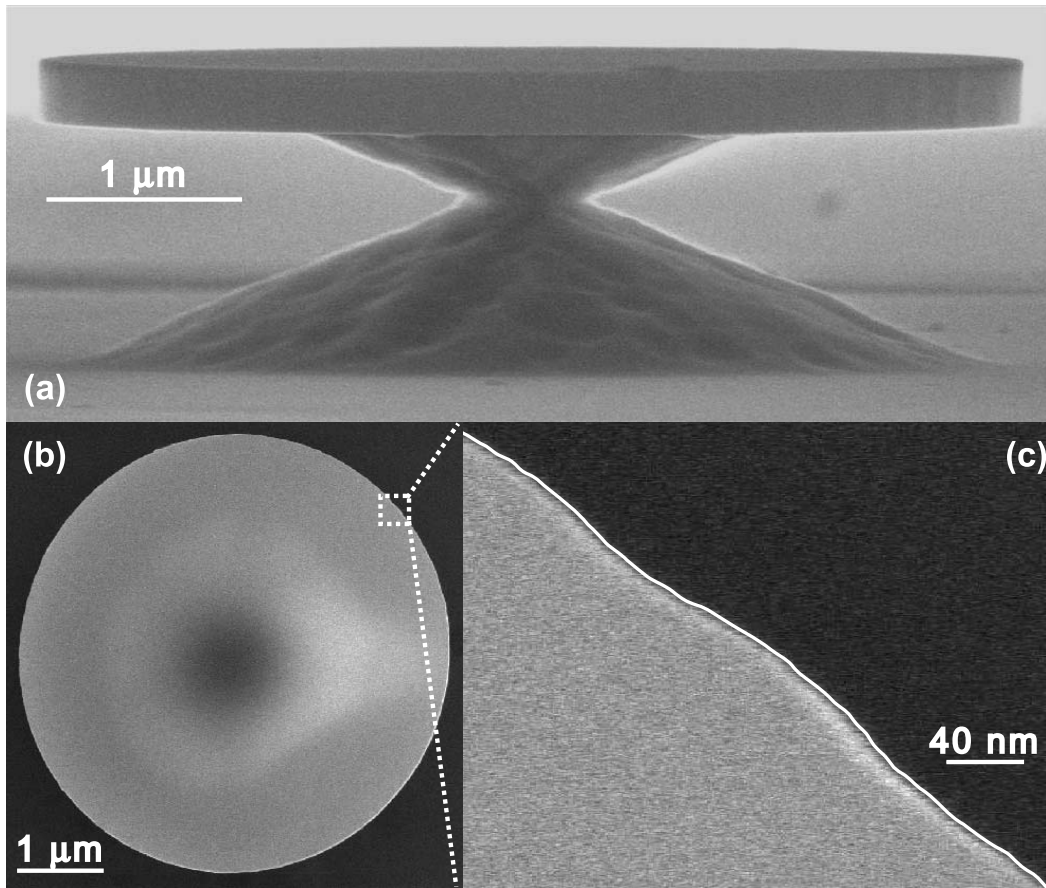


Figure 5.1: SEM micrographs of a  $R = 2.5 \mu\text{m}$  Si microdisk: (a) side-view illustrating SiO<sub>2</sub> undercut and remaining pedestal, (b) high-contrast top-view of disk, and (c) zoomed-in view of top edge showing disk-edge roughness and extracted contour (solid white line).

Table 5.1: Summary of theoretical and measured mode parameters for  $R = 2.5$  and  $4.5 \mu\text{m}$  Si microdisks. Theoretical surface-scattering values for  $Q_{ss}$  and  $\Delta\lambda_{\pm m}$  are shown in parentheses.

$R(\mu\text{m})$	$\text{TX}_{p,m}$	$V_{\text{eff,th.}} (\lambda/n)^3$	$Q_{ss}$ exp. (th.)	$\Delta\lambda_{\pm m}$ (pm) exp. (th.)
2.5	$\text{TM}_{1,23}$	5.3	$4.7 (1.7) \times 10^5$	93 (224)
2.5	$\text{TE}_{1,26}$	7.5	$9.0 (1.1) \times 10^5$	126 (292)
4.5	$\text{TM}_{1,44}$	12.2	$5.2 (3.1) \times 10^5$	37 (93)
4.5	$\text{TE}_{1,50}$	16.2	$1.7 (2.1) \times 10^5$	78 (118)

initially employed to map out the different microdisk modes. The adjustable polarization state in the taper along with the WGMs' strength of coupling and linewidth was used to determine sets of modes with a common free-spectral range. Using this mode identification technique, we found that the highest  $Q$  modes in both sizes of microdisks are consistently of TM polarization, and corresponded to the lowest radial number,  $p \sim 1$ .

In this work, the fiber taper was positioned to the side of the microdisks, with a center height equal to that of the middle of the microdisk in order to take advantage of the vertical mirror symmetry in the disks, providing more selective coupling to TM versus TE modes. The inset of Fig. 5.2(a) shows the evanescent coupling to a  $\text{TM}_{1,44}$  WGM of an  $R = 4.5 \mu\text{m}$  microdisk, with tapered fiber positioned  $1.1 \mu\text{m}$  laterally from the disk edge. The observed double resonance dip (doublet) is a result of Rayleigh scattering from disk surface roughness as discussed above, which lifts the degeneracy of clockwise ( $cw$ ) and counter-clockwise ( $ccw$ ) propagating WGMs in the microdisk [66]. Fitting the shorter wavelength mode of the doublet to a Lorentzian yields a loaded linewidth of  $3.9 \text{ pm}$  with a 5% coupling depth. These measurements were repeated for varying taper-microdisk gaps and are recorded in Figure 5.2(a,b). For  $g > 0.63 \mu\text{m}$ , the data follows a two-port coupled mode theory with simple exponential loading dependence on taper-microdisk gap [30]. Fits based upon this model are shown as a solid line in each of the plots of Fig. 5.2. The fiber loading of the microdisk is characterized here by a dimensionless effective quality factor,  $Q_{\text{ext}}$  (inset to Fig. 5.2(b)). The asymptotic unloaded linewidth is found to be  $3.0 \text{ pm}$  for this WGM, corresponding to a bare-cavity  $Q$  of  $5.2 \times 10^5$ . The observed non-exponential loading dependence for small  $g$  is due to the large phase mismatch between the glass fiber and Si microdisk modes, further studies of which are discussed in Chapter 4.

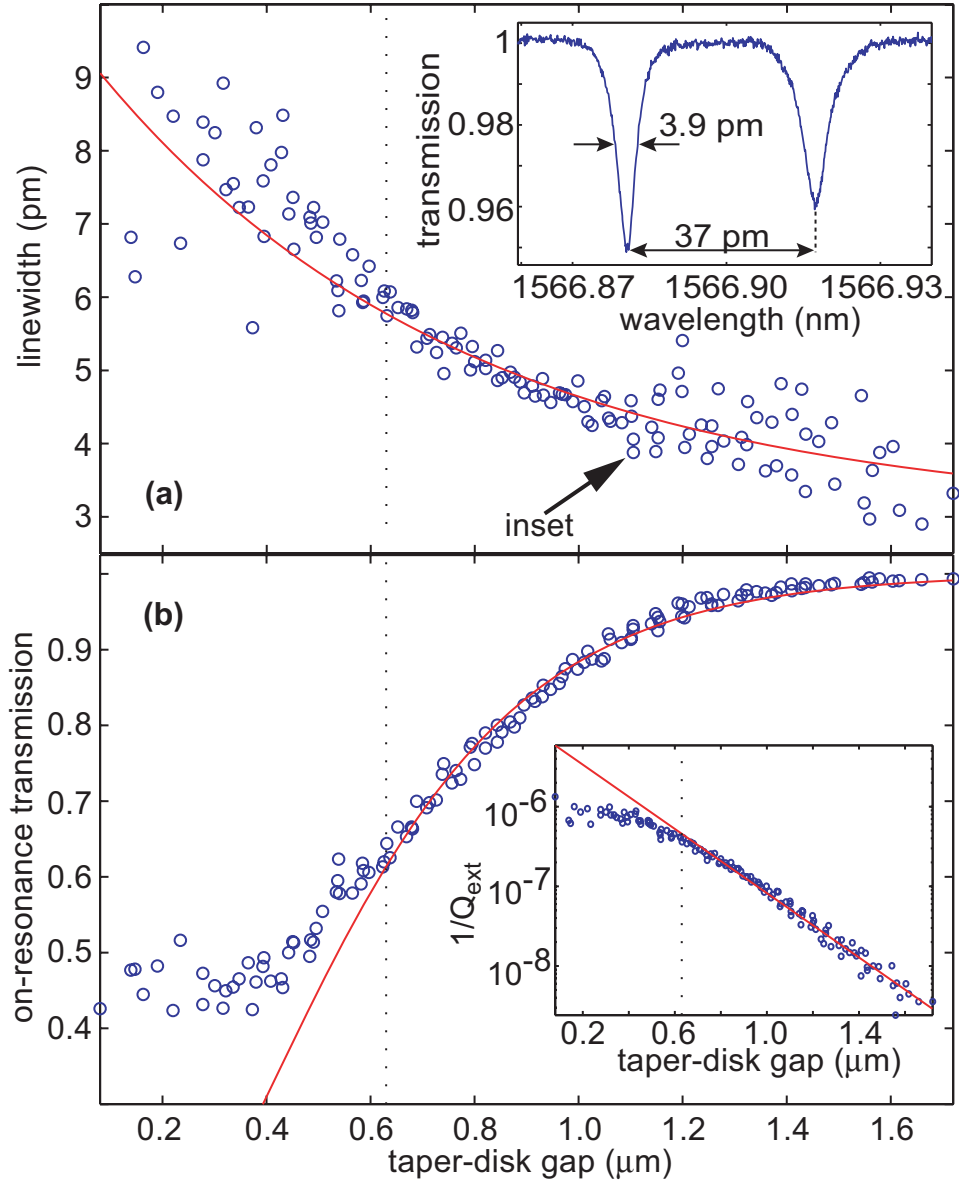


Figure 5.2: Fiber taper measurements of a  $\text{TM}_{1,44}$  WGM of a microdisk with  $R = 4.5 \mu\text{m}$ . (a) Lorentzian full-width half-maximum (FWHM) linewidth versus taper-microdisk gap. (inset) Taper transmission showing high- $Q$  doublet. (b) Resonant transmission depth versus taper-microdisk gap. (inset) loading versus taper-microdisk gap.

Similar measurements were performed for all  $p \sim 1$  modes (of both polarizations) in each of the two different microdisk sizes, and a summary of the measured bare-cavity  $Q$  and doublet mode-splitting values are given in Table 5.1. In order to understand the limiting loss mechanisms and the observed trend of  $Q$  with polarization and radial mode number, a complementary theoretical analysis was also performed. Both the radiation limited  $Q$  ( $\gtrsim 10^{15}$ ) and the free-carrier absorption  $Q$  of the p-doped Si disk layer (estimated to be  $> 10^7$  from Ref. [3]) are far greater than the measured  $Q$  values. Surface state absorption is another possible loss mechanism; however, several trials were performed with differing final chemical cleaning steps with no perceivable change in  $Q$ , contrary to the results presented in Section 5.4. The rather large measured splitting of the  $cw$  and  $ccw$  traveling wave modes indicates strong surface scattering [63], and therefore we believe the dominant source of optical loss to be scattering from index perturbations at the microdisk surface. Surface roughness on the top and bottom surfaces of the microdisks analyzed in this work is negligible in comparison to the azimuthal variation of the disk radius [Fig. 5.1(c)], a result of mask erosion and deformation during the dry-etching step. For this type of roughness, the index perturbation can be approximated by  $\delta\epsilon = \epsilon_0\delta n^2 h\Delta r(s)\delta(r-R)\delta(z)$ , where  $\epsilon_0$  is the free space permittivity,  $\delta n^2 = n_d^2 - n_0^2$ ,  $n_d \sim 3.48$  is the Si refractive index,  $n_0 = 1$  is the index of the surrounding air,  $h$  is the disk height, and  $\Delta r(s)$  is the radial surface roughness relative to the unperturbed disk radius [81].

SEM micrographs such as those shown in Figs. 5.1(b,c) provide high-contrast images from which edge contours with near nanometer resolution can be obtained (Fig. 5.3). From a Gaussian fit to the autocorrelation function of the surface roughness (Fig. 5.4), estimates for  $\sigma_r$  and  $L_c$  were found to be 2.8 nm and 40 nm, respectively, typical of the fabricated microdisks in this work. Using the results from this roughness analysis in Eqs. (5.12) and (5.18), theoretical estimates for  $Q$  and  $\Delta\lambda_{\pm m} \equiv \lambda_0/Q_\beta$  are calculated and tabulated in Table 5.1, with good agreement found between theory and the measured microdisk properties. In these calculations, an effective index model based on Ref. [45] is used to estimate  $\bar{u}_s(\hat{e})$  and the effective mode volume  $V_{\text{eff}}$ , with the approximate TM modes given by a single  $\hat{z}$  field component and the TE modes consisting of  $\hat{r}$  and  $\hat{\phi}$  electric field components. The modes of higher  $p$  number

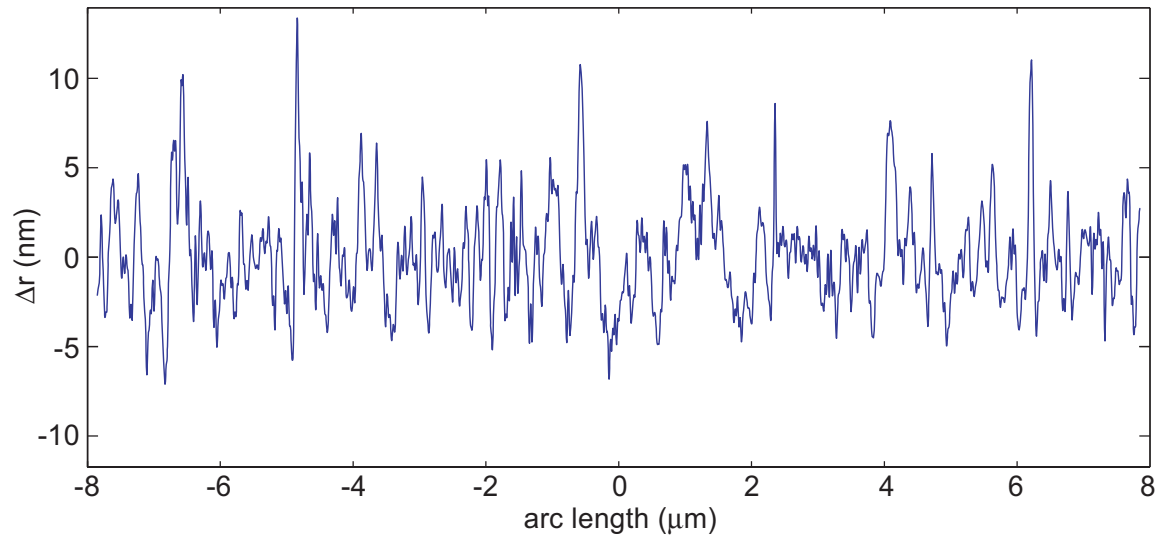


Figure 5.3: Plot of extracted contour versus arc length.

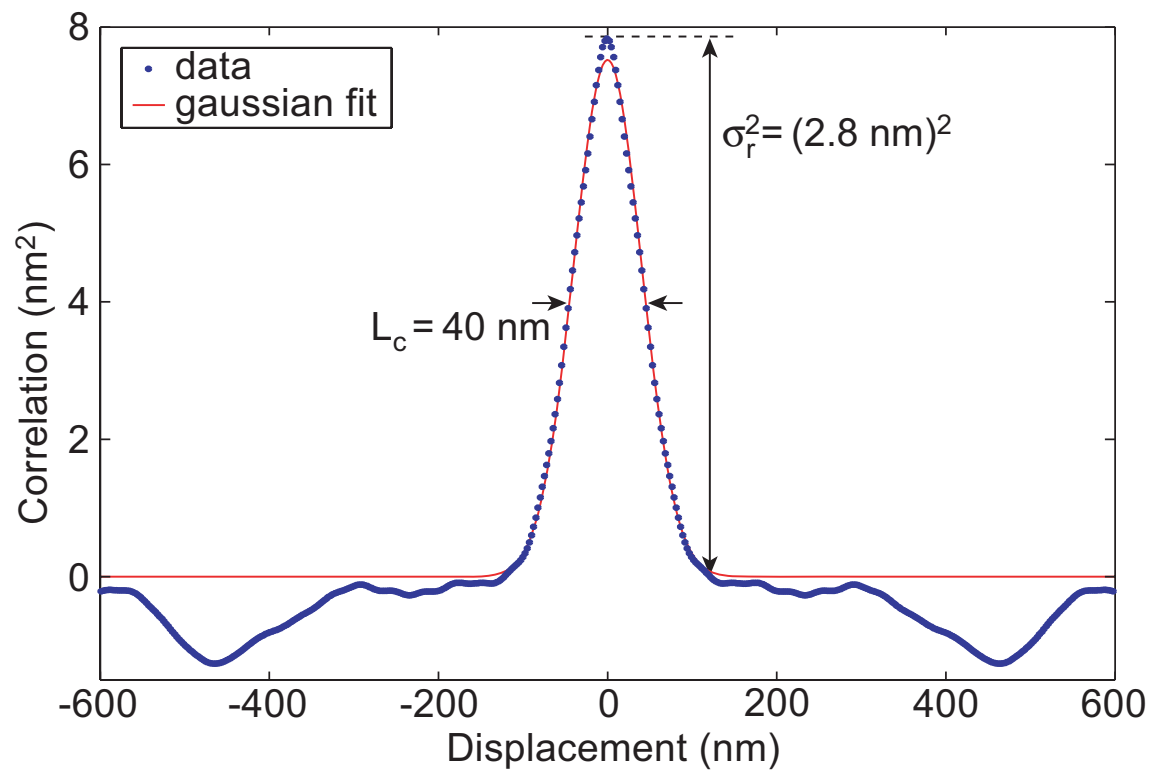


Figure 5.4: Autocorrelation function of the microdisk contour and its Gaussian fit.

are also measured and found to be lower  $Q$  as predicted by the disk-edge surface-scattering theory, although for  $p \geq 2$  the effects of the underlying  $\text{SiO}_2$  pedestal may be significant.

In summary, Si microdisks of a few microns in radius have been fabricated with measured  $Q > 5 \times 10^5$ . In contrast to theoretical predictions for an ideal microdisk, we find that the TM modes have significantly higher measured  $Q$  values than TE modes due to their inherent reduced sensitivity to disk-edge surface roughness. In comparison to previously measured high- $Q$  semiconductor microdisks [78], the  $Q$  of the smallest WGMs measured in this work are  $> 20$  times larger while maintaining a similar effective mode volume.

### 5.3 Beyond the Rayleigh Scattering Limit

Inspired by the ultra-smooth glass microspheres [29,30] and microtoroids [31] formed under surface tension, in this work an electron-beam resist reflow technique is used to significantly reduce surface imperfections in the edge of the microdisk resonator. After a brief description of the fabrication, a comprehensive analysis of the different optical loss mechanisms in these structures is presented below. These measurements indicate that with the reduced level of microdisk surface roughness, we are in fact quantitatively probing the absorption of the surface-states at the edge of the disk (for smaller microdisks) and the bulk Si free-carrier absorption due to ionized dopants (for larger microdisks). Owing to the high finesse of the Si microdisks, the input pump power required to observe even extremely weak nonlinearities, such as two-photon absorption (TPA) and Raman scattering, is reduced to the microwatt level. In what follows, we study the low power thermally-induced optical bistability, including the distortion effects of TPA and free-carrier absorption (FCA), as a second and more direct measure of the linear absorption component of the optical loss. These measurements indicate that for further reduction in the optical loss of high-index contrast Si structures, such as the microdisks studied here, new passivation and annealing techniques, analogous to those used in the manufacture of high-quality Si CMOS devices [82], will need to be developed.

#### 5.3.1 Derivation of $Q_{sa}$

In contrast to surface scattering, surface *absorption* resulting from lattice reconstructions is also present as a source of optical loss. Since great care is taken to preserve the quality of the top and bottom surfaces of the silicon microdisk, it is reasonable to assume that the dominant lattice damage occurs at the disk sidewalls during the etch. While efforts are taken to minimize etch damage, it remains clear that reactive ion etching locally damages the lattice during the material ablation allowing for the incorporation of various lattice impurities and defects [54]. The local surface absorption rate coefficient,  $\gamma_{sa}(\mathbf{r})$ , is used to calculate a spatially averaged loss coefficient according to

$$\bar{\gamma}_{sa} = \frac{\int \gamma_{sa}(\mathbf{r}) n^2(\mathbf{r}) |E(\mathbf{r})|^2 d\mathbf{r}}{\int n^2(\mathbf{r}) |E(\mathbf{r})|^2 d\mathbf{r}}, \quad (5.19)$$

where the appropriate weighting function is proportional to the electric field energy density of the optical mode [83], consistent with the time-dependent perturbation theory of Appendix A. An approximate model for  $\gamma_{sa}(\mathbf{r})$  would be to assume that there exists a reconstruction depth,  $\zeta$ , where the loss rate is a constant  $\gamma_{sa}$  and zero elsewhere. Thus, the electric field in the numerator of Eq. (5.19) is approximately constant over a cylindrical shell with volume  $\delta V_{sa} = 2\pi R\zeta h$ . By using Eq. (5.13) and assuming that the surface reconstruction has approximately the same index of refraction as that of the undisturbed lattice [54], we have

$$\bar{\gamma}_{sa} = \gamma_{sa} n_{\text{Si}}^2 \frac{\int_{\delta V_{sa}} |E(\mathbf{r})|^2 d\mathbf{r}}{\int n^2(\mathbf{r}) |E(\mathbf{r})|^2 d\mathbf{r}} = \frac{1}{2} \gamma_{sa} n_{\text{Si}}^2 \bar{u}_s \delta V_{sa}. \quad (5.20)$$

Defining  $Q_{sa} = \omega/\bar{\gamma}_{sa}$ , we can then write for the surface-absorption quality factor

$$Q_{sa} = \frac{4\pi c}{\lambda_0 \gamma_{sa} n_{\text{Si}}^2 \bar{u}_s \delta V_{sa}}. \quad (5.21)$$

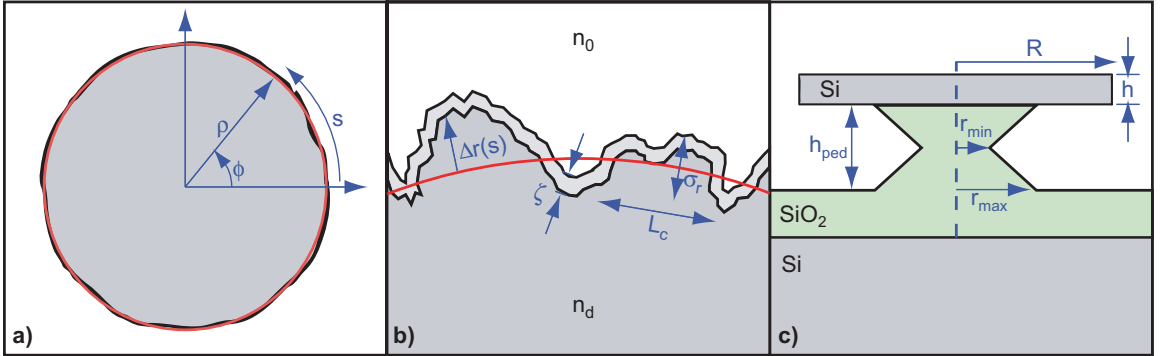


Figure 5.5: Schematic representation of a fabricated silicon microdisk. (a) Top view showing ideal disk (red) against disk with roughness. (b) Top view close-up illustrating the surface roughness,  $\Delta r(s)$ , and surface reconstruction,  $\zeta$ . Also shown are statistical roughness parameters,  $\sigma_r$  and  $L_c$ , of a typical scatterer. (c) Side view of a fabricated SOI microdisk highlighting idealized SiO<sub>2</sub> pedestal.

### 5.3.2 Experimental Results and Analysis

The silicon microdisks characterized in this work were fabricated from a silicon-on-insulator (SOI) wafer with 344 nm thick p-doped Si device layer on a 2  $\mu\text{m}$  SiO<sub>2</sub> layer

(Fig. 5.5(c)). Processing of the microdisks began with the deposition of a 20 nm SiO<sub>2</sub> protective cap layer using plasma-enhanced chemical-vapor-deposition. An electron-beam resist, Zeon ZEP520A, was spin-coated onto the wafer at 6000 rpm for 60 sec, resulting in a 400 nm thick film. Disks of radii ranging from 5 – 30  $\mu\text{m}$  were defined in the electron-beam resist. The wafer was then subjected to a post-lithography bake. By suitable choice of temperature and duration, this bake can significantly reduce imperfections in the electron-beam resist pattern. Temperatures too low do not result in resist reflow, while temperatures too high can cause significant loss of resist to sublimation. A temperature high enough to allow the resist to reflow must be reached and maintained in order for the imperfections in the resist pattern to be reduced. The appropriate duration and temperature for the resist prepared, as described above, was empirically determined to be 5 minutes at 160°C. After the reflow process, the roughness in the patterns was greatly reduced, and the sidewall angle was reduced from 90° to approximately 45°. The resulting angled mask was prone to erosion during the etch process, and so the inductively-coupled plasma reactive-ion etch was optimized to minimize roughness caused by mask erosion.

Due to the near ideal nature of the optical confinement of the silicon whispering-gallery-mode (WGM) resonator, the radiation losses become increasingly negligible as the disk radius is increased ( $Q_r \gtrsim 10^8$  for  $R > 1.5 \mu\text{m}$ ). While all of the disks considered in this work possess inconsequential radiation losses, the better radial confinement of larger radii microdisks pulls the WGMs away from the disk edge, as described in Appendix B. Thus, varying the disk radius provides a means to separate sidewall surface effects, quantified by  $Q_{ss}$  and  $Q_{sa}$ , from bulk effects,  $Q_b$ .

A typical taper transmission spectrum of an  $R = 30 \mu\text{m}$  microdisk is shown in Fig. 5.6. The observed double resonance dip (doublet) is a result of Rayleigh scattering from disk surface roughness, illustrated in Fig. 5.5(b) as  $\Delta r(s)$ . The surface imperfections created during fabrication lift the degeneracy of clockwise (*cw*) and counter-clockwise (*ccw*) propagating WGMs in the microdisk, creating instead standing wave modes [63, 66, 67, 81]. As described in Ref. [28], the highest  $Q$  WGMs in these microdisks were found to be of TM-like polarization and of radial mode number  $p \sim 1$ , where the field interaction with the disk-edge surface is minimized. For the

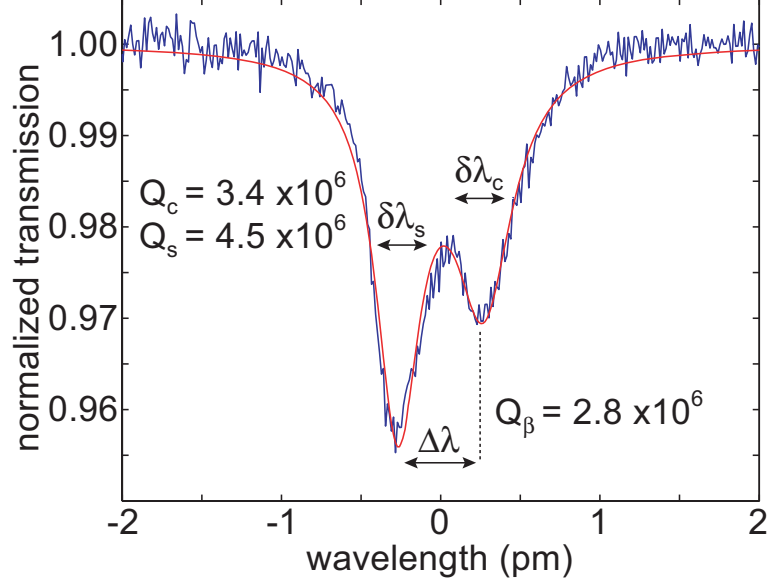


Figure 5.6: Taper transmission versus wavelength showing a high- $Q$  doublet mode for the  $R = 30 \mu\text{m}$  disk.  $Q_c \equiv \lambda_0/\delta\lambda_c$  and  $Q_s \equiv \lambda_0/\delta\lambda_s$  are the unloaded quality factors for the long and short wavelength modes, respectively, where  $\delta\lambda_c$  and  $\delta\lambda_s$  are resonance linewidths. Also shown is the doublet splitting,  $\Delta\lambda$ , and normalized splitting quality factor,  $Q_\beta \equiv \lambda_0/\Delta\lambda$ .

wavelengths studied here, the corresponding azimuthal number is  $m \sim 60$  for the  $R = 5 \mu\text{m}$  disks, and scales approximately linearly with radius for larger microdisks. All of the WGMs studied in this work were confirmed to be of TM-like polarization and of radial number  $p \sim 1$  through studies of their polarization and position dependent coupling to the fiber taper [28].

A statistical model for the doublet splitting is constructed using the effective index model from Section 2.3 and the time-dependent perturbation theory described in Section 5.2.2. The resulting model [63, 67] is used to fit the data in Fig. 5.6 with linewidth parameters  $\delta\lambda_c$  and  $\delta\lambda_s$ , and doublet splitting  $\Delta\lambda$ . Figure 5.7 plots  $Q_\beta$  for each of the measured microdisk radii, where for each microdisk we plot the results for the four highest  $Q_i$  doublet modes in the 1410-1500 nm wavelength range. Combining the results of Section 5.2.2 with an approximate form for disk edge energy density (see Appendix B), we get the following equation for the normalized doublet splitting parameter:

$$Q_\beta \equiv \frac{\lambda_0}{\Delta\lambda} = \frac{1}{\sqrt{2}\pi^{3/4}\xi} \left( \frac{V_d}{V_s} \right), \quad (5.22)$$

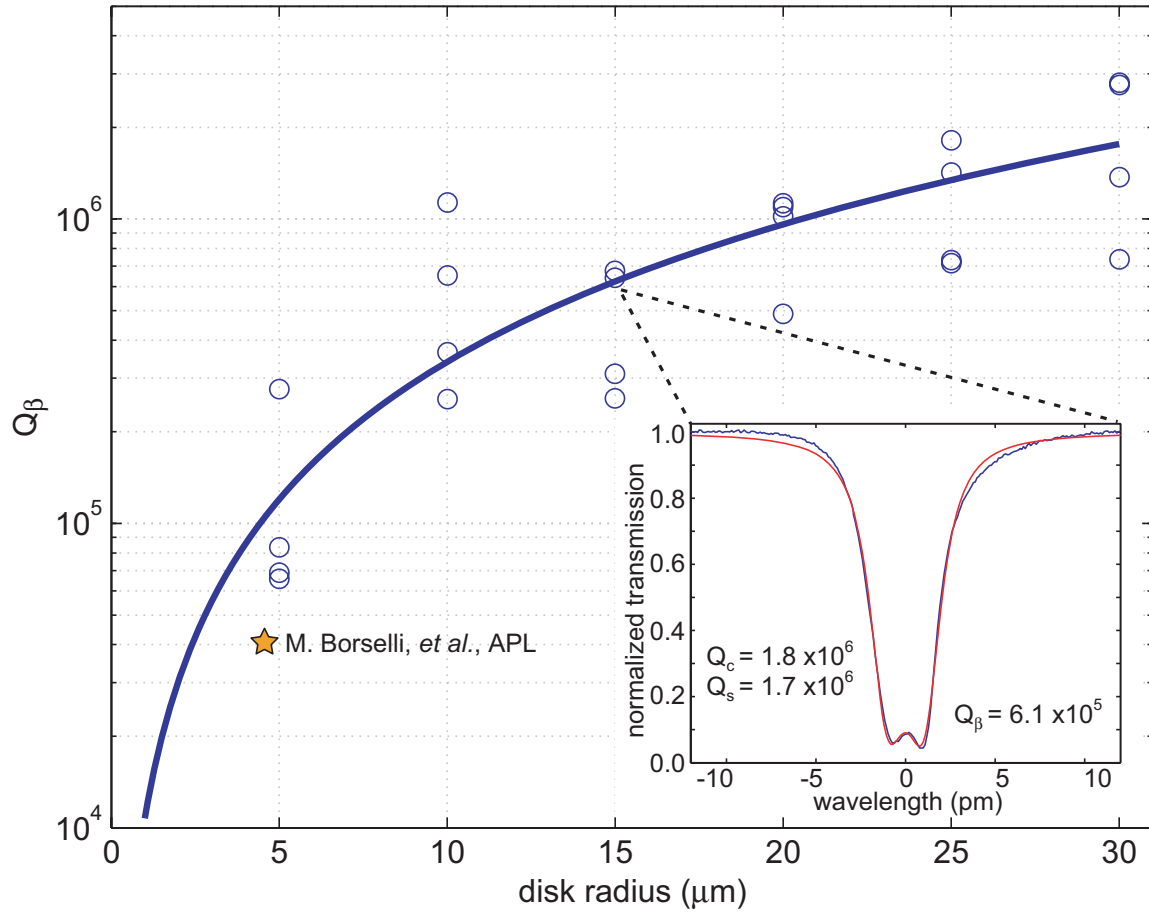


Figure 5.7: Normalized doublet splitting ( $Q_\beta$ ) versus disk radius. (inset) Taper transmission data and fit of deeply coupled doublet demonstrating 14 dB coupling depth.

where  $V_d$  is simply the physical volume of the microdisk and  $\xi$  is the relative dielectric contrast constant defined as

$$\xi = \frac{\bar{n}^2 (n_d^2 - n_0^2)}{n_d^2 (\bar{n}^2 - n_0^2)}. \quad (5.23)$$

$n_d$ ,  $n_0$ , and  $\bar{n}$  are the indices of refraction for the disk, cladding, and 2-D effective slab, respectively [44, 45]. The key parameter from this analysis is the effective volume of a typical scatterer, defined as  $V_s \equiv \sqrt{RL_c}h\sigma_r$ , where  $L_c$  is the correlation length of the roughness,  $h$  is the disk height, and  $\sigma_r$  is the standard deviation of the roughness amplitude (illustrated in Fig. 5.5(b)). Fitting the doublet splitting versus disk radius in Fig. 5.7 (solid blue curve) to the  $Q_\beta \sim R^{3/2}$  dependence shown in Eq. (5.22), gives a value of  $\sqrt{L_c}\sigma_r = 2.7 \text{ nm}^{3/2}$ . This parameter is also useful in estimating optical loss because the same Rayleigh scattering mechanism responsible for lifting the azimuthal degeneracy couples the unperturbed microdisk modes to radiation modes [63, 80].

From an analysis similar to that used for the mode coupling, the surface-scattering quality factor,  $Q_{ss}$ , is approximated as (see Section 5.2.1):

$$Q_{ss} = \frac{3\lambda_0^3}{8\pi^{7/2}n_0\delta n^2\xi} \left( \frac{V_d}{V_s^2} \right), \quad (5.24)$$

where  $\delta n^2 \equiv n_d^2 - n_0^2$ . Figure 5.8 plots the measured linewidths ( $\delta\lambda_{c,s}$ ) of each of the microdisk modes represented in Fig. 5.7 as a dimensionless quality factor,  $Q_i \equiv \lambda_0/\delta\lambda_{c,s}$  (shown as black circles, one for each mode of a doublet pair). From Eq. (5.24), we see that the model of Section 5.2.1 yields a linear dependence versus disk radius of the surface-scattering quality factor,  $Q_{ss}$ . The dash-dotted blue curve shown in Fig. 5.8 represents the resulting surface-scattering component of the total loss as predicted by the fit to  $\sqrt{L_c}\sigma_r$  from the observed doublet splitting. In comparison to recently reported results not incorporating the e-beam resist reflow technique [28] (shown as an \* in Figs. 5.7 and 5.8), the doublet splitting has been reduced by nearly a factor of 2.5. This results in an increase in the predicted  $Q_{ss}$  by more than a factor of 6. Given that the measured quality factor of the current microdisk resonators has only doubled, this suggests that our new work is limited by loss mechanisms not significant in previous work [28].

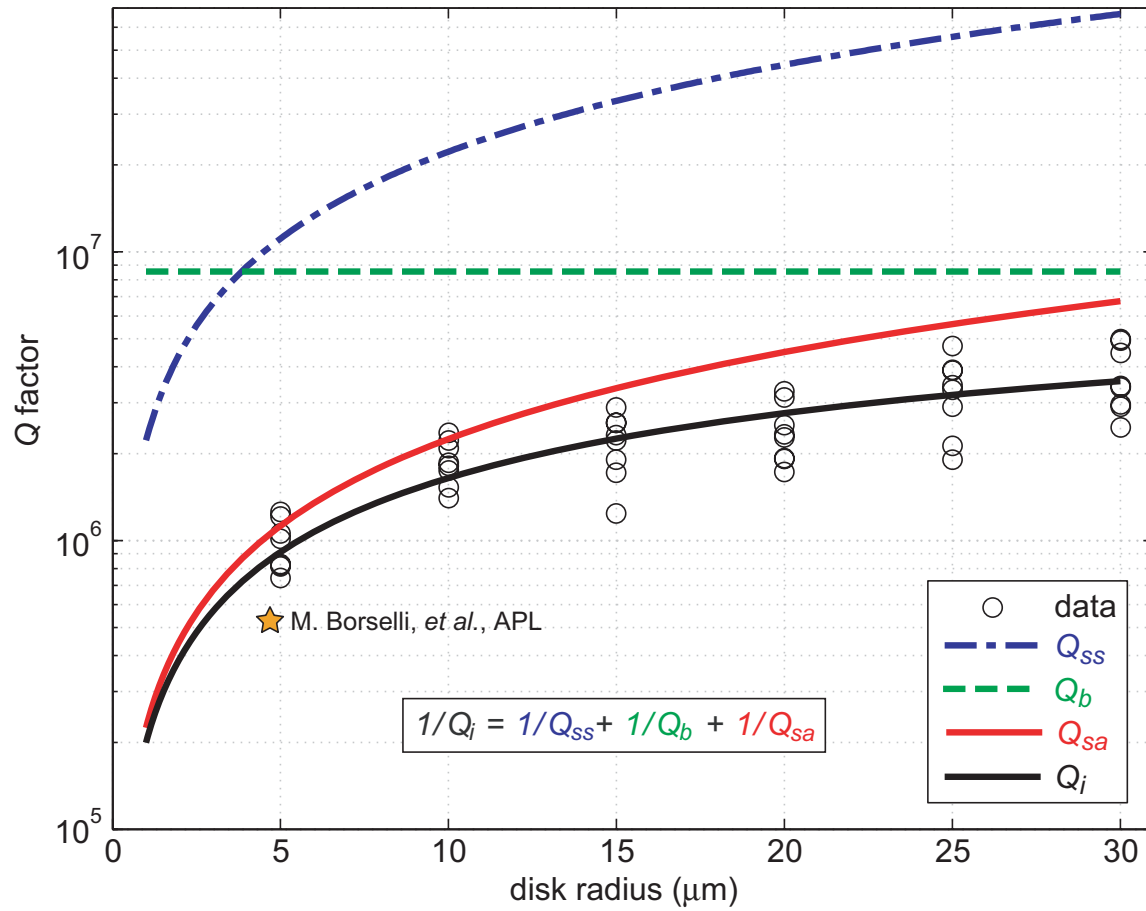


Figure 5.8: Measured intrinsic quality factor,  $Q_i$ , versus disk radius and resulting breakdown of optical losses due to surface scattering ( $Q_{ss}$ ), bulk doping and impurities ( $Q_b$ ), and surface absorption ( $Q_{sa}$ ).

Subtracting the fit to  $Q_{ss}$  from the data, a strong linear dependence with radius still remains. Since the optical losses decrease as the modes are pulled in toward the center of the microdisk, we assume that neither the pedestal nor the top and bottom surfaces are significant sources of optical loss. As shown in Section 5.3.1, a disk edge surface absorption component of optical loss would have a linear dependence with microdisk radius, similar to that of surface scattering. The approximate dependence of the surface absorption quality factor,  $Q_{sa}$ , is found in the analysis from Section 5.3.1 to be given as

$$Q_{sa} = \frac{\pi c (\bar{n}^2 - n_0^2) R}{\lambda_0 \bar{n}^2 \gamma_{sa} \zeta}, \quad (5.25)$$

where  $\gamma_{sa}$  is the bulk absorption rate of a material consisting entirely of that at the microdisk surface. As schematically illustrated in Fig. 5.5(b), we propose that the dominant form of surface absorption occurs at the edge of the microdisk along the etched sidewalls, where reactive ion etch damage of the Si lattice can result in a reconstruction depth,  $\zeta$ , for many monolayers [54]. Fitting the remaining unaccounted for optical loss (i.e., subtracting out the predicted surface scattering component) versus microdisk radius with a linear ( $Q_{sa}$ , solid red curve) and constant ( $Q_b$ , dashed green curve) component, we arrive at the plot shown in Fig. 5.8. From this fit, we find that our microdisks are limited to a  $Q_b \cong 8.5 \times 10^6$ . Using resistivity measurements from the manufacturer of the boron doped SOI material used in this work ( $1-3 \Omega \cdot \text{cm}$ ) and silicon absorption studies [4], residual free carriers in our material should limit  $Q_b \lesssim (3.7 - 8.8 \times 10^6)$ , consistent with our analysis.

To corroborate the above surface absorption conclusions, a series of power-dependent experiments was performed. The small  $\text{SiO}_2$  pedestal ( $r_{\text{max}} \cong 2.5 \mu\text{m}$ ,  $r_{\text{min}} \cong 1 \mu\text{m}$ ,  $h_{\text{ped}} \cong 1.2 \mu\text{m}$ ) in the  $R = 5$  micron microdisk presented here provides relatively poor thermal contact as compared to the larger radii disks. As a result, thermally induced shifts in resonant mode wavelengths (inset to Fig. 5.9) provide a sensitive measure of internal cavity absorption [83–85]. As the input power to the microdisk is increased, the change in resonance wavelength from the “cold-cavity” position can be related to absorbed power inside the microdisk,  $P_{\text{abs}}$ . Since the thermal conductivity of silicon

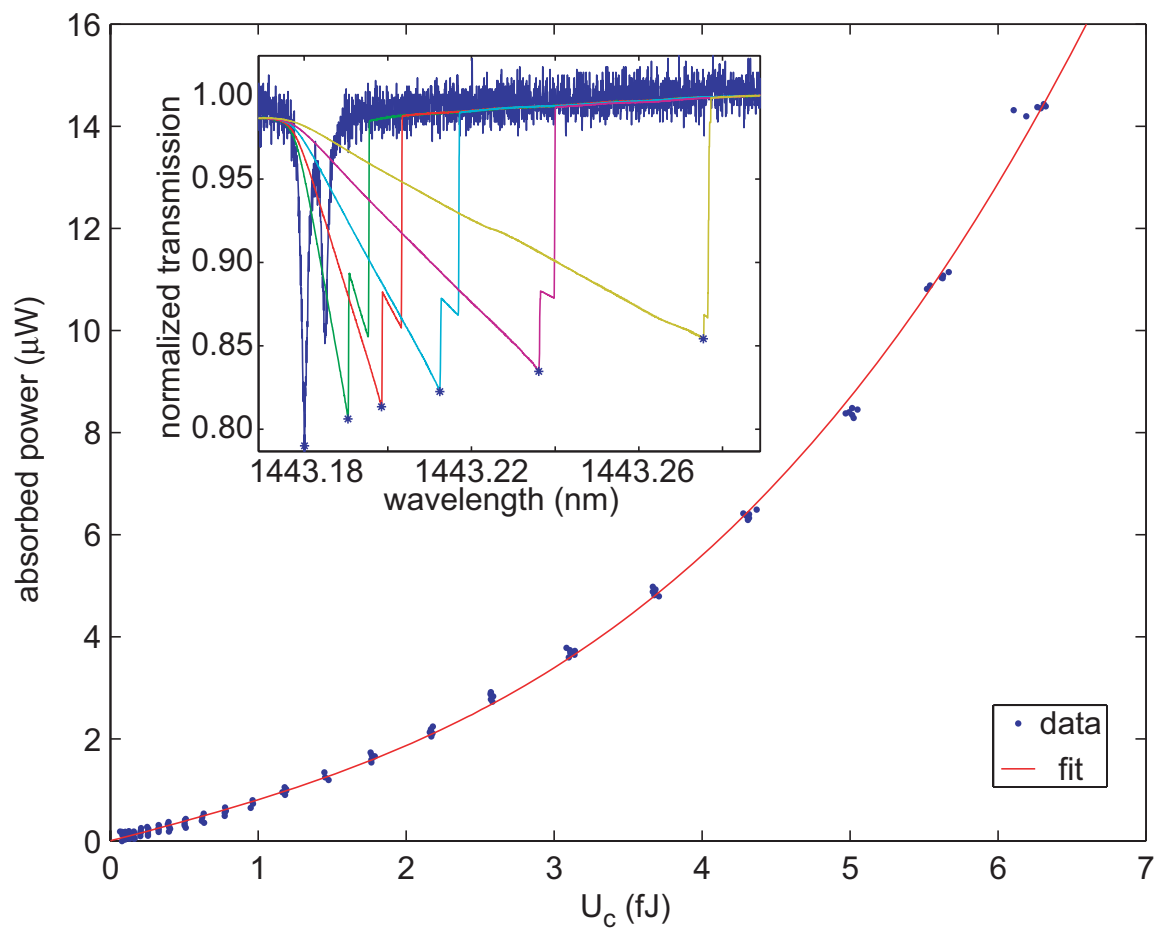


Figure 5.9: Plot showing absorbed power versus intra-cavity energy for a  $R = 5 \mu\text{m}$  disk to deduce linear, quadratic, and cubic loss rates. (inset) normalized data selected to illustrate bistability effect on resonance.

is roughly 100 times greater than that of silica, the steady-state temperature inside the silicon disk is constant (disregarding the negligible heat flow to the ambient N<sub>2</sub> environment). Furthermore, being several orders of magnitude larger in cross-section than the pedestal, the remaining buried oxide and silicon substrate can be assumed to act as a thermal bath of constant temperature. These assumptions reduce the thermal behavior of the microresonator to a time-independent, one-dimensional heat flow problem, depending primarily on the geometry of the pedestal.

The thermal resistance,  $R_{th}$ , of the narrow pedestal can be calculated from the thermal conductivity of thermal oxide ( $\kappa_{\text{SiO}_2} \sim 1.38 \text{ W}\cdot\text{K}^{-1}\text{m}^{-1}$ ) and the geometry of the pedestal (shown schematically in Fig. 5.5(c)):

$$R_{th} = h_{\text{ped}} / (\kappa_{\text{SiO}_2} \pi r_{\text{max}} r_{\text{min}}). \quad (5.26)$$

The change in resonance wavelength can then be approximately related to the optical power absorbed via the linear relationships

$$\Delta\lambda_0 \xrightarrow{n_{\text{Si}}/\lambda_0} \Delta n \xrightarrow{(dn/dT)_{\text{Si}}^{-1}} \Delta T \xrightarrow{R_{th}^{-1}} P_{\text{abs}}, \quad (5.27)$$

where the thermo-optic coefficient of Si is denoted by  $(dn/dT)_{\text{Si}} \sim 1.5 \times 10^{-4} \text{ K}^{-1}$  [83]. We finally arrive at the working equation relating the wavelength shift seen in the inset to Fig. 5.9 to the absorbed power:

$$P_{\text{abs}} = \frac{\kappa_{\text{SiO}_2} \pi r_{\text{max}} r_{\text{min}} n_{\text{Si}}}{h_{\text{ped}} \left. \frac{dn}{dT} \right|_{\text{Si}}} \Delta\lambda_0. \quad (5.28)$$

To calculate the linear absorption rate, the internal cavity energy must also be found from the minima in the normalized transmission spectra,  $T_{\text{min}}$ , and input power,  $P_{\text{in}}$ . Under steady-state conditions, conservation of power requires that the power dropped into the cavity,  $P_d = (1 - T_{\text{min}})P_{\text{in}}$ , be equal to the power lost out of the cavity-waveguide system,  $P_L$ . From the formal definition of *intrinsic* quality factor,  $Q'_i$ , we can relate the cavity energy to the power loss by

$$U_c = \frac{Q'_i}{\omega} P_L = \frac{Q'_i}{\omega} (1 - T_{\text{min}}) P_{\text{in}}, \quad (5.29)$$

where  $\omega$  is the optical frequency and  $U_c$  is the internal cavity energy. Taking into account the external loading from the fiber taper, the total observed quality factor (linewidth) can be written as  $1/Q_t = 1/Q_{\text{ext}} + 1/Q'_i$ , where  $Q_{\text{ext}}$  relates to the coupling of optical power from the fiber taper to the microdisk.  $Q'_i$  in this case includes all intrinsic loss of the microdisk resonator and any additional parasitic loading from the fiber taper. As the resonant mode linewidth cannot be directly measured at high powers (due to nonlinear distortion), it must be inferred from the depths of transmission and the “cold-cavity” linewidth [83]. Using a simple model for the waveguide-resonator system [55], we can find  $Q_{\text{ext}}$  by measuring the total linewidth at *low* powers and using the relation  $Q_{\text{ext}} = 2Q_t/(1 - \sqrt{T_{\text{min}}})$ . We can then show that  $Q'_i = Q_{\text{ext}}(1 - \sqrt{T_{\text{min}}})/(1 + \sqrt{T_{\text{min}}})$  for *all* powers, assuming that the taper loading does not change with input power. With complete knowledge of  $Q_{\text{ext}}$  and  $Q'_i$ , we can finally determine the internal cavity energy versus input power.

Figure 5.9 shows a typical data set for the power-dependent absorption effects for the  $R = 5 \mu\text{m}$  microdisk modes previously described for Figs 5.7 and 5.8. At low powers,  $P_{\text{abs}}$  scales linearly with  $U_c$ , while at higher powers, the onset of two-photon absorption (quadratic term) and free-carrier absorption (cubic term) become readily apparent. A cubic polynomial fit ( $P_{\text{abs}} \sim aU_c^3 + bU_c^2 + \gamma_{\text{lin}}U_c$ ) for the four  $R = 5 \mu\text{m}$  modes yields a linear absorption quality factor of  $Q_{\text{lin}} \equiv \omega/\gamma_{\text{lin}} = (1.5 \pm 0.3) \times 10^6$ . This value is in very good agreement with the estimated  $Q_{sa}$  from the analysis above (solid red curve in Fig. 5.8). Also, as the measurements of the modes in the larger microdisks have significantly higher measured  $Q_i$  than the measured  $Q_{\text{lin}}$ , this is a strong indication that we are indeed quantitatively probing the surface state absorption and not the bulk absorption for the smaller  $R = 5 \mu\text{m}$  microdisks.

### 5.3.3 Conclusion

Using a combination of resist reflow to form a surface-tension limited smooth etch mask and a low DC bias dry etch to reduce roughness and damage in the etched Si sidewalls, we have fabricated high-index contrast Si microdisk microresonators with strong optical confinement and losses as low as 0.1 dB/cm ( $Q > 5 \times 10^6$ ). Passive fiber optic measurements of the scaling of optical loss with microdisk radius, along

with power-dependent measurement of the thermo-optic properties of the microdisks, provide evidence supporting the view that optical loss is dominated in these structures by surface ( $5 < R < 20 \mu\text{m}$ ) and bulk free-carrier absorption ( $R > 20 \mu\text{m}$ ), as opposed to surface roughness on the microdisk. Applications of these devices to nonlinear light scattering, all-optical switching, Si laser resonators, or highly sensitive Si optical sensors are envisioned, where the low loss and tight optical confinement results in extremely large circulating intensities for low optical input powers.

## 5.4 Measuring the Role of Surface Chemistry in Silicon Microphotronics

Historically, studies of Si surface and interface states have primarily focused on their electronic properties [86, 87]. Three exceptions to this are deep-level optical spectroscopy [88], cavity-ringdown spectroscopy [89], and the ultra-sensitive technique of photothermal deflection spectroscopy (PDS) [90, 91], which can measure fractional optical absorption down to  $\alpha l \sim 10^{-8}$ . None of the aforementioned techniques, however, is well suited for studying as-processed microphotonic elements. In this work, we utilize a specially designed microdisk optical resonator to study the optical properties of surfaces typical in silicon-on-insulator (SOI) microphotonic elements in a noninvasive, rapid, and sensitive manner. Shown in Figure 5.10, the high-quality-factor ( $Q$ ) Si microdisk resonators used in this work provide surface-specific optical sensitivity due to the strong overlap of the top and bottom surfaces of the active Si layer with the electric field energy density of appropriately polarized bound optical modes of the microdisk.

The Si/SiO<sub>2</sub> interface is quite possibly one of the most exhaustively studied surface in all of science because of its crucial role in microelectronics device performance [82, 87, 92–98]. As silicon-based photonics [7, 8, 17] becomes more mature, the chemical nature of the optical surfaces becomes increasingly important. It has long been established that aqueous HF etching of  $\langle 100 \rangle$  silicon surfaces results in the removal of the surface oxide and passivates the silicon dangling bonds with atomic hydrogen [82, 92, 93]. Utilizing a test-bed that can characterize silicon surfaces of SOI wafers quickly and with high sensitivity, our results indicate that judicious choice of fabrication steps may be able to improve the quality factor of silicon resonators by up to an order of magnitude. Previous high- $Q$  silicon microdisk results showed it was possible to obtain  $Q > 5 \times 10^6$  using electron-beam lithography and mask reflow [32]. Using the same fabrication procedure, it was found that the average initial quality factor of thin SOI disks ( $Q \sim 0.5 - 1 \times 10^6$ ) was significantly worse by comparison. To remove surface damage and recover quality factors consistent with previous thick SOI fabrication, a series of “wet chemical oxidation” [57, 94] treatments were then

performed on the devices. Repeated chemical oxidation in Piranha and HF oxide stripping were employed to controllably etch the top and bottom surfaces. It was found that repeated cycles of Piranha/HF significantly improved the optical surface quality, not by removing roughness, but rather by passivating interface states found in poor silicon oxides [95]. These initial results have shown quality factors can be significantly and reversibly altered by even the shortest of standard microelectronics treatments, and that surface absorption as opposed to surface roughness plays a significant, if not dominant, role in optical loss within Si micro- and nano-photonic devices.

#### 5.4.1 Design of Surface-Sensitive Optical Modes

The application under consideration was a test-bed that can characterize the silicon surfaces of SOI wafers for use in photonic components quickly and with high sensitivity. A waveguide coupler and an optical resonator were a natural choice for such an application because of the increased interaction time per photon afforded by an optical microcavity. The general design goals for this waveguide-resonator test-bed were to have: (1) a large energy overlap with Si surface layers, (2) a high-quality factor to discern small changes to surfaces, (3) good power transfer from waveguide to microcavity for easy detection, (4) and a large FSR to ensure an easily understood spectra. Leveraging our earlier work [28, 32, 33, 83], the fiber taper probe and thin high-index contrast silicon microdisks were employed to achieve these goals. The fiber taper probe was chosen as the waveguide because of its highly efficient evanescent and externally controlled coupling characteristics. The external control of coupling drastically reduces fabrication constraints, completely removing the necessity of tailoring the separation between waveguide and resonator. Furthermore, the ability to independently change either the waveguide or resonator allowed for unambiguous interpretation of experimental results. By changing the taper-disk gap, measurements of external loading and parasitic losses were obtained, providing true intrinsic photon lifetimes inside the resonator [55].

Changes to the silicon surface can result in both a resonance frequency shift and/or broadening of the resonance. The local surface loss or gain rate,  $\gamma_s(\mathbf{r})$ , was used to

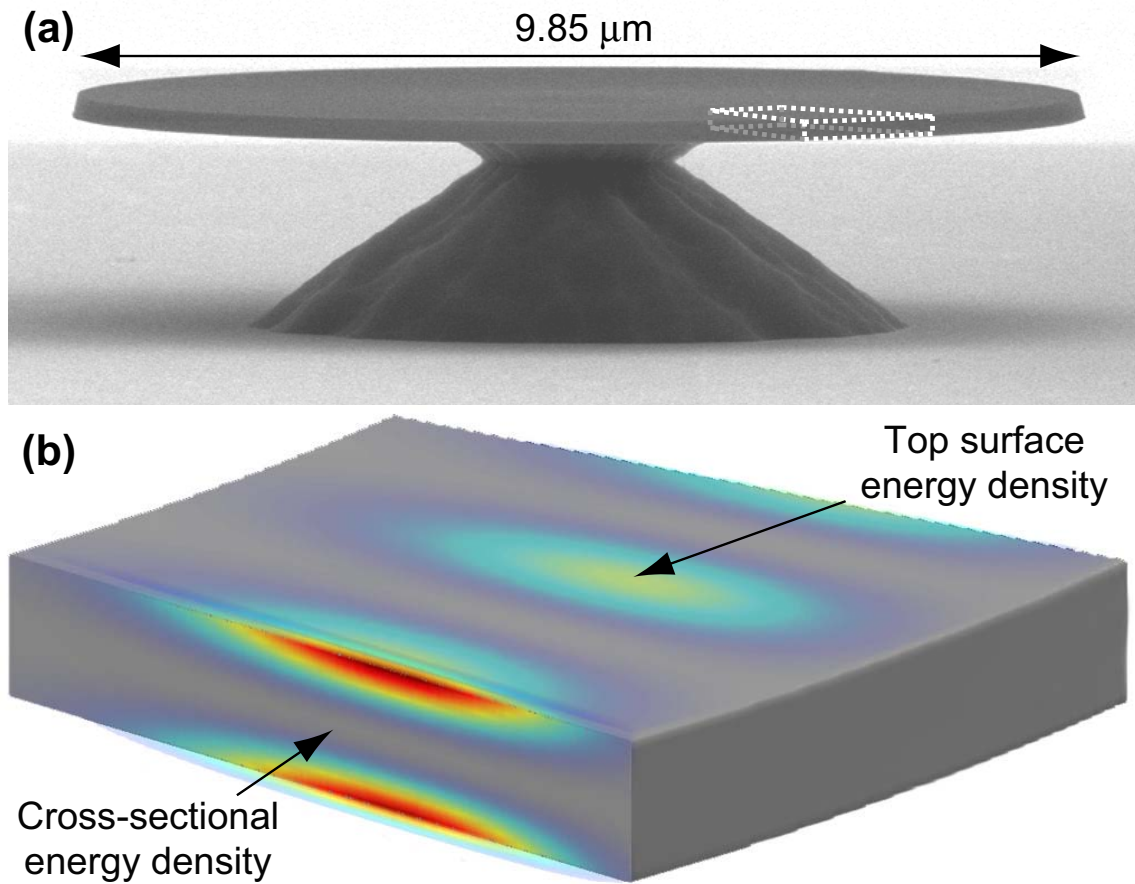


Figure 5.10: Composite of surface-sensitive thin-disk optical resonance. (a) SEM micrograph of a  $5 \mu\text{m}$  radius SOI microdisk. (b) Zoomed-in view of disk edge showing a TM polarized whispering gallery mode (WGM) solved via the finite-element method, emphasizing large electric field in air cladding. (c) Plot of energy density of the same WGM, emphasizing that 78% of the energy remains in the silicon for future opto-electronic integration

calculate the spatially averaged loss or gain rate according to

$$\bar{\gamma}_s = \frac{\int \gamma_s(\mathbf{r}) n^2(\mathbf{r}) |E(\mathbf{r})|^2 d\mathbf{r}}{\int n^2(\mathbf{r}) |E(\mathbf{r})|^2 d\mathbf{r}}, \quad (5.30)$$

where the appropriate weighting function is proportional to the time-averaged electric field energy density of the optical mode (see Appendix A),  $n(\mathbf{r})$  is the local index of refraction, and  $|E(\mathbf{r})|^2$  is the absolute square of the local electric field [83]. Assuming that the physical depth,  $t_s$ , of the perturbation to the silicon surface is much smaller than the wavelength of light in the material,  $\gamma_s(\mathbf{r})$  can be assumed to be constant over the integral of Eq. (5.30). We may then define a fractional energy overlap,  $\Gamma_s$ , with a particular surface to be used to quantify a mode's sensitivity to surface perturbations by

$$\Gamma_s = \frac{\int_{\delta V} n^2(\mathbf{r}) |E(\mathbf{r})|^2 d\mathbf{r}}{\int n^2(\mathbf{r}) |E(\mathbf{r})|^2 d\mathbf{r}}, \quad (5.31)$$

where  $\delta V$  is the volume of the thin surface perturbation. The optical resonances of microdisks can be classified into TE-like (TM-like) whispering gallery modes (WGMs) with dominant electric field parallel (normal) to the plane of the microdisk. The silicon optical microdisk used in this test-bed was designed for TM mode operation in order to provide enhanced sensitivity to top/bottom surfaces while avoiding dry-etched sidewalls [28].

A normalized measure of surface sensitivity for a guided-wave mode in a waveguide or resonator can be defined as  $\Gamma'_s \equiv \Gamma_s/t_s$ . If optical loss is dominated by interactions with the surface, then the modal loss coefficient per unit length ( $\alpha_m$ ) measured from experiment can be related to a fractional loss per pass through the surface given by  $\alpha'_s = \alpha_m/\Gamma'_s$  ( $= (2\pi n_g)/(\lambda_0 Q \Gamma'_s)$ , for a resonator with quality factor  $Q$  and modal group index of refraction  $n_g$ ). As discussed in Ref. [43], for a true two-dimensional surface in which the perturbation depth is infinitesimal,  $\alpha'_s$  is the most relevant quantity describing the surface and is equivalent to the fraction of power lost for a normal incident plane wave propagating across the surface. From finite-element method (FEM) simulations [49], shown in Figure 5.10, the transverse magnetic (TM) WGMs of the microdisk are  $\sim 90\times$  more sensitive to the top and bottom  $\langle 100 \rangle$  Si surfaces than

the etched sidewall at the microdisk periphery; specifically,  $\Gamma'_{top} = \Gamma'_{bot} = 3.5 \times 10^{-3} \text{ nm}^{-1}$  and  $\Gamma'_{side} = 8.1 \times 10^{-5} \text{ nm}^{-1}$ . This implies that  $\sim 0.2\%$  of the optical mode exists in a single monolayer at the top (bottom) Si surface, while little of the mode sees imperfections at the microdisk perimeter. For the measured devices described below ( $Q \sim 1.5 \times 10^6$ ), a surface absorption of one-tenth of the full linewidth was measurable, corresponding to a sensitivity limit of  $\alpha'_s \sim 10^{-7}$ . At this level of sensitivity, surface perturbations at the level of 0.03% of a monolayer, corresponding to  $\sim 10^4$  atomic reconfigurations, would be discernible.

#### 5.4.2 Fabrication and Measurement Technique

The silicon microdisks employed in this work were fabricated from a commercially available silicon-on-insulator (SOI) wafer from SOITEC, consisting of a 215 nm thick silicon device layer (p-type, 14–20  $\Omega\cdot\text{cm}$  resistivity,  $\langle 100 \rangle$  orientation) on top of a 2  $\mu\text{m}$  SiO<sub>2</sub> buried oxide (BOX) layer. Microdisks of 5 and 10  $\mu\text{m}$  radius were fabricated. To enable optical fiber taper probing of the devices (as described below), the wafer surrounding the disks was etched down  $\sim 10$  microns using a photolithographically defined etch-mask of AZ-5214 photoresist. Following a 10 minute acetone soak and a second Piranha etch to remove organic materials, a  $\sim 1$  hour diluted hydrofluoric acid (HF) solution (comprised of five parts 18.2 M $\Omega$  deionized (DI) water to one part concentrated aqueous HF (49%)) was used to remove the protective SiN<sub>x</sub> cap and partially undercut the disk, as shown in the SEM micrograph in Figure 5.10(a). The wafer was then rinsed in deionized water and dried with clean, dry N<sub>2</sub>. Upon completion of the processing, the wafer was immediately removed to an N<sub>2</sub> purged enclosure for characterization. Once inside the N<sub>2</sub> purged enclosure, the microdisks were characterized using a computer-controlled fiber taper probe [28, 33, 83]. For this set of experiments, an optical fiber was adiabatically drawn to a  $1.2 \pm 0.2 \mu\text{m}$  diameter using a hydrogen torch so that its evanescent field could be made accessible to the environment.

Classification of the microdisk modes is done by determining the dominant polarization (TE or TM), the number of radial antinodes in the electric field ( $p$ ), and the number of azimuthal antinodes ( $m$ ). Note that only the fundamental slab modes

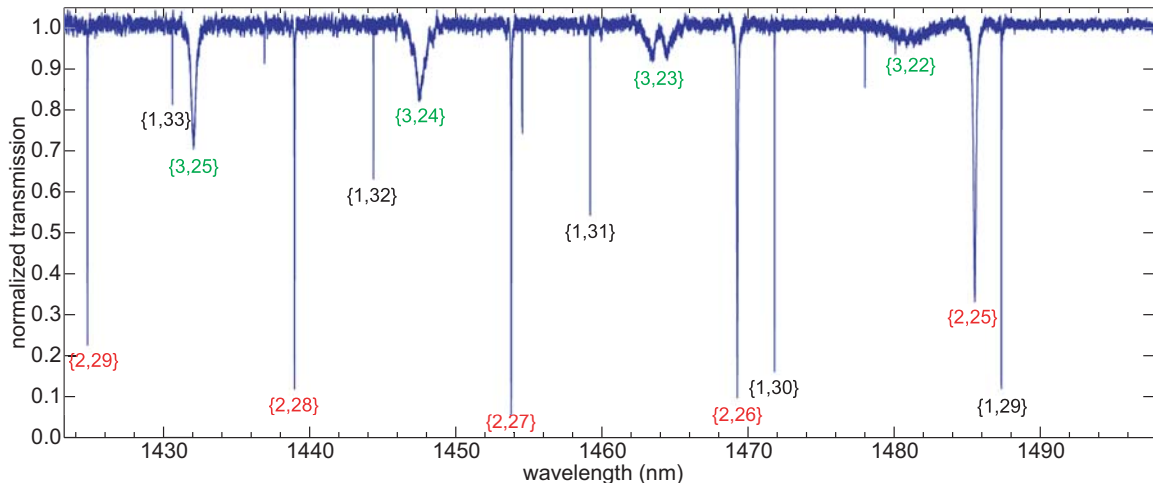


Figure 5.11: Normalized spectral transmission response of a  $5 \mu\text{m}$  radius microdisk resonator with the fiber taper placed  $0.6 \pm 0.1 \mu\text{m}$  away from the disk edge and optimized for TM coupling. The spectrum was normalized to the response of the fiber taper moved  $3 \mu\text{m}$  laterally away from the disk edge. Classification of the modes is done via the notation  $\{p, m\}$  where  $p$  and  $m$  are the number of antinodes radially and azimuthally, respectively.

are supported for our disk heights, so the vertical mode quantization will be omitted. The notation used to specify all three parameters will be either  $\text{TE}_{p,m}$  or  $\text{TM}_{p,m}$ , depending upon the polarization. Figure 5.11 shows the spectral transmission response of the  $5 \mu\text{m}$  radius microdisk resonator with the fiber taper placed  $0.6 \pm 0.1 \mu\text{m}$  away from the disk edge and optimized for TM coupling. The transmission was normalized to the spectral transmission of the fiber taper moved laterally  $3 \mu\text{m}$  away from the microdisk; the ability to normalize out the response of the waveguide underscores a major advantage of fiber taper probe testing. The figure illustrates the clear radial families (same  $p$ ) of modes present in the microdisk each having similar linewidth, doublet splitting [32] (if any), and free-spectral range (FSR). finite-element simulations of the WGMs [49] were able to accurately predict the wavelength and radiation quality factor ( $Q_r$ ) for each of the modes shown in Figure 5.11. The index of refraction for silicon used in these simulations was a Sellmeier-type dispersion fit to the tabulated values given in Reference [52]. The nominal FSRs for these families were 14.2, 15.1, 16.2 in order of increasing radial number. It should be emphasized that due to limited knowledge of the physical dimensions of the disk, the radiation  $Q$ s for the higher order radial modes were used as an important check on the absolute  $m$  assignments. Had ring-resonators been used as a test-bed instead of microdisks, absolute

quantization number assignment could not have been done, thereby decreasing the accuracy of our analysis. In the case of small diameter microdisks, the spectra are simple enough to completely understand, but rich enough to give detailed unambiguous information. A drawback for using microdisks is that accidental degeneracies are possible of TE to TM modes with the same  $m$  and similar wavelengths, as was the case for the  $\text{TM}_{3,23}$  mode shown in Figure 5.11. In the case of these fabricated disks, the TE to TM coupling is mediated through the broken mirror symmetry due to the angled sidewalls. Finite-element simulations show that anti-crossings of up to 4 nm are possible for sidewall angles of  $75^\circ$ .

The coupling depths for each of these modes can be explained through a combination momentum matching and intrinsic loss. Because evanescent coupling is used between the waveguide and resonator, the degree to which taper mode and WGMs are momentum matched has a large effect on the coupling depth. The momentum of the taper mode for the  $1.2 \pm 0.2 \mu\text{m}$  diameter was calculated analytically using the derivation found in Reference [44]. Choosing a cylindrical coordinate system, the angular momentum of the taper mode near the disk was found by dividing the linear momentum by an effective radius of  $5.5 \mu\text{m}$ . The angular momentum of the taper modes was found to range from 30.2 on the blue end of the spectrum under consideration to 28.3 on the red end. Thus, the deepest coupling occurs for the TM  $p = 1, 2$  modes over the extended range, consistent with the identification made from finite-element simulations. Furthermore, the three unlabeled modes in the spectrum are most likely TE  $p = 6$  or  $7$  because of similar momentum matching considerations. The intrinsic loss of each mode sets the rate at which power must be coupled into the resonator, also drastically affecting coupling depth. This power dropped versus power lost balance is most clearly observed in the poor coupling depths of the radiation loss limited  $p = 2$  and  $p = 3$  modes on the red end of the spectrum.

Owing to their large surface sensitivity (see Figure 5.10), the spectral signature of the  $\text{TM}_{1,m}$  modes was used to determine the quality of the optical surfaces. Figure 5.12(a) shows a high-resolution scan across the  $\text{TM}_{1,31}$  mode. The observed double resonance dip, termed a doublet, is a result of surface roughness coupling of the normally degenerate clockwise (CW) and counter-clockwise (CCW) propagating

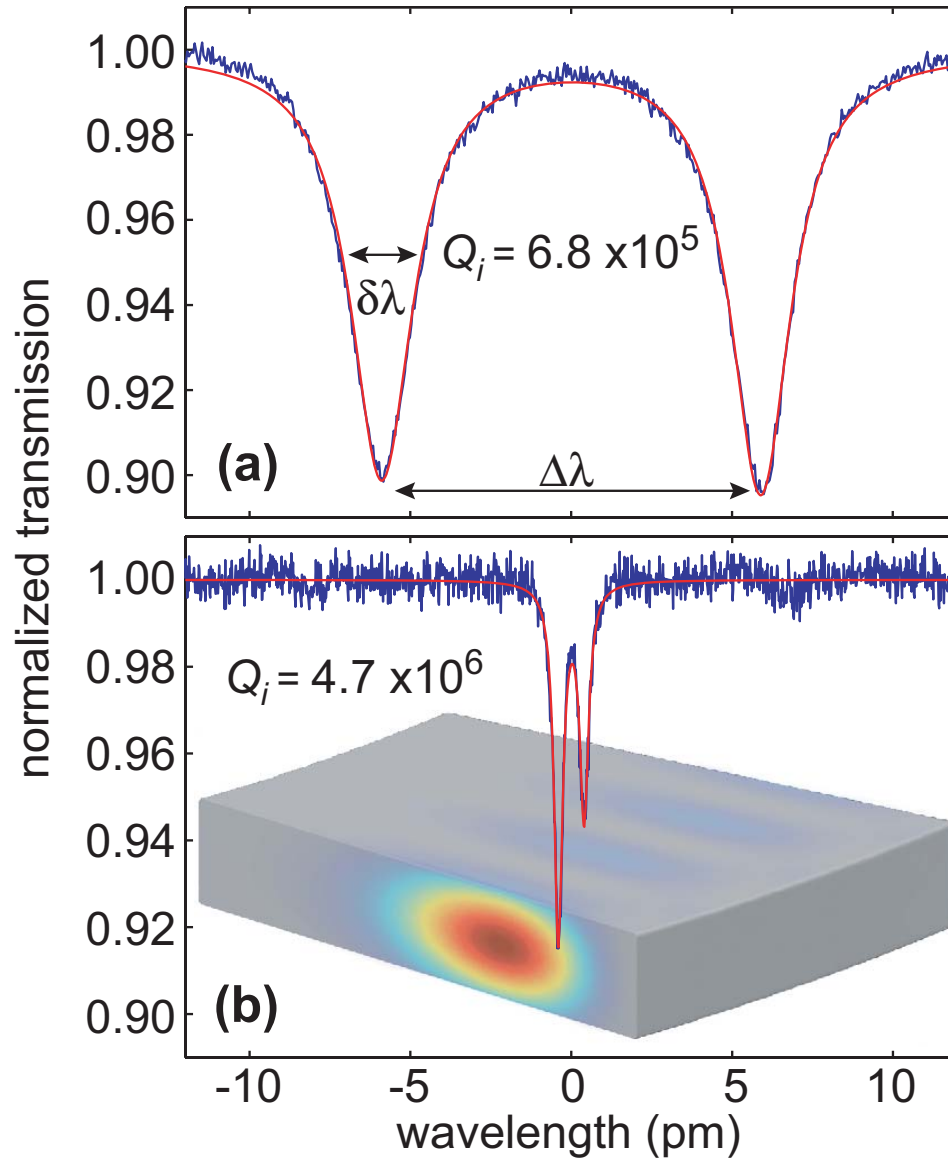


Figure 5.12: (a) Normalized high-resolution scan of the  $TM_{1,31}$  mode at  $\lambda = 1459$  nm in Fig. 5.11.  $\Delta\lambda$  and  $\delta\lambda$  indicate the CW/CCW mode splitting and individual mode linewidth, respectively. (b) Electric energy density plot and high-resolution scan of a  $40 \mu\text{m}$  radius microdisk, showing the reduced loss of a bulk TE WGM.

WGMs [32, 63, 81]. The rate at which photons are back-scattered is quantified by the doublet splitting,  $\Delta\lambda$ , while the rate at which photons are lost from the resonator is quantified by the intrinsic linewidth,  $\delta\lambda$ , of the individual doublet modes. From a fit to the transmission spectrum of Fig. 5.12(a),  $\Delta\lambda = 11.9$  pm and  $\delta\lambda = 2.2$  pm, corresponding to an intrinsic modal quality factor of  $Q_i \equiv \lambda_0/\delta\lambda = 6.8 \times 10^5$  for this  $\text{TM}_{1,31}$  mode. This should be contrasted with the electric field energy density plot and transmission spectrum shown in Fig. 5.12(b) for a more confined, and less surface sensitive, TE WGM of a much larger  $40 \mu\text{m}$  radius microdisk ( $\Gamma'_{top} = \Gamma'_{bot} = 1.2 \times 10^{-3} \text{ nm}^{-1}$  and  $\Gamma'_{side} = 2.3 \times 10^{-5} \text{ nm}^{-1}$ ). From the fit parameters ( $\Delta\lambda = 0.8$  pm,  $\delta\lambda = 0.3$  pm), the  $Q$  of the buried TE mode is  $Q_i = 4.7 \times 10^6$ , corresponding to a loss per unit length of  $\alpha_i = 0.13$  dB/cm. This is nearly an order of magnitude smaller optical loss than that of the as-processed  $\text{TM}_{1,m}$  modes, and provides an upper bound on the bulk Si optical loss of the SOI material.

### 5.4.3 Results and Discussion of Chemical Surface Treatments

Previous high- $Q$  silicon microdisk results showed that it is possible to obtain quality factors in excess of  $5 \times 10^6$  using electron beam lithography and mask reflow [32]. Using the same fabrication procedure as presented in our previous thick SOI work [32], we found the average initial quality factor of the thin SOI disks ( $Q \sim 0.5 - 1 \times 10^6$ ) was significantly worse by comparison. The increased optical loss of the thin 215 nm device layer could not be explained by bulk material effects for two reasons. The first reason is that the resistivity of the thin material ( $14 - 20 \Omega \cdot \text{cm}$ ) was much higher than the thick material ( $1 - 3 \Omega \cdot \text{cm}$ ), theoretically reducing the absorption from residual free carriers. The second reason is that by making extremely large ( $40 \mu\text{m}$  radii) disks, we measured quality factors of  $4.7 \times 10^6$  from highly confined TE modes. In further contrast to our previous thick SOI work, we observed only a modest increase in  $Q$  as we increased the radius of the thin disks. This suggested that the thin disks' optical losses were limited by the top and bottom  $\langle 100 \rangle$  surface quality rather than the vertical sidewall.

One of the main goals of the fabrication detailed in Section 5.4.2 was to protect the top and bottom surfaces from the majority of processing steps. Achieving this

goal implied that the final hour-long HF dip removed the PECVD  $\text{SiN}_x$  cap and native oxide from the top surface while removing the thermally oxidized BOX from the bottom surface. The HF undercut step produced an inert hydrogen terminated silicon surface ready for testing [92,93]. Within 3 minutes, the sample was transferred into the  $\text{N}_2$  purged testing enclosure. For these air exposure times, we estimated that less than 0.2 Angstroms (measured in  $\text{SiO}_2$  equivalent thickness) of native oxide grew on the surface, corresponding to less than one fifteenth a monolayer [97]. Optical fiber taper probing [28, 33, 83] was then used to couple power into the optical resonances of the silicon microdisks.

The spectral signature of the transmitted fiber power was then used to determine the quality of the optical surfaces. Figure 5.13(a) shows a high-resolution scan across the  $\text{TM}_{1,31}$  mode identified in Section 5.4.2 at  $\lambda_0 = 1459.6$  nm. The observed double resonance dip, termed a doublet, is a result of surface roughness produced during fabrication [28, 32, 63, 67]. The mode splitting is a result of elastic scattering events at the roughened surface, effectively grating coupling the normally degenerate clockwise and counter-clockwise propagating WGMs. The rate at which photons are back-scattered is quantified by the doublet splitting,  $\Delta\lambda$ , seen graphically in the left pane of Figure 5.13(a). Conversely, the rate at which photons are lost from the composite waveguide-resonator system is quantified by the unloaded linewidth,  $\delta\lambda$ , of the individual doublet modes. Using a model including back-scattering [32, 63, 67], the intrinsic modal quality factor,  $Q_i \equiv \lambda_0/\delta\lambda$ , was determined to be  $6.8 \times 10^5$  after initial fabrication. The free-space wavelength and fit parameters,  $\Delta\lambda = 11.9$  pm and  $\delta\lambda = 2.2$  pm, are listed in Table 5.2 for this mode. Repeated scans on other  $\text{TM}_{1,m}$  modes on other devices revealed similar doublet splitting and optical losses. While Table 5.2 catalogues the performance of the best  $\text{TM}_{1,m}$  mode, Figure 5.13(e-f) shows a graphical representation of the average behavior of all  $\text{TM}_{1,m}$  modes in the 1420 – 1470 nm span for comparison.

It was hypothesized that the silicon surfaces possessed surface damage resulting from a variety of possible sources including: chemical mechanical polishing from the manufacturer, poor quality native oxide formation during storage, or adventitious organic matter. In addition, the length of time of the HF undercut step could have

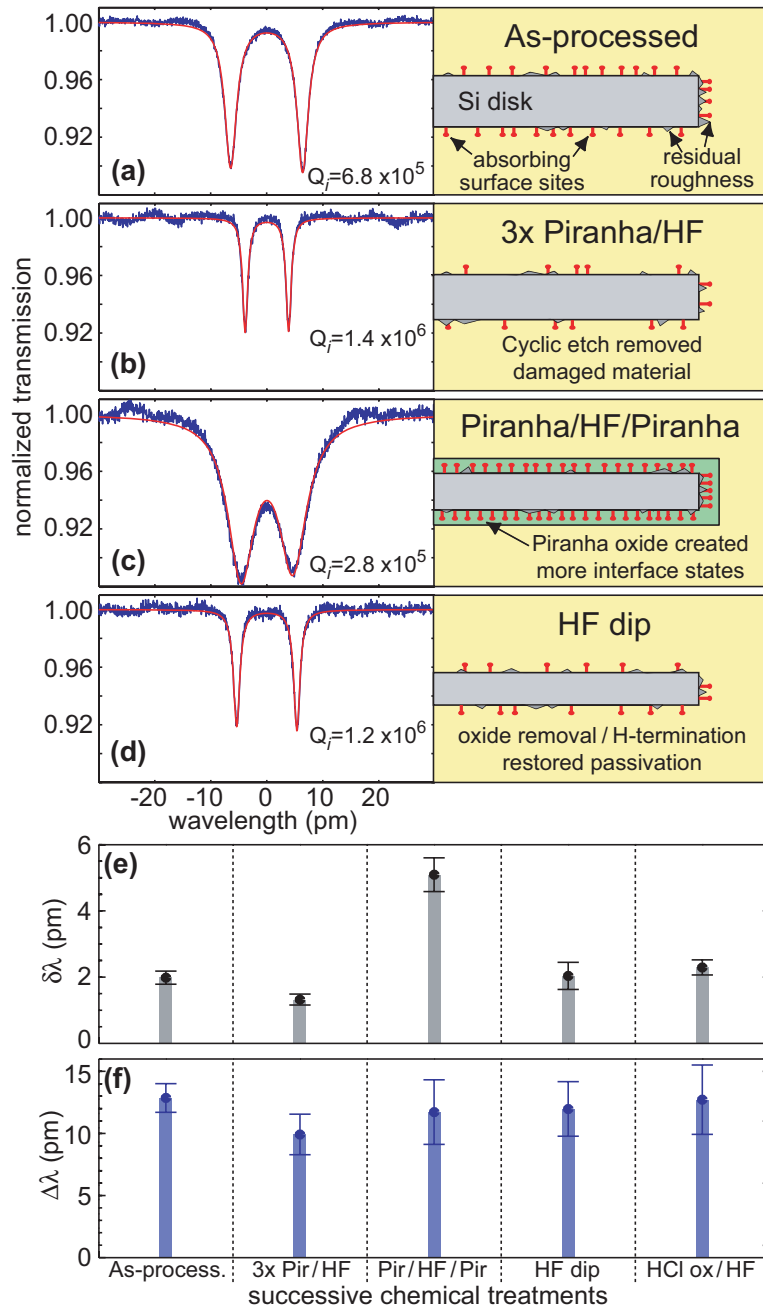


Figure 5.13: Taper transmission versus wavelength showing  $TM_{1,31}$  doublet mode after each chemical treatment and accompanying schematic of chemical treatment. (a) Initial fabrication, illustrating surface roughness and absorption loss mechanisms. (b) Triple Piranha/HF cycle described in Table 5.3 removes damaged material and partially passivates surfaces states. (c) Single Piranha/HF cycle followed by an additional Piranha allowing controlled measurement of Piranha oxide. (d) HF dip to remove chemical oxide from previous treatment and restore passivation.

Table 5.2: Summary of TM<sub>1,31</sub> characteristics after various chemical treatments

Step	$\lambda_0$ (nm)	$\Delta\lambda$ (pm)	$\delta\lambda$ (pm)
Initial fabrication	1459.6	11.9	2.2
Triple Piranha/HF	1442.0	7.2	1.1
Piranha/HF/Piranha	1426.6	8.6	5.1
HF dip	1423.3	9.7	1.2

Table 5.3: Summary of successive steps for a Piranha oxidation surface treatment

Step	Composition <sup>3</sup>	Temp.	Time
Piranha	3:1 H <sub>2</sub> SO <sub>4</sub> /H <sub>2</sub> O <sub>2</sub>	100°C	10 min
Rinse	DI H <sub>2</sub> O	23°C	30 sec
Rinse	DI H <sub>2</sub> O	23°C	30 sec
Rinse	DI H <sub>2</sub> O	23°C	30 sec
HF dip	10:1 H <sub>2</sub> O/HF	23°C	1 min
Rinse	DI H <sub>2</sub> O	23°C	15 sec
Rinse	DI H <sub>2</sub> O	23°C	15 sec

deleterious effects because long submersion etches may increase the amount of adventitious organic matter found on the liquid’s free surface [93]. In order to remove surface damage and recover quality factors consistent with our previous thick SOI fabrication [32], a series of chemical oxidation treatments was then performed on the devices. The well-known process [57,87,92] of repeated chemical oxidation in Piranha (H<sub>2</sub>SO<sub>4</sub>/H<sub>2</sub>O<sub>2</sub>) and HF oxide stripping was employed to controllably etch the top and bottom surfaces. We found that repeated cycles of the recipe shown in Table 5.3 were effective at improving the optical surface quality. Teflon tweezers and beakers were used exclusively for all reagent steps, and 18.2 M $\Omega$  DI water rinses were conducted in glass beakers. All tweezers and beakers were cleaned extensively with Piranha prior to chemical oxidation treatments. The final water dips were confirmed to not affect device performance but were included to ensure HF residue removal before further chemical treatment experiments [97].

After the third Piranha/HF cycle, the sample was immediately returned to the nitrogen-purged testing enclosure. From an analysis similar to that described in Section 5.4.2, the TM<sub>1,m</sub> spectrum was observed to have red shifted by an average of  $16.6 \pm 1.0$  nm. Finite-element simulations show that TM<sub>1,m</sub> modes blue shift by 8.7 nm per nanometer of Si removed, implying that  $1.9 \pm 0.1$  nm of Si was removed from the 3 $\times$  cyclic etch. Further testing indicated that each Piranha/HF cycles removes 0.7–1.2 nm of Si on average. Figure 5.13(b) shows the high-resolution scan of the

TM<sub>1,31</sub> mode (at 1442.0 nm) after the triple Piranha/HF treatment. The fit to the wavelength scan indicated that a significant improvement to the surfaces took place, yielding a  $\Delta\lambda = 7.2$  pm and  $\delta\lambda = 1.1$  pm.

To separate the effects of the Piranha oxidation and the HF etch, a set of further chemical treatments was performed on the same sample. The first follow-up experiment, labelled Piranha/HF/Piranha, was a double Piranha/HF treatment but stopping immediately before the HF dip in Table 5.2. It was hypothesized that the first cycle of Piranha/HF would “refresh” the hydrogen passivation before re-oxidizing the surface with the hot Piranha. On average the TM<sub>1,m</sub> spectrum shifted by  $15.3 \pm 0.3$  nm to the blue. Figure 5.13(c) shows the plot of the resulting transmission spectrum of the same TM<sub>1,31</sub> mode (at 1426.6 nm); the fit to the now barely resolvable doublet yielded a  $\Delta\lambda = 8.6$  pm and  $\delta\lambda = 5.6$  pm. The five-fold increase in linewidth amid a negligible increase in doublet splitting was indicative of a significant activation of absorbing surface states. Figure 5.13(e-f) shows the statistical average of the other TM<sub>1,m</sub> modes, confirming the result.

After testing, the sample was once again removed from the testing chamber and put through the last HF dip omitted in the previously mentioned treatment. Similar measurements showed the TM<sub>1,m</sub> spectrum blue shifted by  $3.5 \pm 0.1$  nm. Finite-element simulations of the silicon microdisk with a thin stoichiometric SiO<sub>2</sub> film revealed that  $2.8 \pm 0.1$  nm of oxide had been present for a commensurate blue shift. Note that the chemical oxide was more likely silicon-rich with a larger index of refraction than that used in these simulations [95]; hence the thickness is quoted as an SiO<sub>2</sub> equivalent film thickness. The fit to the transmission spectrum of the TM<sub>1,31</sub> mode (at 1423.3 nm) in Figure 5.13(d) produced doublet fit parameters  $\Delta\lambda = 9.7$  pm and  $\delta\lambda = 1.2$  pm, consistent with the statistical analysis shown in Fig. 5.13(e-f) of similar modes. This final measurement showed that the damage to the surface caused by Piranha oxidation was reversible, an effect inconsistent with surface roughness reduction.

To investigate the possibility that other wet chemical oxidation treatments may have the same salubrious effects, the sample was subjected to a final chemical treatment. The final treatment consisted of the same 3× oxidation and stripping process as described in Table 5.2, but with an HCl based chemistry (8:1:2 H<sub>2</sub>O:HCl:H<sub>2</sub>O<sub>2</sub>,

heated to 60°C) instead of the H<sub>2</sub>SO<sub>4</sub> based chemistry. The results shown in Figure 5.13(e-f) revealed that the HCl oxidation was slightly less effective at passivating the silicon surface as compared to the Piranha oxidation. Such results are consistent with current understanding that HCl chemical oxidation proceeds via island formation [94,98]; however, it is expected that the optimum solution for chemical oxidation should depend on the crystal orientation and previous chemical treatments [96].

In order to further study the nature of the Piranha/HF passivated surface, a follow-up study was conducted on both 5 and 10  $\mu\text{m}$  radii disks. The 5  $\mu\text{m}$  radii disks confirmed the previous sample's behavior, more than doubling the quality factor ( $Q = (1.4 \pm 0.02) \times 10^6$  for the best mode) after a 3 $\times$  Piranha/HF treatment. Being farther from reaching the radiation limit, the 10  $\mu\text{m}$  radii disks were able to be subjected to a 6 $\times$  Piranha/HF treatment where the lowest loss modes were measured to have  $Q = (2.1 \pm 0.2) \times 10^6$ . Finite element simulations showed that when compared to 5  $\mu\text{m}$  radii disks, 10  $\mu\text{m}$  radii disk have approximately the same fractional energy overlap with the top/bottom surfaces ( $\Gamma'_{\text{top}} = \Gamma'_{\text{bot}} = 3.7 \times 10^{-3} \text{ nm}^{-1}$ ) but have roughly half the fractional energy overlap with the etched sidewalls ( $\Gamma'_{\text{side}} = 3.8 \times 10^{-5} \text{ nm}^{-1}$ ). The lack of complete correlation between optical loss and  $\Gamma'_{\text{side}}$  as radius was varied [32] providing a further indication that the top/bottom surfaces remained to play a large role in device performance.

Although it has recently been observed [57] that repeated chemical oxidation and removal of silicon can provide a smoothing action on etched sidewalls, the large shifts in optical loss with chemical treatment described above can be linked to surface-state absorption as opposed to surface scattering. Whereas the highly confined Si waveguide measurements to date have been sensitive to changes in loss as low as 1 dB/cm, the microdisks of this work are sensitive to changes of loss more than an order of magnitude smaller ( $< 0.03 \text{ dB/cm}$ ) where surface chemistry is more likely to play a role. Indeed, as mentioned above, the TM-polarized microdisk WGMs are selectively sensitive to the top and bottom Si surfaces, which are extremely smooth in comparison to etched surfaces. The negligible change in average mode-splitting,  $\Delta\lambda$ , with chemical treatment (Figure 5.13(e)) is also indicative of little change in surface roughness. A complementary analysis in Section 5.5 of power-dependent transmission

scans showed that  $\sim 50\%$  of residual optical loss, after Piranha/HF treatment and hydrogen surface passivation, is still due to surface-state absorption (bulk absorption is negligible at this level).

Because the amount of optical loss could be reversibly spoiled by leaving the Piranha oxide on the surface, it became possible to measure the absorption coefficient of the thin Piranha oxide layer alone. The intrinsic optical loss, quantified by a modal quality factor  $Q_i$ , in these structures can be separated into four loss channels according to

$$1/Q_i = 1/Q_r + 1/Q_{ss} + 1/Q_{sa} + 1/Q_b, \quad (5.32)$$

where  $Q_r$ ,  $Q_{ss}$ ,  $Q_{sa}$ ,  $Q_b$  are inversely proportional to optical loss due to radiation, surface scattering, surface absorption, and absorption in the bulk Si, respectively [32]. As neither the bulk, radiation, nor surface scattering was expected to change significantly due to such short chemical processes, Eq. (5.32) can be written for both HF and Piranha oxide surfaces and subtracted from each other to obtain  $1/Q_{sa}^{\text{ox}} = (1/Q_i^{\text{ox}} - 1/Q_i^{\text{HF}}) + 1/Q_{sa}^{\text{HF}}$ . Inserting measured quality factors,  $Q_{sa}^{\text{ox}}$  can be bound to  $2.8 \times 10^5 < Q_{sa}^{\text{ox}} < 3.6 \times 10^5$ . The fraction of energy inside the Piranha oxide,  $\Gamma^{\text{ox}}$ , was found to be 0.008 from finite-element simulations, again assuming stoichiometric  $\text{SiO}_2$ . This meant that the Piranha oxide had approximately a material quality factor of  $Q_{mat}^{\text{ox}} = Q_{sa}^{\text{ox}}/\Gamma^{\text{ox}} = 2,800$ , and corresponding loss per unit length of  $\alpha_{mat}^{\text{ox}} > 98$  dB/cm.

By comparing the cavity  $Q$  before and after the Piranha oxide removal, a fractional surface absorption loss per pass of  $\alpha'_{s,ox} \sim 1 \times 10^{-5}$  is estimated for the Piranha oxide. This large fractional absorption in the  $\lambda = 1400$  nm wavelength band ( $\hbar\omega \sim 0.85$  eV) is attributed to single-photon absorption by mid-gap interface states. Such electronic interface states at the Si/(Piranha)SiO<sub>x</sub> interface have been observed in Ref. [99], with three sets of state-density maxima in the bandgap of silicon occurring at 0.3, 0.5, and 0.7 eV referenced to the valence-band maximum, with a Fermi energy of  $\sim 0.4$  eV. Thus, our observed surface absorption is most likely dominated by the transition from the filled 0.3 eV surface-state band to the conduction band at 1.1

eV. In comparison, the modal absorption loss of the hydrogen-passivated Si surface was measured (see Section 5.5) to be as small as  $\alpha_m^H \sim 0.08 \text{ cm}^{-1}$ , corresponding to a fractional surface absorption loss per pass of  $\alpha'_{s,H} \sim 1 \times 10^{-6}$  for the top (bottom) Si active layer surface. These measurements are consistent with those in reference [87] where Linnros noted that Piranha oxide was of poor electronic quality and resulted in very low free-carrier lifetimes as compared to an HF treated surface.

Figure 5.16(b) shows a plot of the wavelength-dependent loss across the full 1420 – 1500 nm span for the  $\text{TM}_{1,m}$  family of modes from a 10  $\mu\text{m}$  radius disk. The black line indicates the intrinsic linewidth for each  $m$  number, with an error bar of  $\pm 0.01$  pm per point (not shown). The delineation between scattering loss and linear absorption was found with a modified version of the power-dependent measurements described in the next section. As the amount of power dropped into the resonator is increased, the added optical absorption raises the local temperature of the silicon microdisk. The change in temperature causes thermally induced shifts in the resonance wavelengths [83,85,100,101]. The inset to Fig. 5.16(b) shows three examples of the power-dependent transmission scans for the 1447.5 nm mode (grey arrow), along with corresponding transmission minima versus wavelength (black dots). The novel aspect of this analysis was that the fraction of absorbed energy was calculated without the need of a thermodynamic model for heat flow. Rather, the onset of two-photon absorption changed the fraction of absorption as a function of power, allowing the linear absorption coefficient to be ascertained directly. Measurements of the radiation limited quality factors for the  $\text{TM}_{1,m}$  family in the 1565 – 1625 nm wavelength range ruled out a radiation component to the optical loss in the 1420 – 1500 nm range. In addition, finite-element simulations showed that  $\Gamma'$  on all of the surfaces changed less than 5% over the same 1420 – 1500 nm span, and the same wavelength-dependent loss was observed across the different devices, including the 5  $\mu\text{m}$  radii disks. Thus, the increase in optical loss at the longer wavelengths was consistent with spectral dependence to the surface layer's complex index of refraction.

#### 5.4.4 Conclusion

All of the measurements described above were performed in an  $N_2$  purged environment over several weeks. Even in such an environment, however, changes in the hydrogen passivated surfaces were observed over times as short as a few days. Left in an unprotected air environment, degradation of the optical surface quality was evident in a matter of hours. Research and development of stable surface passivation techniques optimized for optical quality, akin to the gate oxides of CMOS microelectronics, will be a key ingredient in the future development of Si photonics. Our data suggests that surface chemistry as much as surface roughness will ultimately limit the performance of Si microphotonic devices. As a result, further development of Si passivation techniques should be able to reduce optical losses by as much as an order of magnitude (towards the bulk *c*-Si limit) while improving the stability and manufacturability of future Si photonic components.

## 5.5 Accurately Measuring Absorption in Semiconductor Microresonators

The push for dense integration of photonic elements into existing microelectronics circuits has recently revitalized the interest in semiconductor microresonators [12, 16, 17, 24, 102, 103]. Unfortunately, the benefits of tight optical confinement provided by these high-index-contrast photonic elements have oftentimes been offset by the high-modal overlap with the roughened surfaces. As advances in lithographic etching of these structures continues to reduce the geometrical nonidealities, surface absorption has become an equally dominant source of loss [32, 34]. As a result, many recent articles [32, 34, 83, 101, 104] have detailed methods for backing out the fraction of optical loss due to absorption. Here we present an elegant method achieving the same goal without resorting to complex thermal models or wavelength-dependent absorption fits. Rather, simply by monitoring the resonance wavelength and transmission depth as a function of input power, the amount of non-linear absorption can be directly ascertained. Then, the fraction of loss due to linear absorption is accurately inferred by comparing the regime of linear absorption to non-linear absorption. While this implementation is based upon varying two-photon absorption (TPA) in very high- $Q$  silicon-on-insulator (SOI) microdisks, the method is general enough for any optical resonator exhibiting both a thermal-bistability effect [105] and well-understood, power-dependent absorption.

The Si microdisks were fabricated from an SOI wafer as described in Ref. [32] and a discussion of the various surface chemistries explored can be found in Ref. [34]. The microdisk resonators presented here were subjected to repeated Piranha oxidations ( $\text{H}_2\text{SO}_4:\text{H}_2\text{O}_2$ ) and hydrofluoric acid dips in order to remove surface damage and prepare a hydrogen-passivated surface. The samples were characterized using a tunable external-cavity laser ( $\lambda = 1420\text{-}1498$  nm, linewidth  $< 5$  MHz) connected to a computer-controlled fiber taper waveguide probe [28] and two optical attenuators as in Fig. 5.14(a). The micron-scale fiber taper probe was formed from a standard single-mode optical fiber and was used to evanescently excite the whispering-gallery modes (WGMs) of the microdisk with controllable loading. The optical attenua-

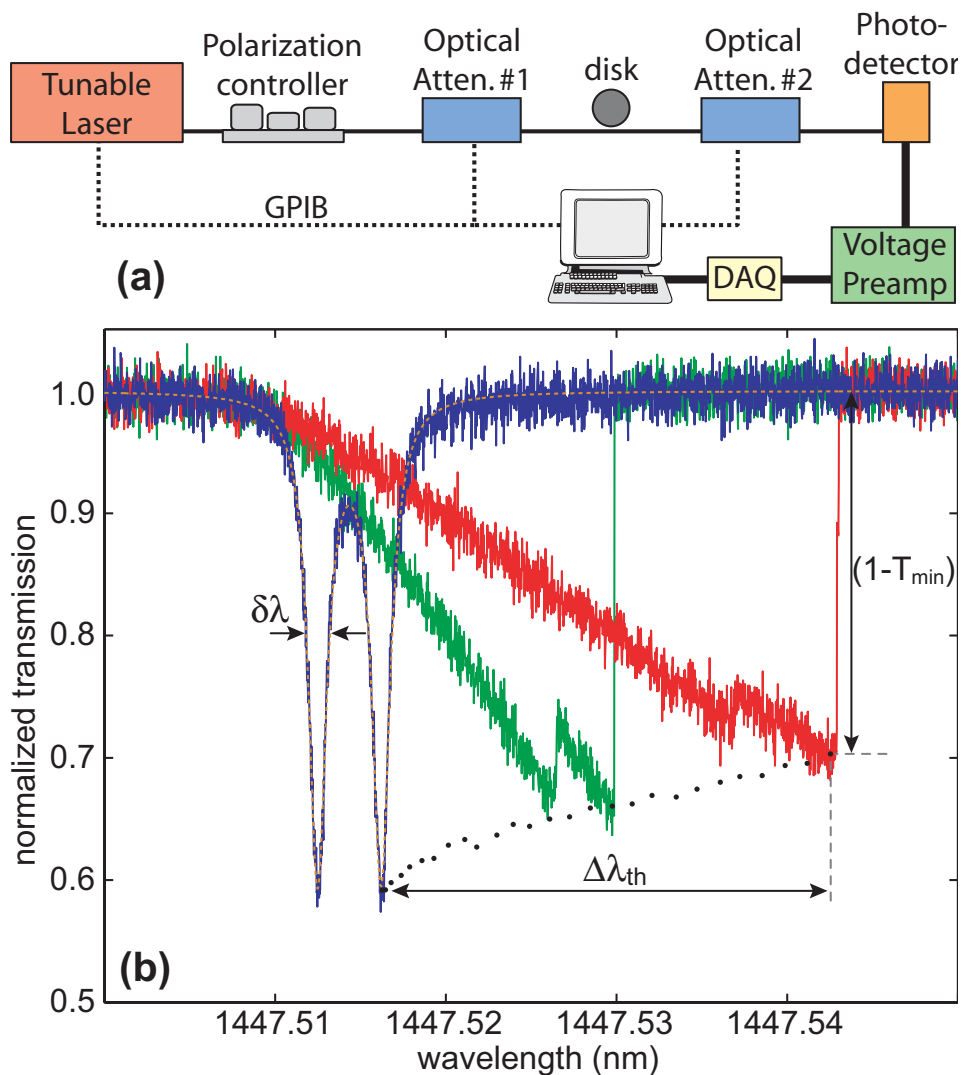


Figure 5.14: (a) Schematic representation of testing apparatus. (b) Examples of power-dependent transmission versus wavelength data used to separate the absorption from the total loss using the thermal bistability effect.

tors were GPIB controlled to provide variable optical power to the resonators while maintaining constant noise characteristics of the detection system.

Figure 5.14(b) shows the normalized spectral transmission response of a  $10\ \mu\text{m}$  radius microdisk for several different input powers. The observed doublet resonance dip (most discernible in the low-power blue curve) is a result of surface roughness coupling of the normally degenerate clockwise (CW) and counter-clockwise (CCW) propagating WGMs [32,63,81]. A simple model [32,67] can be used to find the familiar Lorentzian lineshaped amplitudes for the decoupled standing wave modes  $a_c$  and  $a_s$

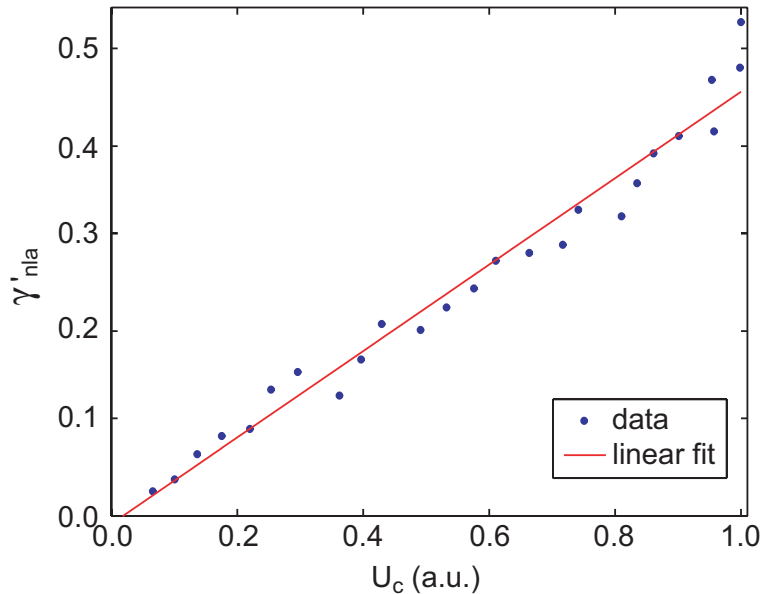


Figure 5.15: Plot of normalized nonlinear absorption versus relative electric-field cavity energy along with a linear fit.

according to

$$a_{c,s} = \frac{-\sqrt{\gamma_e/2}}{-(\gamma_t/2) + i(\Delta\omega \pm \gamma_\beta/2)}, \quad (5.33)$$

where  $\Delta\omega$  is the detuning frequency from the initially degenerate mode frequency  $\omega_0$ ,  $\gamma_t$  is the total decay rate of each individual resonance,  $\gamma_e$  is the total loss rate back into the waveguide, and  $\gamma_\beta$  is the rate of CW to CCW mode coupling. The fraction of optical power that passes the resonator can be found by taking the coherent sum of the Lorentzian responses according to

$$T = |-1 + \sqrt{\gamma_e/2}(a_c + a_s)|^2. \quad (5.34)$$

Note that in this definition,  $a_c$  and  $a_s$  are normalized to maximum cavity energy used in the experiment and are defined by  $U_c = |a_c|^2 + |a_s|^2$ . The resulting fit (orange dashed curve in Fig. 5.14(b)) to the low power data (blue curve) is used to calculate the resonator's total linear loss ( $Q_t \equiv \omega_0/\gamma_t \equiv \lambda_0/\delta\lambda = 1.5 \times 10^6$ ), doublet splitting, and strength of coupling.

The amount of absorbed power ( $P_{\text{abs}}$ ) in a microphotonic resonator can be related to the total rate of energy loss ( $P_{\text{loss}}$ ) via the relationship  $P_{\text{abs}} = (\gamma_a/\gamma_t)P_{\text{loss}}$ , where

$\gamma_a$  is the rate of optical absorption. For a steady-state and lossless coupler, the total power loss will be equal to the power dropped into the cavity given by  $P_d = (1 - T_{\min})P_i$ , where  $T_{\min}$  is the transmission minimum and  $P_i$  is the power inside the bus waveguide just before the coupling region. While the fractional input power change is easily controllable with highly linear optical attenuators, absolute measurements of  $P_i$  are challenging because of the uncertainties in bus waveguide losses. In principle,  $P_{\text{abs}}$  can be related to the power-dependent resonance wavelength shift ( $\Delta\lambda_{th}$ ) utilizing a thermal model and the thermo-optic effect as described in, for example, Refs. [32, 83, 101]. This implies that up to a single proportionality constant ( $C$ ),  $\gamma_a$  could be inferred from the directly measurable relationship  $\Delta\lambda_{th} = C(\gamma_a/\gamma_t)P_d$ , where  $P_d$  has been arbitrarily normalized to the maximum off-resonance input power.

In practice, the compounded uncertainties in thermal resistances, thermo-optic coefficients, and input powers make an accurate determination of  $C$  difficult; however, by controllably changing the fraction of absorption to total loss, the proportionality constant would become an indirectly measurable quantity. For many semiconductor microresonators, nonlinear absorption can be easily inferred by studying the power-dependent change in transmission depth and can be observed in very high- $Q$  resonators at all but the smallest input powers. As shown by the high-power scans in Fig. 5.14(b), the nonlinear absorption can be inferred from the change in transmission depth ( $T_{\min}$ ) using Eqs. (5.33) and (5.34), assuming  $\gamma_e$  and  $\gamma_\beta$  are constant as a function of power. The total loss coefficient can be separated into a cold-cavity loss rate and nonlinear absorption by  $\gamma_t = \gamma_c + \gamma_{nla}$ . Similarly, the absorption coefficient can be separated into linear absorption and nonlinear absorption according to  $\gamma_a = \gamma_{la} + \gamma_{nla}$ . Figure 5.15 shows the measured normalized nonlinear absorption ( $\gamma'_{nla} \equiv \gamma_{nla}/\gamma_c$ ) as a function of cavity energy ( $U_c$ ). The linear dependence of  $\gamma'_{nla}$  versus  $U_c$  indicates that red-shifting two-photon absorption is dominant for these input powers, averting the complication of blue-shifting free-carrier dispersion [16, 83]. Thus the absorbed power is linearly proportional to the thermal resonance shift ( $\Delta\lambda_{th}$ ), so that the linear absorption can be unambiguously calculated using the relationship

$$\Delta\lambda_{th} = C \left[ \frac{\gamma'_{la} + \gamma'_{nla}(P_d)}{1 + \gamma'_{nla}(P_d)} \right] P_d. \quad (5.35)$$

where the losses are normalized by  $\gamma_c$  and  $C$  is a fit proportionality constant.

Figure 5.16(a) shows the measured resonance shift from Fig. 5.14(b) versus  $P_d$  along with the Eq. (5.35) fit and a linear fit to the lowest power data as a visual aid. The inset also plots the global slope,  $\Delta\lambda_{th}/P_d$ , versus  $P_d$  for the same dataset. Note that while this method does not need to have knowledge of absolute powers, maximum input powers for these experiments were  $\sim 100 \mu\text{W}$ , corresponding to absolute cavity energies of  $\sim 30 \text{ fJ}$ . This analysis revealed that  $\gamma'_{la} = 0.57 \pm 0.03$  indicating that linear absorption accounts for more than half the optical loss in these devices. This separation of linear absorption from total loss is plotted in Fig. 5.16(b) at the grey arrow along with similar measurements on the neighboring WGMs of the same radial order and polarization. From the figure, we see that linear absorption persists at a nearly constant level across the wavelength range, providing crucial knowledge as we continue to develop surface passivation techniques for very high- $Q$  silicon microresonators. More generally, this measurement technique should be able to provide similar insights into the nature of other semiconductor microresonator loss mechanisms utilizing its straightforward measurement of *nonlinear* absorption to accurately determine *linear* absorption with only limited knowledge of absolute power, material parameters, and physical geometry of the structure.

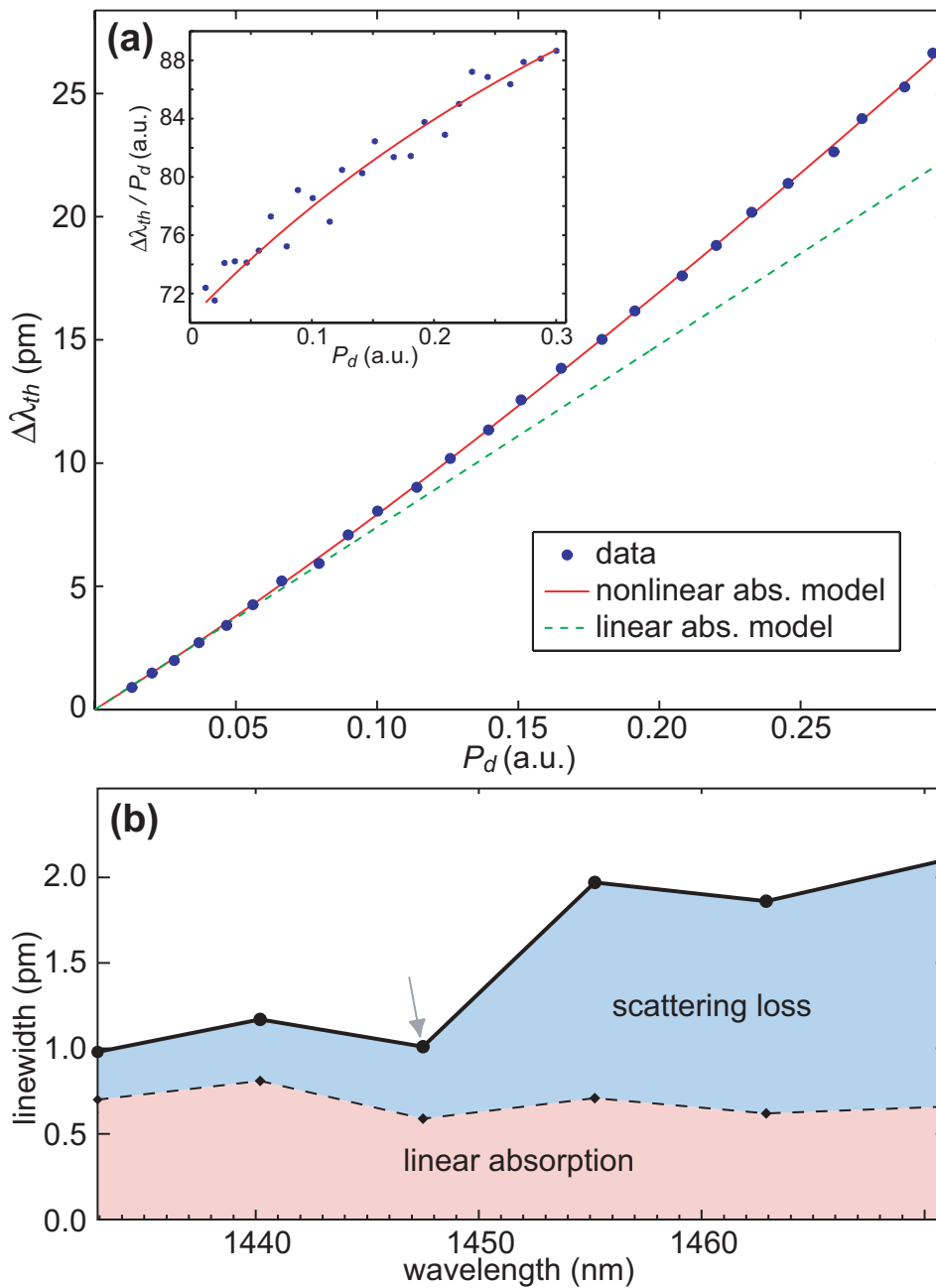


Figure 5.16: (a) Plot of thermally-induced wavelength shift ( $\Delta\lambda_{th}$ ) versus relative dropped power ( $P_d$ ) along with nonlinear and linear absorption model fits. (inset) Global slope,  $\Delta\lambda_{th}/P_d$ , versus  $P_d$  for the same dataset. (b) Wavelength dependent intrinsic linewidth for a family of high- $Q$  WGMs, along with the measured delineation between scattering loss and linear absorption. Note that the fit shown in (a) was used to generate the data point at 1447.5 nm in (b).

## 5.6 Surface Encapsulation Layers

The successful reduction in optical losses with wet chemistries of the previous section was in excellent agreement with the wealth of previous research done on the electronic properties of silicon surfaces [86, 87, 90–99, 106, 107]. Continuing to use the effective free-carrier lifetime as an indirect measure of surface absorption, a “passivation layer” that provided the highest effective lifetimes was sought in order to protect the fragile Si interface. Silicon photovoltaics fabrication [108–111] routinely calls for various passivation layers to be deposited over the silicon surfaces in order to preserve the lifetime of the free-carriers, as well as to form an anti-reflection coating over the solar cell. Several of the latest in solar cell technologies for passivation of the Si interface states were employed to optically passivate and protect the microdisk’s top surfaces. It was found that a short thermal oxidation followed by a long high-temperature N<sub>2</sub> anneal was most effective at preserving the high-quality factors, indicating that the Si/SiO<sub>2</sub> interface provides adequate dangling bond passivation even without the presence of hydrogen. This finding suggests that while effective at protecting the interface states, more research is needed in order to understand the underlying mechanisms of optical loss at dielectric interfaces with silicon. This section will compare the previously successful electronic passivation layers with our empirical study of those same layers in the optical domain.

Schmidt *et al.* [110] found that PECVD SiN<sub>x</sub> passivation layers with or without an underlying thin thermal oxide layer achieved effective free-carrier lifetimes of ~ 1 ms, comparable to the best passivation schemes to date. The optimized PECVD recipe for SiN<sub>x</sub> layers was found to result in nearly stoichiometric Si<sub>3</sub>N<sub>4</sub> films and was generated through a direct parallel-plate reactor system. Furthermore, they found that the effective lifetime increased further for the first 50 min of a 400°C anneal in forming gas (5% H<sub>2</sub>, 95% N<sub>2</sub>) before eventually decaying with increased forming gas annealing (FGA). As the effect of ambient hydrogen was found to be negligible, they attributed the increase of lifetime to the large reservoir of hydrogen in the silicon nitride (~ 15–20 at.%) being released during the deposition and anneal. The effective passivation was also found to benefit from an initial thermal oxide, providing a higher

quality Si interface, before the  $\text{SiN}_x$  deposition and concomitant diffusion of hydrogen through the  $\text{SiO}_2$  to the silicon surface. In a more recent study, McCann *et al.* [111] found that a 25 nm thick thermal oxide grown at  $900^\circ\text{C}$  followed by a 30 min FGA at  $400^\circ\text{C}$  was sufficient to obtain equally high effective lifetimes. In addition, they found that the lifetimes could be spoiled by a 1 hr high-temperature  $900\text{--}1000^\circ\text{C}$   $\text{N}_2$  anneal and subsequently repaired by another FGA. They attributed this effect to reversibly adding or subtracting hydrogen from the Si/ $\text{SiO}_2$  interface.

We hypothesized that the effective lifetime measurements from the previous references would be good indicators of optical loss at the Si interface. Both PECVD  $\text{SiN}_x$  and thermal oxide (TOX) layers were tried as encapsulation layers for silicon microdisks. All of the samples for these trials were fabricated from the same SOI wafer as in Section 5.4, and with a similar method of device layer lithography and device layer etching, consisting of 5, 7.5, and 10  $\mu\text{m}$  radii microdisks. However, these samples did not undergo isolation as described in Section 3.5. Rather, the devices were tested using a dimpled taper probe wherein a small downward  $\sim 70 \mu\text{m}$  radius bend is annealed into a tensionable fiber taper probe (see Chapter 4). All oxidations and anneals were done in a custom built quartz tube oxidation furnace. Electronic grade II  $\text{O}_2$ ,  $\text{N}_2$ , and forming gases were plumbed into the 2 inch diameter furnace. Each gas's flow rate was independently controlled with mass flow controllers. Typical flow rates inside the approximately 3 foot long quartz furnace were 0.3 standard liters per minute. Thermal shock to the samples was avoided by using the unheated portion of the furnace tube as a second and intermediate staging area where the samples were allowed to slowly warm-up and cool-down before transfer to the heated portion of the chamber or being removed from the furnace.

### 5.6.1 Silicon Nitride Cap

The first encapsulation trial was done on a sample that had an initial 50 nm  $\text{SiN}_x$  cap deposited on the surface prior to lithography and etching. After removing the ZEP resist with an hour-long Piranha, the sample was tested with a  $\sim 1.5 \mu\text{m}$  diameter dimpled fiber taper probe in the  $\text{N}_2$  purged testing chamber of Chapter 4. Figure 5.17 shows a bar graph summary of the best linewidths at selected intermediate

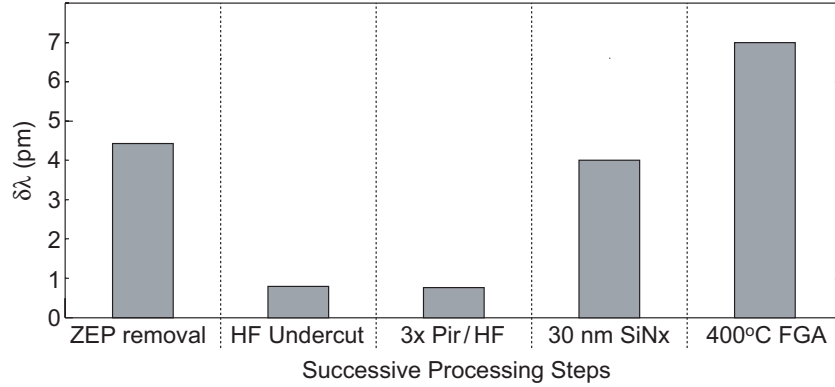


Figure 5.17: Summary of best linewidths after selected processing steps for 5 – 10  $\mu\text{m}$  radii disks fabricated with a stoichiometric  $\text{SiN}_x$  encapsulation layer and forming gas anneal.

points during the fabrication. Having tested many devices on the sample, the best linewidth after the initial Piranha clean was  $\delta\lambda = 4.5$  pm. However, after an hour-long HF undercut, the linewidths reduced considerably to 0.8 pm. Further wet chemical treatment described in Table 5.3 had no discernible effect on the linewidths.

At this point, a nearly stoichiometric 30 nm thick  $\text{SiN}_x$  encapsulation was deposited over the wafer. Immediately prior to loading the wafer into the PECVD chamber, an additional 3 $\times$  Piranha/HF treatment was done on the sample to ensure an exquisitely clean and well-passivated silicon surface. The processing conditions were adapted from Ref. [110], so a gas chemistry of 450 sccm of 5%  $\text{SiH}_4/\text{N}_2$  and 50 sccm of  $\text{NH}_3$  was applied to the chamber held at 200 mTorr and 400°C. The gas was cracked with 60 W of the high frequency (13.56 MHz) source. Contrary to the stress-free  $\text{SiN}_x$  recipe in Section 3.3, no low frequency source was used in an attempt to suppress deposition damage by ion’s oscillating below the  $\sim 4$  MHz plasma frequency. In contradiction to the photoconductance decay measurements of free-carrier lifetimes on silicon solar cells [110], the losses of the cavities significantly increased to 4 pm, a difference of 3.2 pm. After testing with the “as-deposited” silicon nitride cap, the sample underwent a 40 min FGA at 400°C. Subsequent testing revealed that the FGA had further deleterious effects on the samples, where the best linewidth was found to be 7 pm, shown in Figure 5.17.

Assuming a  $\text{SiN}_x$  index of refraction of 1.9, FEM simulations of the composite resonator show that TM modes possessed 11% of the optical energy inside the  $\text{SiN}_x$ .

Thus, if the sources of loss were evenly distributed throughout the  $\text{SiN}_x$ , the material quality factor of the as-deposited material would be  $Q_{\text{SiN}_x,\text{mat}} = \Gamma_{\text{SiN}_x} \lambda_0 / (\delta\lambda_{\text{after}} - \delta\lambda_{\text{before}}) \approx 5.0 \times 10^4$ , or an attenuation coefficient of  $\alpha_{\text{SiN}_x,\text{mat}} = \beta_g / Q_{\text{SiN}_x,\text{mat}} \approx 7.1$  dB/cm. PECVD deposited material is known to have relatively high absorption coefficients (1 – 10 dB/cm) due to Si-H, O-H, N-H bond absorption overtones in the telecommunications wavelength bands. Furthermore, as the FGA anneal would not be expected to harm the Si surfaces, a consistent interpretation of the results shown in Fig. 5.17 is that any benefits of a hydrogenated silicon surface were overwhelmed by the increased hydrogen content in the bulk  $\text{SiN}_x$  layer. However, pure PECVD Si-rich nitride disks were independently fabricated and tested achieving quality factors  $\sim 2 \times 10^5$ . Thus it is likely that the PECVD process damaged the high-index silicon surface during the deposition, which would account for the unaccounted for loss.

### 5.6.2 Thermal Oxide Cap

A second sample underwent identical processing as the sample just described, including the deposition of a silicon nitride cap, lithography, dry-etching, ZEP removal, and  $3\times$  Piranha/HF treatment. As expected, the best measured linewidth of 0.7 pm was very similar to the previous sample and is shown in Fig. 5.18. However, this time a 10 nm TOX layer was grown on the Si surface at  $1000^\circ\text{C}$  for 3.1 minutes in an attempt to form a good Si interface with a hydrogen free material. After switching off the  $\text{O}_2$ , the sample was allowed to cool slowly under an  $\text{N}_2$  ambient for approximately 5 minutes before retesting. The best linewidth after thermal oxidation was 3.5 pm, a result similar to the silicon nitride cap. However, the same 40 min FGA had virtually no impact on the sample with the thermal oxide cap. A 4.5 hr high-temperature anneal in an  $\text{N}_2$  ambient was found to significantly improve the losses, where the best linewidth was measured to be 1.6 pm. The high-temperature anneal consisted of holding the furnace at  $1000^\circ\text{C}$  for 3 hours and then letting the temperature slowly ramp down to  $400^\circ\text{C}$  over the course of the remaining 1.5 hours. Assuming that the high-temperature anneal successfully healed the Si interface and bulk TOX, a 40 min FGA was conducted on the sample. The FGA was found to slightly reduce the quality factor of the best resonance, where the linewidth was measured to be 1.8 pm.

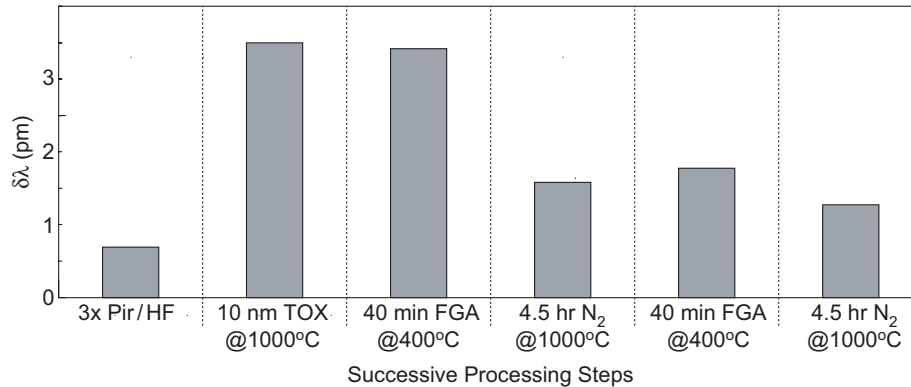


Figure 5.18: Summary of best linewidths after selected processing steps for 5 – 10  $\mu\text{m}$  radii disks fabricated with a thermal oxide encapsulation layer along with various annealing trials.

A second 4.5 hr high-temperature anneal drove out the hydrogen from the sample, resulting in a  $\delta\lambda = 1.2$  pm on the best resonance. This set of four anneals showed that the thermal oxide needed time at high temperature to remove material and surface defects. Also, the FGA had a marginally degrading effect on the optical losses.

A third sample was similarly fabricated but did not have an initial silicon nitride cap prior to lithography and dry-etching. After HF undercutting and 3 $\times$  Piranha/HF treatments, the best linewidths were measured to be 1.0 and 0.6 pm, respectively (shown in Fig. 5.19(a)). The marginal improvement in this case was attributed to a simplified single material dry-etch and a less damaged top Si surface. The latter was confirmed after an identical 10 nm TOX cap with 5 minute cool-down showed a best linewidth of 2.0 pm, much better than the second sample's 3.5 pm linewidth after oxidation. Omitting any FGA step, a final 4.5 hour high-temperature anneal completely healed the Si-interface and bulk silica cap, showing identical linewidths prior to oxidation. Figure 5.19(b) shows a high-resolution transmission spectrum of the 1444.2 nm resonance on a 7.5  $\mu\text{m}$  radius disk after the final high-temperature anneal, along with a doublet model fit. As described in Section 6.3.5, totally oxidized and annealed microdisks had  $Q > 3 \times 10^6$ . As these disks were most likely surface-scattering limited due to their design, quality factors this high indicate that the encapsulating oxide is of extreme quality after high-temperature anneals. Further described in Section 6.3.5, thermal oxide encapsulated and non-undercut microrings were observed to have quality factors  $\sim 5 \times 10^6$ .

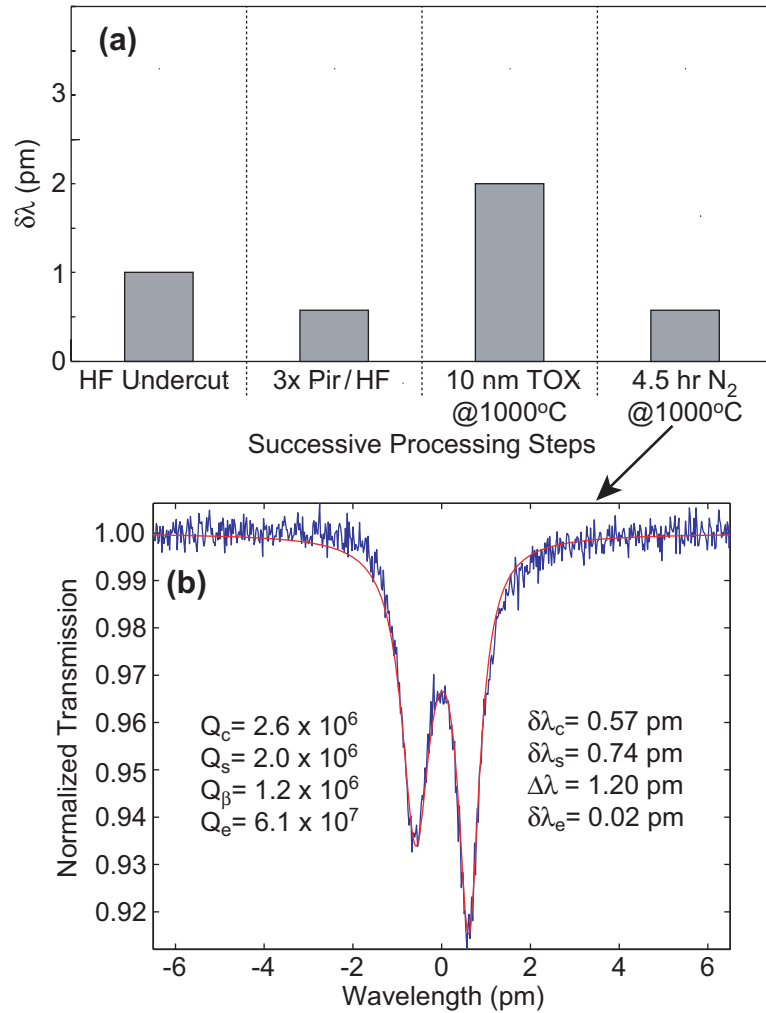


Figure 5.19: (a) Summary of best linewidths after selected processing steps for 5 – 10  $\mu\text{m}$  radii disks fabricated without an initial protective cap. This sample also had a thermal oxide encapsulation layer but no FGA. (b) High-resolution transmission spectrum of 1444.2 nm resonance on a 7.5  $\mu\text{m}$  radius disk after the final high-temperature anneal.

### 5.6.3 Conclusion

The results shown in the previous figure represent the successful encapsulation of the once delicate Si-surfaces, as 10 nm of thermal oxide will completely prevent native or chemical oxide growth during any subsequent fabrication steps. While silicon nitride would have been slightly preferable in terms of chemical resistance, the high-quality thermal oxide is a simple and effective method of sealing the disks from environmental contamination while still allowing optical access to the mode's near-field. Having also demonstrated this technology on a planar resonator represents a significant milestone in ultra-low-loss silicon photonics technology. Any number of functionalized materials can now be placed as claddings over the resonators, allowing for the technologically viable development of biological/chemical sensors, microlasers, and highly nonlinear devices integrated with electronic circuitry on a silicon chip.

## Chapter 6

# Silicon-Based Lasers

### 6.1 Introduction

Despite the recent successes in silicon microphotonics, a practical silicon-based laser remains an elusive goal. Commercial ventures, such as Xponent Photonics and Luxtera, require the use of flip-chip integration of III-V lasers on top of silica or silicon photonic circuits to provide coherent light sources. These companies have made significant progress in reducing the costs associated with this technology, and they have begun to create real markets for silicon-based photonics. However, this type of pick and place technology lacks the scalability to provide hundreds of laser sources for optical interconnect applications [6]. One common idea is to wafer bond a III-V material to the top surface of an SOI wafer. Hattori *et al.* [112] demonstrated the heterogeneous integration of an InP microdisk laser, an SOI strip waveguide, and an InP detector. The optically pumped  $2.5 \mu\text{m}$  radius InP microdisk exhibited good coupling efficiencies. Unfortunately, the large  $500 \mu\text{W}$  thresholds revealed that significant obstacles still exist for this type of technology. Silicon nanocrystals embedded in gate oxide have also been used to produce field-effect electroluminescence [113]. Unfortunately, quantum confinement always raises the radiative transition energies. Thus, all nanocrystals, quantum dots, etc., produced from silicon emit *above* the bandgap where bulk silicon becomes highly absorbing. However, nanopatterning of crystalline silicon was used to create  $1278 \text{ nm}$  stimulated emission just below silicon's bandgap [114]. In this work, it was hypothesized that a defect state, located  $0.17 \text{ eV}$  below the conduction band edge of silicon, allowed direct recombination be-

tween trapped electrons and free holes. Martin Green [108, 109], a pioneer in silicon photovoltaic technology, has also shown that relatively efficient ( $\sim 1\%$ ) one- and two-photon-assisted sub-bandgap emission from silicon is possible [115, 116]. The approximately hundred-fold improvement in electroluminescence efficiencies were made possible in large part by the surface passivation techniques developed for solar cells. Two more approaches to achieve silicon-based lasers are the Raman effect and rare-earth-doped glasses. This chapter will describe these two common technologies in detail as well as provide our experimental progress in regards to achieving silicon lasers. Raman based silicon lasers offer the appeal of an “all-silicon” material system, but suffer from an extremely large drawback: the useful gain bandwidth is less than a nanometer wide. This narrowband gain and the need for coherent excitation relegates the Raman laser to performing wavelength conversion. By contrast, the erbium-doped glasses presented in Section 6.3 have broadband gain and are routinely used for DWDM amplification applications. This material was deposited over high- $Q$  silicon-based microresonators to demonstrate highly efficient single-mode laser sources with sub- $\mu\text{W}$  thresholds.

## 6.2 Raman Effect

The Raman effect has been successfully utilized in silica fiber amplifiers and lasers for years, but it was not until recently that the Raman effect was effectively harnessed for optical microcavities. Spillane et al. created an ultralow-threshold Raman laser inside a silica microsphere [77]. In this work, single-mode Raman lasers were created and exhibited thresholds of  $86 \mu\text{W}$  and unidirectional slope efficiencies of 16%. Similar results were then repeated using microtoroids a year later [117]. Reference [118] describes a Raman silica microlaser on a silicon chip fabricated by the sol-gel process. The high- $Q$ 's in the spin-on glass material allowed for Raman oscillation with a threshold of  $640 \mu\text{W}$ .

The positive results in silica microcavities seemed to bode well for similar types of cavities using crystalline silicon. Additionally, the Raman gain coefficient is approximately  $10^4$  times higher in silicon than in silica [7]. However, the reduced bandgap

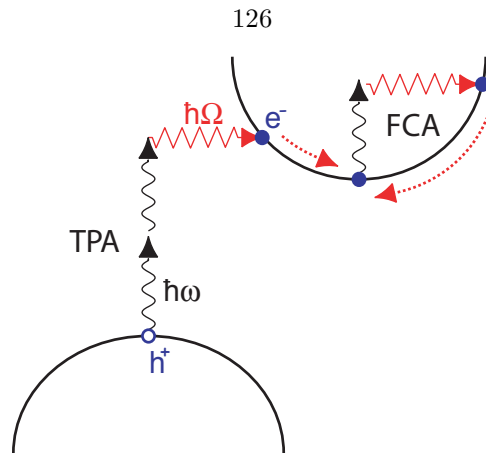


Figure 6.1: Schematic depiction of two-photon absorption (TPA) and the resulting free-carrier absorption (FCA).

of silicon creates a significant complication for efficient production of Stokes photons. At high pump intensities, two photon absorption (TPA) creates a large source of electron-hole pairs, as shown in Fig. 6.1. These electron-hole pairs, in turn, cause a large increase in free-carrier absorption (FCA). Ignoring pump depletion, the basic form of differential equations for the pump mode's intensity,  $I_p(z)$ , and Stokes mode's intensity,  $I_s(z)$ , is

$$\frac{dI_p}{dz} = - [\alpha_p + \alpha_p^{\text{FCA}}(z)] I_p - \beta I_p^2 \quad (6.1a)$$

$$\frac{dI_s}{dz} = - [\alpha_s + \alpha_s^{\text{FCA}}(z)] I_s + (g_R - 2\beta) I_p I_s, \quad (6.1b)$$

where  $\alpha_{p,s}$  and  $\alpha_{p,s}^{\text{FCA}}(z)$  are the linear and FCA loss rates for the waveguide.  $\beta$  is the TPA coefficient and is approximately given by 0.85 cm/GW for crystalline silicon.  $g_R$  is the Raman gain coefficient as is approximately 30 cm/GW for crystalline silicon. From the large disparity between  $g_R$  and  $\beta$ , the presence of TPA alone is of little direct consequence. The same cannot be said for FCA from the TPA generated free-carriers. The free-carrier density that is generated is given by  $\Delta N = \beta I_p^2 \tau_{\text{eff}} / (2\hbar\omega)$ , where  $\tau_{\text{eff}}$  is the effective free-carrier lifetime in the vicinity of the electric fields. Because  $\alpha^{\text{FCA}}$  is linearly proportional to free-carrier density [3,4],  $\alpha^{\text{FCA}}$  can dominate all linear and nonlinear effects at high enough pump powers.

The limitation from FCA induced by TPA was first overcome by Boyraz *et al.* [23]

at UCLA by sending in high-power pulses of pump light. Using pulses only  $\sim 30$  ps long, large free-carrier populations were not built up, resulting in the first silicon Raman laser. At nearly the same time researchers at Intel made all-silicon CW Raman lasers [24, 25] by actively sweeping the carriers out of the waveguide. Using a reverse-biased p-i-n diode fabricated on the same chip, output powers as high as 9 mW were generated with unidirectional slope efficiencies of 4.3%. Unfortunately, the pump powers for these devices remained in the hundreds of milliwatts, making them impractical for many photonic applications.

Due to the extremely large  $Q$  and small effective optical mode volume ( $V_{\text{eff}}$ ) of the Si microdisk resonators discussed, the onset of nonlinear effects appear for input powers as low as a few microwatts. Among the various nonlinear effects seen in these microdisks is resonant Raman scattering. When WGM resonances of a microdisks were separated by the silicon  $\Gamma$ -point optical phonon frequency of 15.57 THz [119], resonantly enhanced Raman scattering was observed (Fig. 6.2) for input power levels as small as 3  $\mu\text{W}$  (inset to Fig. 6.3(b)). While external conversion efficiencies were extremely poor, Fig. 6.2 shows clear Stokes emission 20dB above the noise floor. Figures 6.3(b) and (c) show resolution-bandwidth-limited scans on an optical spectrum analyzer (OSA) over the Raman gain region for a 15 and 5  $\mu\text{m}$  radius disk, respectively. From these figures, the resonant enhancement and off-resonant suppression of the Raman process are apparent. Unfortunately, the maximum bidirectional Stokes power collected in these microdisks was bounded below  $\sim 600$  pW. A subsequent analysis of the data revealed that an average of approximately 10 Stokes photons were maintained inside the silicon microdisk. This would indicate that photon statistics measurements would have shown a large phase transition from spontaneous to stimulated emission.

All the models suggested that the free-carrier absorption was not large enough to account for such poor Raman performance. It was not until an additional “threshold” was discovered in the data that we began to understand the limiting mechanism in the resonator. From power conservation arguments described in Section 4.5.1, any increase in dropped power into the resonator should be accompanied by an increase in reflected signal. However, the Raman data showed a sudden increase in

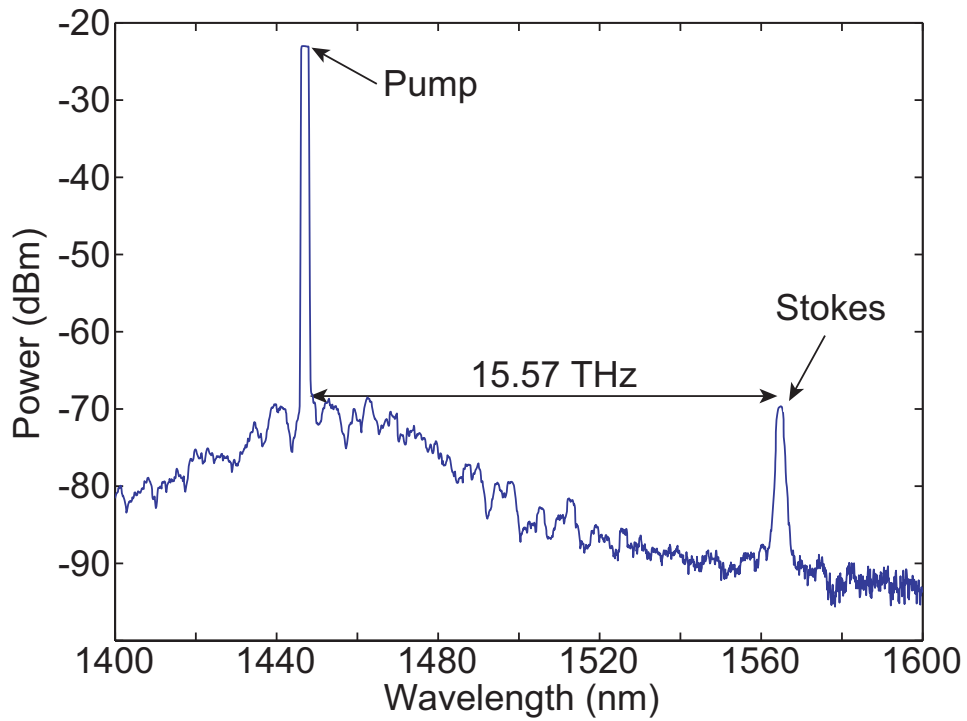


Figure 6.2: Broad OSA scan of reflected power from a  $R = 15 \mu\text{m}$  silicon microdisk showing reflected pump and stimulated Raman line.

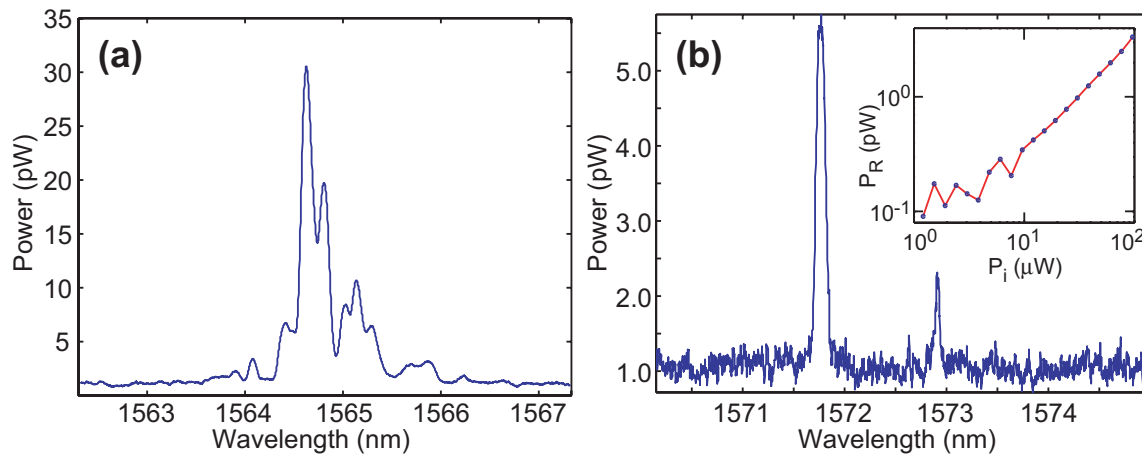


Figure 6.3: (a) Narrow OSA scan with resolution bandwidth of 0.08 nm of Raman emission showing resonantly enhanced behavior, (b) similar narrow scan of a  $R = 5 \mu\text{m}$  disk illustrating decrease in density of modes as compared to (a), (inset to (b)) Raman power,  $P_R$  versus input power,  $P_i$ , for the  $R = 5 \mu\text{m}$  disk.

dropped power with a simultaneous *decrease* in reflected power. Thus, extra power was being dissipated in the resonator above this “threshold.” High speed photodetectors, electronic-spectrum analyzers, and digital communication analyzers were then employed to shed additional light on this process. It was observed that above this “threshold,” the transmitted and reflected signals became heavily amplitude modulated at MHz frequencies. Subsequent models revealed that this modulated transmission was caused by a complex competition between free-carriers and heat dissipation. The heat generated from linear absorption and two-photon absorption caused an increase in the index of refraction through the large thermo-optic effect in silicon [100]. Conversely, the extra free-carriers generated from TPA caused a decrease in the index of refraction via the plasma-dispersion [3,4]. The competition between these two opposing index changes caused the resonance to be continuously pushed and pulled around the pump frequency. These observations and analyses demonstrate that careful consideration needs to be paid to the large number of nonlinearities that are present in the rich silicon material system when designing future silicon photonics elements. Further details of this self-induced modulation of the optical resonances can be found in Ref. [120].

## 6.3 Erbium-Doped Cladding Lasers

### 6.3.1 Introduction

Erbium is an element from the lanthanide<sup>1</sup> group of the periodic table and is most commonly seen as a trivalent ion,  $\text{Er}^{3+}$ . Although generally referred to as one of the “rare earth elements” because these elements were once believed to be scarce, all rare earth elements are in fact orders of magnitude more abundant than many “common” elements such as gold. Rare earths, and in particular erbium, have vastly improved the telecommunications industry with the widespread use of erbium-doped fiber amplifiers (EDFA’s) [1]. Erbium-doped oxides are able to provide high-power and broadband gain in the 1550 nm low-loss window of silica fiber, and as a result, ushered in a new era of telecommunications capacity at very reasonable costs. As the long-haul network has reached a point of maturity, rare earth oxides are now being considered as gain media for chip-based applications. Start-up companies such as Inplane Photonics have commercialized technology to create microfabricated amplifiers called erbium-doped waveguide amplifiers (EDWA’s) [121–123]. Still farther on the horizon is the idea of utilizing erbium-doped glass as lasing elements in true micro- and nano-photonics applications. Recently, Vahala *et al.* have published numerous studies on chip-based erbium-doped lasers with footprints 20 – 100  $\mu\text{m}$  [118, 124–127]. Slope efficiencies on the order of 10 – 20% and dropped power thresholds as low as 660 nW were observed in erbium-doped sol-gel microtoroids [118].

This work hoped to build upon the previously mentioned successes by adding an erbium-doped glass cladding on top of our recently developed high- $Q$  silicon microresonators. Using a thermal oxide buffer layer to mitigate strain effects, both high and low  $\Gamma_{\text{Si}}$  resonators were fabricated and tested. The erbium-doped cladding used in the following work was provided through collaboration with Inplane Photonics and is applied to the surface of the silicon microcavities via physical vapor deposition (PVD). Laser oscillation was observed and modeled for the case of low  $\Gamma_{\text{Si}}$  devices, wherein most of the silicon was converted into thermal oxide. Photoluminescence measurements allowed for determination of the optimum pump mode within seconds.

---

<sup>1</sup>Fittingly, the term comes from the Greek term *lanthanos* meaning hidden.

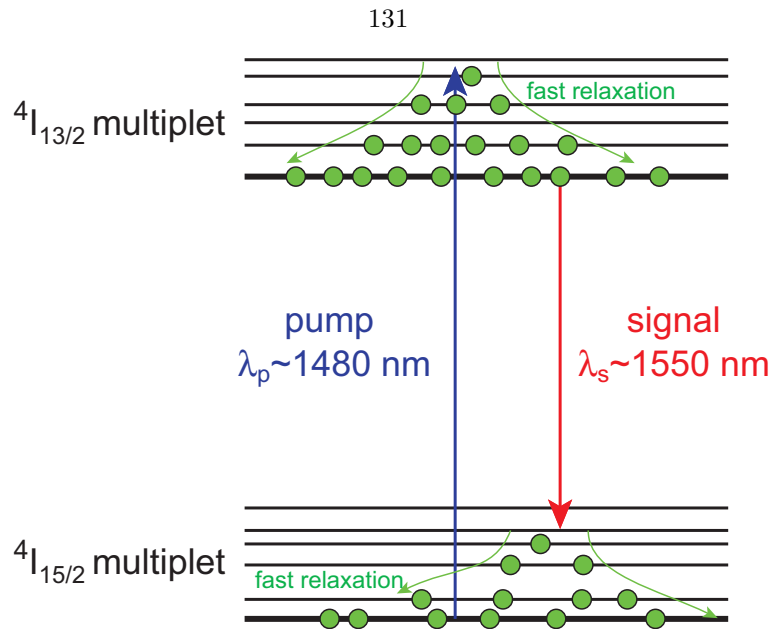


Figure 6.4: Multiplet energy levels for erbium-doped oxides for the telecommunications relevant  $\sim 1550$  nm signal band with a  $\sim 1480$  nm pump. The green dots represent  $\text{Er}^{3+}$  ions in a highly inverted distribution.

In addition, comprehensive measurements of saturable pump absorption were used to provide highly accurate measurements of the relevant erbium laser parameters.

### 6.3.2 Achieving Inversion in a “Two-State” System

In order to achieve complete inversion of the  $4I_{13/2}$  to  $4I_{15/2}$  transition,  $\text{Er}^{3+}$  systems are usually pumped with a 980 nm source. The 980 nm pump excites  $\text{Er}^{3+}$  ions from the ground state into the  $4I_{11/2}$  state, which quickly relaxes down to the long-lived  $4I_{13/2}$  state. This option is not desirable for silicon microphotronics applications<sup>2</sup> as silicon is highly absorbing above its bandgap at 1100 nm. Fortunately, the same crystal-field effects that give  $\text{Er}^{3+}$  its broadband gain also offer an alternative pumping scenario. As schematically depicted in Fig. 6.4, a pump near 1480 nm can excite ground state ions to the highest sublevels within the  $4I_{13/2}$  multiplet. Those excited ions will then quickly thermally relax to the bottom of the  $4I_{13/2}$  multiplet where no further state occurs for another  $\sim 0.8$  eV, creating a population inversion for transitions around 1550 nm. The obvious disadvantage of this scheme is that thermal equilibrium dictates that there are always finite populations at the upper sublevels of

<sup>2</sup>This argument is limited to applications where an appreciable portion of the photon’s energy resides inside silicon.

the multiplets, resulting in significant stimulated emission at the pump wavelength. Keeping track of rates for each transition between all the different sublevels is obviously impractical. Rather, this process can be quantified by introducing spectrally varying absorption and emission cross sections  $\sigma^a(\lambda)$  and  $\sigma^e(\lambda)$ , respectively [1, 128], where a cross section is defined as the amount of power absorbed or emitted per unit intensity at the ion,  $\Delta P = \sigma I$ . Figure 6.5 plots  $\sigma^a(\lambda)$  and  $\sigma^e(\lambda)$  assumed for the analysis in this work. With the definition of spectrally dependent cross sections, only the total populations in each multiplet state need to be taken into account. Defining a number density of ions,  $N(\mathbf{r})$ , the total change in power as an optical wave passes through a volume is then given by

$$\Delta P = \int \sigma N(\mathbf{r}) I(\mathbf{r}) d\mathbf{r}. \quad (6.2)$$

As optical microcavities are not well suited to being described by intensities, one can recast this concept into terms of energy. The magnitude of the energy velocity,  $v_e$ , of an optical wave in a waveguide is equal to the spatially averaged intensity divided by the spatially averaged electromagnetic energy density [39]. By equating the energy velocity to the group velocity [37, 39],  $v_g$ , the previous equation's integral can be performed over the energy density of a cavity with the proportionality constant  $v_g$ .

### 6.3.3 Rate Equations

The most straightforward technique to modeling the performance of a laser is to construct the so-called rate equations for the system. As much as possible, the forthcoming analysis will attempt to meld the analysis in the seminal EDFA modeling paper by Giles and Desurvire (Ref. [128]) with that found in standard treatments on microlasers [50, 129–133]. The majority of dynamical and steady-state properties of erbium-based lasers can be captured by studying the dynamics between the number of photons in each cavity mode,  $M_m$ , and the number *density* of ground-state and excited-state ions,  $N_1(\mathbf{r})$  and  $N_2(\mathbf{r})$ , respectively. Under this framework, each ion must be in one, and only one, of the two states; thus the total number density of  $\text{Er}^{3+}$  ions is given by  $N_T(\mathbf{r}) = N_1(\mathbf{r}) + N_2(\mathbf{r})$ . As a consequence, only one ion pop-

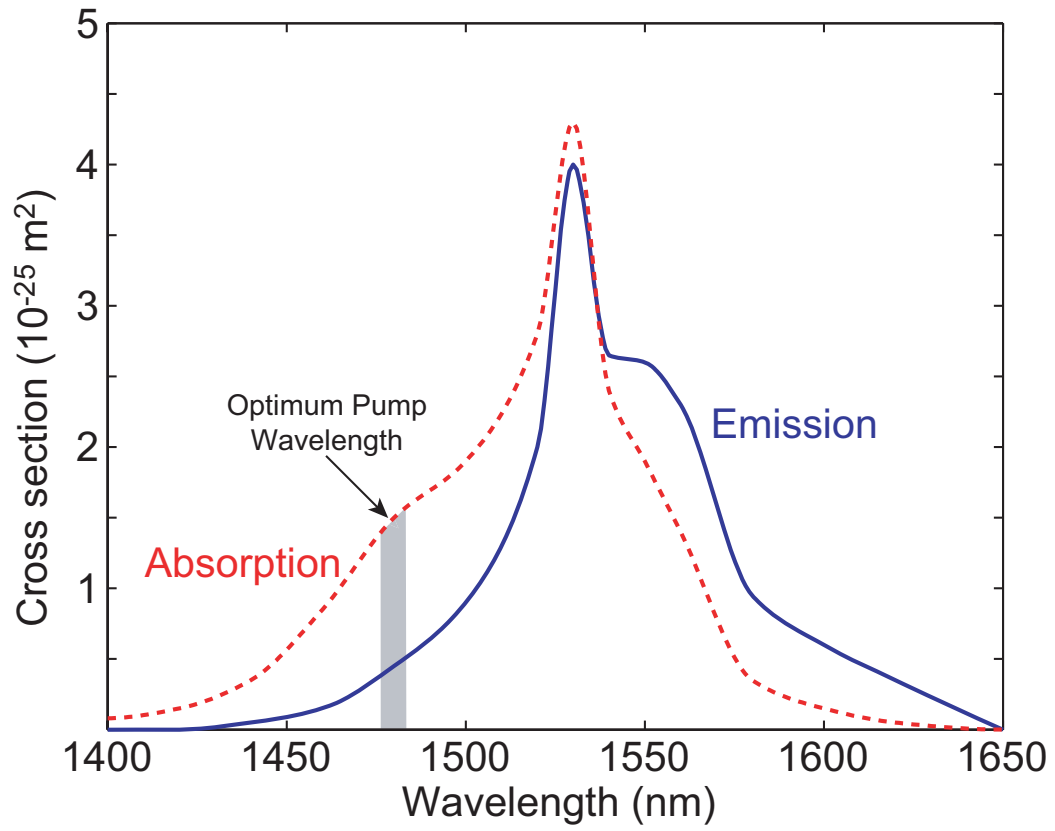


Figure 6.5: Assumed  $\text{Er}^{3+}$  spectrally varying absorption and emission cross sections,  $\sigma^a(\lambda)$  and  $\sigma^e(\lambda)$  used throughout this work (adapted from [1, 2]).

ulation density needs to be accounted for, so the independent differential equations can be written as

$$\frac{dM_m}{dt} = -\gamma_m M_m + \int v_{g,m} \sigma_m^e N_2(\mathbf{r}) \hat{w}_m(\mathbf{r}) (M_m + 1) d\mathbf{r} - \int v_{g,m} \sigma_m^a N_1(\mathbf{r}) \hat{w}_m(\mathbf{r}) M_m d\mathbf{r} \quad (6.3a)$$

$$\frac{dN_2(\mathbf{r})}{dt} = -\frac{N_2(\mathbf{r})}{\tau_{Er}} - \sum_m v_{g,m} \sigma_m^e N_2(\mathbf{r}) \hat{w}_m(\mathbf{r}) M_m + \sum_m v_{g,m} \sigma_m^a N_1(\mathbf{r}) \hat{w}_m(\mathbf{r}) M_m, \quad (6.3b)$$

where  $\gamma_m$  is the  $m$ 'th mode's total decay rate in the absence of  $\text{Er}^{3+}$  ions,  $\sigma_m^a$  and  $\sigma_m^e$  are the absorption and emission cross sections at the  $m$ 'th mode's wavelength,  $\tau_{Er}$  is the lifetime of the  ${}^4I_{13/2}$  to  ${}^4I_{15/2}$  transition, and  $\hat{w}_m(\mathbf{r})$  is the normalized time-averaged electric energy density given by

$$\hat{w}_m(\mathbf{r}) = \frac{\frac{1}{4} \epsilon_0 n^2(\mathbf{r}) |\mathbf{E}(\mathbf{r})|^2}{\int \frac{1}{4} \epsilon_0 n^2(\mathbf{r}) |\mathbf{E}(\mathbf{r})|^2 d\mathbf{r}}. \quad (6.4)$$

The first term on the RHS of Eq. (6.3a) is the time rate of change of the photons out of the cavity. The modal decay rate can be separated into  $\gamma_m = \gamma_{i,m} + \gamma_{\text{ext},m}$ , where  $\gamma_i$  is the intrinsic loss rate and  $\gamma_{\text{ext}}$  is the bidirectional loss back into the taper. The second term on the RHS of Eq. (6.3a) is the time rate of change of stimulated plus spontaneous emission into the  $m$ 'th mode, whereas the following term is the time rate of change of absorption for mode  $m$ . The first term on the RHS of Eq. (6.3b) is the spatially varying total decay rate of excited  $\text{Er}^{3+}$  ions per unit volume. As all interlevel transitions are assumed to be radiative,  $1/\tau_{Er}$  is the average total spontaneous emission rate into all modes. The last two terms are the spatially varying stimulated emission and absorption rates per unit volume where the summation is over all modes, including the pump mode. However, Eq. (6.3a) does not strictly apply to the pump mode as external loading from the taper has not been taken into account. In order to add external loading from the taper, the energy amplitudes including phase for both standing waves must be used along with the knowledge of the external laser's detuning from the resonance center. The experiments to be

presented here calculate the number of pump photons inside the cavity indirectly from the wavelength-dependent transmission past the resonator. An excellent theoretical treatment on the rate equations for the energy amplitudes can be found in Ref. [127] for the case of on-resonance coupling to a single Lorentzian.

The need for a spatial weighting function,  $\hat{w}_m(\mathbf{r})$ , is a critical aspect of formulating the proper rate equations. Each ion's transition rate depends on the per photon electric field strength, which varies spatially. The choice of weighting function then depends on the basis for representing the electric field. For high- $Q$  quasi-normal modes, the natural basis is the resonances of the optical cavity. This implies that a spatial integration over each mode is necessary to account for the total emission from all interacting ions.<sup>3</sup>

In principle, Eqs. (6.3a) and (6.3b) can be solved for the dynamics of the system. In practice, integro-differential equations are computationally intensive and the steady-state behavior is usually sought. By defining the net stimulated emission rate (i.e. stimulated emission – stimulated absorption),

$$g_m = \int v_{g,m} [\sigma_m^e N_2(\mathbf{r}) - \sigma_m^a N_1(\mathbf{r})] \hat{w}_m(\mathbf{r}) d\mathbf{r}, \quad (6.5)$$

the steady-state version of Eqs. (6.3a) and (6.3b) can be written as

$$M_m = \frac{\int v_{g,m} \sigma_m^e N_2(\mathbf{r}) \hat{w}_m(\mathbf{r}) d\mathbf{r}}{\gamma_m - g_m} \quad (6.6a)$$

$$N_2(\mathbf{r}) = N_T(\mathbf{r}) \frac{\sum_m v_{g,m} \sigma_m^a \hat{w}_m(\mathbf{r}) M_m}{1/\tau_{\text{Er}} + \sum_m v_{g,m} (\sigma_m^e + \sigma_m^a) \hat{w}_m(\mathbf{r}) M_m}. \quad (6.6b)$$

Equations (6.6a) and (6.6b) represent a tractable form for calculating the steady-state dynamics of an erbium-doped laser system as a function of pump photon number,  $M_p$ . As will be seen in Section 6.3.4, the spatial dependence to the inversion is especially relevant to lasers where the active material acts as a cladding rather than a core. As the stored energy inside a cavity is raised, the regions of higher energy density will invert before the very tails of the optical mode. The main disadvantage

---

<sup>3</sup>Pedagogically speaking,  $\hat{w}_m(\mathbf{r})$  can also be thought of as an inverted spatially varying mode volume,  $\hat{w}_m(\mathbf{r}) = 1/V_m(\mathbf{r})$ . This should be contrasted from the usual definition of mode volume, which assumes that all dipole moments have been placed at the maxima of the mode's energy density.

of this equation system is of course that integrations must be carried out for every  $M_p$ , preventing much of the intuition-developing algebraic manipulation from being done. It is for this reason that *average* inversion densities will be defined according to

$$\bar{N}_i \equiv \frac{1}{V_a} \int_{V_a} N_i(\mathbf{r}) d\mathbf{r}, \quad (6.7)$$

where  $V_a$  is the volume of the active region that interacts with the optical modes of the microcavity. With this definition, unitless overlap factors of the optical modes and ion densities can be written as

$$\Gamma_{m,i} \equiv \frac{1}{\bar{N}_i} \int \hat{w}_m(\mathbf{r}) N_i(\mathbf{r}) d\mathbf{r}. \quad (6.8)$$

By integrating over Eq. (6.3b) and using the above definitions, the rate equations from Eqs. (6.3a) and (6.3b) become

$$\frac{dM_m}{dt} = -(\gamma_m - g_m)M_m + v_{g,m}\sigma_m^e\Gamma_{m,2}\bar{N}_2 \quad (6.9a)$$

$$\frac{d\bar{N}_2}{dt} = -\frac{\bar{N}_2}{\tau_{Er}} - \sum_m \frac{g_m M_m}{V_a}, \quad (6.9b)$$

where  $g_m$  takes the form  $g_m = v_{g,m} [\sigma_m^e \Gamma_{m,2} \bar{N}_2 - \sigma_m^a \Gamma_{m,1} \bar{N}_1]$ . It should be noted that this form of the rate equations has made no approximation from the original differential equation. Rather, just the volume of the active material was used to aid in the definitions of overlap integrals. However, further simplification can be made by assuming  $\Gamma_m = \Gamma_{m,2} \approx \Gamma_{m,1} \approx \Gamma_{m,T}$  and defining per unit time Giles parameters: [128]

$$\gamma_m^e \equiv v_{g,m}\sigma_m^e\Gamma_m\bar{N}_T \quad (6.10a)$$

$$\gamma_m^a \equiv v_{g,m}\sigma_m^a\Gamma_m\bar{N}_T. \quad (6.10b)$$

The Giles parameters facilitate a particularly simple form of the rate equations where the various rates depend upon the total photon numbers for each mode,  $M_m$ , and the fractional inversion population,  $\bar{N}_2/\bar{N}_T$ . Using these variables, the rate equations

become the change in modal photon numbers and the change in the total number of inverted ions according to

$$\frac{dM_m}{dt} = -(\gamma_m - g_m)M_m + \gamma_m^e \frac{\bar{N}_2}{\bar{N}_T} \quad (6.11a)$$

$$\frac{d}{dt}(\bar{N}_2 V_a) = -\zeta \frac{\bar{N}_2}{\bar{N}_T} - \sum_m g_m M_m, \quad (6.11b)$$

where

$$g_m = \frac{\bar{N}_2}{\bar{N}_T}(\gamma_m^e + \gamma_m^a) - \gamma_m^a, \quad (6.12)$$

and  $\zeta \equiv \bar{N}_T V_a / \tau_{\text{Er}}$ .

As every term in Eqs. (6.11a) and (6.11b) now has the units of transitions per unit time, several connections to microlaser jargon can be made. The term  $\gamma_m^e (\bar{N}_2 / \bar{N}_T)$  is the spontaneous emission rate into the  $m$ 'th mode whereas  $\zeta (\bar{N}_2 / \bar{N}_T)$  is the total spontaneous emission rate into all modes. Furthermore, this implies that  $\zeta = \sum_m \gamma_m^e$ . Thus, the well-known beta factor [50] for any mode can be written simply as  $\beta = \gamma_m^e / \zeta$ , which is the fractional efficiency of the ions' ability to emit into the mode of interest and is dependent upon the physical design of the microcavity.

For the optical microcavities experimentally considered in this thesis, the number of modes interacting with the gain medium is on the order of  $\sim 10 - 1000$ . The sheer number of modes makes a detailed knowledge of their precise field distributions impractical. Thus, Eqs. (6.11a) and (6.11b) have been derived in a concerted effort to strike a balance between defining experimentally measurable quantities while retaining the relevant physics of Eqs. (6.3a) and (6.3b). The steady-state versions of (6.11a) and (6.11b) are the workhorses of the forthcoming analysis and are presented for future reference:

$$M_m = \frac{\gamma_m^e}{\gamma_m - g_m} \frac{\bar{N}_2}{\bar{N}_T} \quad (6.13a)$$

$$\frac{\bar{N}_2}{\bar{N}_T} = \frac{\sum_m \gamma_m^a M_m}{\zeta + \sum_m (\gamma_m^e + \gamma_m^a) M_m}. \quad (6.13b)$$

### 6.3.4 Cavity Design

In order to achieve lasing action, the associated optimal cavity designs must satisfy several requirements similar to any laser, including possessing a low threshold and high external efficiency. From a design perspective, a good rule of thumb is that the available gain of the cavity must be roughly greater than or equal to the decay rate of the cavity. In our case, the material gain has been characterized by Inplane Photonics' EDWA device performance and given to us in the form of a maximum modal gain of 0.6 dB/cm when pumped at 1480 nm. Assuming an overlap factor of approximately unity, the result of Section 2.1.1 can be used to find that our material has a quality factor of  $Q_{\text{Er, material}} \approx -4.25 \times 10^5$ , where the negative sign indicates gain. Based on previous passive device performance, a target loaded quality factor of  $1.5 \times 10^6$  is reasonable. Thus, the energy overlap with the active region must be  $\Gamma_{\text{Er}} \gtrsim 0.3$  as a design goal.

As the cladding material is meant to be deposited over the surface of the microdisks and microrings described in Section 5.6,  $\Gamma_{\text{Er}}$  can be modified in two basic ways: the deposited erbium-doped cladding thickness and the buffer layer thermal oxidation time. The deposited cladding should be thick enough to capture most of the otherwise evanescent field outside the core region but not so thick that fiber taper probing becomes impractical. Designing the modes such that roughly 1 – 10% of the energy is evanescent is a sufficient guiding principle in most cases. The buffer layer thickness should be chosen such that the silicon surfaces are adequately protected from the environment prior to erbium-doped cladding deposition. In addition, the buffer layer should also be thick enough to act as an adhesion layer and provide strain relief for the PVD material. As the optimal ring designs are very “disk-like” (i.e. the width of the ring is large enough such that the inner-etch placement is inconsequential), the following analysis will focus on the conceptually simpler case of an undercut silicon disk.

Figures 6.6, 6.7, and 6.8 show the results of FEM simulations for Er-doped cladding laser modes at 1550 nm for various buffer layer thermal oxidation times. The starting disk was chosen to be  $R = 20 \mu\text{m}$  and made from an SOI wafer with 195 nm thick

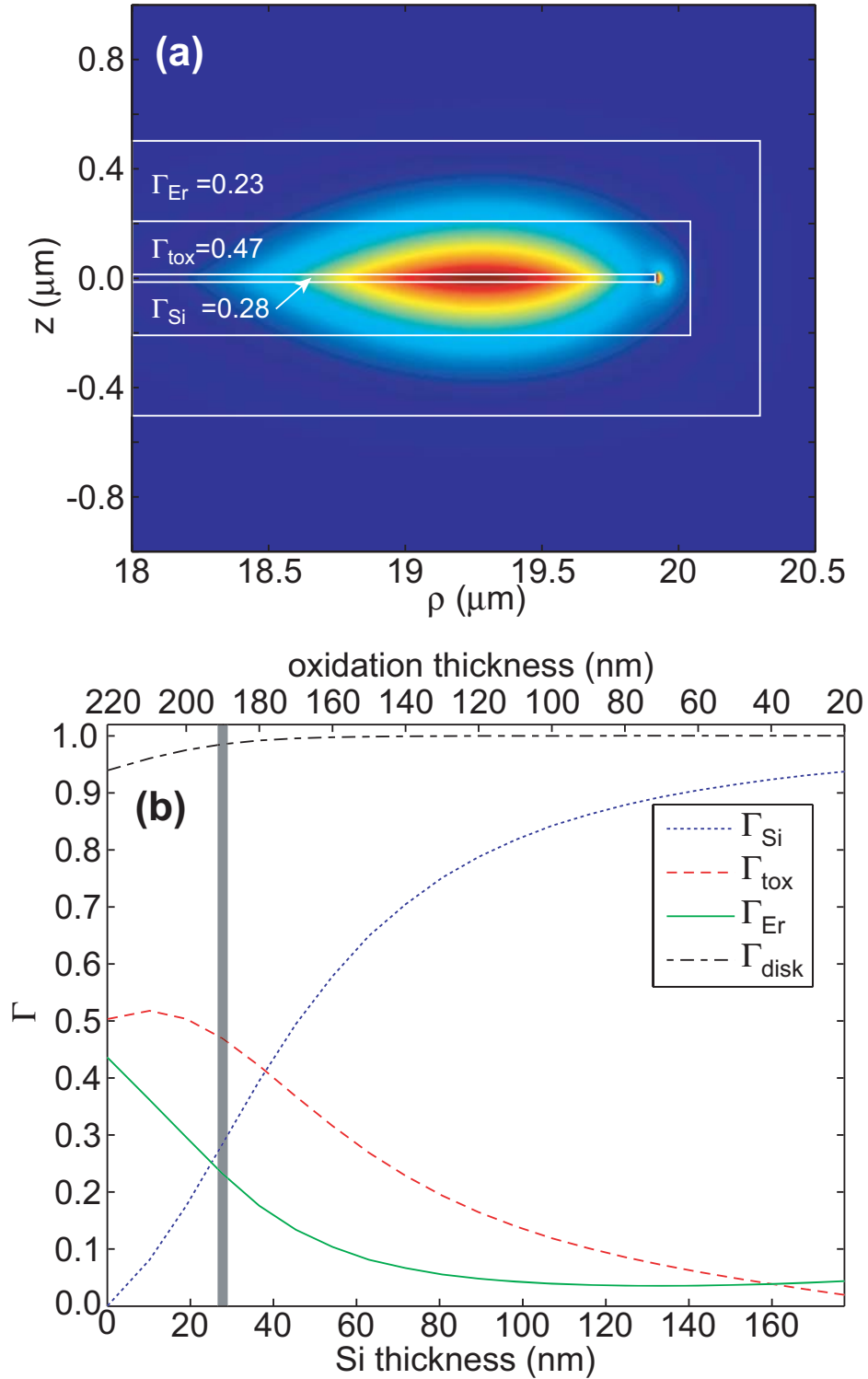


Figure 6.6: FEM simulations of **TE polarized** Er-doped cladding laser modes at 1550 nm for various buffer layer thermal oxidation times. Starting disk parameters were:  $R = 20 \mu\text{m}$  radius,  $h_{\text{Si}} = 195 \text{ nm}$ ,  $h_{\text{Er}} = 300 \text{ nm}$ ,  $t_{\text{BOX}} = 3 \mu\text{m}$ . (a) Spatial dependence of  $|\mathbf{E}(\rho, z)|^2$  for  $\Gamma_{\text{Si}} = 0.28$  (highlighted by gray bar in (b)). (b) Fraction of electric energy in each dielectric component versus buffer layer thickness (and equivalent remaining silicon core).

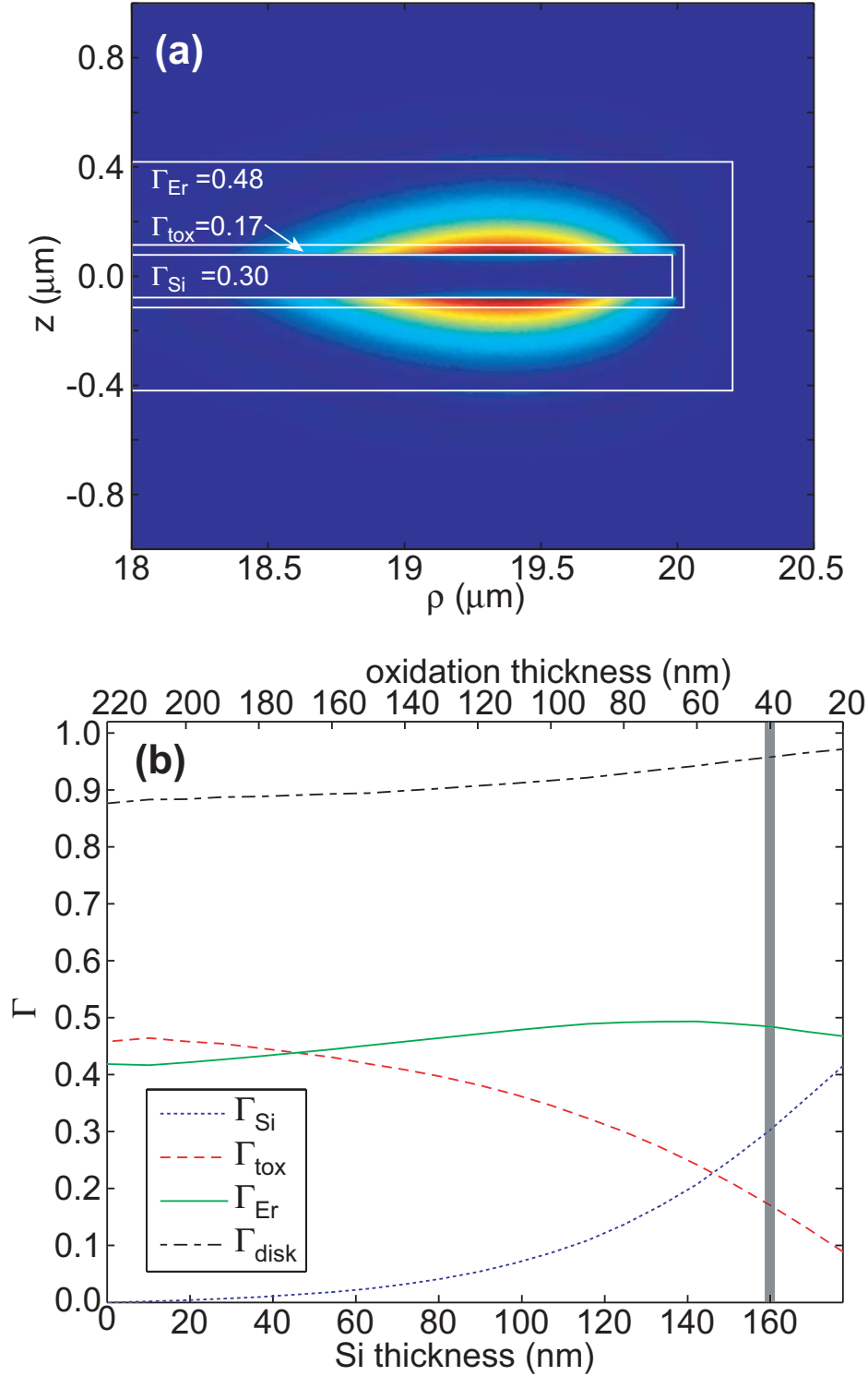


Figure 6.7: FEM simulations of **TM polarized** Er-doped cladding laser modes at 1550 nm for various buffer layer thermal oxidation times. Starting disk parameters were:  $R = 20 \mu\text{m}$  radius,  $h_{\text{Si}} = 195 \text{ nm}$ ,  $h_{\text{Er}} = 300 \text{ nm}$ ,  $t_{\text{BOX}} = 3 \mu\text{m}$ . (a) Spatial dependence of  $|\mathbf{E}(\rho, z)|^2$  for  $\Gamma_{\text{Si}} = 0.30$  (highlighted by gray bar in (b)). (b) Fraction of electric energy in each dielectric component versus buffer layer thickness (and equivalent remaining silicon core).

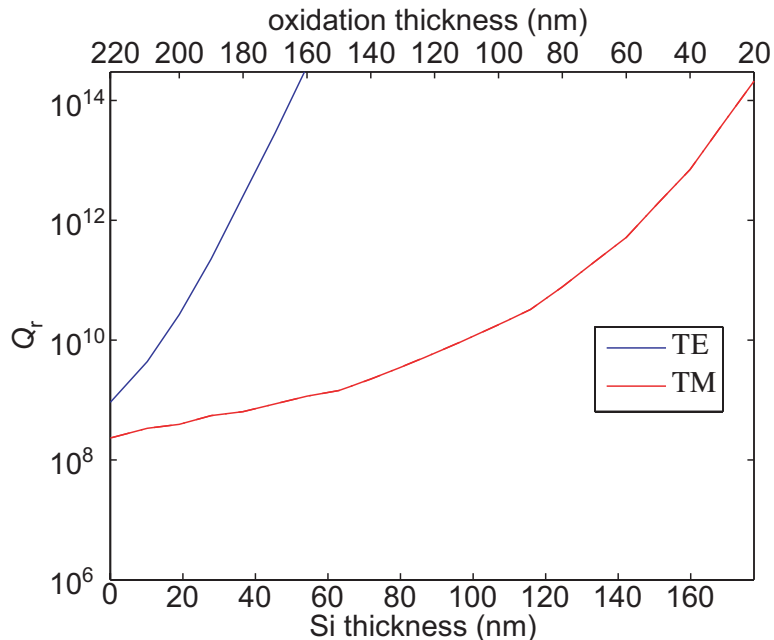


Figure 6.8: FEM simulation of radiation  $Q$  versus the thermal oxide buffer layer thickness (and equivalent remaining silicon core) for  $\lambda_0$  fixed at 1550 nm. Starting disk parameters were:  $R = 20 \mu\text{m}$  radius,  $h_{\text{Si}} = 195 \text{ nm}$ ,  $h_{\text{Er}} = 300 \text{ nm}$ ,  $t_{\text{BOX}} = 3 \mu\text{m}$ .

Si device layer atop a  $3 \mu\text{m}$  thick BOX. Thus, the undercut disk was modelled as a 195 nm thick Si disk floating  $3 \mu\text{m}$  above an Si substrate. The index of the Er-doped cladding was assumed to be equal to that of the thermal oxide,  $n_{\text{tox}} = n_{\text{Er}} = 1.45$ . The remaining aspects of the FEM simulation procedure are described in Section 2.4. Parts (a) of Figs. 6.6 and 6.7 show TE and TM mode profiles<sup>4</sup> for the exemplary case of  $\sim 30\%$  of the electric energy residing in the silicon core. Parts (b) of Figs. 6.6 and 6.7 plot the fraction of electric energy in the silicon core, buffer layer, Er-doped cladding, and the sum of the three components (labelled as:  $\Gamma_{\text{Si}}$ ,  $\Gamma_{\text{tox}}$ ,  $\Gamma_{\text{Er}}$ ,  $\Gamma_{\text{disk}}$ ). Figure 6.8 plots the radiation quality factor,  $Q_r$ , for both the TE and TM case.

As increasing the thermal oxidation time increases the buffer layer thickness,  $h_{\text{tox}}$ , while simultaneously consuming 44% of the oxide's thickness in silicon per surface [53], the simulations specify  $h_{\text{tox}}$  and then reduce  $h_{\text{Si}}$  by the commensurate  $2 \cdot 0.44 \cdot h_{\text{tox}}$ . The Er-doped cladding thickness was fixed at 300 nm, which allowed roughly 1 – 10% of the electric energy to exist outside the disk, as shown by the black dash-dot  $\Gamma_{\text{disk}}$  in Figs. 6.6(b) and 6.7(b). From conformality measurements on Fig. 6.9, the

<sup>4</sup> $|\mathbf{E}(\rho, z)|^2$  was chose to represent the mode profile as opposed to electric energy density in order to provide a more visually continuous profile throughout the different dielectrics where  $n^2(\rho, z)$  differs by up to an order of magnitude.

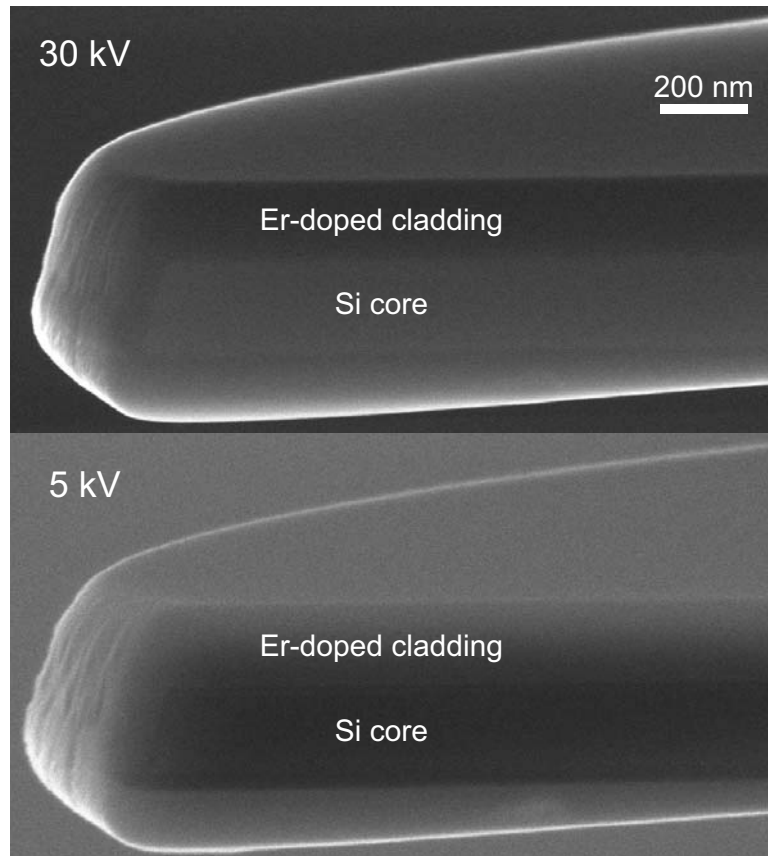


Figure 6.9: SEM micrograph of an early erbium-doped cladding silicon microdisk after FIB cross-sectioning. Top image was taken with a 30 kV accelerating voltage for best resolution, while the bottom image was taken with a 5 kV accelerating voltage for best material contrast (note: 2 nm buffer layer is present but not discernable).

experimental fractional PVD coverage on an undercut disk is roughly 0.65 for both the sidewalls and bottom surface when compared to the top surface, which has the whole hemisphere of deposition solid-angles. However, separation into TE-like and TM-like modes requires that the disk possess a mirror symmetry about its vertical center. When this mirror symmetry is broken, accidental degeneracies between higher radial order “TE” modes and lower radial order “TM” modes of the same azimuthal number exist and result in mode mixing from anti-crossings. As this study’s intention was to follow a single family of modes at a fixed wavelength while the oxidation time is varied, occasional anti-crossing would inevitably occur. Thus, a small approximation has been made by taking the fractional PVD coverage on the side to be a realistic 0.65 while the fractional bottom coverage was raised to unity in order to preserve the mirror symmetry.<sup>5</sup>

The overlap factors present in Fig. 6.6 illustrate a highly core-guided mode for thick silicon (thin buffer layers), which begins a quick transition to a silica cladding-guided mode for  $h_{\text{Si}} \lesssim 60$  nm. Notably, the TE polarized modes have a very poor overlap with the active region until the Si layer becomes extremely thin,  $h_{\text{Si}} \lesssim 30$  nm (shown in Fig. 6.6(a)). From a technological standpoint, a TE polarized mode requires that the Si thickness be controlled better than  $\pm 1$  nm to achieve a  $\pm 0.01$  precision in the relevant overlap factors. The most striking contrast between the TE and TM disk modes of Figs. 6.6 and 6.7 is an overarching theme of this thesis: the TM polarization’s increased overlap with the glass cladding for all parameter space. Intuitively, the disk’s parameters have been chosen so that the TM mode of the Si core is just beginning to approach the traditional “cut-off” point. As a consequence, the otherwise evanescent tails readily assume the field-distribution of silica-cladding guided modes where they enjoy an extended presence as a high- $Q$  resonance (see Fig. 6.8). With just 20 nm of buffer oxide present, the TM mode has a 47% overlap with the Er-doped cladding, which remains nearly constant as the silicon core is removed. This nearly constant erbium overlap drastically relaxes the tolerances necessary to achieve an Er-doped cladding silicon laser because the oxidation time can be tuned independently to optimize other design constraints, such as  $\text{Er}^{3+}$  diffusion or strain-

---

<sup>5</sup>The silicon substrate provides an inconsequential amount of mode mixing for the ultra-high- $Q$  modes under consideration.

induced concentration quenching.

In the limit of total oxidation, both polarizations converge to similar figures of merit. This convergence is due to the fact that the resulting all-silica disk is approximately a wavelength in the material thick where polarization-dependent effects are minimal. Total oxidation also sets a lower limit on the radius of the simulated disk; shown in Fig. 6.8, the radius of the disk was chosen such that  $Q_r$  would be larger than  $10^8$  for all buffer layer thicknesses. For either polarization, it is expected that leaving roughly 30 – 50% of the electrical energy in the silicon will be ideal in order to facilitate electrical tuning on non-undercut, partially etched structures.

### 6.3.5 Fabrication and Test Setup

A series of both undercut microdisks and non-undercut microrings were fabricated utilizing two different SOI wafers commercially available from SOITEC. The first wafer consisted of a 217 nm thick device layer (p-type, 14 – 20  $\Omega\cdot\text{cm}$  resistivity,  $\langle 100 \rangle$ ) atop of a 2  $\mu\text{m}$   $\text{SiO}_2$  BOX and was used for thicker silicon microdisks, whereas the second wafer consisted of 195 nm thick device layer atop a 3  $\mu\text{m}$   $\text{SiO}_2$  BOX and was used for thin silicon microdisks as well as non-undercut microrings. A combination of e-beam lithography, ICP/RIE etching, and wet chemical treatments, as described in Section 5.6, were utilized in order to prepare microdisks and microrings with clean hydrogen-passivated surfaces immediately before growing a range of thermal oxide buffer layers on the various samples. 217 nm thick device layers undercut microdisks with 5 – 10  $\mu\text{m}$  radii were prepared with {20, 40, and 60} nm thermally oxidized buffer layers. The thermal oxide was grown at 1000°C immediately followed by a 4.5 hour  $\text{N}_2$  anneal where the temperature was slowly ramped down to 400°C during the final 1.5 hours. A similar procedure at 1100°C was used to completely oxidize a 195 nm device layer thickness sample consisting of 10 – 40  $\mu\text{m}$  radii undercut microdisks. A final non-undercut microring sample shown in Fig. 6.10 consisting of a 2-D array of 10 – 40  $\mu\text{m}$  radii and 1 – 2  $\mu\text{m}$  widths was also prepared from the 195 nm thick Si material and had a 30 nm thermal oxide cap grown on top of it. The slight undercut visible in Fig. 6.10(b) is due to the repeated Piranha oxidations and HF dips used to chemically passivate the surface prior to thermal oxidation.

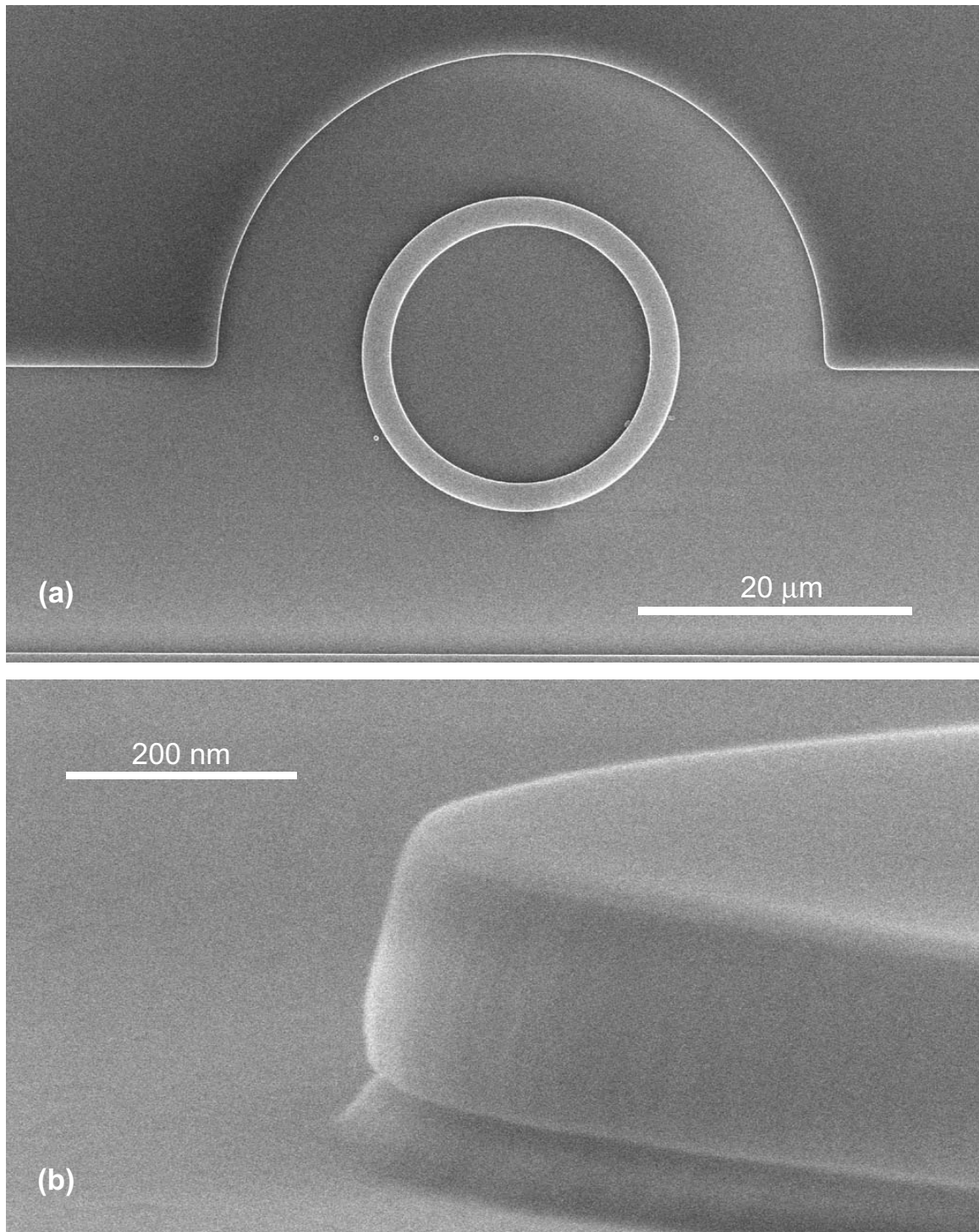


Figure 6.10: SEM images of rings after the final chemical treatments and 30 nm thermal oxidation. (a) Top-view of a  $20\ \mu\text{m}$  diameter,  $2\ \mu\text{m}$  width ring. (b) Side view showing smooth ring sidewalls and a slight BOX undercut due to the final chemical treatment.

The 20 nm cap silicon disk, the fully oxidized disk, and the microrings were then tested with a dimpled fiber taper probe in order to ensure the buffer layer successfully preserved the high- $Q$  of these structures.<sup>6</sup> The 20 nm cap silicon disks had average measured linewidths of 0.8 – 1.2 pm, corresponding to  $Q \sim 1 - 2$  million. The fully oxidized sample was tested at 1250 and 1460 nm ranges, both yielding extremely consistent linewidths of 0.4 – 0.5 pm ( $Q \sim 3 \times 10^6$ ) across the tunable laser ranges. Unfortunately, the largest fully oxidized disks suffered small amounts of strain-induced “flowering” owing to the three-dimensional thermal oxidation problem. This flowering is a general limitation of undercut disks and highlights the technological need for planar structures to be engineered in the future. The microrings proved difficult to test with a fiber taper probe because of the large phase mismatch picked up by the extra dielectric beneath the Si core guided modes. However, with the taper in contact, the coupling depths were more than adequate to assess the devices’ optical loss characteristics. Figure 6.11 shows a transmission spectrum of a high- $Q$  mode at  $\lambda_0 = 1428.7$  nm on a 80  $\mu\text{m}$  diameter, 2  $\mu\text{m}$  width ring after final chemical treatments and 30 nm thermal oxidation. The measured quality factor of  $4.8 \times 10^6$  ( $\alpha < 0.1$  dB/cm) represents the highest quality factor for any planar microresonator to date. Reproducing  $Q$ ’s found previously only in relatively thick and undercut Si disks [32] shows the incredible promise of future planar high- $Q$  silicon microresonator work as higher effective-index probe and integrated coupling waveguide are utilized.

After characterizing the passive devices, the samples were placed in Gelpaks®, sealed inside triple zip-locking bags with cleanroom tape, and shipped to Inplane Photonics in South Plainfield, NJ for further processing. At Inplane, the samples underwent further Piranha cleans in order to remove any adventitious organic contaminants before being rinsed in DI H<sub>2</sub>O, isopropanol, and N<sub>2</sub> dried. All samples were mounted inside the PVD chamber and coated at the same time with 300 nm of multi-component silica glass doped with  $\sim 1-2 \times 10^{20}$  cm<sup>-3</sup> of erbium. Finally, an 875°C anneal in an O<sub>2</sub> ambient was then used to activate the Er<sup>3+</sup> ions in the host matrix.

Cross sections of the deposited structures were conducted with the aid of an FEI

---

<sup>6</sup>The 40 and 60 nm cap silicon disks could not be tested prior to Er-doped cladding deposition because the modes were significantly radiation limited.

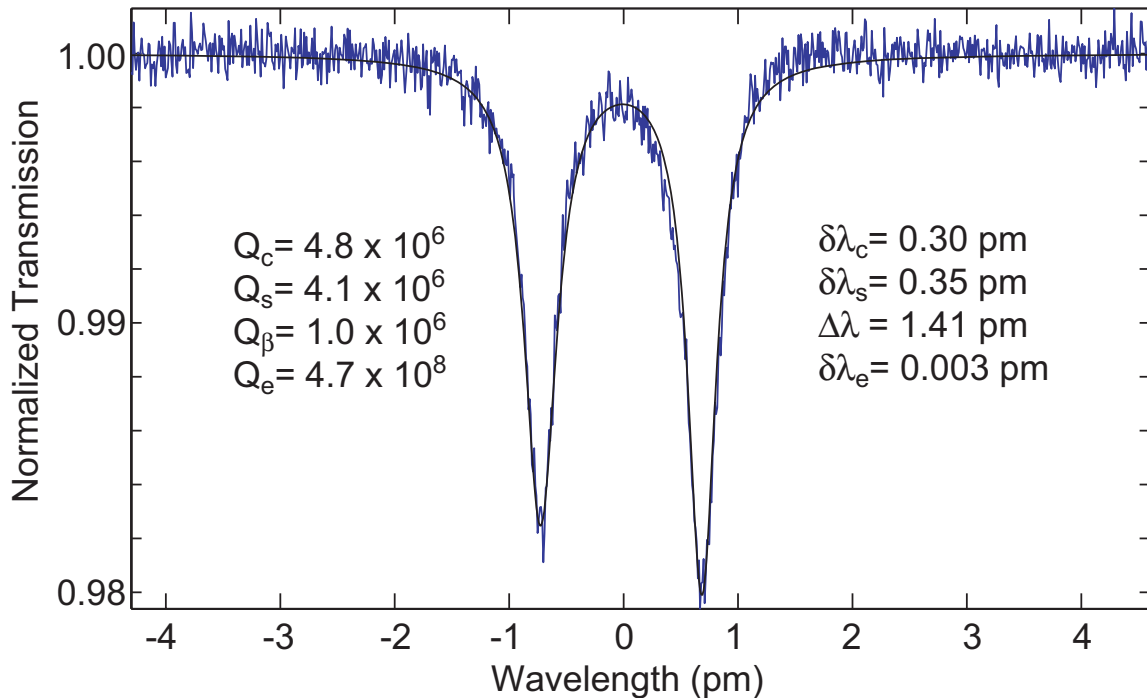


Figure 6.11: Transmission spectrum of a high- $Q$  mode at  $\lambda_0 = 1428.7 \text{ nm}$  on a  $80 \mu\text{m}$  diameter,  $2 \mu\text{m}$  width ring after final chemical treatments and  $30 \text{ nm}$  thermal oxidation.

focused ion beam system. Figure 6.9 shows SEM micrographs of an early erbium-doped cladding silicon microdisk after FIB cross-sectioning. The top image was taken with a  $30 \text{ kV}$  accelerating voltage for best resolution. At  $30 \text{ kV}$ , the top surfaces show virtually no indication of roughness. The bottom image was taken with a  $5 \text{ kV}$  accelerating voltage for the best material contrast at the expense of increased sensitivity to electrostatic charging effects. At  $5 \text{ kV}$ , the silicon core is visible with higher contrast against the Er-doped silica cladding. A comparison between the two different accelerating voltages showed significantly different representations of the sidewall roughness. The  $5 \text{ kV}$  image shows larger amplitudes of roughness but also increased distortion due to charging of the sample. At  $30 \text{ kV}$ , the image quality is much better, but it is likely that the electron beam is passing through some of the roughened material such that the surface appears falsely smoother than in reality. Since the PVD process is done under relatively high vacuum, the deposition thicknesses will be somewhat directional in nature. As a consequence, the deposition thickness on the sidewalls and bottom disk surface is reduced compared to the top surface. Furthermore, the bottom deposition thickness continues to decrease towards the center of the disk.

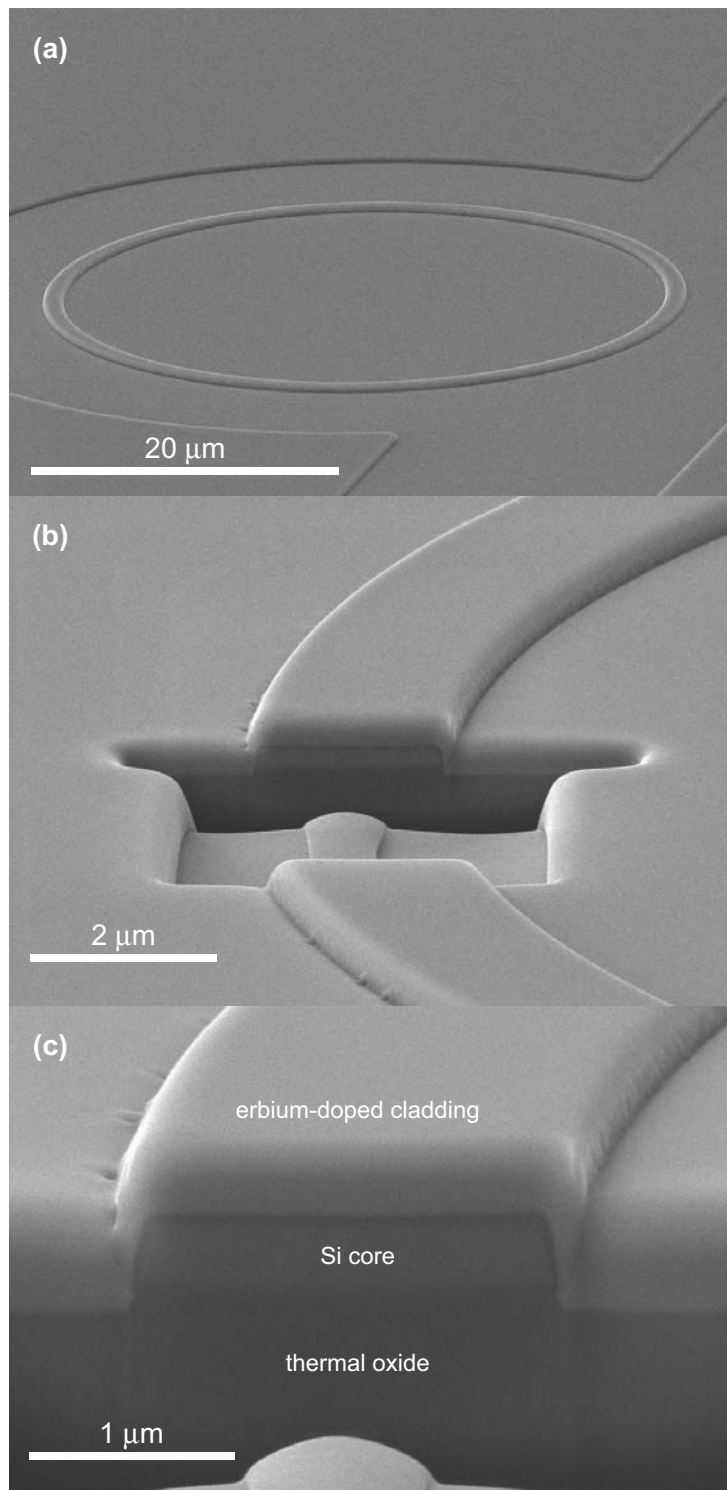


Figure 6.12: SEM micrographs of silicon rings after chemical treatments, 30 nm thermal oxidation, and 300 nm erbium-cladding deposition. (a) 20  $\mu\text{m}$  radius, 1  $\mu\text{m}$  width ring. (b) 2  $\mu\text{m}$  width ring after FIB cross-sectioning. (c) Higher magnification view of cross section where silicon core, thermal oxide and erbium oxide are clearly visible.

Figure 6.12 shows SEM micrgraphs of the previously described silicon rings after chemical treatments, 30 nm thermal oxidation, and 300 nm erbium-cladding deposition. All images were taken at 5 kV in order to enhance the material’s contrast as described before. Figure 6.12(a) shows a broad view of a 20  $\mu\text{m}$  radius, 1  $\mu\text{m}$  width microring. The Er-cladding deposition can be seen to be smooth and uniform across the resonator. Figure 6.12(b) shows a 2  $\mu\text{m}$  width ring after FIB cross sectioning, and Fig. 6.12(c) is a higher magnification view of the cross section where the silicon core, thermal oxide, and erbium oxide are clearly visible. The darkest regions immediately around the Si core are the 30 nm thermal oxide buffer layer on the top and buried oxide layer on the bottom. In general, the deposited glass appears to have no discernible defects on the top surfaces of the rings or dry-etched planes. However, small deposits of cladding material can be seen in the trough formed by the HF chemical treatments. Additionally, the etch roughness appears to have been decorated by the PVD glass, indicating that further optimization of the deposition would be necessary for ultra-low-loss planar structures. Alternatively, future planar resonators could be fabricated with integrated bus waveguides. This would allow the cladding layers to be deposited thick enough such that the rough cladding-air interface would not be seen by the optical modes.

Optical pumping of the  $\text{Er}^{3+}$  was accomplished with the same fiber taper probe as was used for collection of the optical emission. Resonant pumping such as this offers the advantage of extremely low threshold powers but prevents independently loading the pump and lasing resonances. Figure 6.13 depicts the test setup used to resonantly pump the silicon microresonators and collect the emitted light. The external-cavity laser was a fiber-coupled New Focus Velocity ( $\lambda = 1420\text{--}1498\text{ nm}$ ). The two optical attenuators were used in a “dueling attenuator” fashion in order to vary the optical power over a wide dynamic range with extreme precision. “Dueling attenuator” refers to the mode of operation where the sum of the two attenuations was always kept fixed to provide a constant pump detection signal. “SP” refers to a short pass edge filter that passes 1400–1510 nm light and reflects 1510–1625 nm light. The common multiplexed port is depicted by a black rectangle. “LP” refers to a long pass edge filter in an reverse configuration. These edge pass filters made

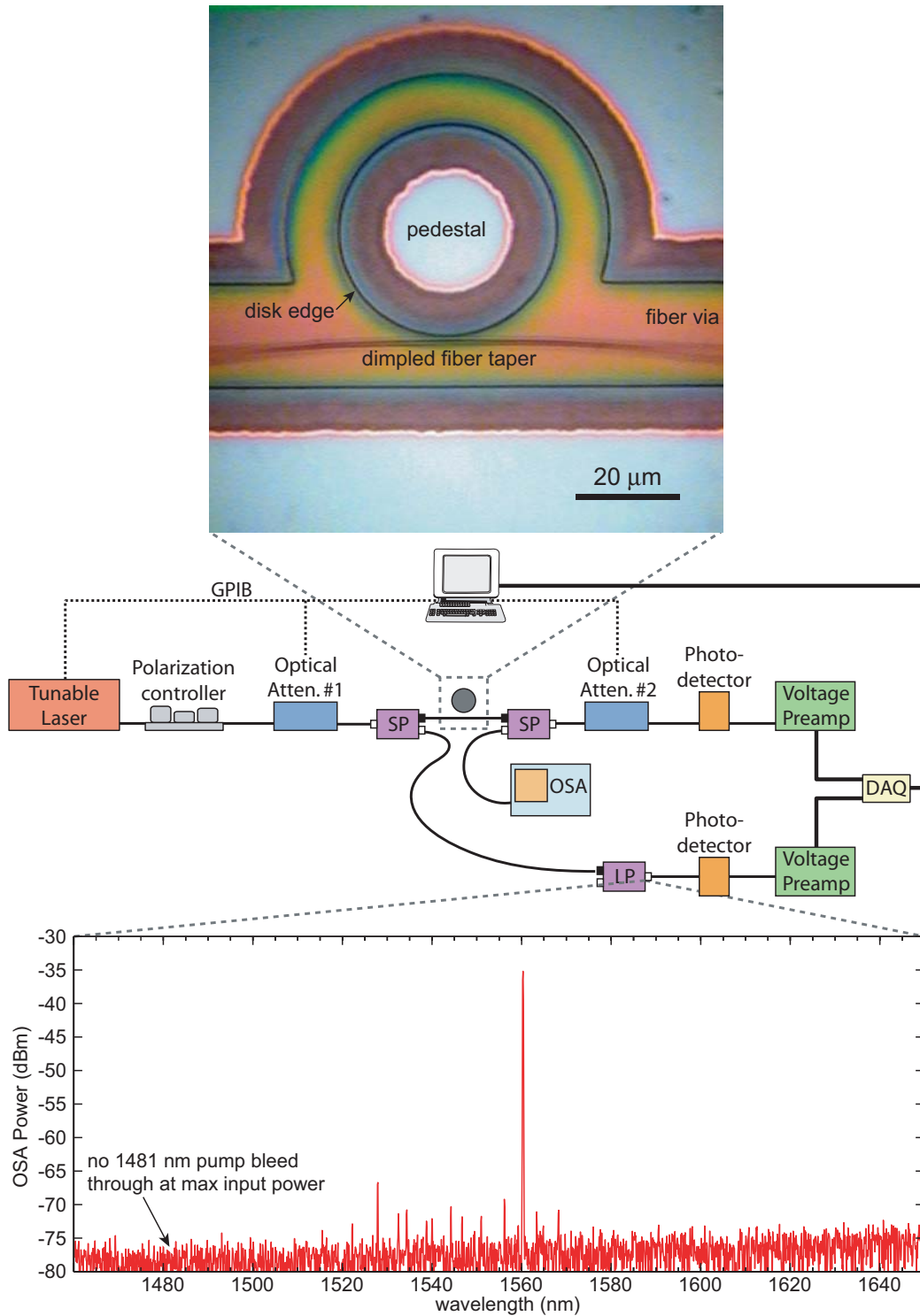


Figure 6.13: Test setup used to resonantly pump the silicon microresonators and collect the emitted light. “SP” (“LP”) refers to a short (long) pass edge filter. The top optical image was taken with a long working distance lens and CCD camera during testing. The dimpled fiber taper and 20  $\mu\text{m}$  radius fully-oxidized microdisk with Er-doped cladding are shown. The bottom plot is an OSA power scan at the output of the two-stage filter at maximum input power showing that only erbium emission is being collected at lower detector.

by Visicore and JDS Uniphase provide 30–45 dB of wavelength rejection in a single stage configuration. While the optical spectral analyzer (OSA) was connected at virtually all of the ports at various times during testing, its typical placement is shown in the figure. The OSA was used to measure total taper loss of 1.2 dB across the entire fiber length. The taper loss was assumed symmetric with respect to the dimple, meaning that all optical signals were assumed to be attenuated by 0.6 dB upon exiting the taper probe. Edge pass filter insertion losses were typically 0.7–1.5 dB. As emission from the excited microdisk modes is azimuthally symmetric, both forward and backward emitted signals were collected with the edge pass filters for further processing. The forward signal was typically sent to the OSA in order to spectrally resolve the individual emitting modes, while the backward signal was sent through a long-pass filter and to a second photodetector. The OSA was temporarily connected after the long pass filter in order to ensure that no pump was being allocated to the emission signal at the second detector. Figure 6.13 shows a plot of a broad OSA scan at the output of the two-stage filter while pumping on a mode at 1481.1 nm under maximum input power ( $\sim 1$  mW before filters). The Stanford voltage pre-amplifiers were used to impedance match the photodetectors to  $50 \Omega$ , low-pass filter the signal to remove noise, and provide up to  $10,000\times$  gain before the National Instruments data acquisition card. Experimentally, the photodetectors were connected directly to the voltage pre-amplifiers with a BNC coupler in order to reduce any inductive electrical noise pick-up. This was verified by analyzing the power spectral distribution of the Fourier transform of the time-domain voltages collected by the DAQ card. It was also found that the photodetector/voltage pre-amp system had to be placed several feet from all other electronics in order to achieve the cleanest signal as the metal case of the voltage pre-amp was an insufficient Faraday cage. The top optical image was taken with a long working distance lens and CCD camera during testing. The dimpled fiber taper and  $20 \mu\text{m}$  radius fully oxidized microdisk with Er-doped cladding are shown.

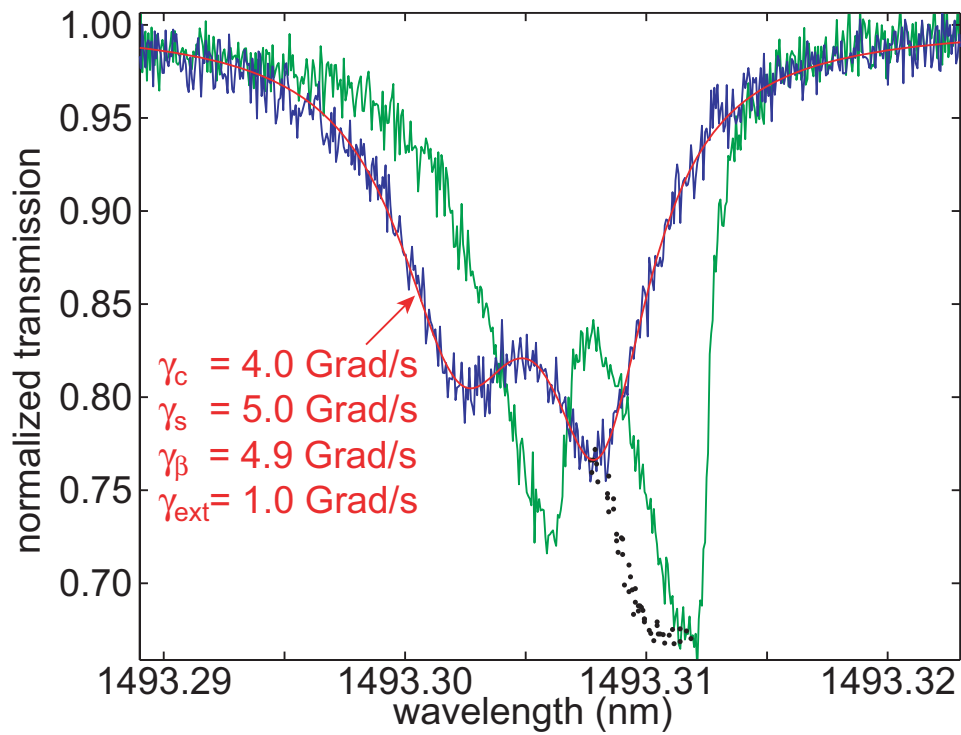


Figure 6.14: Normalized transmission spectra of a  $10 \mu\text{m}$  radius silicon microdisk after a  $60 \text{ nm}$  thermal oxidation and  $300 \text{ nm}$  erbium-doped glass deposition. The blue scan was taken at  $0.14 \mu\text{W}$  of input power, while the green scan was taken at  $45 \mu\text{W}$ . The black dots indicate transmission minima for 50 intermediate powers. The red curve is a doublet fit to the lowest power scan, and fit parameters are listed in red.

### 6.3.6 Saturable Pump Absorption Measurements

Resonant pumping offers a unique advantage such that both the pump photon number ( $M_p$ ) and the net pump absorption rate ( $\ell_p \equiv -g_p$ ) can be measured as a function of input power from the transmission spectrum across the resonances. By increasing the pump power, the  $\text{Er}^{3+}$  becomes more inverted, which decreases the total amount of loss seen by the optical modes. The transmission spectrum shows the resulting interference of the input field and the outcoupled field. As the total modal loss is decreased, the transmission depth increases for a fixed bus waveguide position (see Figure 6.14). Utilizing a similar analysis described in Section 5.5, the  $p$ 'th mode's energy amplitudes for the two standing waves can be written as

$$a_{c,s}^p = \frac{-\sqrt{\gamma_{\text{ext},p}/2}}{-(\gamma_p + \ell_p)/2 + i(\Delta\omega \pm \gamma_{\beta,p}/2)}, \quad (6.14)$$

where  $\Delta\omega$  is the detuning frequency from the initially degenerate mode frequency  $\omega_p$ ,  $\gamma_p$  is the total decay rate of each individual resonance not due to  $\text{Er}^{3+}$  ions,  $\gamma_{\text{ext},p}$  is the total loss rate back into the waveguide, and  $\gamma_{\beta,p}$  is the rate of CW to CCW mode coupling [32, 63, 67, 81]. The fraction of optical power that passes the resonator can be found by taking the coherent sum of the Lorentzian responses according to

$$T = \left| -1 + \sqrt{\gamma_{\text{ext},p}/2} (a_c^p + a_s^p) \right|^2. \quad (6.15)$$

Thus, as long as  $\gamma_{\text{ext},p}$ ,  $\gamma_{\beta,p}$ ,  $\gamma_p$ , and  $\Delta\omega$  can be held constant,  $\ell_p$  can be measured from the change in transmission,  $\Delta T$ . In general, fixing  $\Delta\omega$  can become quite difficult as several nonlinearities cause resonance shifting dispersion, resulting in nontrivial high-power transmission scans. However, the transmission *minimum* occurs at a fixed  $\Delta\omega = \gamma_{\beta,p}/2$  to a very good approximation. Figure 6.14 shows normalized transmission spectra of a 10  $\mu\text{m}$  radius silicon microdisk after a 60 nm thermal oxidation and 300 nm erbium-doped glass deposition. The blue scan was taken at  $P_{\text{in}} = 0.14$   $\mu\text{W}$  of input power, before any nonlinearities could distort the Lorentzian-like spectrum. The red curve is a doublet fit to the lowest power scan using Eqs. (6.14) and (6.15). The resulting fit parameters are listed in red in units of gigaradians/second. The green scan was taken at the much higher power of 45  $\mu\text{W}$ , while the black dots

indicate transmission minima for 50 intermediate powers. The slight resonance wavelength shift is due to the temperature change in the disk as a result of nonradiative relaxation from various forms of linear and nonlinear absorption. The total modal decay rate,  $\gamma_{\text{tot},p} \equiv \gamma_p + \ell_p$ , can be inferred from the transmission minima by adding or subtracting additional loss to the “cold” linewidths until the model’s minima match the data.

The number of pump photons can also be accurately inferred at the transmission minima using the equation

$$M_p = P_{\text{in}} \frac{|a_c^m|^2 + |a_s^m|^2}{\hbar\omega_p} \quad (6.16)$$

and assuming that the standing wave amplitudes are given by Eq. (6.14) with the modal rates determined from the preceding transmission fits. Below threshold,  $M_{m \neq p} \approx 0$  and Eqs. (6.11b) and (6.13b) can be used to solve for the pump’s net absorption rate,

$$\ell_p = \frac{\gamma_p^a}{1 + M_p/M_p^{\text{sat}}}, \quad (6.17)$$

where  $M_p^{\text{sat}} \equiv \zeta/(\gamma_p^e + \gamma_p^a)$ , the number of pump photons required to decrease the net pump absorption rate by one-half. Figure 6.15(a) plots  $\gamma_{\text{tot},p}$  for the resonance described in Fig. 6.14 as a function of  $M_p$ , along with a fit using Eq. (6.17). At low powers, the linewidth is largest because all  $\text{Er}^{3+}$  ions are in the ground state. The erbium ions quickly become inverted as the power is increased, requiring only  $M_p^{\text{sat}} = 700$  photons to bring half of the ions to the excited state. At the highest powers, all of the  $\text{Er}^{3+}$  ions are excited, indicated by the saturated emission shown in Fig. 6.15(b). The remaining unsaturable linewidth is a sum of scattering, linear absorption, waveguide coupling, and dark erbium ions with short lifetimes. The total change in linewidth is equal to the Giles parameter,  $\gamma_p^a \equiv v_{g,p}\sigma_p^a\Gamma_p\bar{N}_T = 1.9$  Grad/sec. From the measured FSR of 15.4 nm,  $n_g = \lambda_0^2/(2\pi R\Delta\lambda_{\text{FSR}}) \approx 2.3$ . At 1493 nm, a typical value for the pump absorption cross section is  $\sigma_p^a \approx 1.8 \times 10^{-25}$  m<sup>-3</sup> (see Fig. 6.5). Furthermore, assuming  $\Gamma_p \approx 0.4$ , the average ion concentration was estimated to be  $\bar{N}_T \sim 2.2 \times 10^{20}$  cm<sup>-3</sup>, a value consistent with Inplane Photonic’s estimates.

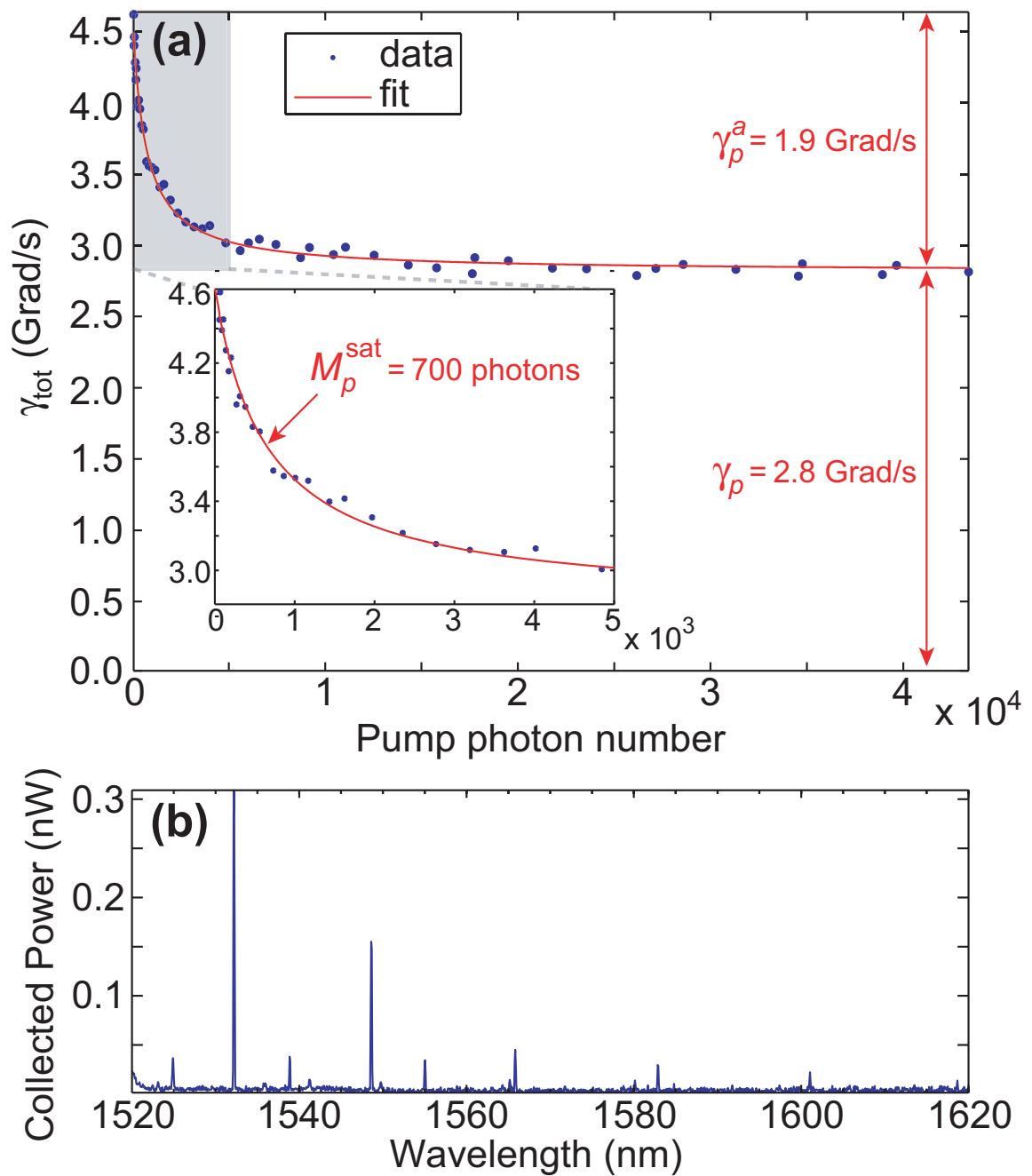


Figure 6.15: (a) Total linewidth for the resonance described in Fig. 6.14 as a function of stored pump photons. The data was taken from a  $10 \mu\text{m}$  radius silicon microdisk after a  $60 \text{ nm}$  thermal oxidation and  $300 \text{ nm}$  erbium-doped glass deposition. (b) OSA scan of saturated emission. (Resolution bandwidth was  $0.1 \text{ nm}$  and sensitivity was  $12 \text{ pW}$ .)

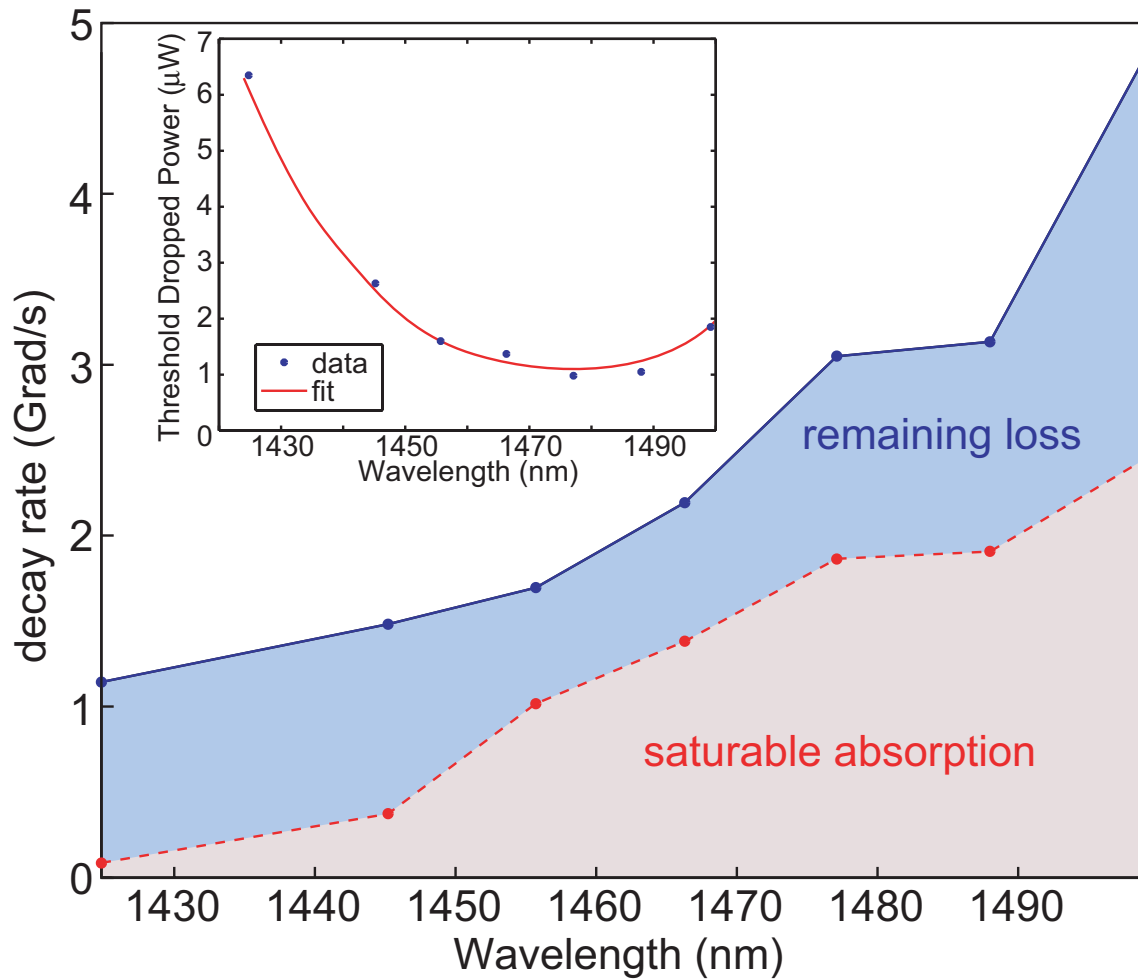


Figure 6.16: Loss characterization for a single family of modes in a  $20 \mu\text{m}$  radius fully oxidized microdisk after  $300 \text{ nm}$  of Er-doped cladding was deposited. Blue dots represent total “cold” decay rate and red dots represent measured  $\gamma_p^a$  at each wavelength for below-threshold data. (Inset) Threshold dropped powers needed to obtain lasing versus wavelength. Lasing was always single mode at  $1560.2 \text{ nm}$ , regardless of pump wavelength. Red curve in inset is a model for expected dropped power threshold using cross sections plotted in Fig. 6.5 and assuming  $\gamma_s = 1.3 \text{ Grad/s}$ .

All of the samples were able to achieve a similar amount of pump absorption saturation, consistent with the plots of  $\Gamma_{\text{Er}}$  from Fig. 6.7. In addition, saturation photon numbers as small as  $M_p^{\text{sat}} \approx 300$  were routinely measured on the 5  $\mu\text{m}$  radii microdisks. The saturated linewidth of 2.8 Grad/sec in Fig. 6.15(a) was a typical value for saturated linewidths on all high  $\Gamma_{\text{Si}}$  samples (i.e. 20, 40, and 60 nm thick buffer layers). These saturated linewidths were roughly 2–3 times larger than the typical linewidths of  $\sim 0.7\text{--}1.5$  Grad/sec prior to Er-doped cladding deposition. The increased  $\gamma_p$  extended across the entire 1420 – 1500 nm wavelength range, ruling out radiation losses and isolated but dark  $\text{Er}^{3+}$  ions. Furthermore, TE modes were found to be less susceptible to the loss increase, indicating that the source of the problem lies at the top/bottom Si surfaces or in the Er-doped cladding itself. As will be discussed in further detail below, the fully oxidized devices possessed a mitigated 1- to 2-fold increase in saturated linewidths(see Fig. 6.16), lending further evidence that the problem lies not within any individual material, but rather with material *interaction*. A likely cause of Er-doped cladding degradation on the high  $\Gamma_{\text{Si}}$  samples is strain from the free-hanging silicon core at the time of PVD. Reference [134] reported that clustered  $\text{Er}^{3+}$  ions in germanosilicate glass fibers had an extended unbleachable absorption spectra as compared to isolated ions. Thus, a small percentage of the otherwise active erbium ions could have clustered together or annealed improperly as a result of being deposited on the free-floating Si core. It is also possible that residual strain in the disk caused enhanced erbium ion diffusion through the host matrix, causing an increased clustering of  $\text{Er}^{3+}$  ions at the top and bottom Si surfaces.

As mentioned above, the fully oxidized and Er-doped cladding devices retained most of their pre-deposition quality factors. Figure 6.16 plots the low-power total decay rates and saturable absorption rates for a single family of modes in a 20  $\mu\text{m}$  radius fully oxidized microdisk after 300 nm of Er-doped cladding was deposited. The blue dots represent total “cold” decay rate, and the red dots represent the measured  $\gamma_p^a$  at each wavelength for below-threshold data. Each of these modes was coupled such that approximately 30% of the input power was coupled into the pump resonance. The most salient feature of these pump modes is that the saturated linewidths,  $\gamma_p$ , were less than the net absorption rate,  $\gamma_p^a$ . Assuming the modes in the 1500 nm

band have approximately the same decay rate as the pumps, this inequality strongly suggests that lasing can be achieved on this device. Indeed, single mode lasing at 1560.2 nm was observed for every mode plotted in Fig. 6.16. The inset to Fig. 6.16 plots the threshold dropped powers,  $P_d^{\text{th}} \equiv (1 - T)P_{\text{in}}$ , needed to obtain lasing versus wavelength. Threshold in this case was measured by a simple linear fit to above threshold L-L curves. The red curve in the inset is a model for expected dropped power threshold using cross sections plotted in Fig. 6.5 and assuming  $\gamma_s = 1.3$  Grad/s. A detailed analysis on the L-L data will be presented in Sections 6.3.8 and 6.3.9.

### 6.3.7 Identification of Optimum Pump Mode

The optimum mode to use for resonant pumping of the  $\text{Er}^{3+}$  ions is the one that has the lowest dropped power threshold while possessing the highest slope efficiency. Achieving a low threshold requires that the pump mode's optical loss be dominated by active erbium ions that are mutually overlapping with the laser mode. High slope efficiencies also require that the two modes approximately critically couple at the same taper position. These requirements oftentimes make finding the optimum mode a nontrivial task. For example, picking a pump mode from the same polarization and radial order as the laser mode usually guarantees a low threshold but does not necessitate large slope efficiencies because of phase matching considerations. The modes of a fiber taper typically have different dispersion than WGMs, preventing uniform coupling across hundreds of nanometers. Fortunately, a simple experimental technique can be used to identify the optimum pump mode within seconds.

Figure 6.17(a) plots a broad-scan transmission spectrum for the previously mentioned fully oxidized 20  $\mu\text{m}$  radius microdisk. All of the resonances seen in the figure are undercoupled, and families with FSR's  $\sim 11$  nm can be clearly seen. Utilizing the two photodetector configuration depicted in Fig. 6.13, the photoluminescence for each pump mode can be simultaneously collected at scan speeds up to 10 nm/s. Figure 6.17(b) plots the amount of collected power from  $\text{Er}^{3+}$  photoluminescence while scanning the pump laser. This type of plot is typically referred to as photoluminescence excitation (PLE) spectra and was popularly used to determine band structures of III-V semiconductors [135]. The most striking feature of Fig. 6.17 is that a second,

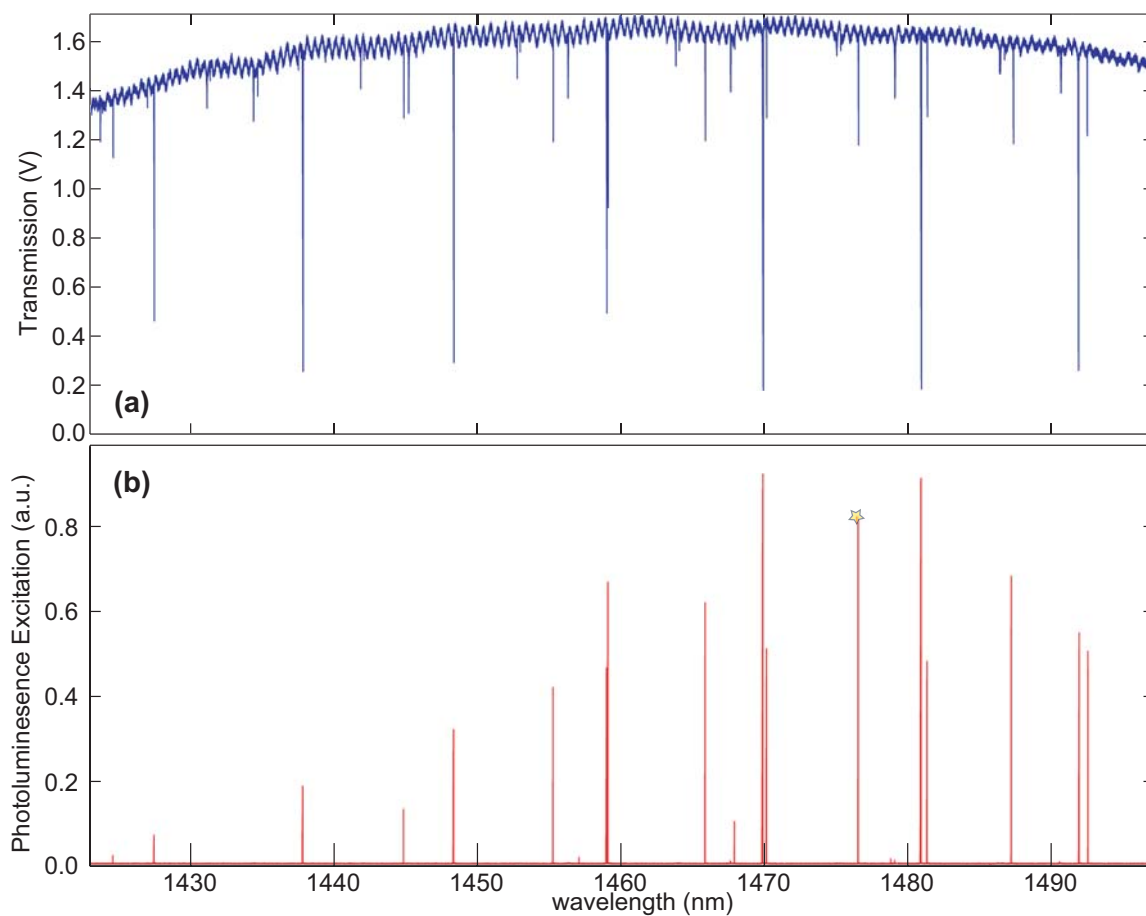


Figure 6.17: Broad external pump laser scan of an undercoupled fully oxidized  $20\ \mu\text{m}$  radius microdisk. Scan speed was  $10\ \text{nm/s}$ , and input power was  $670\ \mu\text{W}$ . (a) Undercoupled broad-scan transmission spectrum (b) Corresponding photoluminescence excitation spectrum. Starred mode shows highest external efficiency.

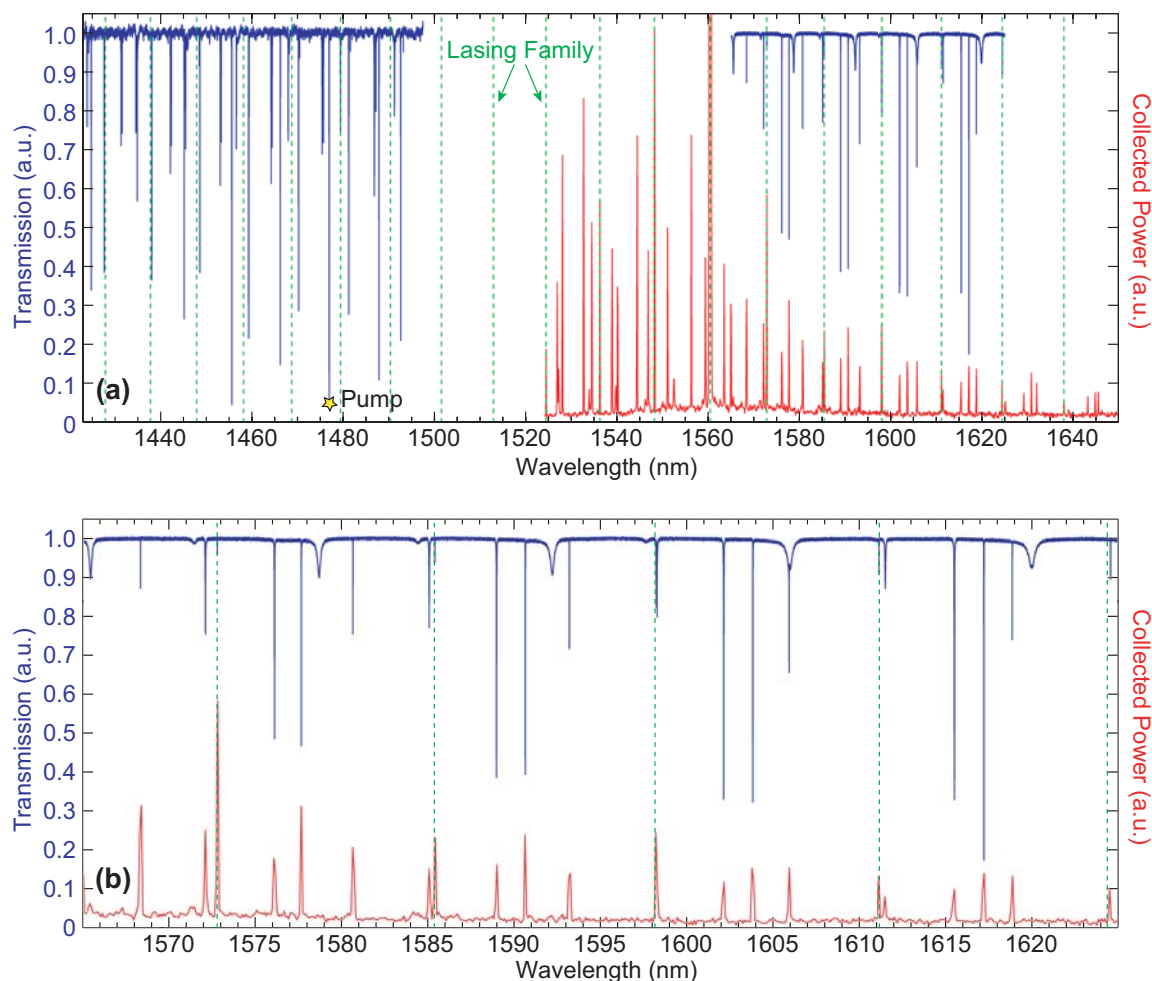


Figure 6.18: (a) Composite spectrum of a fully oxidized  $20\ \mu\text{m}$  radius microdisk. 1400 nm spectrum is normalized external pump laser scan, with taper position optimized for critical coupling to 1477.1 nm resonance. Red curve is normalized collected photoluminescence while pumping on 1477.1 nm resonance. Green dashed lines indicate the laser's family. 1560 nm spectrum is normalized external laser scan with  $1.4\ \mu\text{W}$  input power. (b) Zoomed-in view between 1560 – 1625 nm.

weakly coupled family produced almost the same amount of PLE as the dominant, deeply coupled family. Within seconds, this technique experimentally showed that the optimum external efficiency occurred using the 1477.1 nm resonance (starred in Fig. 6.17). Upon closer examination, the first family of modes was found to be radiation limited towards the red end of the scan range. In contrast, the second, optimum family showed no signs of being radiation limited and was the family used to produce Fig. 6.16.

Having found the optimum pump family, a set of follow-up experiments were conducted to characterize the laser and the rest of the photoluminescence. Figure 6.18(a)

shows a composite spectrum of the fully oxidized 20  $\mu\text{m}$  radius microdisk. The 1400 nm spectrum is a normalized external pump laser scan, with taper position now optimized for critical coupling to 1477.1 nm resonance and family. The red curve is the normalized collected photoluminescence while pumping on the 1477.1 nm resonance (starred in the figure) collected with an OSA and plotted on an arbitrary linear scale (the lasing mode is highly cropped). From the OSA spectrum, the lasing mode's family could be clearly identified, shown by vertical green dashed lines. The 1560 – 1625 nm spectrum (Fig. 6.18(b) shows a zoomed-in view) is a normalized external New Focus Vidia laser scan with 1.4  $\mu\text{W}$  input power, with the taper retracted to minimize waveguide loading on the lasing mode's family. Excellent correspondence between the Vidia scan and OSA spectrum can be seen, allowing an easy identification of the lasing mode's family in the transmission spectrum. The measured cold linewidths from blue to red were: {2.4, 1.7, 2.3, 1.4} pm, gradually improving with increased wavelength and decreased spectral overlap with the  $\text{Er}^{3+}$  transitions.

A third-order polynomial was used to extrapolate the lasing family's resonance locations into the 1400 nm band. Figure 6.19 shows a zoomed-in view of Fig. 6.18(a) between 1420 – 1500 nm, where the vertical green dashed lines represent the extrapolated lasing family resonance locations. Figure 6.19(b) plots the corresponding photoluminescence excitation spectrum, plotted on an arbitrary logarithmic scale (the highest peak is approximately two orders of magnitude larger than the smallest discernible peak). The lasing family cannot be seen in Fig. 6.18(a) because a resonance must couple with at least  $\sim 1\%$  of transmission contrast to be observable. By contrast, a small amount of photoluminescence excitation is observable where the lasing family should exist in the pump range even without any measurable transmission contrast. This is an excellent illustration of the nontrivial selection of an optimum pump mode. Had a critically coupled lasing family been used to pump the erbium ions, the waveguide loading on the lasing mode would have severely degraded the loaded linewidth, resulting in drastically increased thresholds.

With its high external efficiency, the 1477.1 nm resonance was used to determine the maximum amount of collected power that could be extracted from the microdisk. To accomplish this, the taper probe was moved laterally to and from the disk edge

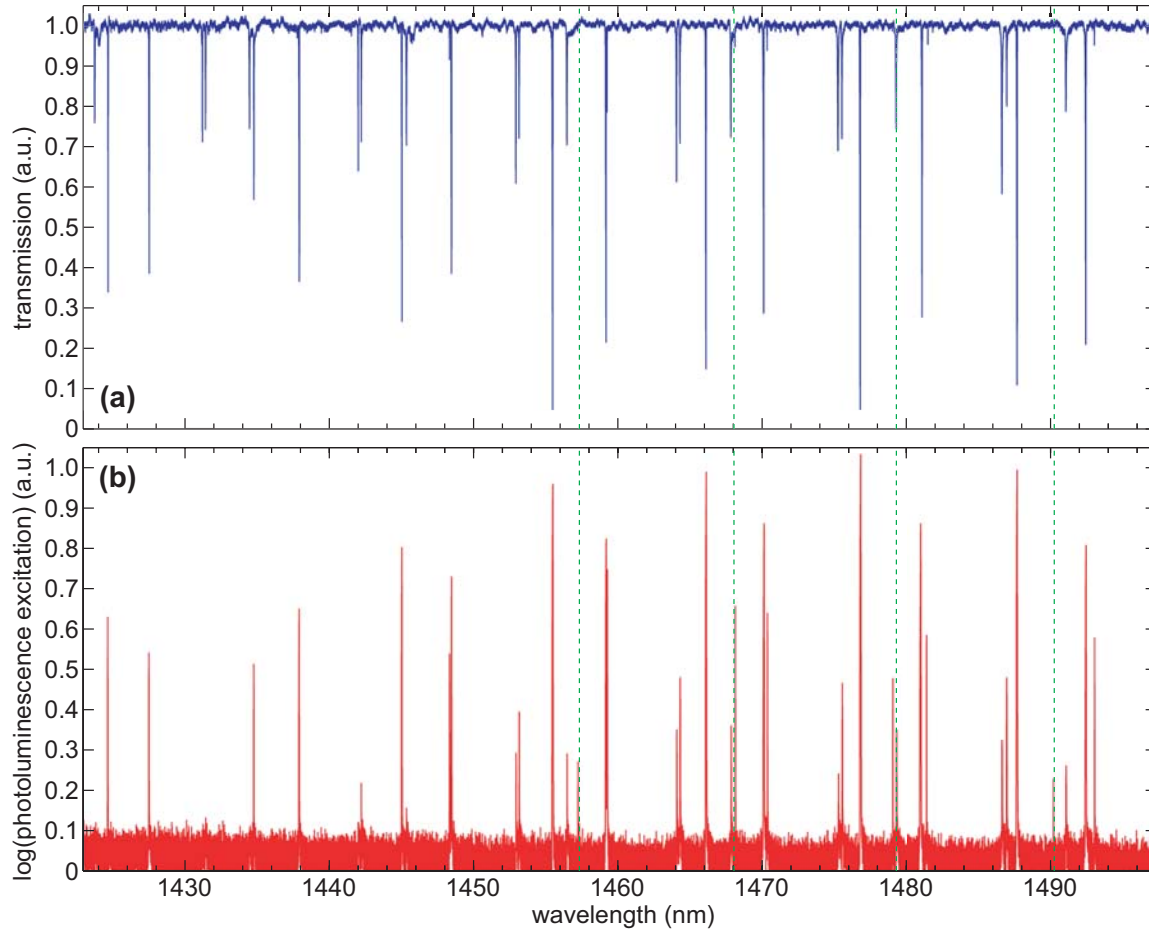


Figure 6.19: (a) Zoomed-in view of Fig. 6.18(a) between 1420 – 1500 nm. (b) Corresponding photoluminescence excitation spectrum, plotted on an arbitrary logarithmic scale (max peak to min peak is approximately two orders of magnitude). Green dashed lines indicate laser's family (seen only in PLE).

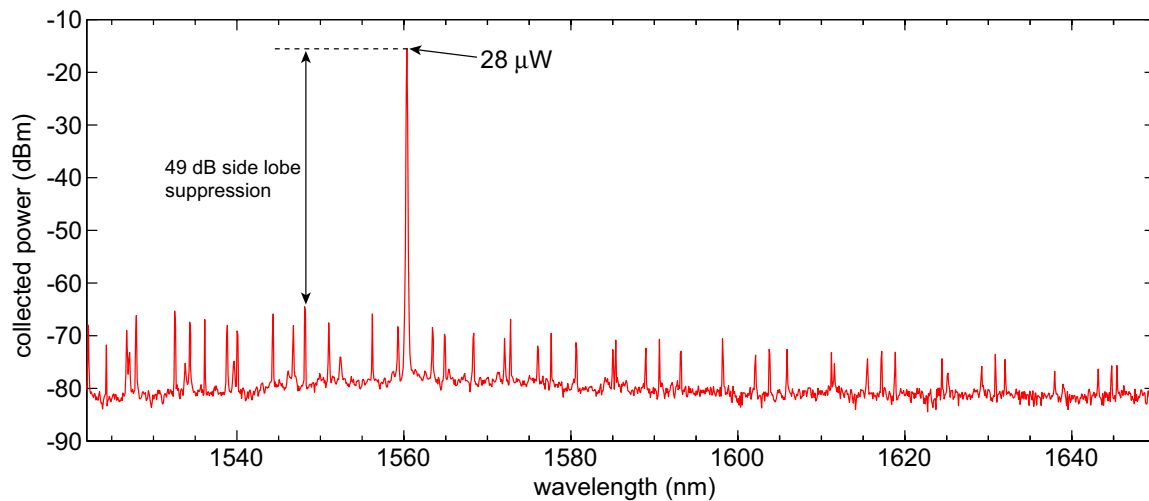


Figure 6.20: Unidirectional photoluminescence spectrum, pumped at 1477.1 nm with 600  $\mu\text{W}$  of input power. (Resolution bandwidth was 0.1 nm and video bandwidth was 60 Hz).

while repeatedly piezo-scanning across the pump resonance and monitoring the PLE on the second detector. At maximum PLE power, the external laser was tuned into resonance with the pump mode, and the OSA scan shown in Fig. 6.20 was taken. As seen in the figure, the microdisk maintained single mode lasing even at the highest available input power of  $600 \mu\text{W}$ , which provided  $28 \mu\text{W}$  of unidirectionally extracted power. As many technologies could easily use both forward and backward emission directions,<sup>7</sup> this amounts to an external efficiency of 9.4%. The rest of the power was lost primarily to other sources of pump and laser mode optical loss including reflected pump power from the standing waves, Rayleigh scattering, radiation loss, and linear absorption (including dark erbium ions). An additional source of loss is also the background spontaneous emission into all other modes. However, at maximum input power, 49 dB of side-lobe suppression was observed. Thus, even assuming  $\beta \sim 10^{-3}$ , spontaneous emission would account for 1% of the lost power at most.

### 6.3.8 Swept Piezo Scans

The rapid identification of the optimum pump modes relied on sweeping the DC motor on the New Focus Velocity lasers. However, the New Focus Velocity laser also possesses a high-resolution piezo tuning option, which allows external laser linewidth limited spectroscopy. Using the piezo to sweep across the optimum pump mode, a large amount of additional information can be attained by again using two-photodetectors to simultaneously collect the transmitted pump signal and the emitted signal power. Because of the increased stability afforded by piezo control, highly accurate L-L curves can be generated from the data. Figure 6.21 shows the swept piezo spectra of a fully oxidized  $20 \mu\text{m}$  radius microdisk after 300 nm erbium-doped glass deposition. Figure 6.21(a) plots four of the 26 normalized transmission spectra ranging from 0.1 to 38  $\mu\text{W}$  of input power. The black asterisks indicate the transmission minima. Just as in Section 6.3.6, the red curve is a doublet fit to the lowest power scan, and the fit parameters are listed in red. In contrast to the previous saturable absorption analysis, Fig. 6.21(b) also plots selected photoluminescence excitation spectra simul-

---

<sup>7</sup>An example would be to use the backward emission as a laser power tap and the forward direction as the usable signal.

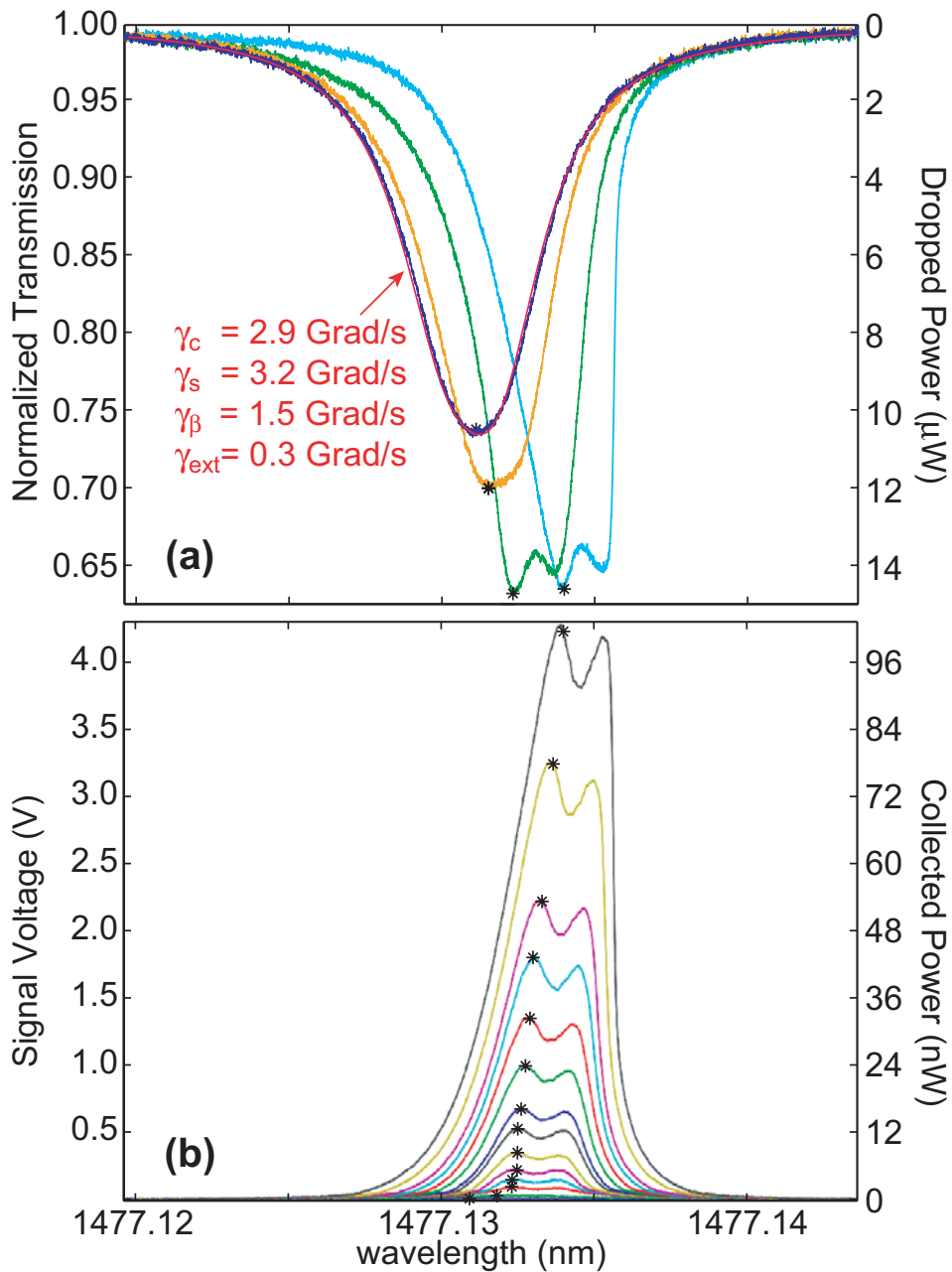


Figure 6.21: Swept piezo spectra of a fully oxidized  $20 \mu\text{m}$  radius microdisk after  $300 \text{ nm}$  erbium-doped glass deposition. (a) Selected normalized transmission spectra for  $0.1$  to  $38 \mu\text{W}$  of input power. The black asterisks indicate transmission minima. The red curve is a doublet fit to the lowest power scan, and fit parameters are listed in red. (b) Selected corresponding photoluminescence excitation spectra, along with black asterisks marking the “on-resonance” condition.

taneously collected during the transmission acquisition. The collected signal power,  $P_s$ , is the sum of the laser mode's power,  $P_L$ , and all other emission above 1500 nm,  $P_x = \sum_{m \neq L} P_m$ .

Because this data was collected in order to capture the transition from below to above threshold, the analysis presented in Section 6.3.6 must be modified slightly. Using the simplified Eq. 6.17 to model the pump absorption rate assumes that the pump mode possesses the only appreciable photon population, an assumption only valid below threshold. Figure 6.22 plots the total linewidth for the resonance described in Fig. 6.21 as a function of stored pump photons. The red curve is a saturable absorption fit using Eq. (6.17) for the below threshold data ( $M_p < 3000$ ) and was used to provide the spectroscopic data for Fig. 6.16. This fit yielded that the pump's saturated decay rate was  $\gamma_p = 1.4 \pm 0.1$  Grad/s while the pump's absorption Giles parameter was  $\gamma_p^a = 1.9 \pm 0.1$  Grad/s equal to that of the fit from Fig. 6.15 for the case of the 60 nm oxidation. Given that  $\gamma_p^a \equiv v_{g,p} \sigma_p^a \Gamma_p \bar{N}_T$ , a comparison of the average active erbium ion concentrations can be readily made. Using the measured FSR  $\sim 11$  nm, the pump modes have a group index of  $n_g = \lambda_0^2 / (2\pi R \Delta \lambda_{\text{FSR}}) = 1.57$ . Assuming again a pump-erbium overlap of  $\Gamma_p \approx 0.4$  and the cross-section of Fig. 6.5, the average  $\text{Er}^{3+}$  ion concentration for the pump mode is  $\bar{N}_T \sim 1.8 \times 10^{20} \text{ cm}^{-3}$ , a value again consistent with Inplane Photonic's estimates. The bottom portion of Fig. 6.22 shows a zoomed-in view of the excellent correspondence between the below threshold  $\gamma_{\text{tot}}$  and Eq. 6.17. From the saturable absorption fit, the pump photon saturation number was found to be  $M_p^{\text{sat}} \equiv \zeta / (\gamma_p^a + \gamma_p^e) = 600 \pm 150$  photons. Above threshold, it was observed that the pump's decay rate became constant because the lasing mode has clamped the available gain.

A more accurate model based on the full steady-state rate equations makes it possible to fit both the saturable absorption data as well as the collected signal with self-consistent assumptions. The resulting model, although more complicated than Eq. (6.17), provides extra information as well as an added degree of certainty regarding the physics of the microlaser system. The basic rate equation derivation of Section 6.3.3 remains unchanged, but now we must account for all erbium ion emission in a tractable way. By summing over all emitting modes except the laser

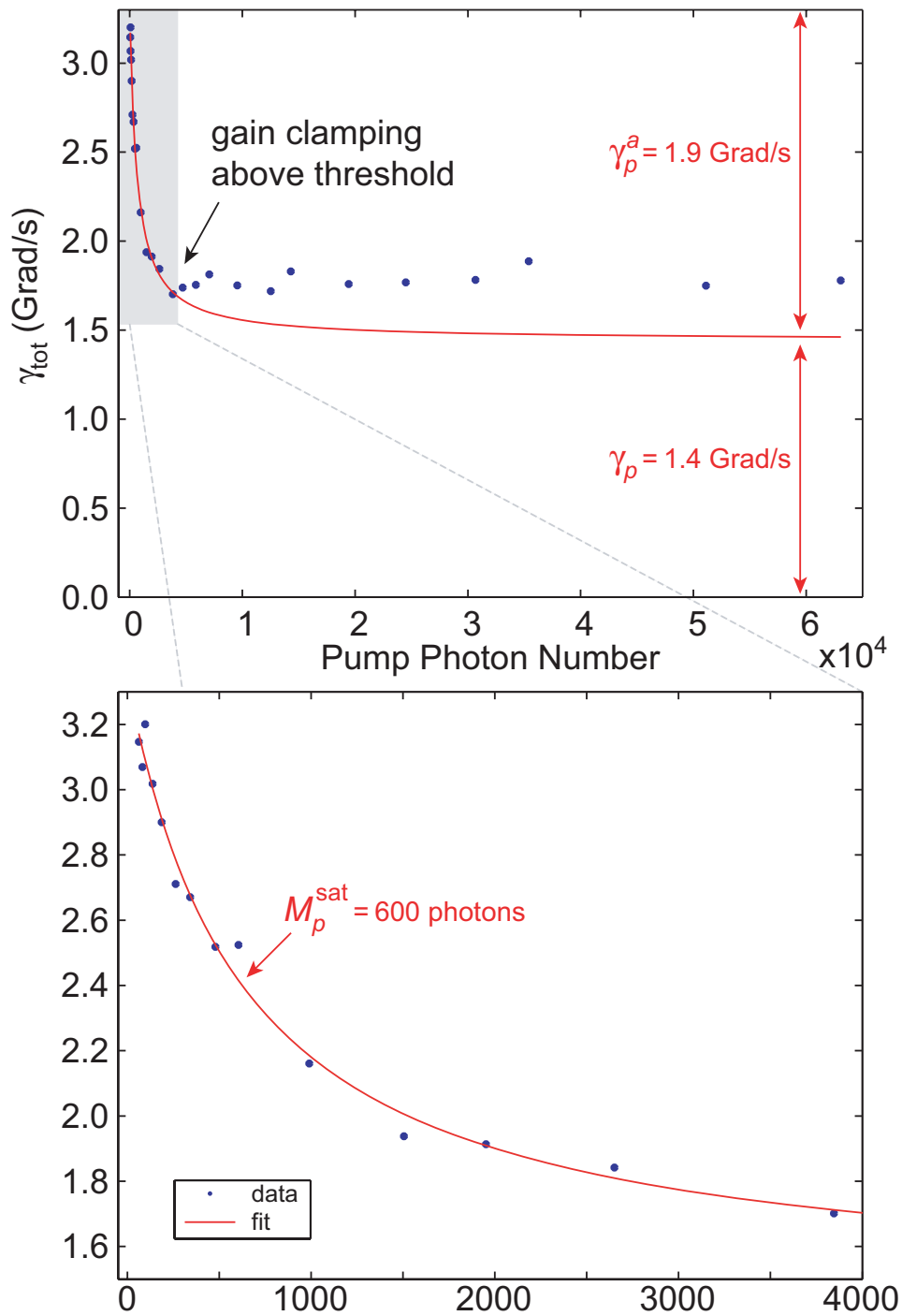


Figure 6.22: Total linewidth for the resonance described in Fig. 6.21 as a function of stored pump photons. The data was taken on a fully oxidized  $20 \mu\text{m}$  radius microdisk after 300 nm erbium-doped glass deposition. Red curve is a saturable absorption fit using Eq. (6.17) for the below threshold data ( $M_p < 3000$ ).

mode, Eq. (6.11a) can be used to find the total rate of change of “other” photons [50] given by

$$\frac{dM_x}{dt} = -(\bar{\gamma}_x - \bar{g}_x)M_x + (\zeta - \gamma_L^e)\frac{\bar{N}_2}{\bar{N}_T}, \quad (6.18)$$

where  $M_x \equiv \sum_{m \neq L} M_m$  is the total number of “other” photons, and  $\bar{\gamma}_x \equiv \sum_{m \neq L} \gamma_m (M_m/M_x)$  is an average decay rate for all background emitting modes weighted by the relative number of photons in each mode.  $\bar{\gamma}_x^e$ ,  $\bar{\gamma}_x^a$ , and  $\bar{g}_x$  are similarly defined as weighted averages over the background emitting modes. The last term in Eq. 6.18 is the total spontaneous emission rate into all background modes and used the fact that  $\sum_{m \neq L} \gamma_m^e = \zeta - \gamma_L^e$ . Thus, Eqs. (6.18), (6.13a), and (6.13b) can be used to find the new set of nonlinear equations that must be solved, and are given by

$$M_L = \frac{\gamma_L^e}{\gamma_L - g_L} \frac{\bar{N}_2}{\bar{N}_T} \quad (6.19a)$$

$$M_x = \frac{\zeta - \gamma_L^e}{\bar{\gamma}_x - \bar{g}_x} \frac{\bar{N}_2}{\bar{N}_T} \quad (6.19b)$$

$$\frac{\bar{N}_2}{\bar{N}_T} = \frac{\gamma_p^a M_p + \gamma_L^a M_L + \bar{\gamma}_x^a M_x}{\zeta + (\gamma_p^e + \gamma_p^a)M_p + (\gamma_L^e + \gamma_L^a)M_L + (\bar{\gamma}_x^e + \bar{\gamma}_x^a)M_x}. \quad (6.19c)$$

These equations must be solved self-consistently for each pump input power. Additionally, neither the number of stored laser photons,  $M_L$ , nor the number of stored background photons,  $M_x$ , are measured experimentally. Rather the experiment determines the total collected signal power,

$$P_s = P_L + P_x = \frac{\gamma_{\text{ext,L}}}{2} M_L \hbar \omega_L + \frac{\gamma_{\text{ext,x}}}{2} M_x \hbar \omega_x \quad (6.20a)$$

$$\approx \frac{\gamma_{\text{ext}}}{2} \hbar \omega_L (M_L + M_x), \quad (6.20b)$$

where the factor of 1/2 comes from the fact that the setup detects only one direction of the collected emission in the taper. Since the lasing mode occurs near the center of the gain region,  $\bar{g}_x \approx g_L$ . Assuming the spectral cross sections of Fig. 6.5 can be used to find all Giles parameters once  $\gamma_p^a$  is known, the remaining free parameters

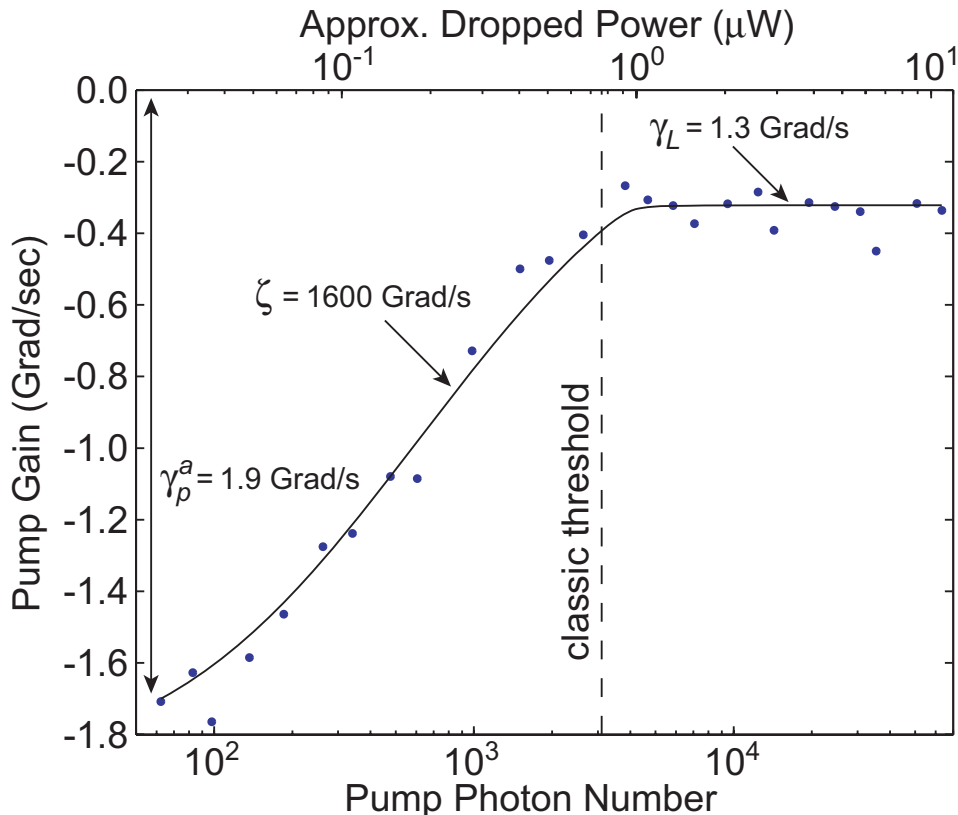


Figure 6.23: Pump gain ( $g_p \equiv \gamma_p - \gamma_{\text{tot},p}$ ) for the resonance described in Fig. 6.21 as a function of stored pump photons. The data was taken on a fully oxidized 20  $\mu\text{m}$  radius microdisk after 300 nm erbium-doped glass deposition. Black curve is a full rate equation fit using Eqs. (6.19a - 6.19c).

are  $\zeta$ ,  $\gamma_L$ , and  $\bar{\gamma}_x$ , and  $\gamma_{\text{ext}}$ .<sup>8</sup> Fortunately, each of these parameters can be uniquely determined from the data, creating an accurate model below and above threshold.

The linewidth data collected from the transmission minima,  $\gamma_{\text{tot},p}$ , was used to plot the pump gain,  $g_p = \gamma_p - \gamma_{\text{tot},p}$ , versus  $M_p$ , shown in Figure 6.23. The data has been plotted on a semilog scale in order to emphasize the below threshold data and the gain clamping at threshold. Figure 6.24 also plots the collected signal power versus the number of stored pump photons for the same dataset. The black curves are full rate equation fits using Eqs. (6.19a-6.19c), after optimizing the four fit parameters. As the system of equations is highly nonlinear, the parameter optimization was done in a piecewise fashion. The data was broken down into semi-orthogonal regions over which a single parameter was optimized.

The pump gain,  $g_p = \frac{\bar{N}_2}{N_T}(\gamma_p^e + \gamma_p^a) - \gamma_p^a$ , provides a sensitive measure of the fractional

<sup>8</sup>From this point forward,  $\gamma_{\text{ext}}$  will refer to the coupling rate for the signal modes, not the pump mode.

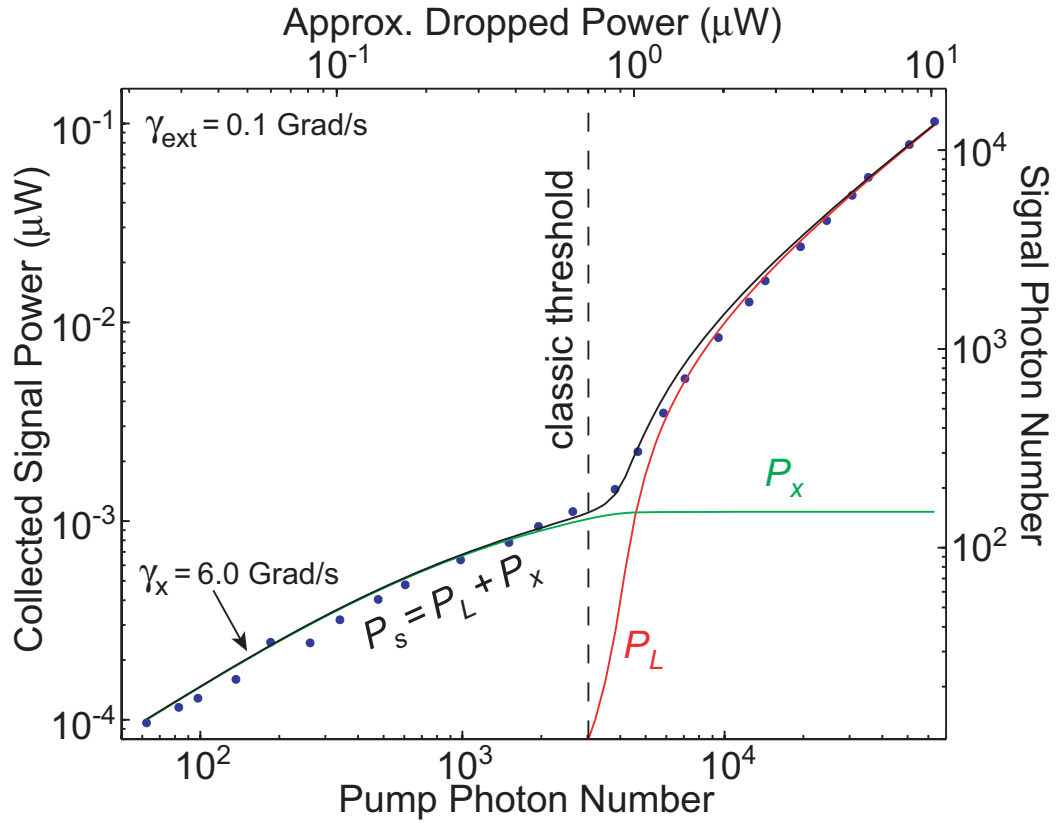


Figure 6.24: Collected signal power for the resonance described in Fig. 6.21 as a function of stored pump photons. The data was taken on a fully oxidized  $20 \mu\text{m}$  radius microdisk after 300 nm erbium-doped glass deposition. Red curve is collected lasing mode emission  $P_L = (\gamma_{\text{ext}}/2)(M_L \hbar \omega_L)$ , and green curve is collected spontaneous emission  $P_x = (\gamma_{\text{ext}}/2)(M_x \hbar \omega_x)$  from all other modes. Black curve is total collected power  $P_s = P_L + P_x$ .

erbium ion concentration. As a result, the total modal emission rate,  $\zeta$ , can be most accurately determined from the fits to  $g_p$  in Fig. 6.23. Using a least-squares fit for the below threshold data, the total modal emission rate was determined to be  $\zeta = 1600$  Grad/s, which is consistent with a  $M_p^{\text{sat}} \equiv \zeta/(\gamma_p^a + \gamma_p^e) = 600$  found from the saturable absorption analysis. Similarly, a least-squares fit for the above threshold  $g_p$  and  $P_s$  data was used to optimize  $\gamma_L = 1.3$  Grad/s, a slightly smaller decay rate than the pump's saturated decay rate of  $\gamma_p = 1.4$  Grad/s. The collected signal power above threshold was used in order to determine  $\gamma_{\text{ext}} = 0.1$  Grad/s, and the below threshold signal power was used to fit the average spontaneously emitting modal decay rate,  $\bar{\gamma}_x = 6.0$  Grad/s. This decay rate was consistent with the average measured linewidths from the Vidia scan of Fig. 6.18 where the linewidths ranged from 1.2 to 17 Grad/s for deeply coupled modes. As this data/parameter orthogonalization was not exact, the above procedure was iterated until good convergence by visual inspection had been reached. A noteworthy example is that the choice of  $\bar{\gamma}_x$  has a small affect on the shape of  $g_p$  below threshold because spontaneously emitting modes can use up some of the available gain if the stored photon numbers become appreciable compared to  $M_p$ .

Because the density of modes is significantly changed for  $\beta > 10^{-3}$ , great care in discussing thresholds must be used for small mode volume lasers [129–131]. Having determined  $\zeta$  accurately, the beta factor for this laser mode can be easily calculated as  $\beta = \gamma_L^e/\zeta = 2 \times 10^{-3}$ . Thus, this microlaser system is in the nebulous region where Purcell-type effects can just begin to be seen. Using the classic definition of laser threshold, round-trip gain must equal roundtrip loss for the lasing mode,  $g_L \simeq \gamma_L$ . Strictly speaking, this equality could never exist in steady-state because of the spontaneous emission term of Eq. (6.11a) and the requirement of finite photon populations. An alternate definition has been proposed by G. Björk and A. Karlsson and Y. Yamamoto in Ref. [131] and is given by the pump power or photon number that is needed to bring the mean lasing mode photon number to unity. Still a third and much cruder definition of laser threshold is to extrapolate a linear fit above threshold back to zero laser power. As will be seen, these definitions vary by up to a factor of six. Despite the large discrepancy, the classic definition proves to be quite adept at

predicting where the “kink” exists in the microlasers under study here, an intuition satisfying requirement of threshold.

Using the classic definition of threshold,  $g_L \simeq \gamma_L$ , the fractional ion inversion,  $\hat{N}_2 \equiv \bar{N}_2/\bar{N}_T$ , at threshold is

$$\hat{N}_2^{\text{th}} \simeq \frac{\gamma_L + \gamma_L^a}{\gamma_L^e + \gamma_L^a}, \quad (6.21)$$

which is  $\hat{N}_2^{\text{th}} = 0.65$  from the previous rate equation fits. Assuming only pump photons have an appreciable population at threshold, Eq. (6.19c) can be used to find that the fractional ion inversion is also given in terms of  $M_p$  by

$$\hat{N}_2^{\text{th}} \simeq \frac{\gamma_p^a M_p^{\text{th}}}{\zeta + (\gamma_p^e + \gamma_p^a) M_p^{\text{th}}}, \quad (6.22)$$

where  $M_p^{\text{th}}$  is the number of stored pump photons at threshold. Solving Eqs. (6.21) and (6.22) for  $M_p^{\text{th}}$  yields

$$M_p^{\text{th}} = \frac{\hat{N}_2^{\text{th}}}{\hat{N}_2^{\text{max}} - \hat{N}_2^{\text{th}}} M_p^{\text{sat}}, \quad (6.23)$$

where  $\hat{N}_2^{\text{max}} \equiv \gamma_p^a/(\gamma_p^e + \gamma_p^a)$  is the maximum possible fractional inversion in the absence of lasing and is a function only of the spectrally dependent cross sections. Equation (6.23) shows that as long as  $\hat{N}_2^{\text{th}} < \hat{N}_2^{\text{max}}$ , lasing is always possible. Furthermore, it states that the threshold pump population will be equal to the saturation pump population if the threshold inversion is half of its maximum possible inversion. For the cross sections assumed in Fig. 6.5,  $\hat{N}_2^{\text{max}} = 0.78$  at 1480 nm. Thus, the classic definition of threshold for this microlaser system is  $M_p^{\text{th}} = 3100$  stored pump photons and is plotted by a vertical dashed line in Figs. 6.23 and 6.24. As can be seen in the figures, the classic threshold also occurs for a dropped power of  $P_d^{\text{th}} = 690$  nW, a value nearly equal to the lowest threshold erbium-doped microlaser to date [118]. Interestingly, the classic threshold occurs when there are  $M_L^{\text{th}} \simeq 14$  laser mode photons in the cavity. Had  $M_L^{\text{th}} = 1$  been used as the threshold condition, the required pump photon number,  $M_p^{\text{th}} = 700$ , would have decreased by more than a factor of four.

Up until this point, the quoted powers have always been dropped power. Dropped

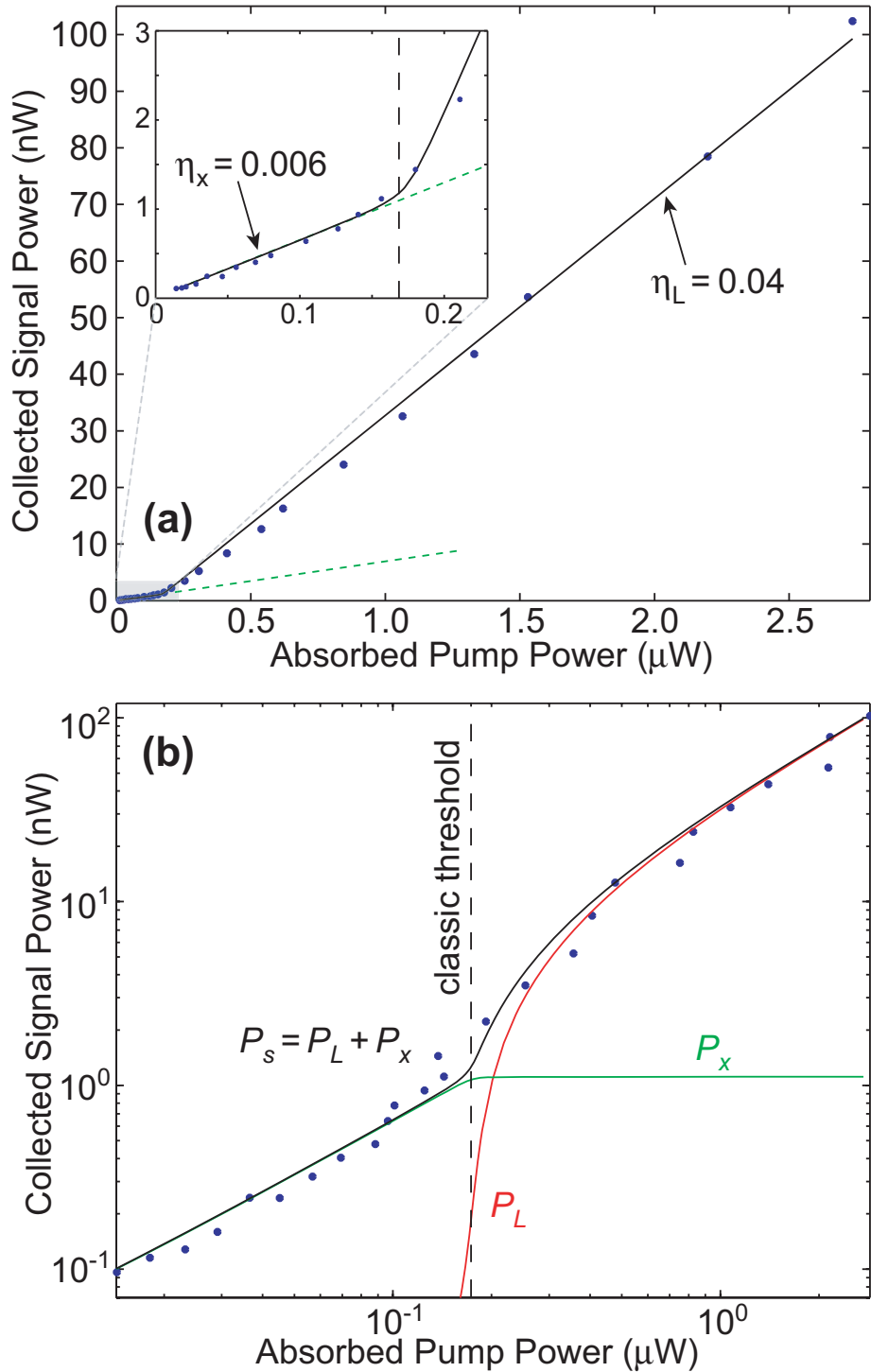


Figure 6.25: (a) Collected signal power for the resonance described in Fig. 6.21 as a function of absorbed power,  $P_{\text{abs}} = \ell_p(M_p \hbar \omega_p)$ . The data was taken on a fully oxidized  $20 \mu\text{m}$  radius microdisk after 300 nm erbium-doped glass deposition. Red curve is collected lasing mode emission  $P_L = (\gamma_{\text{ext}}/2)(M_L \hbar \omega_L)$ , and green curve is collected spontaneous emission  $P_x = (\gamma_{\text{ext}}/2)(M_x \hbar \omega_x)$  from all other modes. Black curve is total collected power  $P_s = P_L + P_x$ . (b) logarithmic version of (a) to emphasize low-power region.

power is the most technologically relevant power to quote because erbium-doped cladding lasers are expected to operate in a  $1 \times N$  fanout type configuration, where one external source of semi-coherent light pumps  $N$  single-mode lasers. Thus, the power not dropped to the first laser is available to pump the next laser and so on. In contrast, many excellent experimental microlaser papers [42, 118, 124, 125] choose to use the terminology “absorbed power” as the label for the L-L plot’s abscissa. These treatments usually make assumptions on the fraction of lost pump power that is effectively “absorbed” by the gain medium. One novel aspect of the analysis presented here is that an assumption regarding pump efficacy is not necessary because the time rate of pump absorption  $\ell_p$  is a measured quantity. Thus the true absorbed power can be written as  $P_{\text{abs}} = \ell_p(M_p \hbar \omega_p)$ . Figure 6.25 plots the collected signal power against the true absorbed power in linear and logarithmic scales. As before, the red curve is the collected lasing mode emission  $P_L = (\gamma_{\text{ext}}/2)(M_L \hbar \omega_L)$ , the green curve is the collected spontaneous emission  $P_x = (\gamma_{\text{ext}}/2)(M_x \hbar \omega_x)$  from all other modes, and the black curve is the total collected signal power  $P_s = P_L + P_x$ . When plotted versus  $P_{\text{abs}}$ , the laser’s classic threshold becomes  $P_{\text{abs}}^{\text{th}} = 170$  nW, four times smaller than what it was for the dropped power.

An analysis of the differential efficiencies for each optical mode provides essential insight into the performance characteristics of the microlaser system, including the large discrepancy between the dropped versus absorbed power thresholds. The interpretation of saturable absorption measurements such as that seen in Fig. 6.22 can be readily recast in terms of a pump efficiency. The loss channels for the dropped pump power are intrinsic losses, net active erbium absorption, and coupling into the backward fiber taper mode. Thus the fraction of dropped power that is absorbed by the  $\text{Er}^{3+}$  ions can be written as a pumping efficiency,  $\eta_p$  according to

$$\eta_p \equiv \frac{P_{\text{abs}}}{P_d} = \frac{\ell_p}{\gamma_{i,p} + \gamma_{\text{ext},p}/2 + \ell_p}. \quad (6.24)$$

The reason that only half of  $\gamma_{\text{ext}}$  is used in this definition is that the forward coupling loss into the taper is effectively not dropped into the resonator at all. Because  $\ell_p$  is a function of dropped power,  $\eta_p$  is also a function of pump power. As can be

seen in Fig. 6.22, the pump efficiency drops from 58% to 20% as the input power is increased, making the erbium ions more transparent. Furthermore it can be seen that at threshold,  $\eta_p = 0.25$ , which accounts for the factor of four discrepancy between the dropped versus absorbed power thresholds.

Well above threshold, spontaneous emission becomes negligible. In the absence of nonradiative recombination, this implies that the rate of absorbed pump photons must equal the rate at which the laser mode loses photons,  $\ell_p M_p \simeq \gamma_L M_L$ , which accounts for the linearization of such a nonlinear phenomena (see Fig. 6.22). Thus the quantum efficiency of pump to laser photon conversion is  $\eta_L^{\text{qu}} = \ell_p / \gamma_L$  well above threshold. Because  $\ell_p$  was clamped at 0.3 Grad/s above threshold, the quantum efficiency for this microlaser system was found to be 24%. Below threshold, the number of laser mode photons is negligible. In this regime, Eq. (6.11b) and (6.18) can be used to show that the rate of absorbed pump photons equals the rate at which the spontaneously emitting modes lose photons,  $\ell_p M_p \simeq \bar{\gamma}_x M_x$ . This implies that the quantum efficiency of pump to “other” photon conversion is given by  $\eta_x^{\text{qu}} = \ell_p / \bar{\gamma}_x$  below threshold, a rapidly decreasing function of input power.

The inability to define constant slope efficiencies for  $\{M_x, M_L\}$  versus  $M_p$  or  $P_d$  underscores the utility of being able to accurately represent the true absorbed power. As can be seen in Fig. 6.25,  $P_s$  versus  $P_{\text{abs}}$  is extremely linear both above and below threshold. For both cases, the slope efficiency is simply equal to the signal collection efficiency,

$$\eta_{\text{slope}} = \begin{cases} \eta_x = \frac{\gamma_{\text{ext}}/2}{\bar{\gamma}_x} & \text{below threshold} \\ \eta_L = \frac{\gamma_{\text{ext}}/2}{\gamma_L} & \text{above threshold} \end{cases} \quad (6.25)$$

When plotted against absorbed power, the change in slope at threshold from  $\eta_x = 0.006$  to  $\eta_L = 0.04$  is due solely to the change in loss of the dominant signal modes. Thus, if all modes within the gain region had similar decay rates, no kink would be observable at all. Obviously this predicted behavior rests on the assumption that no nonradiative recombination exists that stimulated emission would have to overwhelm.

While the high-resolution data presented above allows for a realistic rate equation model to be developed, neither the output powers nor the collection efficiencies were

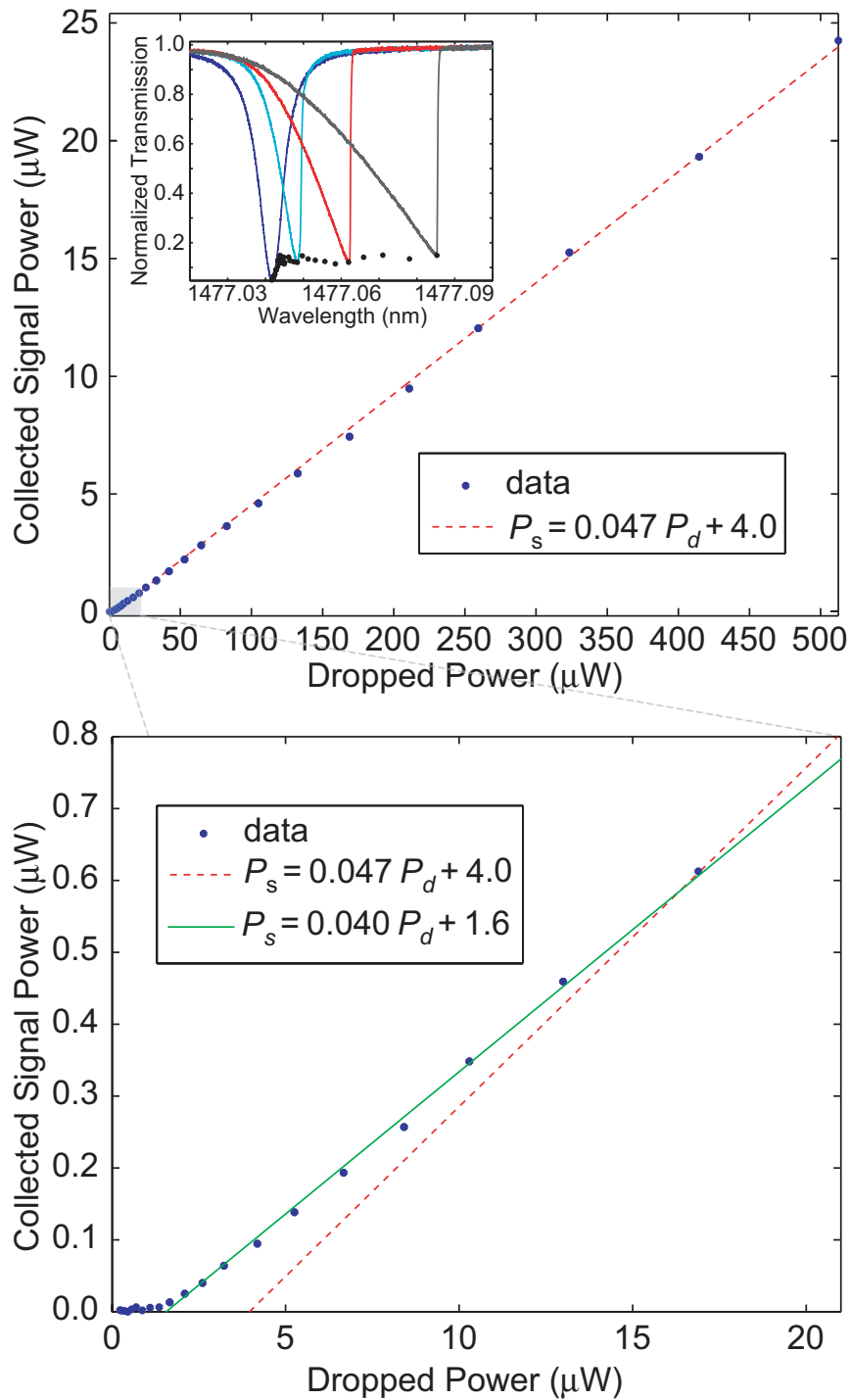


Figure 6.26: (a) High-power data showing collected signal power for the resonance described in Fig. 6.21 as a function of dropped power. The data was taken on a fully oxidized  $20 \mu\text{m}$  radius microdisk after  $300 \text{ nm}$  erbium-doped glass deposition. (Inset) Normalized transmission versus wavelength for several input powers. (b) Zoomed-in view of the low power end of the dataset. Red dashed curve is a linear fit to all above threshold data, and green curve is a linear fit to above threshold data for  $P_d < 20 \mu\text{W}$ .

optimal for technological purposes. In order to be detectable at high speeds, laser output powers of tens of microwatts are necessary. In addition, the external efficiencies,  $\eta_{\text{ext}} \equiv P_s/P_d$  for the previous analysis were too low for most chip-based laser applications at  $\eta_{\text{ext}} = \eta_L \cdot \eta_p = 0.008$ . However, at high powers a slightly increased threshold becomes less important, so the fiber taper can be adjusted such that a maximum amount of collected signal power is obtained. Figure 6.26 shows an L-L curve of collected signal power versus dropped power for the pump and laser modes previously described, but after optimizing signal power with taper position. As can be seen in the inset, maximum signal power occurs when the pump is slightly overcoupled. For an overcoupled pump mode, an increase in input power results in a *decrease* in transmission depth because the increase in pump  $Q$  pushes it further into the overcoupled regime. Utilizing a simple linear fit to the high power data, a measured unidirectional external efficiency of  $\eta_{\text{ext}} = 0.047$  was obtained. Assuming both directions of laser output could be utilized, this implies a bidirectional external efficiency of  $\eta_{\text{ext}} = 0.094$  was demonstrated, a number suitable for real-world technologies. The bottom portion of the figure highlights a deficiency in crudely measuring thresholds with a linear fit to above threshold powers. The red dashed curve is a linear fit to all above threshold data and quotes a threshold of  $4 \mu\text{W}$ , whereas the green curve is a linear fit to above threshold data for  $P_d < 20 \mu\text{W}$  and quotes a threshold of  $1.6 \mu\text{W}$ . Clearly the subtle differences between the two linearized slopes result in drastic differences in extrapolated threshold. Though a variety of subtleties can cause the slight increase in external efficiency with increased dropped power, the most likely cause is the continued erbium inversion at the very tails of the optical modes. This effect would have been captured by the computationally intensive integro-differential form of the rate equations.

### 6.3.9 Stepped Piezo OSA Scans

While extremely rapid and informative, a minor disadvantage of the preceding swept piezo analysis is the lack of spectral content for the erbium emission. An optical spectrum analyzer (OSA) has the ability to accurately separate the emitted power into the respective optical resonances of the microcavity. Unfortunately, the typical scan

times for high-sensitivity OSA measurements are on the order of tens of seconds, which make OSA generated L-L curves time-consuming at best. To make matters worse, the pump resonance will inevitably shift small amounts due to thermal fluctuations and potentially large amounts due to thermal bistabilities present in the microresonator. These resonance shifts make any attempt at individually maximizing the dropped power for every value of input power an impossibly tedious task. Fortunately an alternative solution exists. By holding the input power fixed, the dropped power can be accurately varied by “stepping” the piezo voltage across the resonance. At each step, an OSA scan is recorded for that amount of detuning from the resonance and commensurate dropped power. The major advantage of this procedure is that the time per scan is kept to exactly that needed by the OSA to take a spectrum.

Figure 6.27 shows transmission and OSA spectra used for a stepped piezo L-L curve. In part (a), the blue curve is a swept piezo scan taken immediately prior to stepping the piezo voltage (red dots) down the resonance for a fixed input power of  $P_{\text{in}} = 6 \mu\text{W}$ . The  $\sim 1$  pm drift was caused by small temperature shifts between the sample and external laser over the course of the 60 stepped scans. At each piezo step, an OSA spectrum was collected, and Fig. 6.27(b) shows a representative OSA spectrum taken just above laser threshold (marked with a star in part (a)). The coupling depth was chosen to correspond with the low power swept piezo analysis of Section 6.3.8. The experimental apparatus was as depicted in Fig. 6.13 with the optical attenuators adjusted to give the best S/N on the transmitted pump signal for the fixed input power. The Velocity 6328 piezo tuning was stepped using the GPIB controlled DC-offset of an Agilent 33120A Arbitrary Waveform Generator. The OSA scanned from 1565 to 1565 nm, at 0.1 resolution bandwidth and 200 Hz video bandwidth, in order to collect emission from five optical modes including the laser mode. The scan range was chosen to extend over only part of the gain region in order minimize the total experiment time while also collecting a sufficient number of high sensitivity data points. “Collected power” refers to the amount of power collected into the forward direction of the fiber taper and was calculated by subtracting half the 1.2 dB taper loss and the 0.6 dB insertion loss from the JDS demultiplexer.

Section 6.3.8 always used the transmission minimum in order to fix the detuning

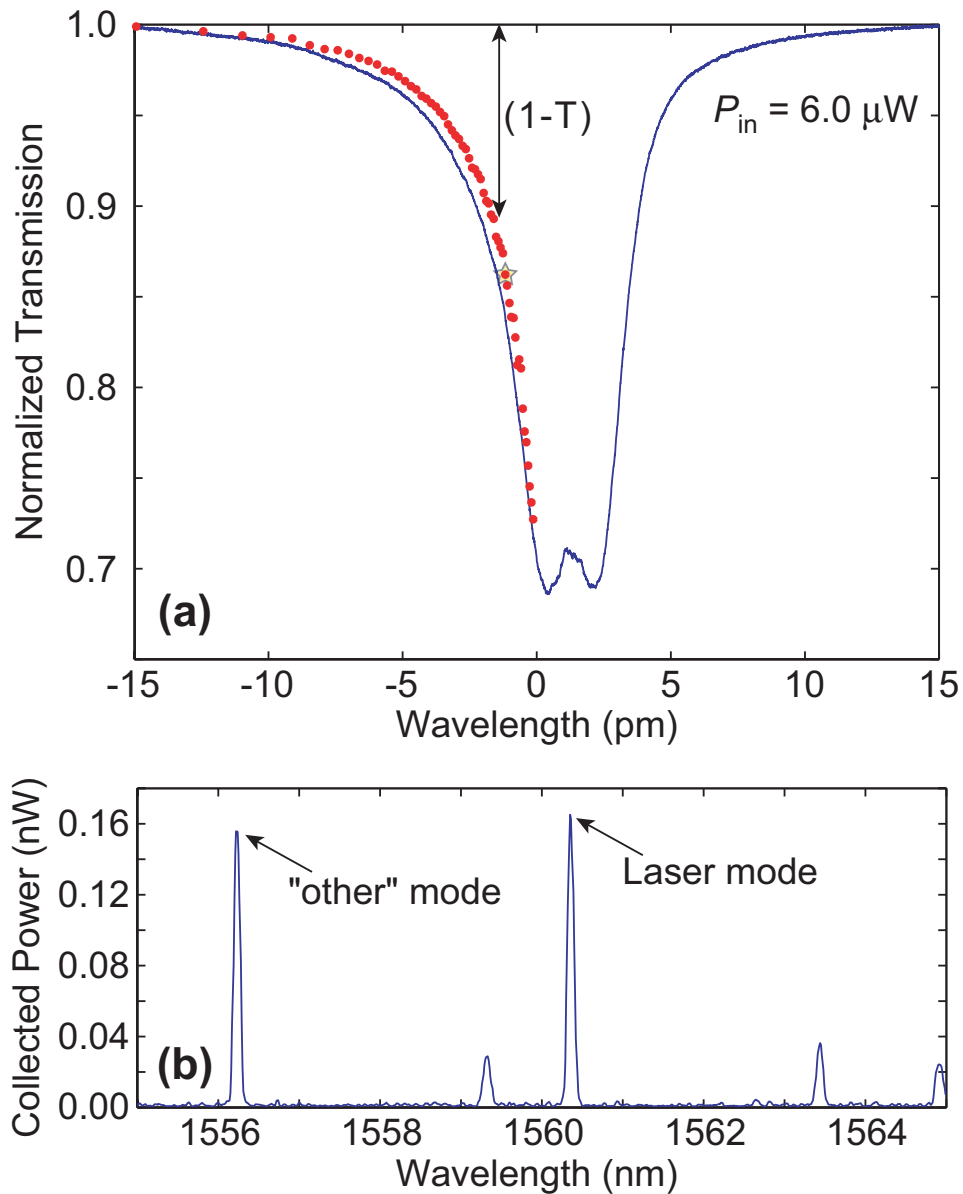


Figure 6.27: Transmission and OSA spectra used for a stepped piezo L-L curve. (a) Blue curve is a swept piezo scan taken immediately prior to stepping the piezo voltage (red dots) down the resonance for a fixed input power. An  $\sim 1$  pm drift caused by small temperature shifts between sample and external laser over the course of the stepped scan. (b) A representative OSA spectrum for each stepped piezo voltage. The specific scan was chosen to be near laser threshold and is marked with a star in (a).

from the resonance,  $\delta\omega$ , which allowed the accurate estimate of the number of stored pump photons,  $M_p$ . In this case, the amount of detuning is a power and external wavelength dependent process. To adequately model the transmission spectrum, the solution for the steady-state behavior of the interactions between the thermodynamics and the various loss and gain mechanisms must be solved for each step. As many of the thermal parameters are unknown for this microcavity, a simpler approach was adopted. By only coupling to the “far side” of one of the standing-wave resonances, a good approximate form for the number of pump photons can be found from power conservation and the definition of  $Q$ . Assuming that all dropped power is lost to intrinsic losses, erbium ion absorption, and backward coupling into the taper, the number of pump photons is approximately

$$M_p \approx \frac{P_d}{(\gamma_{i,p} + \ell_p + \gamma_{\text{ext},p}/2)\hbar\omega_p}. \quad (6.26)$$

The intrinsic decay rate used in this formula is the dominant standing wave that is being coupled to (the short wavelength in Fig. 6.27).  $\ell_p$  was approximated by fitting the saturable absorption data versus dropped power shown in Fig. 6.22. For fixed but unequal intrinsic standing wave losses, Eq. (6.26) has less than a 2% error when compared to the true spectral dependence of stored cavity energy.

Using Eq. (6.26) to estimate the number of stored pump photons, Fig. 6.28 shows the L-L curve for the data extracted from the stepped piezo OSA scans plotted on both linear and logarithmic scales. The blue dots represent the laser mode’s photon population,  $M_L$ , while then green circles represent a typical strongly coupled but nonlasing mode at 1556.3 nm (marked in Fig. 6.27). The noise floor of the measurement was approximately one stored photon and is marked by the horizontal dotted black line. The red curve is a rate equation fit for  $M_L$  based on Eqs. (6.19a–6.19c). The parameters used in the rate equation fit were exactly the same as for the swept piezo data with the exception of a slightly modified  $\gamma_{\text{ext}}$  in order to account for slightly different taper positions. Initial fits excluding  $M_x$  from the analysis suffered from an inability to properly model the laser mode’s below threshold L-L behavior; it was not until the PLE-based fit from Section 6.3.8 was applied that excellent

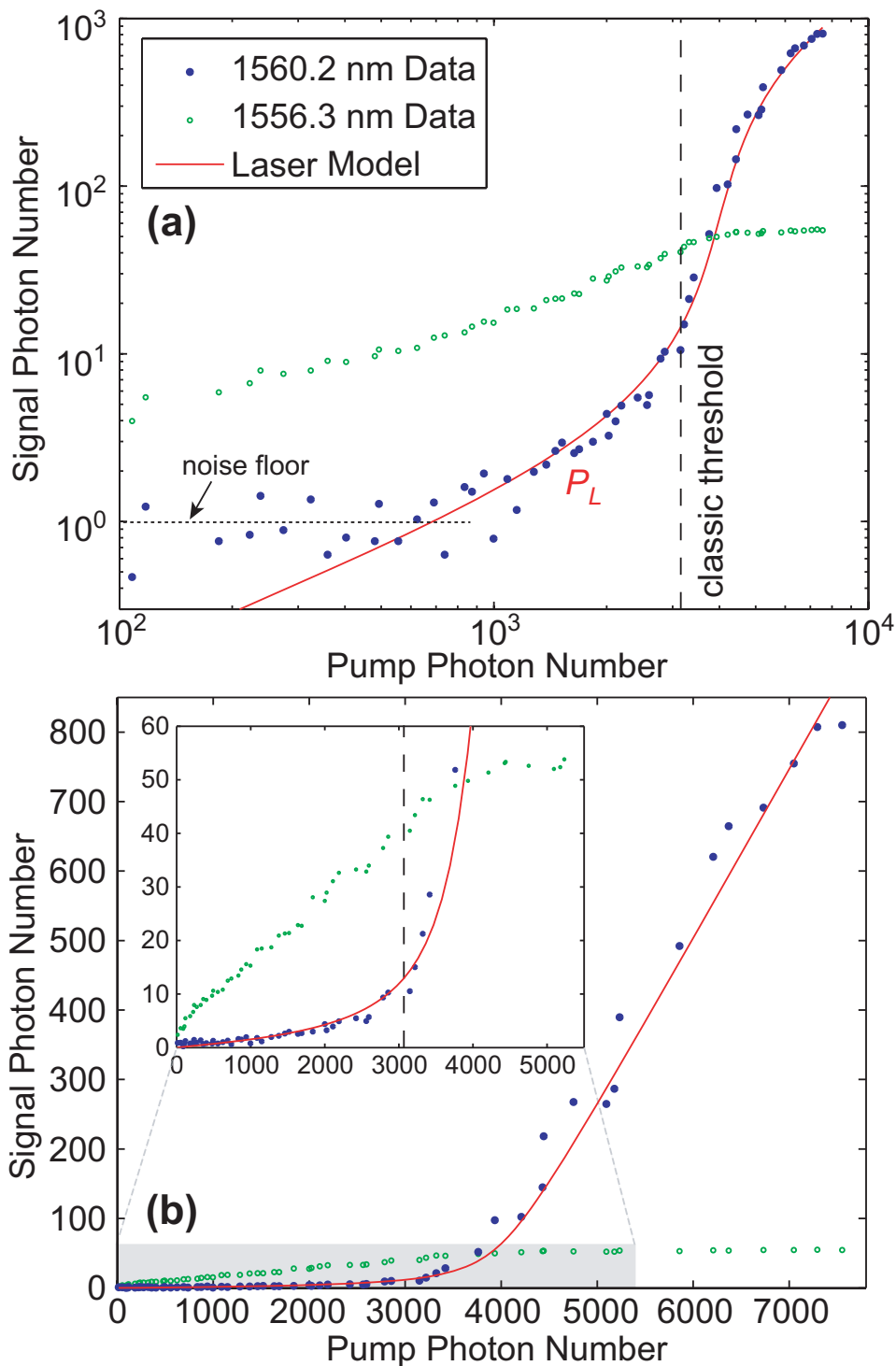


Figure 6.28: L-L curve for data extracted from stepped piezo scans. Blue dots represent laser mode's photon population while green circles represent a typical strongly coupled but nonlasing mode at 1556.3 nm. Red curve is the same fit as used in Fig. 6.24 except for a slightly modified  $\gamma_{\text{ext}}$  to account for slightly different taper positions. (b) Linear scale of (a) with inset of threshold region.

agreement for all values of  $M_L$  was observed. The addition of the other spontaneously emitting modes into the rate equation fits was essential because the other modes stole gain that otherwise allowed a premature build-up of  $M_L$  below threshold. As can be clearly seen in the 1556.3 nm mode's data, it was not until the laser mode built up  $M_L \sim 50$  photons that spontaneous emission was completely clamped.

## 6.4 Outlook

The success of a such a simple rate equation model is a testament to the future viability of erbium-doped cladding microlasers. Silicon microdisks have proved to be an excellent prototypical device to measure the various material properties and solve the many technological challenges. Approximate and numerically exact models of the microdisks were developed to aid in understanding the rich transmission spectra. Electron-beam lithography, resist reflow, and low-DC bias etches were developed to create highly circular and smooth microdisks. Dimpled fiber taper probes mounted inside a sophisticated test setup allowed for the rapid characterization of the microdisks. Wet chemistries and encapsulation layers were optimized to ensure the quality factors could be maintained in real-world scenarios. Silicon's opportunities and limitations were made clear through the development of a deep understanding of the complex nonlinear dynamics present in high- $Q$  semiconductor cavities. Finally, ultra-low threshold and high-efficiency lasers were fabricated, tested, and modeled as a proof of concept for on-chip silicon lasing elements.

The years of hard work that went into these successes were done for more than just scientific interest. The results and knowledge gained during the course of this thesis work will hopefully provide a pathway for the real optical engineering that must now take place. Improvements in the rapid testing of planar structures must be made, such as the development of a high-index microfabricated probe. Planar structures offer the promise of reduced strain, increasing the efficacy of thinner buffer layers. The possible incorporation of thin diffusion barriers, such as  $\text{SiN}_x$ , may make it possible to move  $\text{Er}^{3+}$  ions within a few tens of nanometers of the silicon surface. Partially etched structures also offer the promise of electrical tuning of the laser wavelength

through carrier-dependent plasma dispersion. These advances coupled with continued research into electrically pumped gain materials will aid in the development of the ultimate photonic component: an electrically-pumped high performance laser made alongside microelectronics in a CMOS compatible manner. Until such materials exist, the continued transition to planar erbium-doped cladding silicon structures integrated with electronic functionality will begin to take advantage of the economies of scale present in silicon photonics.

## Appendix A

# Time-Dependent Perturbation Theory

For high- $Q$  resonators, the quasi-modes of the optical cavity become an excellent basis set to represent the electric field inside the resonator. As radiation loss has already been taken into account in the basis, the remaining sources of loss in the resonator can be treated in a perturbative fashion. Using this technique, approximate formulas can in principle be derived for surface scattering and absorption as well as nonlinear effects such as nonlinear absorption or gain. In practice, the most useful of the perturbation approaches are for modal coupling and absorption effects because the small number of interacting modes. For example, surface roughness on microdisks will couple the degenerate clockwise (*cw*) and counterclockwise (*ccw*) modes [66]. Lifting this degeneracy creates a downshifted- and upshifted-frequency standing wave mode. Based on the work of Gorodetsky, *et al.* [63], a time-dependent perturbation theory was formulated to quantify this doublet splitting, but is generally applicable to any small real or imaginary dielectric perturbation. Starting from the time-dependent form of the master equation in Eq. (2.14), the assumption of a piecewise homogeneous media yields

$$\nabla^2 \mathbf{E} - \mu_0 (\epsilon^0 + \delta\epsilon) \frac{\partial^2 \mathbf{E}}{\partial t^2} = 0, \quad (\text{A.1})$$

where  $\epsilon^0(\mathbf{r})$  is the dielectric structure for the ideal resonator. The unperturbed modes with an assumed harmonic time dependence, denoted by  $\mathbf{E}_j^0(\mathbf{r}, t) = \mathbf{E}_j^0(\mathbf{r}) \exp(-i\omega_j t)$ , are a solution of

$$\nabla^2 \mathbf{E}_j^0(\mathbf{r}) + \mu_0 \epsilon^0(\mathbf{r}) \omega_j^2 \mathbf{E}_j^0(\mathbf{r}) = 0. \quad (\text{A.2})$$

Now assuming slowly varying envelopes  $a_j(t)$ , the perturbed modes are given by

$$\mathbf{E}(\mathbf{r}, t) = \exp(-i\omega_0 t) \sum_j a_j(t) \mathbf{E}_j^0(\mathbf{r}). \quad (\text{A.3})$$

Substituting Eq. (A.3) into Eq. (A.1) and keeping terms to first order yields

$$\sum_j \left( 2i\omega_0 \epsilon^0 \frac{da_j}{dt} + \delta\epsilon \omega_0^2 a_j - \epsilon^0 (\omega_j^2 - \omega_0^2) a_j \right) \mathbf{E}_j^0(\mathbf{r}) = 0. \quad (\text{A.4})$$

Using the fact that  $\int \epsilon^0 (\mathbf{E}_j^0(\mathbf{r}))^* \mathbf{E}_k^0(\mathbf{r}) d\mathbf{r} = 0$  for  $j \neq k$  (shown in Ref. [46]), Eq. (A.4) can be multiplied by  $(\mathbf{E}_j^0(\mathbf{r}))^*$  and integrated over all space to obtain

$$\frac{da_k}{dt} + i\Delta\omega_k a_k(t) = i \sum_j \beta_{jk} a_j, \quad (\text{A.5})$$

$$\text{with } \beta_{jk} = \frac{\omega_0 \int \delta\epsilon (\mathbf{E}_j^0(\mathbf{r}))^* \mathbf{E}_k^0(\mathbf{r}) d\mathbf{r}}{2 \int \epsilon^0 |\mathbf{E}_k^0(\mathbf{r})|^2 d\mathbf{r}}, \quad (\text{A.6})$$

where  $\Delta\omega_k = \omega_k - \omega_0$ .

## Appendix B

# Approximate $\bar{u}_s$ for the TM case

Considering the TM case only, the normalized disk-edge energy density,  $\bar{u}_s(\hat{\mathbf{z}})$  (defined in Eq. (5.13)), may be estimated analytically for low radial numbers [63]. Having an approximate form for  $\bar{u}_s(\hat{\mathbf{z}})$  is extremely important if we are to develop intuition from the previous results. As an approximation to the actual (unperturbed) normalized disk-edge energy density for all points within the disk-edge perturbations, an average value over a thin cylindrical shell is used. Defining the peak radial amplitude of the roughness to be  $\delta r$ , the averaged intensity is given by

$$|\mathbf{E}|_{s,avg}^2 = \frac{1}{\delta V} \int_{R-\delta r}^{R+\delta r} \int_{-h/2}^{h/2} \int_0^{2\pi} \rho d\rho d\phi dz |\mathbf{E}|^2, \quad (\text{B.1})$$

where  $\delta V = 4\pi\delta r R h$ . Note that while surface absorption reconstruction depth does not necessarily correlate with surface roughness amplitude, this mathematical formalism is identical with  $\zeta = 2\delta r$ . For high-index-contrast structures, the cavity mode energy can be approximated as existing only inside the cavity. Therefore we have,

$$U_c = \frac{1}{2} \int \epsilon^0(\mathbf{r}) |\mathbf{E}|^2 d\mathbf{r} \approx \frac{1}{2} \epsilon_0 n_d^2 \int_0^R \int_{-h/2}^{h/2} \int_0^{2\pi} \rho d\rho d\phi dz |\mathbf{E}|^2. \quad (\text{B.2})$$

Since the  $\phi$  and  $z$  integrations in Eqs. (B.1) and (B.2) are identical, only the radial integrals need to be considered. Since  $\mathbf{E} \sim J_m(k_0 \bar{n} \rho)$ , we can write

$$\bar{u}_s(\hat{\mathbf{z}}) = \frac{2}{n_d^2 \delta V} \frac{\int_{R-\delta r}^{R+\delta r} \rho d\rho [J_m(k_0 \bar{n} \rho)]^2}{\int_0^R \rho d\rho [J_m(k_0 \bar{n} \rho)]^2}. \quad (\text{B.3})$$

As an alternative to solving Eq. (B.3) numerically, a closed form expression can be

obtained by reintroducing the  $\delta$ -function approximation for the radial integral over the thin shell. Using several Bessel identities along with the continuity conditions for Maxwell's equations, Eq. (B.3) can be reduced to

$$\bar{u}_s(\hat{\mathbf{z}}) = \frac{[J_m(k_0\bar{n}R)]^2}{\pi h n_d^2 \int_0^R \rho d\rho [J_m(k_0\bar{n}\rho)]^2} \approx \frac{2\bar{n}^2}{V_d n_d^2 (\bar{n}^2 - n_0^2)}, \quad (\text{B.4})$$

where  $V_d = \pi R^2 h$ . This approximate form for  $\bar{u}_s(\hat{\mathbf{z}})$  shows that the sensitivity to the disk edge decreases as the radius of the disk is increased. Substituting Eq. (B.4) into Eqs. (5.12, 5.18, 5.21) gives the working equations for the analysis presented in the main text of this thesis:

$$Q_{ss} = \frac{3\lambda_0^3}{8\pi^{7/2} n_0 \delta n^2 \xi} \left( \frac{V_d}{V_s^2} \right), \quad (\text{B.5})$$

$$Q_\beta = \frac{1}{\sqrt{2}\pi^{3/4} \xi} \left( \frac{V_d}{V_s} \right), \quad (\text{B.6})$$

$$Q_{sa} = \frac{\pi c (\bar{n}^2 - n_0^2) R}{\lambda_0 \bar{n}^2 \gamma_{sa} \zeta}, \quad (\text{B.7})$$

where a relative dielectric contrast constant  $\xi$  is defined to be

$$\xi = \frac{\bar{n}^2 (n_d^2 - n_0^2)}{n_d^2 (\bar{n}^2 - n_0^2)}. \quad (\text{B.8})$$

This approximate form is plotted in Fig. B.1 and compared to FEM simulations for both polarizations. Note that one can convert between  $\bar{u}_s$  and  $\Gamma'_{\text{side}}$  with the relation:  $\Gamma'_{\text{side}} = \pi R h \tilde{n}^2 \bar{u}_s$ , where  $\tilde{n}^2 \equiv (n_d^2 + n_0^2)/2$ .

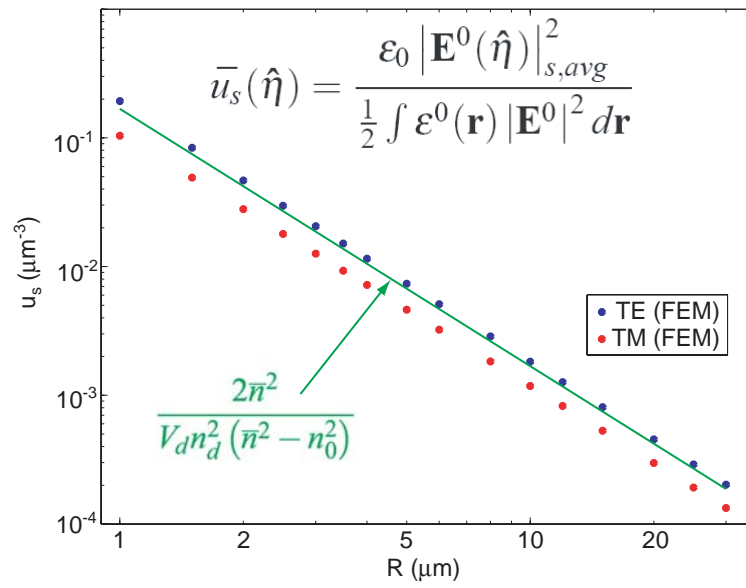


Figure B.1: Comparison of approximate form of  $\bar{u}_s(\hat{\mathbf{z}})$  and total  $\bar{u}_s$  calculated using the FEM.

# Bibliography

- [1] P. C. Becker, N. A. Olsson, and J. Simpson, *Erbium-Doped Fiber Amplifiers: Fundamentals and Technology* (Academic Press Inc., San Diego, 1999).
- [2] M. J. F. Digonnet, *Rare-Earth-Doped Fiber Lasers and Amplifiers, Second Ed.* (Marcel Dekker, New York, 2001).
- [3] R. A. Soref and J. P. Lorenzo, “All-Silicon Active and Passive Guided-Wave Components for  $\lambda = 1.3$  and  $1.6\mu\text{m}$ ,” *IEEE J. Quan. Elec.* **22**, 873–879 (1986).
- [4] R. A. Soref and B. R. Bennett, “Electrooptical effects in silicon,” *IEEE J. Quan. Elec.* **23**(1), 123–129 (1987).
- [5] D. A. Muller, “A sound barrier for silicon?” *Nature Materials* **4**, 645–647 (2005).
- [6] M. J. Kobrinisky, B. A. Block, J. Zheng, B. C. Barnett, E. Mohammed, M. Reshotko, F. Robertson, S. List, I. Young, and K. Cadien, “On-Chip Optical Interconnects,” *Intel Technology Journal* **08**(02), 129–141 (2004).
- [7] L. Pavesi and D. Lockwood, *Silicon Photonics* (Springer-verlag, New York, 2004).
- [8] G. Reed and A. Knights, *Silicon Photonics: An Introduction* (John Wiley, West Sussex, 2004).
- [9] A. Liu, R. Jones, L. Liao, D. Samara-Rubio, D. Rubin, O. Cohen, R. Nicolaescu, and M. Paniccia, “A high-speed silicon optical modulator based on a metal-oxide-semiconductor capacitor,” *Nature* **427**(6975), 615–618 (2004).
- [10] L. Liao, D. Samara-Rubio, M. Morse, A. Liu, D. Hodge, D. Rubin, U. D. Keil, and T. Franck, “High speed silicon Mach-Zehnder modulator,” *Opt. Express* **13**, 3129–3135 (2005).

- [11] V. R. Almeida, C. A. Barrios, R. R. Panepucci, and M. Lipson, “All-optical control of light on a silicon chip,” *Nature* **431**(7012), 1081–1084 (2004).
- [12] Q. Xu, B. Schmidt, S. Pradhan, and M. Lipson, “Micrometre-scale silicon electro-optic modulator,” *Nature* **435**(7040), 325–327 (2005).
- [13] S. F. Preble, Q. Xu, B. S. Schmidt, and M. Lipson, “Ultrafast all-optical modulation on a silicon chip,” *Opt. Lett.* **30**(21), 2891–2893 (2005).
- [14] M. Notomi, A. Shinya, S. Mitsugi, G. Kira, E. Kuramochi, and T. Tanabe, “Optical bistable switching action of Si high- $Q$  photonic-crystal nanocavities,” *Opt. Express* **13**(7), 2678–2687 (2005).
- [15] T. Tanabe, M. Notomi, S. Mitsugi, A. Shinya, and E. Kuramochi, “All-optical switches on a silicon chip realized using photonic-crystal nanocavities,” *Appl. Phys. Lett.* **87**(15), 151,112–1–151,112–3 (2005).
- [16] T. Tanabe, M. Notomi, S. Mitsugi, A. Shinya, and E. Kuramochi, “Fast bistable all-optical switch and memory on a silicon photonic crystal on-chip,” *Opt. Lett.* **30**(19), 2575–2577 (2005).
- [17] B. Song, S. Noda, T. Asano, and Y. Akahane, “Ultra-high- $Q$  photonic double-heterostructure nanocavity,” *Nature Materials* **4**, 207–210 (2005).
- [18] T. Asano, B. Song, and S. Noda, “Analysis of the experimental  $Q$  factor ( $/ 1$  million) of photonic crystal nanocavities,” *Opt. Express* **14**, 1996–2002 (2006).
- [19] K. Srinivasan and O. Painter, “Momentum space design of high- $Q$  photonic crystal optical cavities,” *Opt. Express* **10**(15), 670–684 (2002).
- [20] K. Srinivasan and O. Painter, “Fourier space design of high- $Q$  cavities in standard and compressed hexagonal lattice photonic crystals,” *Opt. Express* **11**(6), 579–593 (2003).
- [21] K. Srinivasan and O. Painter, “Analysis of localized TM defect states in two-dimensional photonic crystal slab waveguides,” *J. Opt. A* (2003). Manuscript in preparation.

- [22] K. Srinivasan, P. E. Barclay, O. Painter, J. Chen, A. Y. Cho, and C. Gmachl, “Experimental demonstration of a high quality factor photonic crystal microcavity,” *Appl. Phys. Lett.* **83**(10), 1915–1917 (2003).
- [23] O. Boyraz and B. Jalali, “Demonstration of a silicon Raman laser,” *Opt. Express* **12**(21), 5269–5273 (2004).
- [24] H. Rong, A. Liu, R. Jones, O. Cohen, D. Hak, R. Nicolaescu, A. Fang, and M. Paniccia, “An all-silicon Raman laser,” *Nature* **433**, 292–294 (2005).
- [25] H. Rong, R. Jones, A. Liu, O. Cohen, D. Hak, A. Fang, and M. Paniccia, “A continuous-wave Raman silicon laser,” *Nature* **433**, 725–728 (2005).
- [26] K. Okamoto, *Fundamentals of Optical Waveguides* (Academic Press, San Diego, 2000).
- [27] B. E. Little, “A VLSI Photonics Platform,” in *Optical Fiber Communication Conference* (2003).
- [28] M. Borselli, K. Srinivasan, P. E. Barclay, and O. Painter, “Rayleigh scattering, mode coupling, and optical loss in silicon microdisks,” *Appl. Phys. Lett.* **85**(17), 3693–3695 (2004).
- [29] D. W. Vernooy, V. S. Ilchenko, H. Mabuchi, E. W. Streed, and H. J. Kimble, “High- $Q$  measurements of fused-silica microspheres in the near infrared,” *Opt. Lett.* **23**(4), 247–249 (1998).
- [30] M. Cai, O. Painter, and K. Vahala, “Observation of critical coupling in a fiber taper to a silica-microsphere whispering-gallery mode system,” *Phys. Rev. Lett.* **85**(1), 74–77 (2000).
- [31] D. K. Armani, T. J. Kippenberg, S. M. Spillane, and K. J. Vahala, “Ultra-high- $Q$  toroid microcavity on a chip,” *Nature* **421**, 925–928 (2003).
- [32] M. Borselli, T. J. Johnson, and O. Painter, “Beyond the Rayleigh scattering limit in high- $Q$  silicon microdisks: theory and experiment,” *Opt. Express* **13**(5), 1515–1530 (2005).

- [33] K. Srinivasan, P. E. Barclay, M. Borselli, and O. Painter, “Optical-fiber-based measurement of an ultrasmall volume, high- $Q$  photonic crystal microcavity,” *Phys. Rev. B* **70**, 081,306(R) (2004).
- [34] M. Borselli, T. J. Johnson, and O. Painter, “Measuring the role of surface chemistry in silicon microphotonics,” *Appl. Phys. Lett.* **88**, 131,114 (2006).
- [35] M. Borselli, T. J. Johnson, and O. Painter, “Accurately measuring absorption in semiconductor microphotonics,” (2006). In preparation.
- [36] L. Rayleigh, “The Problem of the Whispering Gallery,” *Philosophical Magazine* **20**, 1001–1004 (1910).
- [37] A. Yariv and P. Yeh, *Photonics: Optical Electronics in Modern Communications*, 6th ed. (Oxford University Press, New York, 2007).
- [38] J. D. Jackson, *Classical Electrodynamics*, 2nd ed. (John Wiley & Sons, Inc., New York, NY, 1975).
- [39] K. Sakoda, *Optical Properties of Photonic Crystals* (Springer-Verlag, Berlin, Germany, 2001).
- [40] K. Srinivasan, M. Borselli, T. J. Johnson, P. E. Barclay, O. Painter, A. Stintz, and S. Krishna, “Optical loss and lasing characteristics of high-quality-factor AlGaAs microdisk resonators with embedded quantum dots,” *Appl. Phys. Lett.* **86**, 151,106 (2005).
- [41] K. Srinivasan, A. Stintz, S. Krishna, and O. Painter, “Photoluminescence measurements of quantum-dot-containing semiconductor microdisk resonators using optical fiber taper waveguides,” *Phys. Rev. B* **72**, 205,318 (2005).
- [42] K. Srinivasan, M. Borselli, O. Painter, A. Stintz, and S. Krishna, “Cavity  $Q$ , mode volume, and lasing threshold in small diameter AlGaAs microdisks with embedded quantum dots,” *Opt. Express* **14**(3), 1094–1105 (2006).
- [43] P. Blood, “On the Dimensionality of Optical Absorption, Gain, and Recombination in Quantum-Confined Structures,” *IEEE J. Quan. Elec.* **36**(3), 354–362 (2000).

- [44] A. Yariv, *Optical Electronics*, 4th ed. (Saunders College Publishing, Orlando, 1991).
- [45] B. E. Little and S. T. Chu, "Estimating surface-roughness loss and output coupling in microdisk resonators," *Opt. Lett.* **21**, 1390–1392 (1996).
- [46] J. D. Joannopoulos, R. D. Meade, and J. N. Winn, *Photonic Crystals* (Princeton University Press, Princeton, New Jersey, 1995).
- [47] J. Jin, *The Finite Element Method in Electromagnetics, Second Ed.* (Wiley-IEEE Press, New York, 2002).
- [48] S. M. Spillane, "Fiber-coupled Ultra-high- $Q$  Microresonators for Nonlinear and Quantum Optics," Ph.D. thesis, California Institute of Technology (2004).
- [49] S. M. Spillane, T. J. Kippenberg, K. J. Vahala, K. W. Goh, E. Wilcut, and H. J. Kimble, "Ultrahigh- $Q$  toroidal microresonators for cavity quantum electrodynamics," *Phys. Rev. A* **71**(1), 013,817 (2005).
- [50] R. K. Chang and A. J. Campillo, eds., *Optical Processes in Microcavities* (World Scientific, Singapore, 1996).
- [51] T. J. A. Kippenberg, "Nonlinear Optics in Ultra-high- $Q$  Whispering-Gallery Optical Microcavities," Ph.D. thesis, California Institute of Technology (2004).
- [52] E. Palik, *Handbook of Optical Constants of Solids* (Academic Press Inc., New York, 1985).
- [53] S. Wolf and R. N. Tauber, *Silicon Processing for the VLSI era* (Lattice Press, Sunset Beach, California, 1986).
- [54] M. Haverlag, D. Vender, and G. S. Oehrlein, "Ellipsometric study of silicon surface damage in electron cyclotron resonance plasma etching using  $\text{CF}_4$  and  $\text{SF}_6$ ," *Appl. Phys. Lett.* **61**(24), 2875–2877 (1992).
- [55] S. M. Spillane, T. J. Kippenberg, O. J. Painter, and K. J. Vahala, "Ideality in a fiber-taper-coupled microresonator system for application to cavity quantum electrodynamics," *Phys. Rev. Lett.* **91**, 043,902 (2003).

- [56] T. Baehr-Jones, M. Hochberg, C. Walker, and A. Scherer, “High-Q ring resonators in thin silicon-on-insulator,” *Appl. Phys. Lett.* **85**(16), 3346–3347 (2004).
- [57] D. K. Sparacin, S. J. Spector, and L. C. Kimerling, “Silicon Waveguide Sidewall Smoothing by Wet Chemical Oxidation,” *J. Lightwave Tech.* **23**(8), 2455–2461 (2005).
- [58] K. Srinivasan, P. E. Barclay, M. Borselli, and O. Painter, “An optical fiber-based probe for photonic crystal microcavities,” *IEEE Journal on Selected Areas in Communications* **23**(7), 132–139 (2005).
- [59] J. Knight, G. Cheung, F. Jacques, and T. Birks, “Phase-matched excitation of whispering-gallery-mode resonances by a fiber taper,” *Opt. Lett.* **22**(15), 1129–1131 (1997).
- [60] C. Grillet, C. Smith, D. Freeman, S. Madden, B. Luther-Davies, E. C. Magi, D. J. Moss, and B. J. Eggleton, “Efficient Coupling to Chalcogenide Glass Photonic Crystal Waveguides via Silica Optical Fiber Nanowires,” *Opt. Express* **14**(3), 1070–1078 (2006).
- [61] H. A. Haus, *Waves and Fields in Optoelectronics*, 1st ed. (Prentice-Hall, Englewood Cliffs, New Jersey 07632, 1984).
- [62] H. A. Haus, W. P. Huang, and A. W. Snyder, “Coupled-mode formulations,” *Opt. Lett.* **14**(21), 1222–1224 (1989).
- [63] M. Gorodetsky, A. Pryamikov, and V. Ilchenko, “Rayleigh scattering in high-Q microspheres,” *J. Opt. Soc. Am. B* **17**(6), 1051–1057 (2000).
- [64] A. W. Snyder and J. D. Love, *Optical Waveguide Theory* (Chapman and Hall, New York, NY, 1983).
- [65] S. G. Johnson, M. Ibanescu, M. A. Skorobogatiy, O. Weisberg, J. D. Joannopoulos, and Y. Fink, “Perturbation theory for Maxwell’s equations with shifting material boundaries,” *Phys. Rev. E* **65**, 066,611 (2002).

- [66] D. Weiss, V. Sandoghdar, J. Hare, V. Lefèvre-Seguin, J. Raimond, and S. Haroche, “Splitting of high- $Q$  Mie modes induced light backscattering in silica microspheres,” *Opt. Lett.* **22**, 1835–1837 (1995).
- [67] T. J. Kippenberg, S. M. Spillane, and K. J. Vahala, “Modal coupling in traveling-wave resonators,” *Opt. Lett.* **27**, 1669–1671 (2002).
- [68] C. Manolatou, M. J. Khan, S. Fan, P. R. Villeneuve, H. A. Haus, and J. D. Joannopoulos, “Coupling of Modes Analysis of Resonant Channel Add-Drop Filters,” *IEEE J. Quan. Elec.* **35**(9), 1322–1331 (1999).
- [69] L. A. Coldren and S. W. Corzine, *Diode Lasers and Photonic Integrated Circuits* (John Wiley & Sons, Inc., New York, NY, 1995).
- [70] P. E. Barclay, K. Srinivasan, M. Borselli, and O. Painter, “Experimental demonstration of evanescent coupling from optical fibre tapers to photonic crystal waveguides,” *IEE Elec. Lett.* **39**(11), 842–844 (2003).
- [71] P. E. Barclay, K. Srinivasan, M. Borselli, and O. Painter, “Probing the dispersive and spatial properties of planar photonic crystal waveguide modes via highly efficient coupling from optical fiber tapers,” *Appl. Phys. Lett.* **85**(1) (2004).
- [72] P. E. Barclay, K. Srinivasan, M. Borselli, and O. Painter, “Efficient input and output optical fiber coupling to a photonic crystal waveguide,” *Opt. Lett.* **29**(7), 697–699 (2004).
- [73] K. Srinivasan, P. Barclay, and O. Painter, “Fabrication-tolerant high quality factor photonic crystal microcavities,” *Opt. Express* **12**(7), 1458–1463 (2004).
- [74] B. E. Little, S. T. Chu, W. Pan, D. Ripin, T. Kaneko, Y. Kokubun, and E. Ippen, “Vertically Coupled Glass Microring Resonator Channel Dropping Filters,” *IEEE Photonics Tech. Lett.* **11**(2), 215–217 (1999).
- [75] V. S. Ilchenko, A. A. Savchenkov, A. B. Matsko, and L. Maleki, “Nonlinear Optics and Crystalline Whispering Gallery Mode Cavities,” *Phys. Rev. Lett.* **92**, 043,903 (2004).

- [76] H. J. Kimble, “Strong Interactions of Single Atoms and Photons in Cavity QED,” *Physica Scripta* **T76**, 127–137 (1998).
- [77] S. M. Spillane, T. J. Kippenberg, and K. J. Vahala, “Ultralow-threshold Raman laser using spherical dielectric microcavity,” *Nature* **415**, 621–623 (2002).
- [78] B. Gayral, J. M. Gérard, A. Lemaître, C. Dupuis, L. Manin, and J. L. Pelouard, “High- $Q$  wet-etched GaAs microdisks containing InAs quantum boxes,” *Appl. Phys. Lett.* **75**(13), 1908–1910 (1999).
- [79] S. J. Choi, Q. Yang, Z. Peng, S. J. Choi, and P. D. Dapkus, “High- $Q$  Buried Heterostructure Microring Resonators,” in *Conference on Lasers and Electro-Optics*, OSA Technical Digest Series (2004). CThF1.
- [80] M. Kuznetsov and H. A. Haus, “Radiation Loss in Dielectric Waveguide Structures by the Volume Current Method,” *IEEE J. Quan. Elec.* **19**(10), 1505–1514 (1983).
- [81] B. E. Little, J.-P. Laine, and S. T. Chu, “Surface-Roughness-Induced Contradirectional Coupling in Ring and Disk Resonators,” *Opt. Lett.* **22**, 4–6 (1997).
- [82] E. Yablonovitch, D. L. Allara, C. C. Chang, T. Gmitter, and T. B. Bright, “Unusually Low Surface-Recombination Velocity on Silicon and Germanium Surfaces,” *Phys. Rev. Lett.* **57**(2), 249–252 (1986).
- [83] P. E. Barclay, K. Srinivasan, and O. Painter, “Nonlinear response of silicon photonic crystal microresonators excited via an integrated waveguide and a fiber taper,” *Opt. Express* **13**(3), 801–820 (2005).
- [84] V. R. Almeida and M. Lipson, “Optical bistability on a silicon chip,” *Opt. Lett.* **29**(20), 2387–2389 (2004).
- [85] H. Rokhsari, S. M. Spillane, and K. J. Vahala, “Loss characterization in microcavities using the thermal bistability effect,” *Appl. Phys. Lett.* **85**(15), 3029–3031 (2004).
- [86] D. V. Lang, “Deep-level transient spectroscopy: A new method to characterize traps in semiconductors,” *J. Appl. Phys.* **45**(7), 3023–3032 (1974).

- [87] J. Linnros, “Carrier lifetime measurements using free carrier absorption transients. II. Lifetime mapping and effects of surface recombination,” *J. Appl. Phys.* **84**(1), 284–291 (1998).
- [88] A. Chantre, G. Vincent, and D. Bois, “Deep-level optical spectroscopy in GaAs,” *Phys. Rev. B* **23**(10), 5335–5358 (1981).
- [89] I. M. P. Aarts, B. Hoex, A. H. M. Smets, R. Engeln, W. M. M. Kessels, and M. C. M. van de Sanden, “Direct and highly sensitive measurement of defect-related absorption in amorphous silicon thin films by cavity ringdown spectroscopy,” *Appl. Phys. Lett.* **84**(16), 3079–3081 (2004).
- [90] W. B. Jackson and N. M. Amer, “Direct measurement of gap-state absorption in hydrogenated amorphous silicon by photothermal deflection spectroscopy,” *Phys. Rev. B* **25**(8), 5559–5562 (1982).
- [91] G. Amato and F. Fizzotti, “Gap-states distribution in amorphous-silicon films as obtained by photothermal deflection spectroscopy,” *Phys. Rev. B* **45**(24), 14,108–14,113 (1992).
- [92] Y. Chabal, G. Higashi, and K. Raghavachari, “Infrared spectroscopy of Si(111) and Si(100) surfaces after HF treatment: Hydrogen termination and surface morphology,” *J. Vac. S. Tech. A* **7**(3), 2104–2109 (1989).
- [93] D. Fenner, D. Biegelsen, and R. Bringans, “Silicon surface passivation by hydrogen termination: A comparative study of preparation methods,” *J. Appl. Phys.* **66**(1), 419–424 (1989).
- [94] Y. Sugita and S. Watanabe, “In Situ Infrared Spectroscopy on the Wet Chemical Oxidation of Hydrogen-Terminated Si Surfaces,” *Jap. J. Appl. Phys.* **37**, 3272–3277 (1998).
- [95] Y. Yamashita, A. Asano, Y. Nishioka, and H. Kobayashi, “Dependence of interface states in the Si band gap on oxide atomic density and interfacial roughness,” *Phys. Rev. B* **59**(24), 872–881 (1999).

- [96] H. Kobayashi, Y. Yamashita, Y. Nakato, T. Komeda, and Y. Nishioka, "Interface states at ultrathin oxide/Si(111) interfaces obtained from x-ray photoelectron spectroscopy measurements under biases," *Appl. Phys. Lett.* **69**(15), 2276–2278 (1996).
- [97] F. Li, M. K. Balazs, and S. Anderson, "Effects of Ambient and Dissolved Oxygen Concentration in Ultrapure Water on Initial Growth of Native Oxide on a Silicon (100) Surface," *J. Electrochem. Soc.* **152**(8), G669–G673 (2005).
- [98] S. Petitdidier, V. Bertagna, N. Rochat, D. Rouchon, P. Besson, R. Erre, and M. Chemla, "Growth mechanism and characterization of chemical oxide films produced in peroxide mixtures on Si(100) surfaces," *Thin Solid Films* **476**, 51–58 (2005).
- [99] Y. Yamashita, K. Namba, Y. Nakato, , Y. Nishioka, and H. Kobayashi, "Spectroscopic observation of interface states of ultrathin silicon oxide," *J. Appl. Phys.* **79**(9), 7051–7057 (1996).
- [100] G. Cocorullo and I. Rendina, "Thermo-optical modulation at 1.5  $\mu\text{m}$  in silicon etalon," *IEE Elec. Lett.* **28**, 83–85 (1992).
- [101] C. A. Barrios, V. R. Almeida, R. R. Panepucci, B. S. Schmidt, and M. Lipson, "Compact Silicon Tunable Fabry-Pérot Resonator With Low Power Consumption," *IEEE Photonics Tech. Lett.* **16**, 506–508 (2004).
- [102] S. J. Choi, K. D. Djrodjev, Z. Peng, Q. Yang, S. J. Choi, and P. D. Dapkus, "A high-Q wavelength filter based on buried heterostructure ring resonators integrated with a semiconductor optical amplifier," *IEEE Photonics Tech. Lett.* **17**, 2101–2103 (2004).
- [103] M. A. Webster, R. M. Pafchek, G. Sukumaran, and T. L. Koch, "Low-loss quasi-planar ridge waveguides formed on thin silicon-on-insulator," *Appl. Phys. Lett.* **87**, 231,108 (2005).
- [104] I. Alvarado-Rodriguez and E. Yablonovitch, "Separation of radiation and absorption losses in two-dimensional photonic crystal single defect cavities," *J. Appl. Phys.* **92**(11), 6399–6402 (2002).

- [105] H. M. Gibbs, *Optical Bistability: Controlling Light with Light* (Academic Press Inc., Orlando, 1985).
- [106] A. R. Stivers and C. T. Sah, “A study of oxide traps and interface states of the silicon-silicon dioxide interface,” *J. Appl. Phys.* **51**(12), 6292–6304 (1980).
- [107] C. T. Sah and J. W. Walker, “Thermally stimulated capacitance for shallow majority-carrier traps in the edge region of semiconductor junctions,” *Appl. Phys. Lett.* **22**(8), 384–386 (1973).
- [108] J. Zhao, A. Wang, P. Altermatt, and M. A. Green, “Twenty-four percent efficient silicon solar cells with double layer antireflection coatings and reduced resistance loss,” *Appl. Phys. Lett.* **66**, 3636–3638 (1995).
- [109] M. A. Green, “Photovoltaic Principles,” *Physica E* **14**, 11–17 (2002).
- [110] J. Schmidt, M. Kerr, and A. Cuevas, “Surface passivation of silicon solar cells using plasma-enhanced chemical-vapour-deposited SiN films and thin thermal SiO<sub>2</sub>/plasma SiN stacks,” *Semiconductor Science and Technology* **16**, 167–170 (2001).
- [111] M. McCann, K. Weber, and A. Blakers, “Surface Passivation by Rehydrogenation of Silicon-nitride-coated Silicon Wafers,” *Progress in Photovoltaics: Research and Applications* **13**, 195–200 (2005).
- [112] H. T. Hattori, C. Seassal, E. Touraille, P. Rojo-Romeo, X. Letartre, G. Hollinger, P. Viktorovitch, L. D. Cioccio, M. Zussy, L. E. Melhaoui, and J. M. Fedeli, “Heterogenous Integration of Microdisk Lasers on Silicon Strip Waveguides for Optical Interconnects,” *IEEE Photonics Tech. Lett.* **18**, 223–225 (2006).
- [113] R. J. Walters, G. I. Bourianoff, and H. A. Atwater, “Field-effect electroluminescence in silicon nanocrystals,” *Nature Materials* **4**, 143–146 (2005).
- [114] S. G. Cloutier, P. A. Kosyrev, and J. Xu, “Optical gain and stimulated emission in periodic nanopatterned crystalline silicon,” *Nature Materials* **4**, 887–891 (2005).

- [115] M. A. Green, J. Zhao, A. Wang, P. J. Reece, and M. Gal, “Efficient silicon light-emitting diodes,” *Nature (London)* **412**, 805–808 (2001).
- [116] M. A. Green, J. Zhao, A. Wang, and T. Trupke, “High-efficiency silicon light-emitting diodes,” *Physica E* **16**, 351–358 (2003).
- [117] T. J. Kippenberg, S. M. Spillane, D. K. Armani, and K. J. Vahala, “Ultralow-threshold microcavity Raman laser on a microelectronic chip,” *Opt. Lett.* **29**, 1224–1226 (2004).
- [118] L. Yang, T. Carmon, B. Min, S. M. Spillane, and K. J. Vahala, “Erbium-doped and Raman microlasers on a silicon chip fabricated by the sol-gel process,” *Appl. Phys. Lett.* **86**, 091,114 (2005).
- [119] P. A. Temple and C. E. Hathaway, “Multiphonon Raman Spectrum of Silicon,” *Phys. Rev. A* **7**, 3685 (1973).
- [120] T. J. Johnson, M. Borselli, and O. Painter, “Self-induced optical modulation of the transmission through a high- $Q$  silicon microdisk resonator,” *Opt. Express* **14**(2), 817–831 (2006).
- [121] P. G. Kik and A. Polman, “Erbium-Doped Optical-Waveguide Amplifier on Silicon,” *MRS Bulletin* pp. 48–54 (April 1998).
- [122] J. Shmulovich, A. wong, Y. H. Wong, P. C. Becker, A. J. Bruce, and R. Adar, “Er<sup>3+</sup> Glass Waveguide Amplifier at 1.5  $\mu\text{m}$  on Silicon,” *IEE Elec. Lett.* **28**(13), 1181–1182 (1992).
- [123] R. N. Ghosh, J. Shmulovich, C. F. Kane, M. R. X. de Barros, G. Hykolak, A. J. Bruce, and P. C. Becker, “8-mW threshold Er<sup>3+</sup>-Doped Planar Waveguide Amplifier,” *IEEE Photonics Tech. Lett.* **8**(4), 518–520 (1996).
- [124] L. Yang and K. J. Vahala, “Gain functionalization of silica microresonators,” *Opt. Lett.* **28**(8), 592–594 (2003).
- [125] L. Yang, D. K. Armani, and K. J. Vahala, “Fiber-coupled erbium microlasers on a chip,” *Appl. Phys. Lett.* **83**(5), 825–826 (2003).

- [126] A. Polman, B. Min, J. Kalkman, T. J. Kippenberg, and K. J. Vahala, “Ultralow-threshold erbium-implanted toroidal microlaser on silicon,” *Appl. Phys. Lett.* **84**(7), 1037–1039 (2004).
- [127] B. Min, T. J. Kippenberg, L. Yang, and K. J. Vahala, “Erbium-implanted high- $Q$  silica toroidal microcavity laser on a silicon chip,” *Phys. Rev. A* **70**, 033,803 (2004).
- [128] C. R. Giles and E. Desurvire, “Modeling Erbium-Doped Fiber Amplifiers,” *J. Lightwave Tech.* **9**(2), 271–283 (1991).
- [129] Y. Yamamoto and G. Björk, “Lasers without Inversion in Microcavities,” *Jap. J. Appl. Phys.* **30**(12A), 2039–2041 (1991).
- [130] G. Björk and Y. Yamamoto, “Analysis of Semiconductor Microcavity Lasers Using Rate Equations,” *IEEE J. Quan. Elec.* **27**(11), 2386–2396 (1991).
- [131] G. Björk, A. Karlsson, and Y. Yamamoto, “Definition of a laser threshold,” *Phys. Rev. A* **50**(2), 1675–1680 (1994).
- [132] C. H. Henry, “Theory of the Phase Noise and Power Spectrum of a Single Mode Injection Laser,” *IEEE J. Quan. Elec.* **19**(9), 1391–1397 (1983).
- [133] O. J. Painter, “Optical Nanocavities in Two-Dimensional Photonic Crystal Planar Waveguides,” Ph.D. thesis, California Institute of Technology (2001).
- [134] B. N. Samson, W. H. Loh, and J. de Sandro, “Experimental evidence of differences in the absorption spectra of clustered and isolated ions in erbium-doped fibers,” *Opt. Lett.* **22**(23), 1763–1765 (1997).
- [135] B. Monemar, “Fundamental energy gap of GaN from photoluminescence excitation spectra,” *Phys. Rev. B* **10**(2), 676–681 (1974).